

ABSTRACT

Title of Document: MADDEN-JULIAN OSCILLATION AND SEA SURFACE TEMPERATURE INTERACTIONS IN A MULTI-SCALE FRAMEWORK

Lei Zhou, Ph. D., 2009

Directed By: Prof. Murtugudde, Department of Atmospheric and Oceanic Sciences/ESSIC

The ocean-atmosphere coupling can play a role in initiating and sustaining the Madden-Julian Oscillations (MJOs), which are the major intraseasonal oscillations in the atmosphere. In this thesis, the oceanic influence on MJOs is studied with reanalysis products, numerical models, and idealized theoretical models.

The energy sources for MJOs are calculated with NCEP reanalysis. The perturbed potential energy is found to be the most important energy source for most MJO events. In some MJO events, the sea surface is warmed due to the reduced latent heat flux during the suppressed phase of MJOs. As a result, warm sea surface temperature anomalies (SSTAs) occur, which appear to prolong the life time of these MJO events. In a minority of the MJO events, warm SSTAs can drive the atmosphere actively and trigger MJO events. In these events, the warm SSTAs are attributable to the internal oceanic processes influenced by the warm Indonesian Throughflow (ITF), which spreads from the southeastern Indian Ocean to the western Indian Ocean and modifies

the subtle balance between stratification and mixing in the western Indian Ocean. In addition, during the transit period between monsoon seasons, a few MJO events are sustained by the energy obtained from the mean kinetic energy. Since the MJO events have different energy sources, their mechanisms should be considered in the context of these energy sources.

While the spatial scale of the SSTAs in the Indian Ocean is only of order 100 km, the scale of MJOs is of order 1000 km, raising the potential for interactions between the oceanic and the atmospheric oscillations with different scales and this is demonstrated to be possible with analytical solutions to idealized linear governing equations. With a reasonable choice of parameters, the meso-scale oceanic and the large-scale atmospheric oscillations can interact with each other and lead to unstable waves in the intraseasonal band in this linear coupled model. The coupling and frequency shifts between oscillations with different scales and the atmospheric/oceanic responses to small variations in the external forcing are also tested with numerical models.

Incorporating the oceanic influence on MJOs and the multi-scale interaction appropriately in a numerical model is supposed to help improve the simulation and forecast of MJOs. The hypothesis of multi-scale interaction is also expected to have wide applications in other studies, in addition to the MJO-SST interaction. The theoretical and numerical approach adopted here should also serve as a prototype for enhancing the process understanding of intraseasonal variability and lead to improved predictive understanding.

MADDEN-JULIAN OSCILLATION AND SEA SURFACE TEMPERATURE
INTERACTIONS IN A MULTI-SCALE FRAMEWORK

By

Lei Zhou

Dissertation submitted to the Faculty of the Graduate School of the
University of Maryland, College Park, in partial fulfillment
of the requirements for the degree of
Doctor of Philosophy
2009

Advisory Committee:

Professor Raghu Murtugudde, Chair
Dr. Markus Jochum
Professor Antonio Busalacchi
Professor James Carton
Professor Sumant Nigam
Associate Professor Michael Evans

© Copyright by
Lei Zhou
2009

Acknowledgements

I would like to express my deep gratitude to Prof. Raghu Murtugudde. He grants me enormous free space to explore my own research interest. Meanwhile, his insightful guidance leads me to the right way and his continuous encouragements keep me rolling on this way. In addition, he provides me various and abundant opportunities to prepare myself for future career, such as giving presentations in conferences, giving lectures in classes, reviewing journal papers, and writing proposals. I am sincerely thankful to Dr. Markus Jochum for invaluable and heuristic suggestions on all my work ever since the first one until the current dissertation. Special thanks go to Prof. Antonio Busalacchi, who lent me powerful supports during my application to the postdoc position. I am also indebted to Eric Hackert and James Beauchamp for their great help during my work.

I really enjoy my life in Maryland for the past four years. All faculties in AOSC and ESSIC are supportive, all staff are helpful, and all students are nice and friendly. I cannot explicitly mention everyone's name in this acknowledgement due to limited space. For me, the joyful experience is as important as the scientific knowledge I learned here. Especially, I am grateful to Dr. Quanan Zheng for his considerate advice on many things, which makes my life much easier in the US.

Most importantly, I have to thank my family from the bottom of my heart, my parents, my wife, and my brother. None of my achievements so far would have been possible without their firm supports and endless love.

I appreciate the NASA Earth System Science Program for the financial support. The computing resources supporting the work in Chapter 4.2 are provided by the NASA High-End Computing (HEC) Program through the NASA Center for Computational Sciences (NCCS) at Goddard Space Flight Center.

Table of Contents

Acknowledgements.....	ii
Table of Contents.....	iii
List of Tables	v
List of Figures.....	vi
Chapter 1: Introduction.....	1
1.1 Theories and simulations of Madden-Julian Oscillations.....	1
1.2 Oceanic intraseasonal variabilities in the tropical and southern Indian Ocean ..	5
1.3 Ocean-atmosphere interaction in a multi-scale system.....	8
1.4 Thesis organization.....	10
Chapter 2: OISVs in the SWIO.....	11
2.1 Dynamics of the intraseasonal oscillations in the Indian Ocean South Equatorial Current	11
2.1.1 Introduction.....	11
2.1.2 Model description and comparison.....	13
2.1.3 Properties of ISOs in the SWIO.....	15
2.1.4 Dynamic processes responsible for OISOs in the SWIO.....	18
2.1.5 Conclusions and discussions.....	29
2.2 Seasonal influence of Indonesian Throughflow in the southwestern Indian Ocean	32
2.2.1 Introduction.....	32
2.2.2 Model description and comparison.....	34
2.2.3 Westward propagation of the ITF waters.....	38
2.2.4 Influence of ITF on the dynamics in the SWIO: Scale selection.....	46
2.2.5 Influence of ITF on the SSTs in SWIO	46
2.2.6 Discussion and conclusion.....	54
2.2.7 Appendix.....	56
Chapter 3: Energy sources for Madden-Julian Oscillations	58
3.1 Introduction.....	58
3.2 Data and reanalysis products	60
3.3 Energy sources for the MJO events	63
3.3.1 Events where $P' \cdot K'$ dominates	68
3.3.2 The events with dominant R'	77
3.3.3 The events where $K' \cdot \bar{K}$ dominates.....	81
3.4 Conclusions and discussion	83
3.5 Appendix.....	87

Chapter 4: Ocean-Atmosphere coupling on distinct scales	89
4.1 Ocean-atmosphere coupling on different spatio-temporal scales: A mechanism for intraseasonal instabilities.....	89
4.1.1 Introduction.....	89
4.1.2 Coupled system.....	93
4.1.3 Discussion on the approximations	110
4.1.4 Conclusions.....	112
4.2 Frequency shifts in the ocean and the atmosphere in response to small forcing changes.....	116
4.2.1 Introduction.....	117
4.2.2 Theory	122
4.2.3 Model experiments with realistic configurations.....	136
4.2.4 Conclusions and discussion	150
Chapter 5: Conclusions and future plans	154
5.1 Summary	154
5.2 Significance of current results	159
5.3 Implications and future plans.....	161
Bibliography	169

List of Tables

Table 3.1 The MJO events defined based on the MJO index (Wheeler and Hendon 2004) and the two criteria in the main text.	62
Tabel 4.1.1 Parameters used in the analytical solutions. They are selected based on Anderson and McCreary (1985).	98

List of Figures

Figure 1.1 Outgoing longwave radiation (OLR) anomalies (after band-pass filtering with cut-off periods of 20-100 days) for the eight phases of MJOs, which are defined with the daily MJO index from 1979 to 2006 (Wheeler and Hendon 2004). The unit is W m^{-2} .	2
Figure 1.2 Sea surface heights (SSH) from TOPEX/POSEIDON data averaged between 8°S and 12°S after a band-pass filtering with the cut-off periods of 20 and 100 days. The unit is cm.	6
Figure 1.3 Mean temperature from SODA (Carton et al. 2000a, b) over 10 years, averaged between 5°S and 10°S .	7
Figure 2.1.1 <i>RMS</i> of intraseasonal SSHAs of 20-year model simulations (a) and of TOPEX/POSEIDON data from 1992 – 2006 (b) and the <i>RMS</i> of the annual mean values for the 20-year model simulations (c) and the 15-year TOPEX/POSEIDON data (d). All fields are cm.	15
Figure 2.1.2 Intraseasonal model SSHAs at 6°S , 66°E for four years and the corresponding wavelet spectrum (both in cm).	16
Figure 2.1.3 Longitude-time plot of model intraseasonal SSHAs along 8°S .	17
Figure 2.1.4 Annual mean of $q_y = \beta - U_{yy}$ (a) and $q_y = \beta - U_{yy} - (f_0^2 U_z / N^2)_z$ (b). The black contour is the contour of zero. The units are $10^{10} \text{ m}^{-1} \text{ s}^{-1}$.	20
Figure 2.1.5 Barotropic (a) and baroclinic (b) energy conversions averaged over twenty years and above the thermocline in the SWIO.	21
Figure 2.1.6 Baroclinic energy conversion (in 10^{-3} W m^{-3}) averaged over twenty years and above the thermocline in 4 months.	23
Figure 2.1.7 Longitude-depth plots of baroclinic energy conversions for January, April, July, and December. The contour interval is $1 \times 10^{-3} \text{ W m}^{-3}$. Regions with positive values are shaded.	24
Figure 2.1.8 Vertical shears of zonal currents around the thermocline ($\sim 100 \text{ m}$) along 8°S for 6 random years (contours) superposed with the baroclinic energy conversions (shaded area). The units for velocity shear are 10^{-3} s^{-1} . The light gray area shows the energy conversion of $1 \times 10^{-2} \text{ W m}^{-3}$ and the dark gray shows that of $4 \times 10^{-2} \text{ W m}^{-3}$.	25
Figure 2.1.9 Vertical profiles of squared Brunt-Väisälä frequency (a) and the eigenfunctions of the first three baroclinic modes (b).	27
Figure 2.1.10 Projections of intraseasonal velocities onto the first two baroclinic modes in four years.	28
Figure 2.1.11 Baroclinic energy conversion of the first baroclinic mode (a), of the second baroclinic mode (b), of the first baroclinic mode in December (c), and of the second baroclinic mode in December (d). The unit is 10^{-3} W m^{-3} .	29
Figure 2.2.1 Mean SSTs of the 20-year model outputs (a) and of AVHRR data averaged from 1992-2005 (b). (c) and (d) are the same as (a) and (b) but for the <i>STDs</i> . All fields are $^{\circ}\text{C}$. The contour interval for the mean SSTs is 1°C , and for	

the $STDs$ is $0.4^{\circ}C$. The SWIO, which is defined as a rectangular region from $5^{\circ}S$ to $8^{\circ}S$ and from $63^{\circ}E$ to $73^{\circ}E$, is identified with a thick rectangle in (a). The Karimata Strait, which is open in the Java run, is identified with an oval in (a).	37
Figure 2.2.2 Zonal velocity (a), potential density (b), Ertel potential vorticity (c), and zonal temperature advection (d) averaged from $10^{\circ}S$ to $15^{\circ}S$ along $114^{\circ}E$ in three years.	38
Figure 2.2.3 T - S diagram of the monthly 20-year mean model outputs. The circles represent the T - S at 20 meters below and above those represented by the crosses in the same color. Each symbol represents T - S at one specific depth, latitude, and longitude, as shown in the legend. For example, the twelve black crosses represent the T - S properties at two layers (50 m and 60 m), one longitude point ($113^{\circ}E$), and six latitude points (from $12^{\circ}S$ to $14^{\circ}S$ with a latitudinal resolution of $1/3^{\circ}$).	40
Figure 2.2.4 EPV (a) and horizontal temperature advection (b) projected onto the surface of $\sigma_0 = 23.3$ along $6^{\circ}S$ from $63^{\circ}E$ - $81^{\circ}E$, along $8^{\circ}S$ from $81^{\circ}E$ - $92^{\circ}E$, and along $12^{\circ}S$ from $92^{\circ}E$ - $115^{\circ}E$, which are smoothed with 5° zonal running mean. The latitude shift from $12^{\circ}S$ to $6^{\circ}S$ follows the spreading of ITF waters shown in Fig. 3. The contours in (a) are the wind stress curl ($10^{-6} Pa m^{-1}$) and the contours in (b) are the zonal velocities on the $\sigma_0 = 23.3$ surface in $m s^{-1}$.	41
Figure 2.2.5 (a) Mean Brunt-Väisälä frequency (shades in $10^{-2} s^{-1}$) and the vertical temperature gradient (contours in $K m^{-1}$) within a rectangular region $6^{\circ}S$ - $7^{\circ}S$, $63^{\circ}E$ - $73^{\circ}E$, calculated with the model outputs. (b) The same as (a), but calculated with the monthly high-resolution WOA.	42
Figure 2.2.6 The intraseasonal SSTAs and SSHs averaged in the SWIO ($6^{\circ}S$ - $7^{\circ}S$, $63^{\circ}E$ - $73^{\circ}S$) in the Java run (solid line) and in the control run (dash line).	44
Figure 2.2.7 Wavelength of the maximum instability ($L_{max} = 3.9L_d$) in December (a) and the inverse of the corresponding maximum growth rate ($\sigma_{max} = 0.3U/L_d$) in December (b).	45
Figure 2.2.8 SST variation, net surface heat flux, entrainment, and horizontal temperature advection averaged within a rectangular region $6^{\circ}S$ - $7^{\circ}S$, $63^{\circ}E$ - $73^{\circ}E$, which are smoothed with the one-month running mean. Positive values mean that the upper mixed layer gain heat, while negative values mean that the upper mixed layer lose heat.	47
Figure 2.2.9 Temperature variations (color codes) and mixed layer depth (solid line), which are averaged in the region of $6^{\circ}S$ - $7^{\circ}S$, $63^{\circ}E$ - $73^{\circ}E$.	48
Figure 2.2.10 Solar radiation penetration heating rate (shades, in the unit of $K/month$) and the barrier layer depth (contours, in the unit of m) in October.	50
Figure 2.2.11 Weekly mean SSTs (color codes) and the surface velocities (vectors) from Nov. 16 to Nov. 21 of Year 7, when the warm entrainment reaches its maximum.	50
Figure 2.2.12 Intraseasonal entrainment and intraseasonal SSHAs at $8^{\circ}S$, $63^{\circ}E$ for 18 years.	53
Figure 2.2.13 Correlations between the intraseasonal entrainment and the intraseasonal SSHAs, which are statistically significant at the 95% confidence level.	53

Figure 2.2.14 Sketch of the influence of ITF on the SWIO. See the text for detailed descriptions.	55
Figure 3.1 Correlations between the MJO index and the vertically averaged perturbed kinetic energy. Only the correlations statistically significant at a 95% confidence level are shown.	63
Figure 3.2 Ratios between $P' \cdot K'$ (blue bars), $K' \cdot \bar{K}$ (green bars), R' (red bars) and the total energy conversions TE for the MJO events listed in Table 3.1. For each event, the energy conversions are averaged between 50°E-100°E and 0°-10°S in the horizontal, from 1000 hPa to 250 hPa in the vertical, and from the beginning date to the end date (Table 3.1) in time.	67
Figure 3.3 Energy conversions for four MJO events: No. 9 (a), No. 25 (b), No. 44 (c), and No. 48 (d). Dash lines: R' ; dot lines: $K' \cdot K$; dash-dot lines: $P' \cdot K'$; solid lines: TK . All terms are averaged between 50°E-100°E and 0°-10°S, and from 1000 hPa to 250 hPa. The units are 10^{-3} W m^{-3}	69
Figure 3.4 Latent heat fluxes (dot lines), net shortwave radiation at the sea surface (dash lines), total heat flux at the surface (solid lines), and SST anomalies (dash-dot lines) for four MJO events. The units of the energy fluxes are W m^{-2} and the unit for SST anomalies is 10^{-2} Kelvin. All variables are averaged between 50°E-100°E, 0°-10°S.	70
Figure 3.5 The ratio between Term II and Term III in Eq. (3.13) during the MJO event No. 9. The thick gray contour corresponds to a value of 0.5. Intraseasonal SST anomalies are superimposed with the thin contours. The unit of SST anomalies is Kelvin. All variables are averaged between 0° and 10°S.	73
Figure 3.6 Intraseasonal SSTAs from Jan 1, 1985 to Jan 22, 1985, with a unit of Kelvin (color shades). The intraseasonal vorticity of surface winds averaged between the equator and 10°S are superimposed (black contours) with a unit of 10^{-5} s^{-1}	74
Figure 3.7 Moist static energy (solid lines with cycles), Lq at 1000 hPa (dash lines) and 500 hPa (dash-dot lines), and the difference of Lq at the two pressure levels (solid lines) during four MJO events. The units are J kg^{-1}	75
Figure 3.8 (a) Energy conversions for the MJO event from Feb 27, 1990 to Mar 23, 1990. (b) The corresponding perturbed kinetic energy. All variables are averaged between 50°E-100°E, 0°-10°S and from 1000 hPa to 250 hPa.	78
Figure 3.9 The ratio between Term II and Term III in Eq. (3.13) during the MJO event No. 21. The thick gray contour represents a value of 0.5. Intraseasonal SST anomalies are superimposed with the thin contours. The unit of SST anomalies is Kelvin. All variables are averaged between 0° and 10°S.	79
Figure 3.10 Intraseasonal SSTAs from Feb 7, 1990 to Mar 23, 1990, with a unit of Kelvin (color shades). The intraseasonal vorticity of surface winds averaged between the equator and 10°S are superimposed (black contours) with a unit of 10^{-5} s^{-1}	80
Figure 3.11 Energy conversions for two MJO events. All variables are averaged between 50°E-100°E, 0°-10°S and from 1000 hPa to 250 hPa.	81

- Figure 3.12 dq/dy averaged between 0° and 10°S during the MJO event No. 42 (a) and No. 9 (b). (c) and (d) are two snapshots of dq/dy on two days. The black contours in (c) and (d) are the zero contours. The units are $10^{-12} \text{ m}^{-1} \text{ s}^{-1}$ 83
- Figure 3.13 Ratios between $P \cdot K'$ (blue bars), $K \cdot \bar{K}$ (green bars), R' (red bars) and the total energy conversions TE for four MJO events in boreal summer. The energy conversions are averaged between the equator and 10°S for the left group in each panel (the same as Fig. 2), while they are averaged between 10°S and 10°N for the right group in each panel. 84
- Figure 3.14 Comparisons between the three energy sources calculated with the Lorenz energy cycle equations (solid lines) and with the temporal perturbations (dash lines) during 4 typical MJO events. For clearance, only the dominant energy sources in each MJO event are shown. The gray solid line in (c) is the intraseasonal part (obtained with band-pass filtering between 20 and 100 days) of the corresponding black solid line. The units are 10^{-3} W m^{-3} 87
- Figure 4.1.1 Climatological NCEP winds at 10-meter (Kalnay et al. 1996) averaged from 10°N to 10°S . The gray scales in the lower panel show the ratio between the standard deviation and the climatological mean of the zonal NCEP winds at 10-meter. The contours are from 0.1 to 0.5, with an interval of 0.1 95
- Figure 4.1.2 (a) Dispersion relations of the solutions ω_1 and ω_2 to Eq. (4.1.13). (b) Dispersion relations of the solutions ω_3 and ω_4 . The dashed line is the dispersion relation of the theoretical Rossby waves. (c) and (d) show the phase speeds (solid lines) and group velocities (dashed lines) of the corresponding solutions. The subscript r stands for the real parts of the solutions and the subscript i stands for the imaginary parts of the solutions. 99
- Figure 4.1.3 Hovemueller diagram of the solutions to Eq. (4.1.13) with an initial unit amplitude and a wavelength of 5000 km at the equator ($y = 0$). (a) ω_1 (gray scale) and ω_2 (contour). (b) ω_3 (gray scale) and ω_4 (contour). 100
- Figure 4.1.4 Ratio between β_c and β , with respect to the wavelength in the atmosphere. 103
- Figure 4.1.5 (a) Dispersion relations of the solutions to Eq. (4.1.18) with the wavelength of 6000 km in the atmosphere. Solid lines represent the real parts and dashed lines represent the imaginary parts. (b) The corresponding phase speeds and group velocities, solid lines for phase speeds and dashed lines for group velocities. Black lines are for ω_{o1} , red lines are for ω_{o2} , and blue lines are for ω_{o3} 104
- Figure 4.1.6 Hovemueller diagram of the solutions to Eq. (4.1.18) with an initial unit amplitude at the equator ($y = 0$). The wavelength in the atmosphere is 6000 km and that in the ocean is 850 km. (a) ω_{o1} , (b) ω_{o2} (gray scale) and ω_{o3} (contour). 106
- Figure 4.1.7 Period of $2\pi/\omega_{o2i}$ with the unit of day. The blank region represents that $\omega_{o2i} = 0$, i.e. the solution ω_{o2} is a real solution with these parameters. 107

Figure 4.1.8 (a) Dispersion relations of the solutions to Eq. (4.1.22) with the wavelength of 850 km in the ocean. Solid lines represent the real parts and dashed lines represent the imaginary parts. (b) The corresponding phase speeds and group velocities, solid lines for phase speeds and dashed lines for group velocities. Black lines are for ω_{a1} , red lines are for ω_{a2} , and blue lines are for ω_{a3}	108
Figure 4.1.9 Hovemueller diagram of the solutions to Eq. (4.1.22) with an initial unit amplitude at the equator ($y = 0$). The wavelength in the atmosphere is 6000 km and that in the ocean is 850 km. (a) ω_{a3} , (b) ω_{a1} (gray scale) and ω_{a2} (contour).	109
Figure 4.1.10 Period of $2\pi / \omega_{a3i}$ with the unit of day.....	110
Figure 4.1.11 Sketches of the proposed two types of ocean-atmosphere interactions. (a) Piston-like coupling, in which the oceanic and atmospheric oscillations have similar temporal and spatial scales. (b) Gear-like coupling, in which the oceanic and atmospheric oscillations have different temporal and spatial scales.....	114
Figure 4.2.1 $F(\omega; k)$ with a wavelength of 8000 km. The embedded figure is zoomed-in around the turning pint. Points A, B, and C represent the three zero-crossing points of the curve, i.e. three solutions to $F(\omega; k) = 0$. See text for the definition of $F(\omega; k)$	123
Figure 4.2.2 (a) $2\pi / \omega_p$, where ω_p is obtained from Eq. (4.2.8). (b) Absolute values of $F(\omega_p; k)$ normalized by βk	126
Figure 4.2.3 Power spectra of meridional velocities in the 10-day run. The contours show the logarithm of the spectrum values.....	131
Figure 4.2.4 Power spectra of meridional velocities at 10° latitude in the (a) 9-day run, (b) 10-day run, and (c) 11-day run. The dash lines show the 95% confidence limits. (d) The power spectra in the three model runs are shown together to favor the inter-comparisons.....	133
Figure 4.2.5 (a) Mean zonal current at the surface and (b) mean zonal current at 140°W with respect to depth. The westward currents are shaded. The contours for eastward currents start from 0.2 m s^{-1} and the contours for westward currents start from -0.2 m s^{-1} . The contour interval is 0.1 m s^{-1} . The black region is the continent.....	138
Figure 4.2.6 Power spectra of zonal currents at four different locations in the four scenarios and the control run (with dashed gray lines). The gray line shows the 95% confidence limits. See texts in Section 4.2.3.1 for detailed descriptions.	140
Figure 4.2.7 (a) Intraseasonal SST anomalies on Feb 17, 1990. Gray scales show the high-pass-filtered SSTs from AVHRR data with cut-off periods of 20 and 100 days. The contours show the analytical SST anomalies with a zonal wavelength of 1000 km. (b) Analytical SST anomalies with a zonal wavelength of 1000 km. The centers of SST anomalies are marked with diamonds at every ten day intervals. For clarity, the SST anomaly fields are only shown on Jan 1 and Mar 1. The unit for SST is $^\circ\text{C}$ and the contour interval is 0.2°C	143

Figure 4.2.8 Zonal winds at 850 hPa averaged between the equator and 5°S from Feb 15, 1990 to Mar 31, 1990. (a) NCEP/NCAR reanalysis, (b) control run, (c) total-SST run, and (d) the difference between (c) and (b) (the former minus the latter). The units are m s^{-1} . Note that the color scales in (d) are different from the other panels. 145

Figure 4.2.9 Mean (a) and STD (b) of differences in zonal winds at 850 hPa between the R1100 run and the R800 run. Mean (c) and STD (d) of the zonal winds at 850 hPa in R800 run. The model runs are conducted in 1990. The seasonal cycle is removed. The unit is m s^{-1} 146

Figure 4.2.10 Power spectra of the zonal winds at 70°E in four atmospheric model runs for the MJO events in 1990 (a) and in 1994 (b). The gray line shows the 95% confidence limits. 147

Figure 4.2.11 (a) Differences between wavelet spectra of the zonal winds on Mar 1, 1990 in the R1100 run and R800 run ($R1100 - R800$). (b) is the same as (a), but on Feb 20, 1994. The unit is $\text{m}^2 \text{s}^{-2}$. The dark gray areas are larger than $2 \text{ m}^2 \text{ s}^{-2}$, while the light gray areas are smaller than $-2 \text{ m}^2 \text{ s}^{-2}$ 149

Figure 4.2.12 Wavelet spectra of the zonal winds at 70°E and on Mar 1, 1990 (a) and on Feb 20, 1994 (b) in the four atmospheric model runs. The gray lines are the 95% confidence limits, calculated following Torrence and Compo (1998). 151

Chapter 1: Introduction

1.1 Theories and simulations of Madden-Julian Oscillations

Madden-Julian oscillations (MJOs) are the most well-known intraseasonal oscillations in the ocean-atmosphere system, and are characterized by an eastward-propagating precipitation signal (Madden and Julian 1971, 1972). Typically, they first appear over the western tropical Indian Ocean and remain pronounced as they reach the eastern Indian Ocean and the western Pacific Ocean (Fig. 1.1). They are barely detectable over the cool eastern Pacific Ocean, but sometimes are reinforced over the tropical Atlantic Ocean. Each cycle lasts for 30-60 days, so MJOs are also known as 30-60-day oscillations. The structure and properties of MJOs are summarized in detail by Madden and Julian (2005). In addition to the impact on the tropical regions, MJOs are also found to have a global influence. They can contribute to the low-frequency ENSO by rectifying its amplitude and life cycle (Kessler and Kleeman 2000; Zavala-Garay et al. 2005). They can also affect the strength and the onsets/breaks of the Asian Monsoons (Webster et al. 1998). They are even found to be related with the jet stream in the mid-latitude (Madden and Julian 1994) and the North Atlantic Oscillation (Cassou 2008; Lin et al. 2009) with consequences for North American climate anomalies (Yang et al. 2002).

There have been many theories and model studies on MJOs thus far. As summarized in Wang (2005), MJOs were first attributed to the equatorial Kelvin waves. But the associated convection, which is recognized as a ubiquitous feature of the MJOs, could not be explained. Convection was found to be associated with the

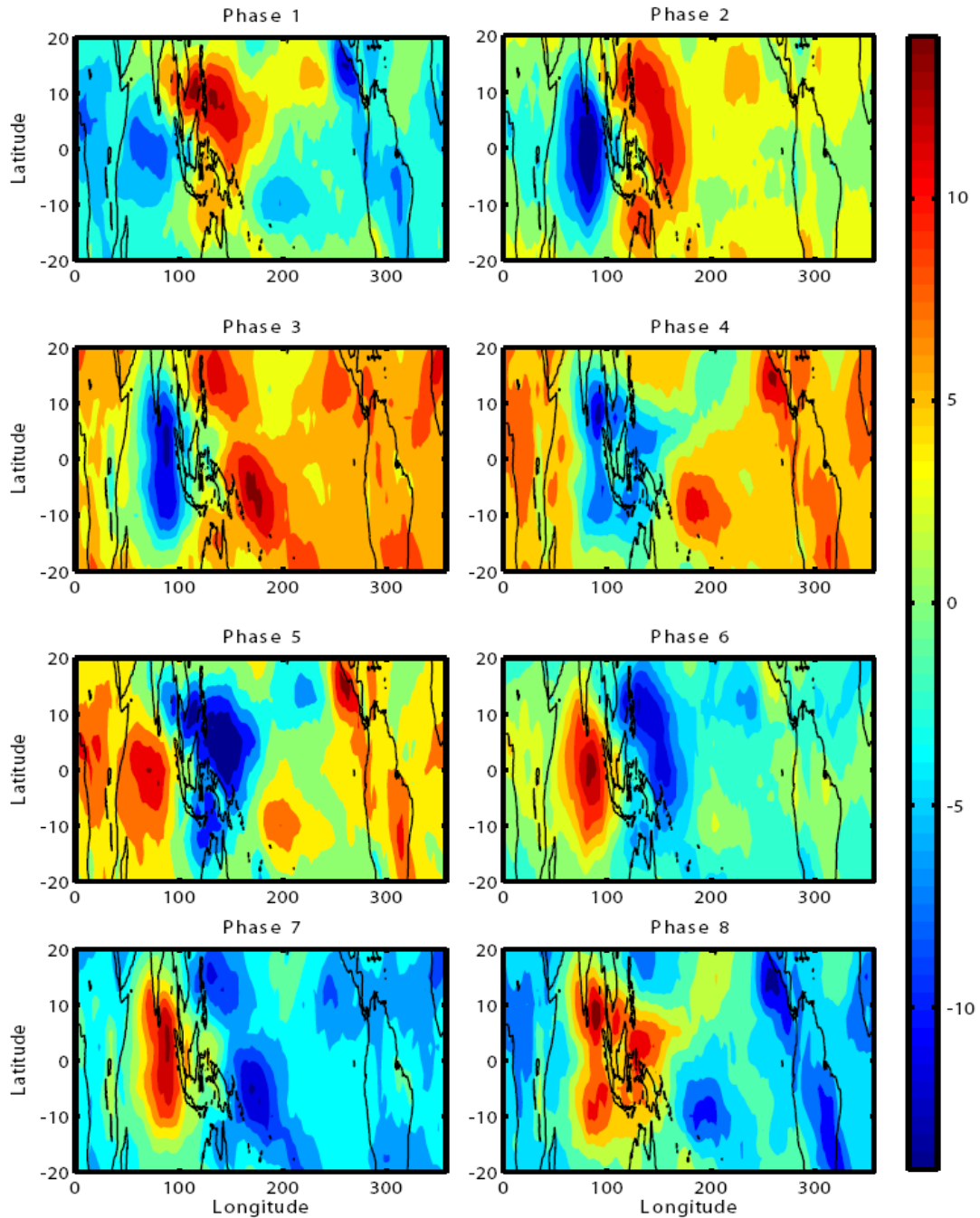


Figure 1.1 Outgoing longwave radiation (OLR) anomalies (after band-pass filtering with cut-off periods of 20-100 days) for the eight phases of MJOs, which are defined with the daily MJO index from 1979 to 2006 (Wheeler and Hendon 2004). The unit is W m^{-2} .

Kelvin-Rossby wave pairs, but the selection of the eastward propagation associated with Kelvin waves, rather than the westward propagation associated with Rossby

waves could not be fully explained. The theory invoking the Convective Instability of the Second Kind, viz., wave-CISK, can also explain the convection (Lindzen 1974). But this process favors small-scale convection (a phenomenon called CISK catastrophe, Crum and Stevens 1983), which is much smaller than the observations. Lau and Peng (1987) introduced the ‘mobile wave-CISK’, which favors a realistic large-scale convection, though the heating profile they used was larger than observations. A theory called ‘wind-induced surface heat exchange’ (WISHE, Emanuel 1987; Neelin et al. 1987) can explain both the convection and the eastward propagation of MJOs. Unfortunately, theoretically, WISHE also favors small-scale convections. Practically, a weak, rather than a strong, evaporation usually leads the convection (Woolnough et al. 2001). Thus, none of the existing theories can explain all of the complex features of MJOs.

There are also several substantial deficiencies in model simulations of MJOs. Particularly, the simulated periodicity is generally 25-30 days, clearly shorter than the observations (Sperber et al. 1997). The MJOs are observed to be strongest in boreal winter, but this seasonality cannot be well resolved in model simulations. Moreover, the eastward propagation of the convection over the maritime continent of Indonesia and the western Pacific warm pool is not well simulated either (Slingo et al. 1996). Therefore, realistic simulation of MJOs still eludes models and remains a major challenge.

One aspect that has received more and more attention is the role of the sea surface temperatures (SSTs) on the genesis and evolution of MJOs. All the aforementioned theories assumed *a priori* that MJOs are mainly atmospheric processes and ignored

oceanic feedbacks by prescribing SSTs to drive the models. However, more and more evidence has emerged over time to show that the variability of the surface heat flux and SSTs indeed have a significant influence on MJOs. Krishnamurti et al. (1988) was a pioneering examination of SST variability associated with MJOs. Some recent observations (e.g. Jones et al. 1998; Lau and Sui 1997; Zhang 1996; Fu et al. 2003) also support the positive feedback hypothesis in which SST variations are purported to enhance the amplitude of the MJOs and affect their eastward propagation. Waliser et al. (1999) coupled a slab ocean mixed layer, which provided prognostic SST anomalies to an AGCM, to demonstrate that the simulated MJOs with coupling possessed more realistic amplitudes, time-scale, eastward phase speed, and seasonal variability. Woolnough et al. (2001) showed that the most intense convection in the tropical atmosphere occurs over the western Indian Ocean, where SST gradients reach a maximum. With the reanalysis products, Sperber (2003) showed that favorable SST anomalies occur 5 days before the organization of deep convection. This feedback may be responsible for extending the life-cycle of the simulated MJOs and improve the propagation of convection in models (Sperber et al. 1997). With a simple coupled model, Bellon et al. (2008) showed that the ocean-atmosphere coupling modulated the period of the atmospheric intraseasonal oscillations, so that the simulated period was closer to the observations. Kim et al. (2008) showed that increasing the frequency of prescribed SST forcing (from monthly to daily) also improved the MJO simulations. Recently, Pegion and Kirtman (2008a) argued that the intraseasonal SST anomalies were a key factor in the better prediction of the atmospheric ISVs (i.e. MJOs) in the NCEP's operational Climate Forecast System. Therefore, a better

understanding of the oceanic feedbacks to MJOs and an accurate simulation of the MJO-modified SSTs will definitely contribute to the understanding and prediction of the complex features of the MJOs. Since MJOs mostly originate in the western Indian Ocean, it is crucial to examine the SST anomalies in this region. This is the primary motivation for the following analyses.

1.2 Oceanic intraseasonal variabilities in the tropical and southern Indian Ocean

Oceanic intraseasonal variabilities (OISVs) are found to be an important part of the ocean dynamics and thermodynamics in the upper layer over the global oceans (e.g. Hansen and Paul 1984; Kessler et al. 1995; Farrar and Weller 2006; Jochum and Malanotte-Rizzoli 2003; Waliser et al. 2003, 2004; Jochum and Murtugudde 2005). In the tropical Indian Ocean, the OISVs are enhanced due to internal oceanic instabilities and in response to intraseasonal atmospheric forcing (Waliser et al. 2003a; Reppin et al. 1999; Sengupta et al. 2001). Feng and Wijffels (2002) analyzed satellite altimeter data and reported that the wavelength of the OISVs in the southeastern Indian Ocean (SEIO) ranges from 600 to 900 km, the period varies from 40 to 80 days, and the westward phase speed spans 15 to 19 cm s⁻¹. They attribute the enhanced OISVs during the second half of the year to baroclinic instability, which draws most of its energy from the available potential energy associated with the Indonesian Throughflow (ITF). Yu and Potemra (2006) concluded that barotropic and baroclinic instabilities contribute almost equally to the genesis of OISVs in the Indo-Australian basin, by analyzing a numerical ocean model. They found that baroclinic instability was sensitive to the warmer and fresher ITF and barotropic instability was attributable to the strong zonal shear between the Eastern Gyral Current and the South

Equatorial Current, which is strengthened by the ITF. In addition to the strong dependence on the ITF (Potemra et al. 2002), the OISVs in SEIO also respond to the intraseasonal atmospheric forcing (Sprintall et al. 2000; Iskandar et al. 2006).

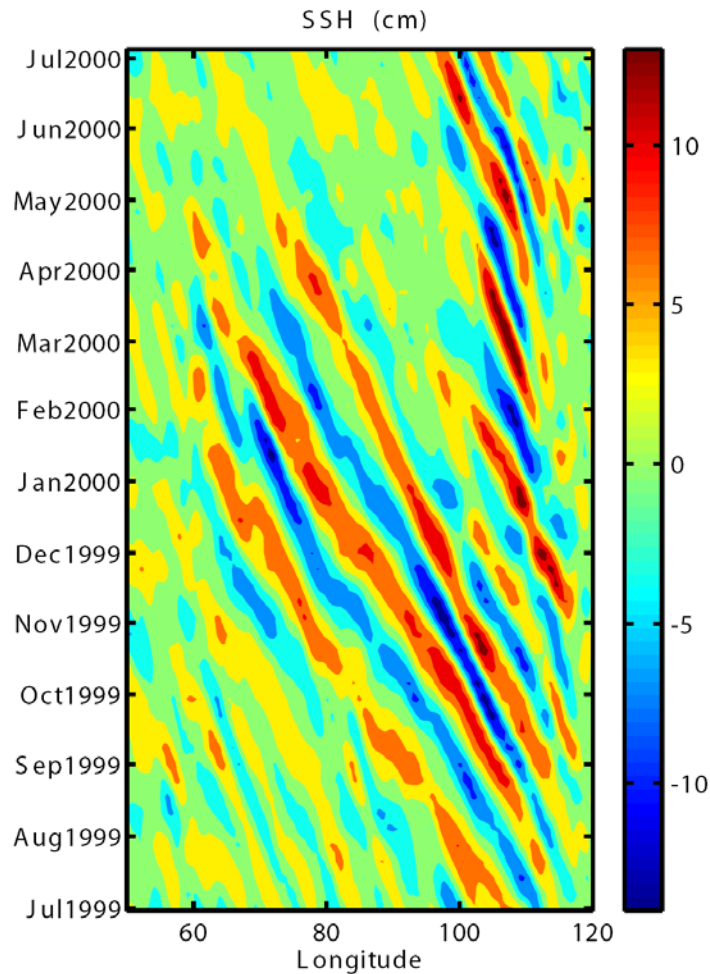


Figure 1.2 Sea surface heights (SSH) from TOPEX/POSEIDON data averaged between 8°S and 12°S after a band-pass filtering with the cut-off periods of 20 and 100 days. The unit is cm.

The OISVs in SEIO propagate westward as Rossby waves (Morrow and Birol 1998), which can influence the southwestern Indian Ocean (SWIO; Fig. 1.2). For example, Sengupta et al. (2001) used a model driven by NCEP reanalysis to show that the 30-50 day oscillations were due to the westward propagating Rossby waves and were enhanced by the oceanic instability in the western equatorial Indian Ocean. In an

analysis of observational data, Klein et al. (1999) reported that surface heat flux anomalies explain the basin-wide warming over most of the tropical Indian Ocean, the only exception being the SWIO. Masumoto and Meyers (1998) argued that the large SST variations in the SWIO are mainly attributable to the forced Rossby waves propagating from SEIO rather than to the local wind forcing. Moreover, SWIO is an upwelling region, where the subsurface thermocline variability also has a clear influence on SSTs (Fig. 1.3; Murtugudde and Busalacchi 1999; Schott et al. 2002). Xie et al. (2002) further concluded that much of the SST variability in the SWIO is not due to local winds or surface heat fluxes, but is rather due to oceanic Rossby waves that propagate from the east which affect the temperature of upwelled waters.

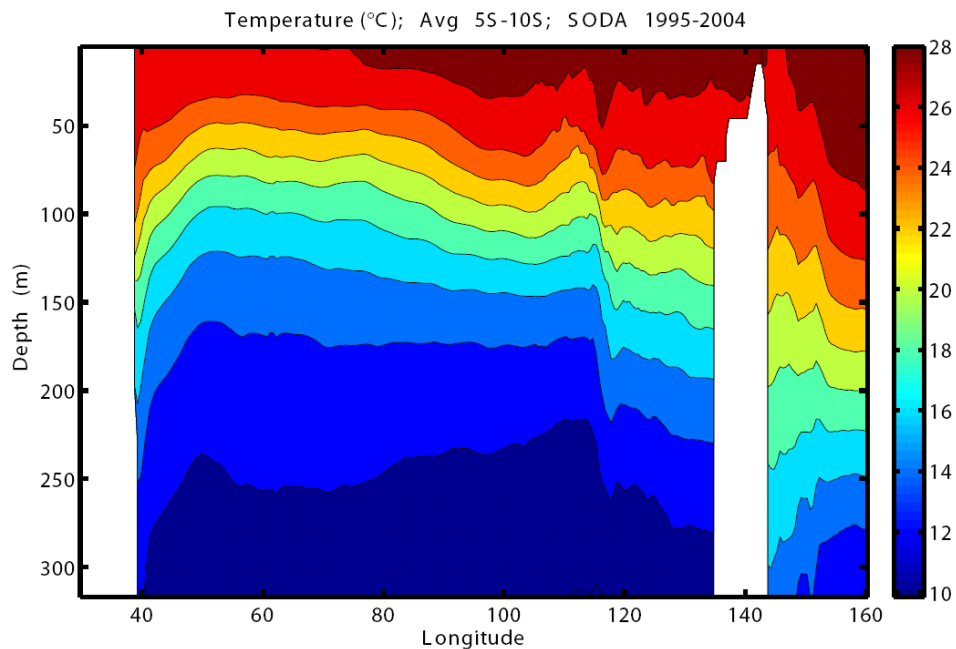


Figure 1.3 Mean temperature from SODA (Carton et al. 2000a, b) over 10 years, averaged between 5°S and 10°S.

As discussed above, MJO events typically originate in the SWIO (Madden and Julian 2005) and in the context of MJOs depending on SSTs, the OSIVs in the SWIO, especially those leading to warm SSTAs, can be expected to influence the

development of MJOs. Potential drivers of MJOs from warm SSTAs include air-sea heat exchanges, low-level convergence in the atmosphere, and the genesis of deep convection. This process of oceanic impact on the atmosphere is likely to be analogous to the Bjerknes feedback (Bjerknes 1969) during ENSO in the equatorial Pacific. With reanalysis and model outputs, Annamalai et al. (2003) showed that the Bjerknes feedback is also important for strengthening the SST anomalies in the thermocline ridge region in the SWIO. Therefore, I set out to examine the MJOs in the ocean-atmosphere coupled system. I expect the approach to contribute to a better understanding of the ocean-atmosphere interactions in the intraseasonal band and the oceanic influence on MJOs.

1.3 Ocean-atmosphere interaction in a multi-scale system

Although there has been much evidence for the ocean's influence on MJOs from both observations and model simulations, there is a clear discrepancy between the spatial scales of the MJOs and those of the OISVs, especially in the SWIO; the spatial scale of the SSTAs tends to be only on the order of hundred kilometers while that of MJOs is clearly on the order of thousand kilometers (see the review by Madden and Julian 1994). Thus, an important question arises as to whether the processes in the ocean and the atmosphere with such different scales can interact with each other and lead to coupled instabilities. Actually, both MJOs and OISVs interact closely with processes at other temporal and spatial scales. For example, Biello and Majda (2005) established a multi-scale model which resolved both the upscale and downscale energy transfer associated with MJOs. Dewitte et al. (2008) showed that the low-frequency modulation of intraseasonal oceanic Kelvin waves was attributable to the

change in the oceanic mean state. Neale et al. (2008) demonstrated that including a parameterization for the meso-scale convective momentum transport can improve the simulation of ENSO (which has a period of 2-7 years in nature) in the NCAR Community Climate System Model (CCSM3). With observations and NCEP reanalysis, Roundy and Kravitz (2009) studied the connections between the intraseasonal tropical atmospheric variations which are closely related to MJOs and the interannual variations which are associated with ENSO. On the one hand, the ISVs have a clear influence on different phases of ENSO, thus their net influence on interannual time scales is not negligible. On the other hand, the interannual ENSO mode can affect the evolution of the ISVs, so that the latter are not purely stochastic forcing or trigger for ENSO. Hence, I suppose that any investigation of the ISVs in either the ocean or the atmosphere should span not only the intraseasonal band but also the time-scales that interact with the ISVs. It will thus be obviously useful to examine the interactions between MJOs and SST anomalies in a multi-scale framework. In addition, it is being recognized more and more that weather and climate are closely-related through the subseasonal or intraseasonal bridge in a single multi-scale system. Thus, research on a continuum of scales is clearly necessary to improve our understanding of the integrated climate system and in fact, the Earth System. Therefore, as a further step to the MJO exploration in the ocean-atmosphere coupled system, I propose to examine the MJO-SST interactions on different scales with theoretical and numerical models.

1.4 Thesis organization

The ITF influence on the OISVs in the SWIO is discussed in Chapter 2 with model simulations. It is shown that the warm ITF waters have a detectable influence on the SWIO by weakening the vertical stratification and reducing the stability of the water column. As a result, warm SST anomalies occur in boreal winter, which is argued to have an influence on the genesis and evolution of MJOs, as hypothesized above. In Chapter 3, the energy budgets for MJO events are analyzed with the NCEP reanalysis. It is concluded that for most MJO events, their kinetic energy is derived from the perturbed atmospheric potential energy. The oceanic feedbacks are found to be helpful to prolong the lifetime of an MJO event. A few MJO events are preceded by an enhanced surface heat flux, which is caused by the warm SST anomalies in the western Indian Ocean and a few other MJO events obtain energy from the mean kinetic energy in the atmosphere. In Chapter 4, the possibility of the ocean-atmosphere interactions at different temporal and spatial scales is studied with simple and idealized theoretical models of the ocean, the atmosphere, and the coupled ocean-atmosphere system. Then with atmospheric GCM simulations, it is shown that the distinctive periods of ISVs in the atmosphere over the Indian Ocean are shifted with relatively small changes in forcing due to the meso-scale SST anomalies in the SWIO, which provides evidence to the hypothesis that SST anomalies can influence the MJO life-cycle, and also supports the assumption that processes with distinctly separate scales can interact with each other in a multi-scale system. Finally, conclusions along with discussion on further work are offered in Chapter 5.

Chapter 2: OISVs in the SWIO

2.1 Dynamics of the intraseasonal oscillations in the Indian Ocean South

Equatorial Current

Abstract

The spatial and temporal features of intraseasonal oscillations in the southwestern Indian Ocean are studied by analyzing model simulations for the Indo-Pacific region. The intraseasonal oscillations have periods of 40-to-80 days, with a wave length of ~ 650 km. They originate from the southeastern Indian Ocean and propagate westward as Rossby waves, with a phase speed of ~ 25 cm s⁻¹ in boreal winter and spring. The baroclinic instability is the main driver for these intraseasonal oscillations. The first baroclinic mode dominates during most of the year but during boreal winter and spring, the second mode contributes significantly and often equally. Consequently, the intraseasonal oscillations are relatively strong in boreal winter and spring. Whether the atmospheric intraseasonal oscillations are also important for forcing the oceanic intraseasonal oscillations in the southwestern Indian Ocean needs further investigation.

2.1.1 Introduction

Oceanic intraseasonal oscillations (OISOs) are found to be important part of the ocean dynamics in the upper layer over the global oceans (e.g. Kessler et al. 1995; Farrar and Weller 2006; Jochum and Malanotte-Rizzoli 2003). In the tropical Indian Ocean, the OISOs are enhanced due to the internal oceanic instability and the

response to the intraseasonal atmospheric forcing (Waliser et al. 2003a; Reppin et al. 1999; Sengupta et al. 2001). As for the southern Indian Ocean, there have been some observational and modeling studies in the southeastern Indian Ocean (SEIO). Feng and Wijffels (2002) analyzed the satellite altimeter data and reported that the wavelength of the OISOs in SEIO is from 600 to 900 km (the length scale is from 100 to 150 km), the period is from 40 to 80 days, and the westward phase speed is from 15 to 19 cm s⁻¹. They attribute the enhanced OISOs during the second half of the year to the baroclinic instability, which drew most energy from the available potential energy associated with the Indonesian Throughflow (ITF). Yu and Potemra (2006) concluded that the barotropic and the baroclinic instabilities contribute almost equally to the genesis in the Indo-Australian basin, by analyzing a numerical ocean model. They found that the baroclinic instability was sensitive to the warmer and fresher ITF and the barotropic instability is attributable to the strong zonal shear between the Eastern Gyral Current and the South Equatorial Current, which is strengthened by the ITF. In addition to the close relations with the ITF (Potemra et al. 2002), the OISOs in SEIO also respond to the intraseasonal atmospheric forcing (Sprintall et al. 2000; Han 2005; Iskandar et al. 2005, 2006). The OISOs in SEIO propagate westward as Rossby waves, which may influence the southwestern Indian Ocean (SWIO). For example, Sengupta et al. (2001) used a model driven by NCEP data to show that the 30-50 day oscillations appeared due to the westward propagating Rossby waves and were enhanced due to the oceanic instability in the western equatorial Indian Ocean.

To the best of our knowledge, there have been neither systematic observations nor modeling studies of OISOs thus far in SWIO (e.g., Murtugudde and Busalacchi

1999). Therefore, the purpose of this paper is to describe the spatial and temporal dynamic properties of OISOs in SWIO, and then to provide the dynamic reasons for their development. In Section 2.1.2, the model is described and the model results are compared with the observations. In Section 2.1.3, the features of OISOs in SWIO are described. In Section 2.1.4 the dynamic reasons for their genesis and enhancement are explored by analyzing the stability and the vertical modes of the ocean currents. The conclusions and discussions are presented in Section 2.1.5.

2.1.2 Model description and comparison

2.1.2.1 Model description

The model used in this study is a reduced gravity, sigma-coordinate, primitive equation OGCM, with a horizontal resolution of $1/3^\circ$ in latitude and $1/2^\circ$ in longitude over the Indo-Pacific domain covering 32°E - 76°W , 30°S - 30°N (Murtugudde et al. 1996, 1998). There are 15 sigma layers in the vertical below the variable depth mixed layer with a resolution of ~ 20 m in the thermocline in the SWIO, so that the vertical oscillation in the interior ocean can be adequately resolved. Surface mixed layer is determined by the hybrid mixing scheme of Chen et al. (1994) which explicitly accounts for the entrainment induced by the surface turbulent kinetic energy, shear-induced dynamic stability mixing, and convective mixing to remove static instabilities. The last sigma-layer is a prognostic variable whereas the other sigma layers are specified constant fractions of the total depth below the mixed layer to the motionless abyssal layer. The model is driven by the climatological weekly NCEP Reanalysis winds (see Murtugudde et al. 2000 for details). The model outputs for all the analyses presented here are weekly mean fields from the last 20 years of a 270

year simulation. Note that we only focus on OISOs in the climatological run to avoid contributions from interannual forcings (also see Jochum and Murtugudde 2005).

2.1.2.2 Model-data intercomparisons

The OGCM has been reported in many previous applications demonstrating its ability to simulate the ocean dynamics and thermodynamics reasonably well in the tropical oceans. The westward south equatorial current (SEC) stretches from 8°S to 20°S, which is consistent with the observations in Schott et al. (2002).

Obviously, what we are concerned most with is the model's ability to resolve OISOs in the Indian Ocean. Since we intend to study the internal intraseasonal variability in the ocean, the model is driven by the climatological winds as in Jochum and Murtugudde (2005). This also means that we do not expect perfect matches between the model results and interannual observations. The root-mean-square (RMS) of the intraseasonal SSHAs, which are high-pass filtered with a cut-off frequency of 100 days, and the uncertainty of its annual mean values from the model simulation and the satellite observations are shown in Fig. 2.1.1. The eddy kinetic energy (EKE) as determined from SSHA is well captured in the model, especially the 2 zonal bands of high EKE at 5°S and 10°S. Moreover, the high EKE along the Somali coast and in the southern Bay of Bengal are also resolved. The main shortcomings of the model are the weak EKE along the Sumatra coast and along 10°S west of 80°E.

In our model, the main period of the OISOs in SEIO is from 40 to 80 days. The wavelength is about 700 km to the east of 110°E and extends to about 1000 km to the

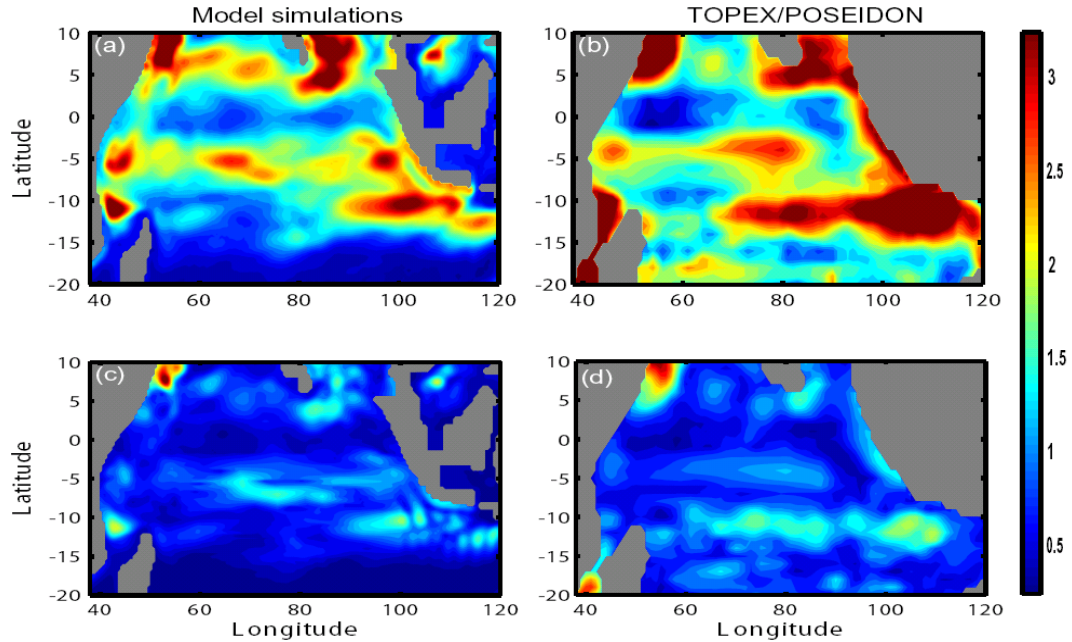


Figure 2.1.1 *RMS* of intraseasonal SSHAs of 20-year model simulations (a) and of TOPEX/POSEIDON data from 1992 – 2006 (b) and the *RMS* of the annual mean values for the 20-year model simulations (c) and the 15-year TOPEX/POSEIDON data (d). All fields are cm.

west of this longitude. These estimations are almost identical to the observations reported in Feng and Wijffels (2002), which examined the intraseasonal variability in SEIO by analyzing TOPEX/POSEIDON altimeter data and WOCE data. Therefore, with these comparisons between the model data and observations in SEIO, we conclude that the model ably resolves both the spatial and temporal properties of OISOs in the Indian Ocean.

2.1.3 Properties of ISOs in the SWIO

All calculations that follow are based on the weekly-mean model outputs. Before describing the properties of OISOs in SWIO, we would like to confirm that they are a significant part of the variability in the SWIO. The standard deviations (*STDs*) of the

intraseasonal SSHAs account for 20%-40% of the total *STDs* of SSHAs in the zonal belt. The maximum ratio can be as large as 50%. Therefore, OISOs are indeed a non-negligible component of the variability in the region and are important for understanding the oceanic processes in the SWIO.

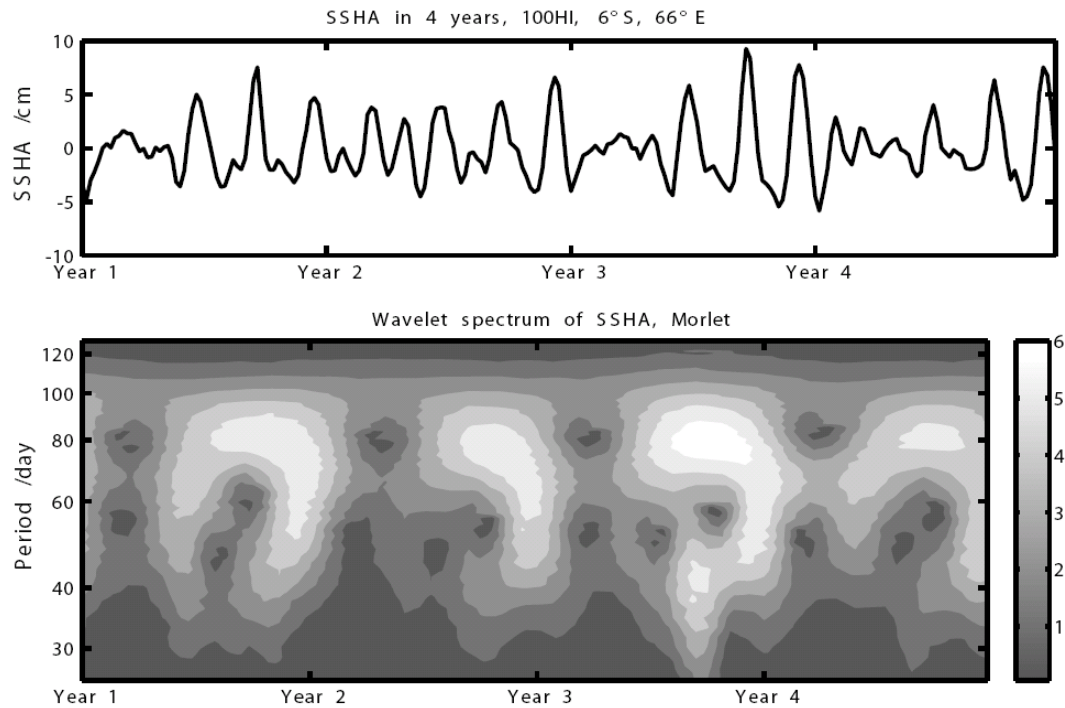


Figure 2.1.2 Intraseasonal model SSHAs at 6°S, 66°E for four years and the corresponding wavelet spectrum (both in cm).

Fig. 2.1.2 shows the wavelet spectrum of SSHAs at 6°S, 66°E. This point is chosen because the *STDs* of the intraseasonal SSHAs at this point are large. The obvious peak is from 40 days to 90 days, centered at 80 days. The OISOs in SWIO strengthen in boreal winter and spring. Their wavelength is ~650 km, which is comparable to the wavelength of 600-to-900 km in SEIO (Feng and Wijffels 2002). There is a westward propagation with a phase speed of about 25 cm s⁻¹ in boreal winter and spring (Fig. 2.1.3). For example, there is a strong positive signal starting at 77°E in early November and ending at 65°E in the late December of the first year.

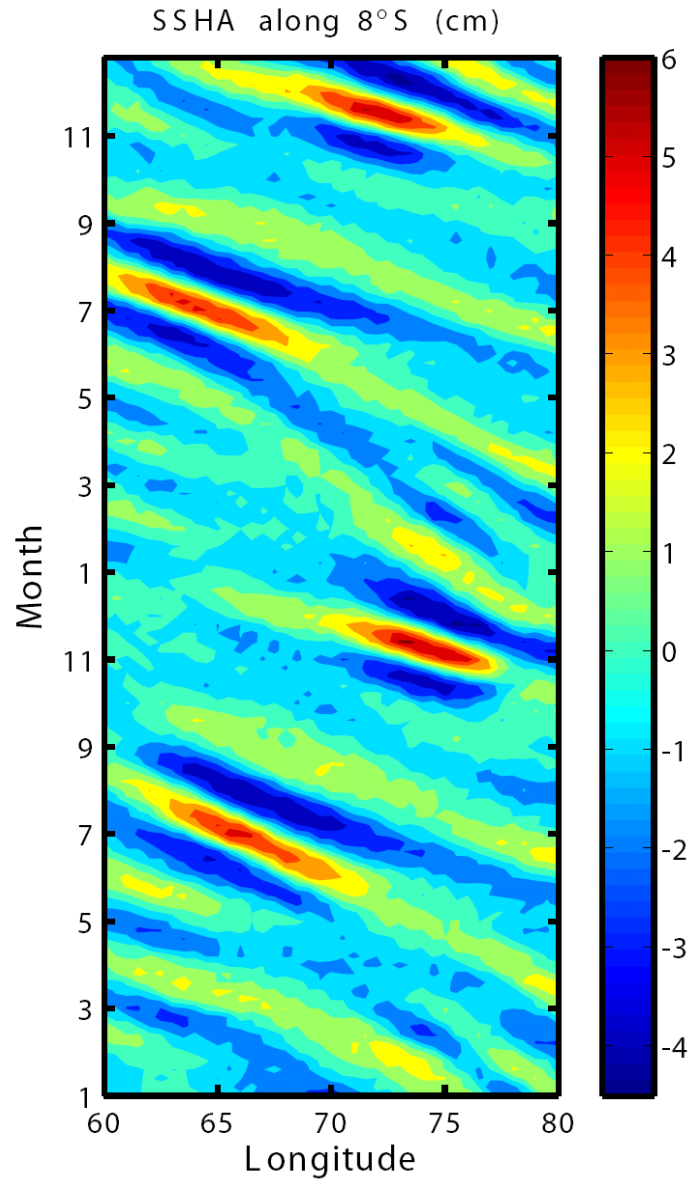


Figure 2.1.3 Longitude-time plot of model intraseasonal SSHAs along 8° S.

The phase speed reduces to about 17 cm s^{-1} in other seasons, as seen by a positive anomaly at 80°E in late March of the second year reaching 60°E in late August. The seasonal change of phase speed is attributable to the variability of ocean stratification. We also note that the phase speed changes with longitude. For instance, there is a negative signal around 75°E in February of the second year which speeds up at about 67°E in May. This phase speed change is caused by the interactions between the local

forcing and the Rossby waves (Wang et al. 2001). The range of estimated phase speed is comparable to the theoretically expected range. In addition, the dispersion relation of the westward propagation signals is consistent with that of the linear theoretical Rossby waves (not shown). Therefore, it can be concluded that the westward propagations of the signals are caused by the Rossby waves (Masumoto and Meyers 1998).

2.1.4 Dynamic processes responsible for OISOs in the SWIO

Generally, there are two reasons for the genesis of OISOs. One is external forcing, e.g. intraseasonal winds, and the other is internal instability, e.g. local barotropic and baroclinic instabilities. Both are explored in this section, to determine the dynamic reasons for OISOs in the SWIO.

High frequency wind stresses are one of the leading candidates. However, the climatological wind stresses used to force the model do not have pronounced peaks in the intraseasonal band. The low-frequency currents are significantly correlated with the geostrophic flow, which indicates that they are generally driven by the winds and satisfy the Sverdrup relation. On the other hand, the correlations between the intraseasonal currents (i.e. OISOs) and the geostrophic flow are statistically negligible over the entire south Indian Ocean indicating that the OISOs in SWIO in our model simulation are not caused by the local response to external wind forcing. Also because of the climatological forcing, the ITF in the southeastern Indian Ocean, where it just enters the Indian Ocean ($10^{\circ}\text{S} - 15^{\circ}\text{S}$ at 114°E), does not have pronounced intraseasonal variabilities. Comparing with the SODA reanalysis (Carton

et al. 2000a, b), the simulated ITF in the above region is consistent with SODA, but much smoother (not shown). Therefore, the OISOs in the SWIO discussed below are not attributable to the intraseasonal variabilities in the ITF.

Naturally, we assume that OISOs in SWIO are attributable to the internal instabilities of the ocean currents. The prerequisite for the instability analysis is the determination of the basic flow (Pedlosky, 1987), where by definition, the basic flow is the flow that is not disturbed by the eddy flow. Thus it is not simply equivalent to the mean flow. In the model, the low-pass filtered velocity has a large *STD* for the whole period of 20 years, but small *STDs* in each month. On the contrary, the high-pass filtered velocity has large *STDs* in each month, but a relatively small *STD* for the 20 year period. Since the model is driven by the climatological winds, the *STD* of the wind stresses is large while the wind stress in each month is identically the same (*STD* of interannual variability is zero). The low-frequency velocity is mainly a response to external wind forcing, hence it has a large annual cycle but changes very little in the same month of different years (interannual variability is small; see Jochum and Murtugudde, 2005). However, the high frequency velocity is mainly caused by the internal oceanic processes, especially eddies, hence changes significantly in the same month of different years, even though the wind forcing is the same. With these considerations, various cut-off periods are tried. It turns out that the low-pass filtered velocity with a cut-off period of 150 days is the optimal basic flow for the model outputs. Note that this optimal basic flow is not selected due to the spectrum separation between the low-frequency and the high-frequency parts. It is based on the criterion that the basic flow is the one that is not modified by the eddy.

2.1.4.1 Barotropic and Baroclinic Instabilities in the SWIO

The necessary condition for barotropic instability is that $dq/dy = \beta - \partial^2 U / \partial y^2$, where q is the quasi-geostrophic potential vorticity (QGPV) and U is the basic flow, should change sign in the domain under consideration. Fig. 2.1.4(a) shows the annual mean dq/dy in the SWIO, which is always positive in SEC, because the relative vorticity gradient $\partial^2 U / \partial y^2$ is too small to overcome the planetary vorticity gradient β . Since the condition that dq/dy change sign is a necessary condition for barotropic instability, it is very unlikely that the barotropic instability can be triggered in SWIO.

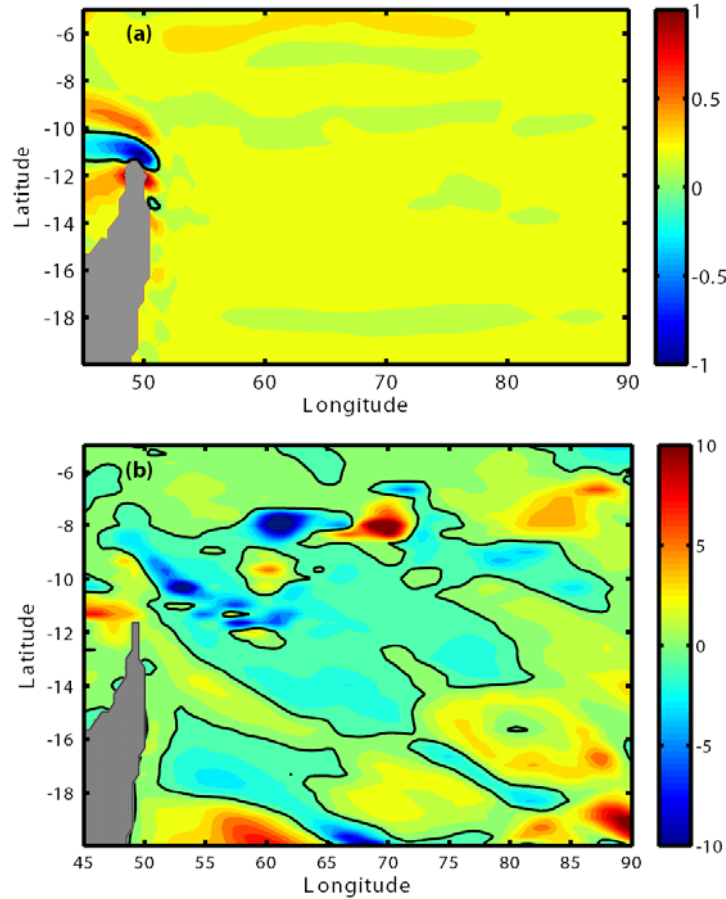


Figure 2.1.4 Annual mean of $q_y = \beta - U_{yy}$ (a) and $q_y = \beta - U_{yy} - (f_0^2 U_z / N^2)_z$ (b). The black contour is the contour of zero. The units are $10^{10} \text{ m}^{-1} \text{ s}^{-1}$.

The necessary condition for baroclinic instability is also that the meridional gradient of QGPV, viz. dq/dy should change sign in the domain. However, in the baroclinic situation, $\frac{dq}{dy} = \beta - \frac{\partial^2 U}{\partial y^2} - \frac{\partial}{\partial z} \left(\frac{f_0^2}{N^2} \frac{\partial U}{\partial z} \right)$. Fig. 2.1.4(b) shows the distribution of the annual mean dq/dy in the SWIO. Since the areas with positive and negative signs are similar and the positive and negative magnitudes are comparable, the baroclinic instability is very likely to occur in the SWIO. However, since satisfying the necessary condition alone cannot guarantee the triggering of instability, the energy conversions are examined with the model fields below.

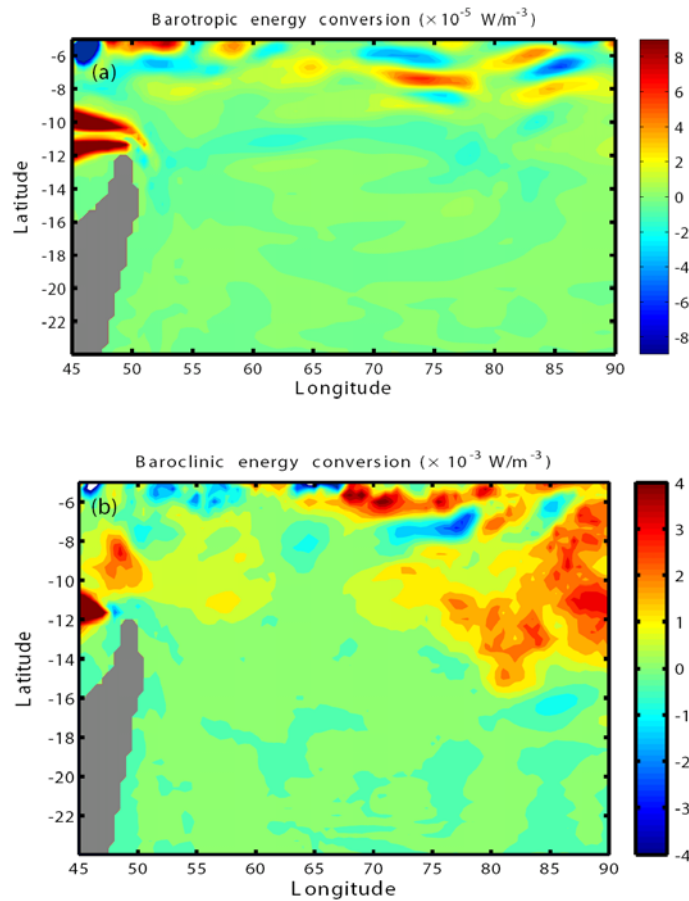


Figure 2.1.5 Barotropic (a) and baroclinic (b) energy conversions averaged over twenty years and above the thermocline in the SWIO.

The energy conversions caused by the barotropic and the baroclinic instability are calculated with the equation in Weisberg and Weingartner (1988),

$$\begin{aligned} EBT &= -\rho_0 \left[\langle u'u' \rangle U_x + \langle u'v' \rangle (V_x + U_y) + \langle v'v' \rangle V_y \right] \\ EBC &= -g \left[\langle u'\rho' \rangle \rho_{0x} + \langle v'\rho' \rangle \rho_{0y} \right] / |\rho_{0z}| \end{aligned}$$

where *EBT* stands for the barotropic energy conversion and *EBC* stands for the baroclinic energy conversions, g is the gravitational acceleration, $\rho_0 = \rho_0(z)$ is the water density averaged in horizontal, ρ' is the density perturbation to ρ_0 , U and V are the zonal and meridional basic currents as defined above, and u' and v' are the zonal and meridional intraseasonal currents. The barotropic energy conversion is small in the southern Indian Ocean, as shown in Fig. 2.1.5(a). South of 10°S, the barotropic energy conversion is almost zero. Between 5°S and 10°S, the barotropic energy conversion is slightly larger, because the horizontal shears are large. However, the barotropic energy conversion is always smaller than 10^{-4} W m^{-3} , since the zonal shears are not very strong. The baroclinic energy conversion are at least 2 orders of magnitude larger than the barotropic energy conversion (Fig. 2.1.5b), and can be as large as $4 \times 10^{-3} \text{ W m}^{-3}$. Thus, the energy conversion between eddy flow and mean flow in the southern Indian Ocean should be dominated by the baroclinic energy conversion. This is consistent with the above calculations of the necessary conditions for the instability that the barotropic instability is not likely to contribute, while the baroclinic instability dominates in the SWIO.

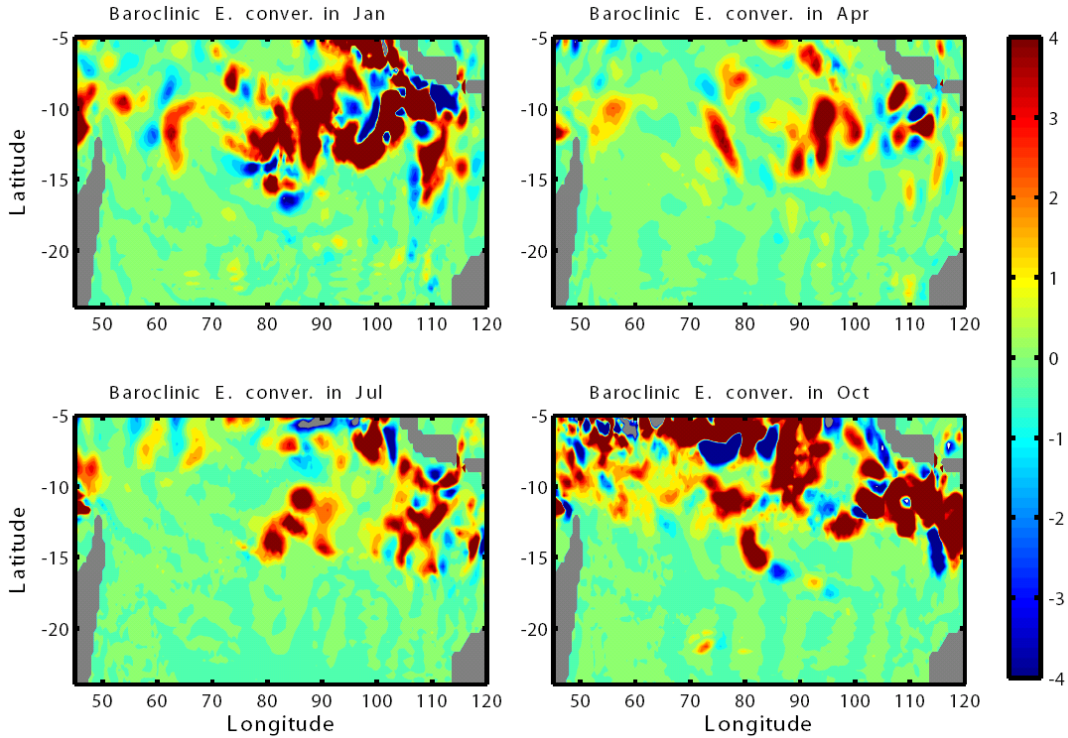


Figure 2.1.6 Baroclinic energy conversion (in 10^{-3} W m^{-3}) averaged over twenty years and above the thermocline in 4 months.

2.1.4.2 Seasonality of Baroclinic Energy Conversion and OISOs

Monthly mean baroclinic energy conversion for four months representing the four seasons are shown in Fig. 2.1.6. In SWIO, the seasonal changes are pronounced. In April and July, the baroclinic energy conversion is small with only a few patches of moderate conversion rate of 10^{-3} W m^{-3} . At the end of boreal summer, the conversion rates begin to increase and in October, they are larger than $2 \times 10^{-3} \text{ W m}^{-3}$ in almost the entire SWIO exceeding $10 \times 10^{-3} \text{ W m}^{-3}$ in some areas. During boreal winter, the baroclinic conversion rates decrease, but there are still large areas with conversion rates of $2 \times 10^{-3} \text{ W m}^{-3}$. The seasonal changes in Fig. 2.1.6 are consistent with the seasonal changes of intraseasonal zonal currents which confirm that the strong OISOs in the SWIO are caused by baroclinic instability.

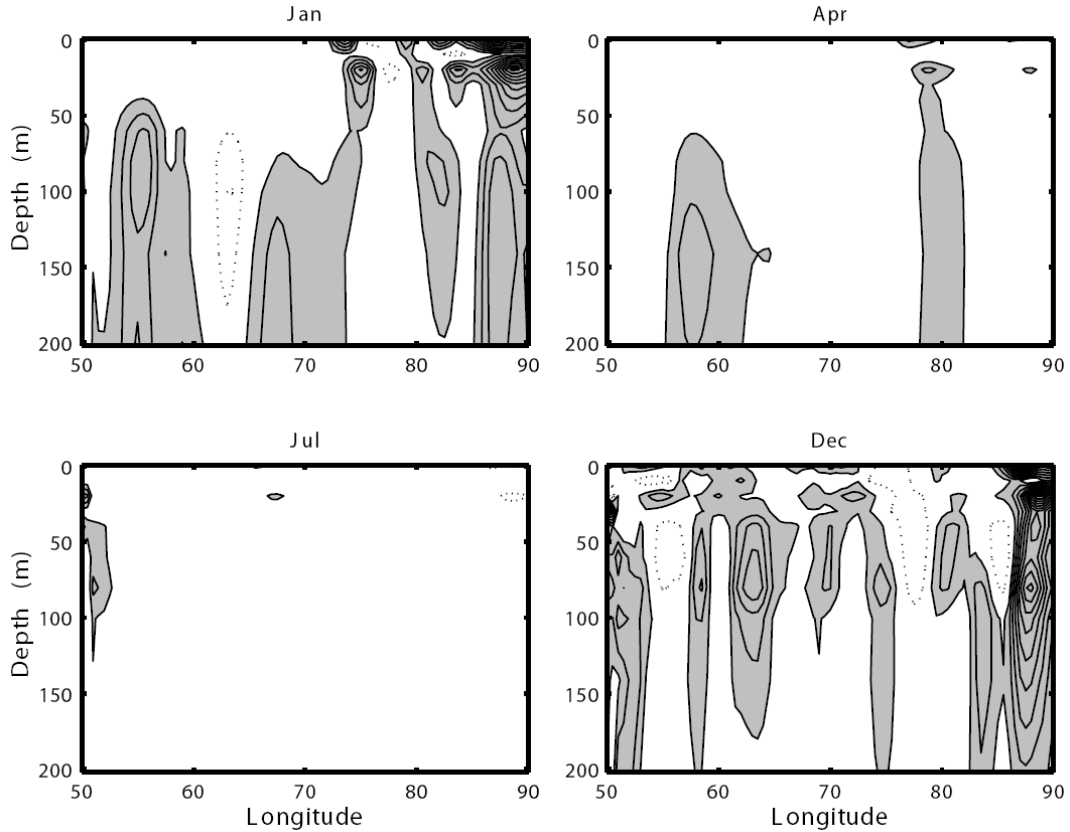


Figure 2.1.7 Longitude-depth plots of baroclinic energy conversions for January, April, July, and December. The contour interval is $1 \times 10^{-3} \text{ W m}^{-3}$. Regions with positive values are shaded.

Fig. 2.1.7 shows the longitude-depth section of baroclinic energy conversion, averaged between 8°S to 10°S for the four months. The conversions in SWIO are strong in January and October, but negligible in April and July, which is consistent with the seasonal variability shown in the horizontal plain (Fig. 2.1.6). However, the strong conversions in the SWIO are not at the surface, but in the depth range from 50 m to 100 m, which coincides with the upper part of the thermocline. This thermocline-intensification is examined further in Section 2.1.4.3.

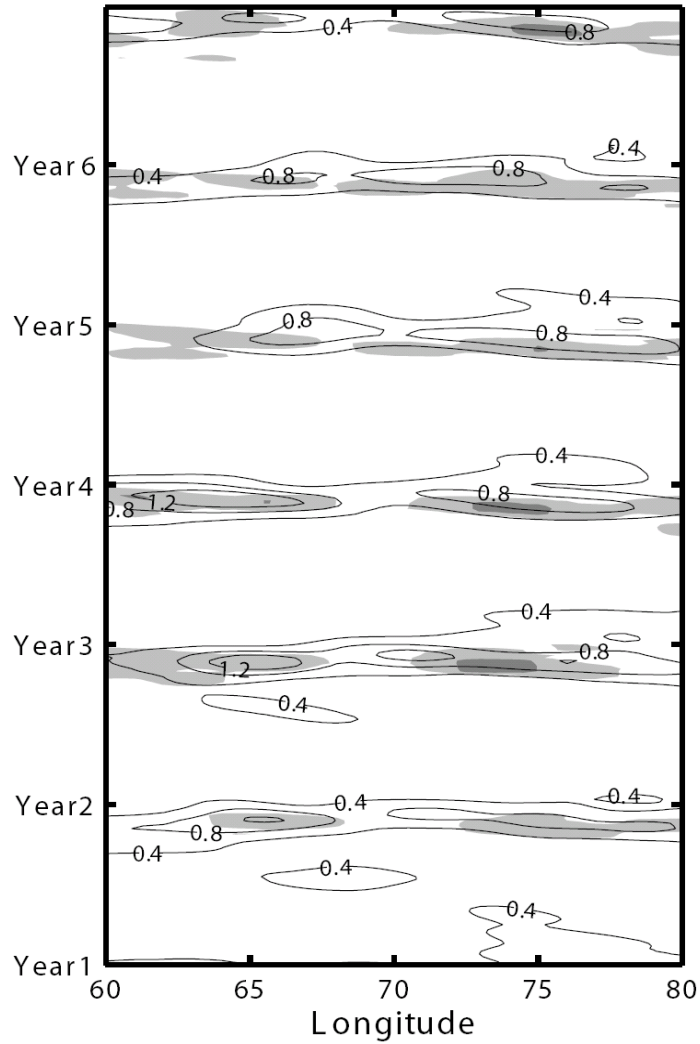


Figure 2.1.8 Vertical shears of zonal currents around the thermocline (~100 m) along 8°S for 6 random years (contours) superposed with the baroclinic energy conversions (shaded area). The units for velocity shear are 10^{-3} s^{-1} . The light gray area shows the energy conversion of $1 \times 10^{-2} \text{ W m}^{-3}$ and the dark gray shows that of $4 \times 10^{-2} \text{ W m}^{-3}$.

Generally, baroclinic instability is mainly caused by the vertical velocity shear. Fig. 2.1.8 shows the vertical velocity shears around the thermocline (~100 m) where they reach maximum, along with the corresponding baroclinic energy conversions. In boreal winter and spring, the vertical velocity shear increases due to the thermocline-intensified zonal advection from the SEIO (see Section 2.1.4.3). Thus, the strong baroclinic energy conversion is caused by a larger density gradient around the

thermocline and by the vertical shear between the SEC and the eastward currents underneath. Moreover, the patterns in Fig. 2.1.8 also show a similar westward propagation as in Fig. 2.1.3, especially the vertical velocity shear from 80°E to 70°E. This indicates that the large vertical shears around the thermocline are caused by the strong currents propagating from the SEIO.

2.1.4.3 Dominant baroclinic modes

In order to explain why the baroclinic energy conversions or the vertical shears of horizontal currents are intensified around the thermocline (Fig. 2.1.7), a modal decomposition method is applied. The horizontal velocities, u and v , are decomposed into vertical modes following Gill (1982). The vertical profile of Brunt-Väisälä frequency and the first three baroclinic modes at 10°S, 60°E are shown in Fig. 2.1.9. The first baroclinic mode reaches maximum at the surface and has a zero crossing at around 100 m, which is the position of the thermocline in our model, while the second baroclinic mode reaches a maximum at around 100 m.

The projections of the intraseasonal zonal currents onto the first two modes are shown in Fig. 2.1.10. The motions in the first mode are strong in the layers above the thermocline (around 100 m). Generally, they are larger than the motions in other modes. Only during boreal winter and spring are the motions in the second mode comparable to the first mode. In most areas in SWIO, the first mode explains more than 50% of the intraseasonal variability while the second mode explains about 40% of the total variability. However, it turns out that the currents of the second baroclinic

mode are mainly responsible for the enhancement of the velocity shear around the thermocline, i.e. for the genesis of OISOs in the SWIO, as shown below.

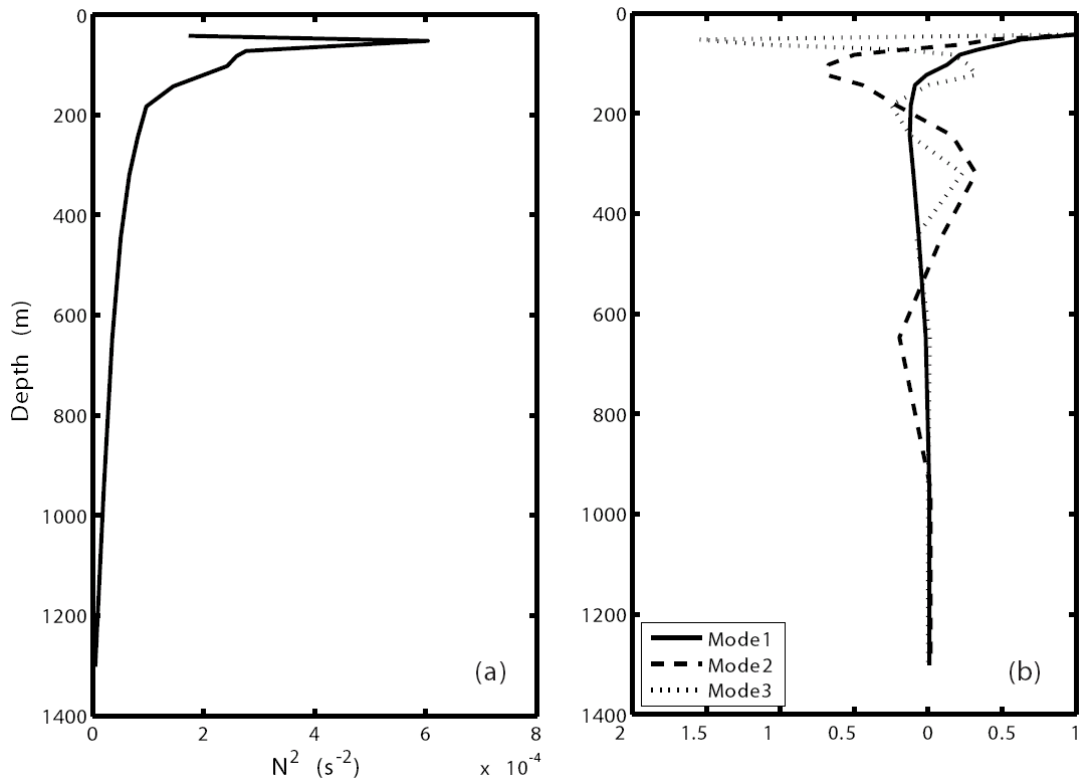


Figure 2.1.9 Vertical profiles of squared Brunt-Väisälä frequency (a) and the eigenfunctions of the first three baroclinic modes (b).

The baroclinic energy conversion caused by various baroclinic modes is calculated. If the 20-year average is taken, the baroclinic conversion of the first mode dominates (Fig. 2.1.11). However, as shown above, the OISOs in SWIO are strong in boreal winter and spring. If the average in December is examined, one would find that the second baroclinic mode is the dominant cause for the OISOs, because the baroclinic energy conversion caused by the second mode is slightly larger than that of the first mode (Fig. 2.1.11). Therefore, the intensification of baroclinic energy conversion around the thermocline (Fig. 2.1.7) is caused by the second baroclinic mode currents (Fig. 2.1.10).

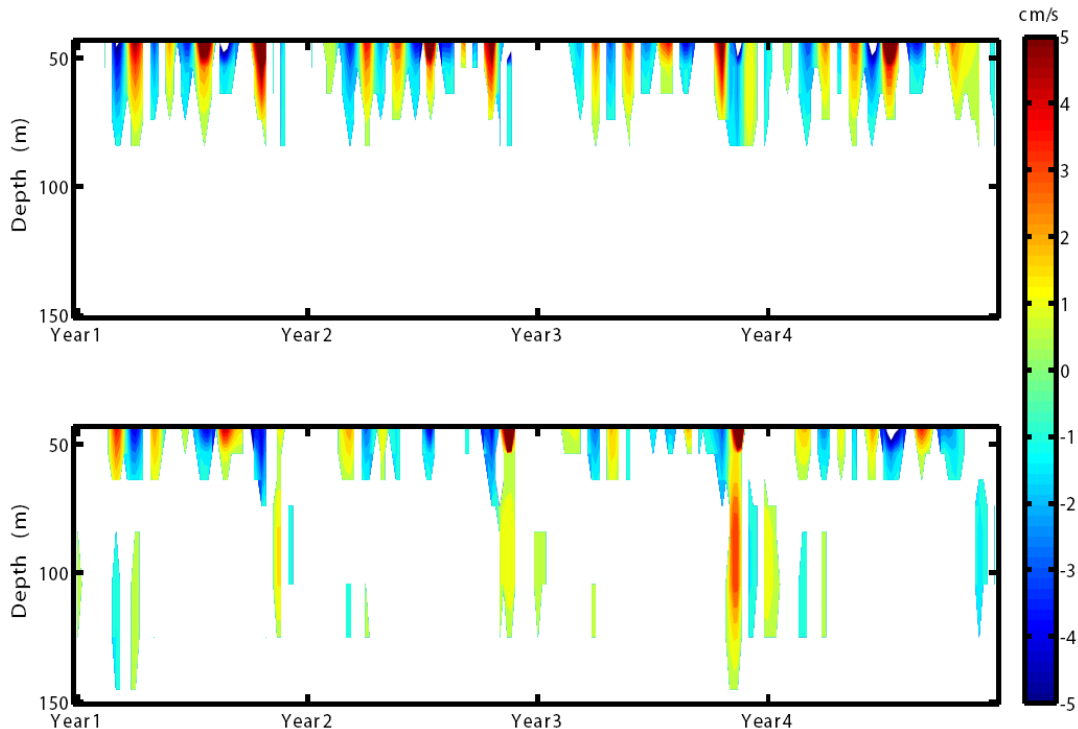


Figure 2.1.10 Projections of intraseasonal velocities onto the first two baroclinic modes in four years.

Furthermore, enhancement of the currents of the second baroclinic mode indicates the relation between the OISOs in the SWIO and the SEIO. Iskandar et al. (2006) found that the OISOs forced by winds over SEIO off Sumatra were mainly captured by the second baroclinic mode. These wind-driven OISOs propagate westward as baroclinic Rossby waves (Masumoto and Meyers 1998; Xie et al. 2002), leading to baroclinic instability in the SWIO. Thus the reinforcement of OISOs in SWIO should be significantly influenced, or even determined, by the OISOs in the SEIO. The in-depth analyses of these remote forcings are part of our future study but beyond the scope of this paper.

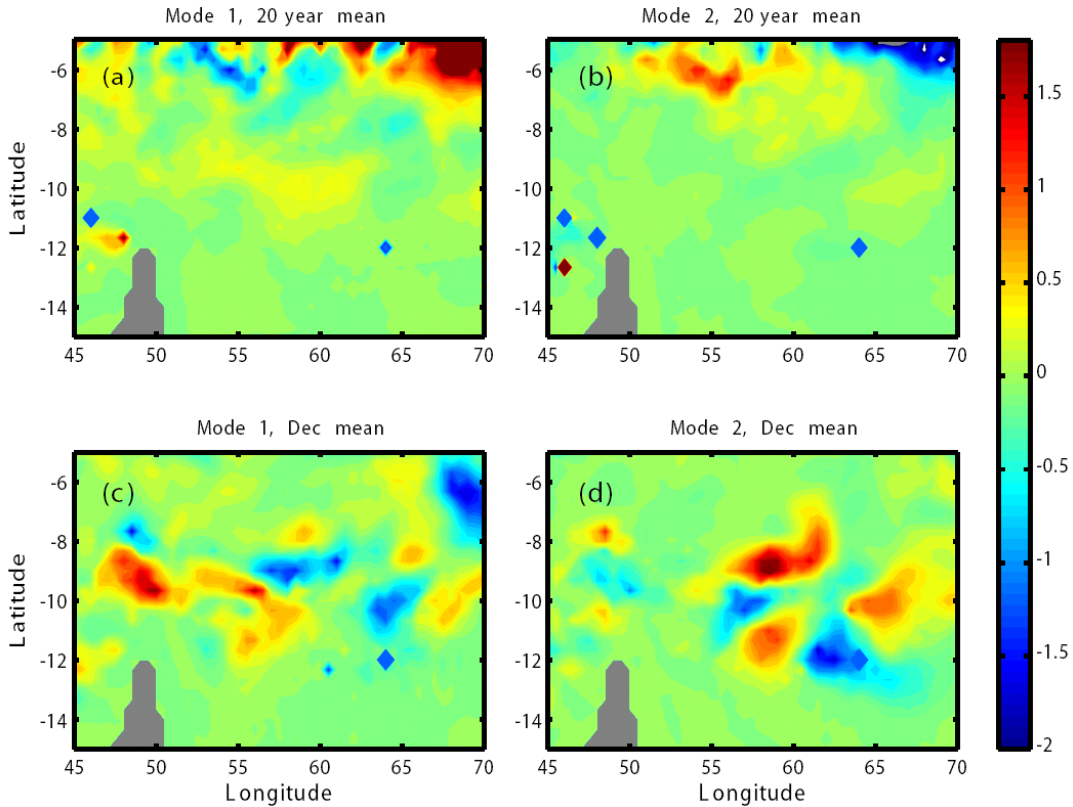


Figure 2.1.11 Baroclinic energy conversion of the first baroclinic mode (a), of the second baroclinic mode (b), of the first baroclinic mode in December (c), and of the second baroclinic mode in December (d). The unit is 10^{-3} W m^{-3} .

2.1.5 Conclusions and discussions

The OISOs in the SWIO are studied by analyzing a model simulation to demonstrate that they have a period of 40-to-80 days and propagate westward as Rossby waves, with a phase speed of about 25 cm s^{-1} in boreal winter and spring and have a wave length of nearly 650 km. The main dynamic reason for OISOs in our model is the baroclinic instability caused by the vertical shear and the density gradients. They are strong in boreal winter and spring, due to the second baroclinic mode waves propagating from the SEIO. Our study indicates that the OISOs in the SWIO have a close relation with those in SEIO.

According to our model, the baroclinic instability is confirmed to be important for OISOs in the SWIO even though we cannot completely exclude the effect of AISOs on the OISOs. The first reason is that in the wavenumber spectrum, the high-frequency part of the NCEP Reanalysis data decreases much faster than the QSCAT surface winds. Thus the NCEP wind data may not be able to resolve the wind fields with horizontal scale smaller than 800-1000 km (Milliff et al. 2004). Secondly, parts of the AISOs are excluded in the climatological winds, even though we use weekly mean winds. Therefore, by comparing the model results driven by the interannual wind stresses and the present model results, the effects of the external forcing and the internal instabilities on OISOs in the SWIO are assumed to be separable for evaluation, which will be reported elsewhere.

The OISOs are an important part of the ocean dynamics in the oceanic mixed layer. In the SWIO, ocean dynamic processes contribute more to the SST variability than the surface heat fluxes do (Klein et al. 1999; Chambers et al. 1999; Murtugudde and Busalacchi 1999). Jochum and Murtugudde (2005) argued that the internal variability with a period of ~ 100 days is important and may be critical for predicting SSTs in the Indian Ocean, because it may significantly affect the Indian monsoon. Xie et al. (2002) pointed out that the SST variability in SWIO is not locally forced but due to the Rossby waves that propagate from SEIO. Since OISOs in SWIO are enhanced due to the second baroclinic mode waves propagating from the SEIO, they are potentially critical to the SST variability. Via their putative impacts on SST, the OISOs probably also have influence on the rainfall over Eastern Africa and have feedbacks to the atmospheric intraseasonal oscillations, like the Madden-Julian

oscillations (Waliser et al. 1999), adding to the growing evidence for the importance of this region to regional climate variability. Therefore, OISOs in SWIO need to be better understood. The thermodynamic properties of the OISOs and their feedbacks to the atmosphere are a focus of our future explorations.

2.2 Seasonal influence of Indonesian Throughflow in the southwestern Indian Ocean

Abstract

The influence of the Indonesian Throughflow (ITF) on the dynamics and the thermodynamics in the southwestern Indian Ocean (SWIO) is studied by analyzing a forced ocean model simulation for the Indo-Pacific region. The warm ITF waters reach the subsurface SWIO from August to early December, with a detectable influence on weakening the vertical stratification and reducing the stability of the water column. As a dynamical consequence, baroclinic instabilities and oceanic intraseasonal variabilities (OISVs) are enhanced. The temporal and spatial scales of the OISVs are determined by the ITF-modified stratification. Thermodynamically, the ITF waters influence the subtle balance between the stratification and mixing in the SWIO. As a result, from October to early December, an unusual warm entrainment occurs and the SSTs warm faster than just net surface heat flux driven warming. In late December and January, the signature of the ITF is seen as a relatively slower warming of SSTs. A conceptual model for the processes by which the ITF impacts the SWIO is proposed.

2.2.1 Introduction

Sea surface temperature (SST) variations in the southern Indian Ocean are generally modest. But they are significantly larger in the southwestern Indian Ocean (SWIO, Annamalai et al. 2003). In an analysis of observational data, Klein et al. (1999) reported that surface heat flux anomalies explain the basin-wide warming over

most of the tropical Indian Ocean, the only exception being the SWIO. Masumoto and Meyers (1998) argued that the large SST variations in the SWIO are mainly attributable to the forced Rossby waves propagating in from the southeastern Indian Ocean (SEIO). Moreover, due to Ekman pumping, the SWIO is an upwelling region, where the subsurface thermocline variability has a significant influence on SSTs (Murtugudde and Busalacchi 1999, Schott et al. 2002). Xie et al. (2002) further concluded that much of the SST variability in the SWIO is not due to local winds or surface heat fluxes, but is instead due to oceanic Rossby waves that arrive from the east modifying the temperature of upwelled waters.

The oceanic intraseasonal variabilities (OISVs) have been shown by several recent studies to be important for the heat budget in the oceanic mixed layer, via their impact on horizontal heat transport and related non-linear advective effects (Waliser et al. 2003a, 2004; Jochum and Murtugudde 2005). In the southern Indian Ocean, Du et al. (2005) studied the seasonal mixed layer heat budget by analyzing a high-resolution OGCM to argue that maximum upwelling occurred when the Indonesian Throughflow (ITF) reaches its annual maximum. Moreover, the warm advection associated with the ITF in their model neutralized the cold upwelling, leading to a slight damping of SST variability off Java and Sumatra (also see Murtugudde et al. 1998). They also found that the residual heat flux in their OGCM was not negligible during boreal winter, which might be attributable to the local intraseasonal variations. By comparing the model runs with open and closed ITF, Hirst and Godfrey (1993) noted that maximum temperature and salinity perturbations are along the thermocline

in the open ITF run in the region between 28°S and 8°S, in addition to a strong vertical velocity shear.

To the best of our knowledge, there have been very few observational and modeling studies of OISVs thus far in the SWIO (e.g., Murtugudde and Busalacchi 1999). We showed in Section 2.1 (Zhou et al. 2008a) that the OISVs are strong from October to January, when they are mainly strengthened by the baroclinic instabilities. Some interesting questions remain unexplored. Since the OISVs in the SWIO are hypothesized to originate in the east (Xie et al. 2002; also see Section 2.1), what is the relation between the ITF and the OISVs in SWIO? Do the OISVs in SWIO have a significant impact on local SST variability? In this study, we attempt to address these questions by analyzing an OGCM output along with the World Ocean Atlas data (WOA, Conkright et al. 2002).

In Section 2.2.2, the model is described and compared with satellite SST product (comparisons to altimeter data were presented in Section 2.1). In Section 2.2.3, the westward propagation of ITF waters and its primary influence in the SWIO is examined. In Section 2.2.4, the dynamical influence of the ITF in the SWIO is discussed. Section 2.2.5 discusses the thermodynamic influence of the ITF, focusing on SST variability and the unusual warm entrainment. A conceptual model for the influence of ITF in SWIO, along with Discussion and Conclusion, is presented in Section 2.2.6.

2.2.2 Model description and comparison

The SWIO has noticeably large OISVs (Waliser et al. 2003; Jochum and Murtugudde 2005), which are mainly attributable to the oceanic internal baroclinic

instabilities (also see Section 2.1). The wind-forcing used here are weekly mean climatologies which retain very little energy in the intraseasonal band, consistent with the hypothesis that the OISVs are generated internally by the ocean. Interannual variability in the atmospheric intraseasonal variabilities (AISVs) may in fact modulate these OISVs especially since the oceanic background state itself varies on interannual time-scales. To simplify the analyses, it is assumed that the interannual variability in the AISV forcing will not significantly affect the basic processes of oceanic internal instabilities and the generation of OISVs. SST anomalies associated with the OISVs are a significant fraction of the total SST variability in the SWIO which supports our assumption (Jochum and Murtugudde 2005). Therefore, climatological model outputs are analyzed in this paper, from which the responses to the intraseasonal atmospheric forcing are largely removed.

The model used is a reduced gravity, sigma-coordinate, primitive equation OGCM, with a horizontal resolution of $1/3^\circ$ in latitude and $1/2^\circ$ in longitude over the Indo-Pacific domain covering 32°E - 76°W , 30°S - 30°N (Murtugudde et al. 1996, 1998). There are 15 sigma layers in the vertical below the variable depth mixed layer with a resolution of ~ 15 m in the thermocline in the SWIO, so that vertical oscillations in the interior ocean can be adequately resolved. Surface mixed layer is determined by the hybrid mixing scheme of Chen et al. (1994) which explicitly accounts for the entrainment induced by the surface turbulent kinetic energy, shear-driven dynamic instability mixing, and convective mixing to remove static instabilities. The last sigma-layer thickness is a prognostic variable whereas the other sigma layers are specified constant fractions of the total depth below the mixed layer

to the motionless abyssal layer. The temperature and salinity from the climatological WOA (Conkright et al. 2002) are interpolated onto the sigma layers and the model temperature and salinity are relaxed to the interpolated WOA in the sponge layer (south of 25°S) with a time-scale of 5 days. The model is driven by the climatological weekly NCEP Reanalysis winds as mentioned above (see Murtugudde et al. 2000 for details) with the surface heat fluxes computed by an advective atmospheric mixed layer model which allows SSTs to be directly determined by the variables internally calculated in the model, such as the air temperature and humidity (Seager et al. 1995; Murtugudde et al. 1996). The model outputs for all the analyses presented here are weekly mean fields from the last 20 years of a 270-year simulation.

The OGCM has been reported in many previous applications, demonstrating its ability to simulate the ocean dynamics and thermodynamics reasonably well in the tropical oceans. Mean SSTs (temperatures of the surface mixed layer in the model) and standard deviations (*STDs*) of the model outputs and the gridded AVHRR data (McClain et al. 1985) are shown in Fig. 2.2.1. Model simulations match satellite observations very well in the tropics; e.g. the 28°C isotherm in the model, which is the critical threshold for the occurrence of deep convection in the atmosphere, is almost identical to observations. However, there are obvious cold biases, as in the Bay of Bengal, where simulated SSTs are generally cooler than the observations by ~0.5°C. Maximum cold bias (~1°C) occurs between 10°S and 20°S centered at 15°S, 70°E. *STDs* of the SSTs are generally small (< 1°C) in the tropical Indian Ocean, where the SSTs are higher than 28°C. In the SWIO, *STDs* are generally larger than 1.5°C. Moreover, large *STDs* to the northwest of Australia and around the northern

tip of Madagascar are also well resolved. These simulated features are consistent with the observations. However, SST variances are smaller than observations in the western Arabian Sea and the northern Bay of Bengal by $\sim 0.5^{\circ}\text{C}$ and around 20°S , 80°E by $\sim 1^{\circ}\text{C}$. Small SST variances are mainly attributable to the removal of AISVs from the external wind forcing.

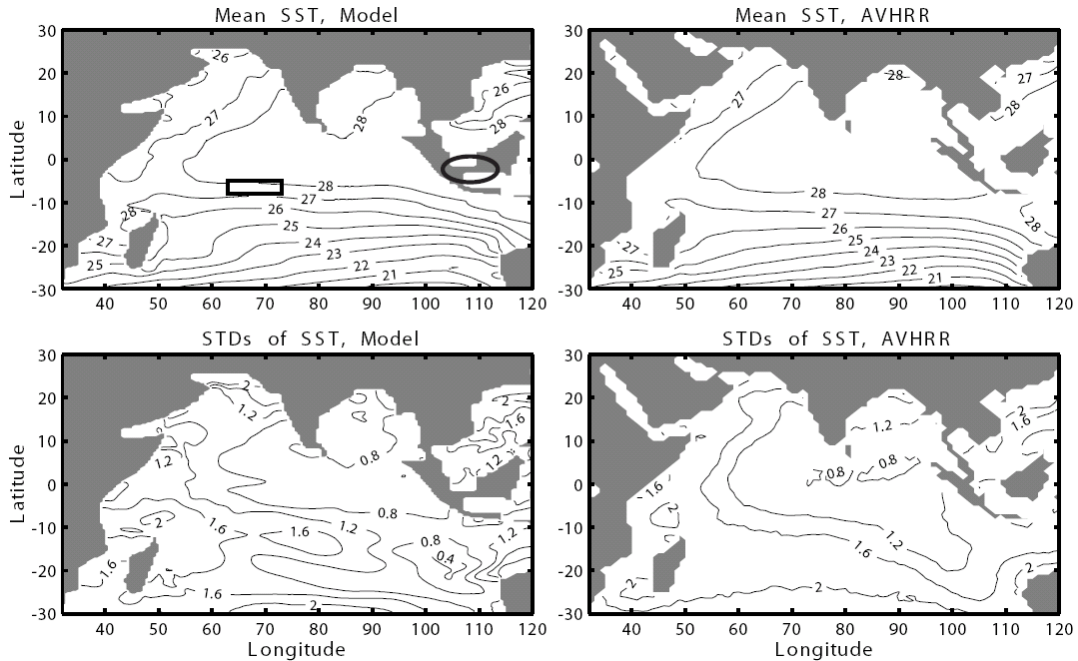


Figure 2.2.1 Mean SSTs of the 20-year model outputs (a) and of AVHRR data averaged from 1992-2005 (b). (c) and (d) are the same as (a) and (b) but for the *STDs*. All fields are $^{\circ}\text{C}$. The contour interval for the mean SSTs is 1°C , and for the *STDs* is 0.4°C . The SWIO, which is defined as a rectangular region from 5°S to 8°S and from 63°E to 73°E , is identified with a think rectangle in (a). The Karimata Strait, which is open in the Java run, is identified with an oval in (a).

Local maximum in SST variance centered around 12°S , which is attributable to the internal variability of the Indian Ocean, has been discussed in Jochum and Murtugudde (2005). In this paper, we focus on the variabilities in the SWIO, which is identified by a rectangle in Fig. 2.2.1(a). The cold bias and small SST variance to the south of 10°S do not have significant impact on the following discussions. We

conclude that the model performance is acceptable for this study in the low latitudes in the Indian Ocean.

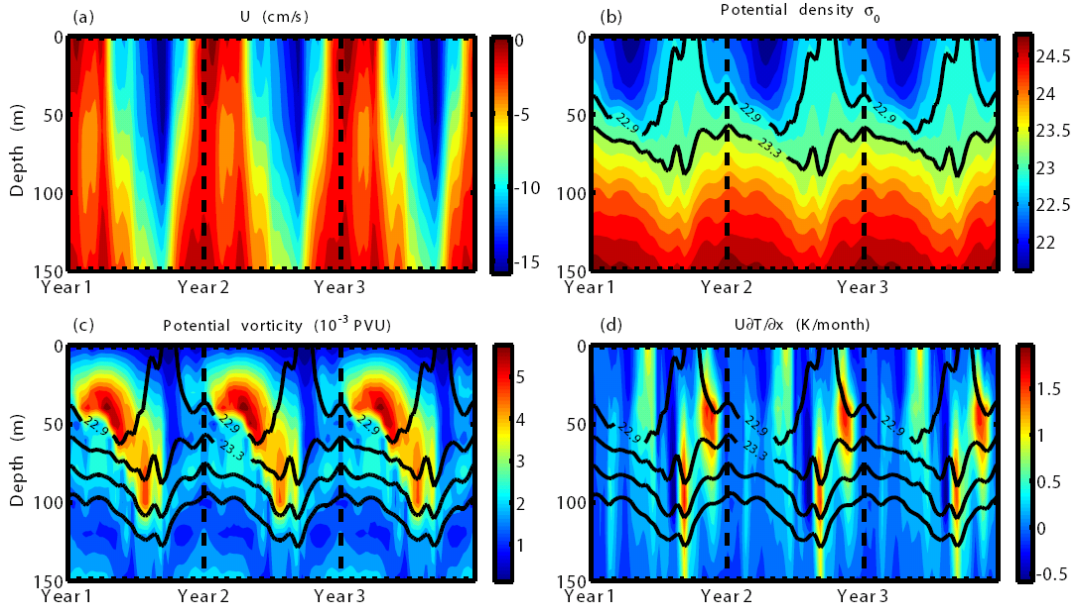


Figure 2.2.2 Zonal velocity (a), potential density (b), Ertel potential vorticity (c), and zonal temperature advection (d) averaged from 10°S to 15°S along 114°E in three years.

2.2.3 Westward propagation of the ITF waters

2.2.3.1 Indonesian Throughflow in the model

While there is no precise or universally accepted definition of ITF, observational estimates have typically focused on zonal geostrophic transports between Java and Australia in the upper ocean (Meyers 1996). A similar measure was used to demonstrate the impact of ITF in the Indian Ocean dynamics and thermodynamics as in Murtugudde et al. (1998). The zonal transport in the model averaged down to 400 m between 10°S and 15°S along 114°E reaches a maximum of 15 Sv (1 Sv = $10^6 \text{ m}^3 \text{ s}^{-1}$) in August with an annual mean of about 7 Sv, as in Murtugudde et al. (1998), which is slightly smaller than the commonly accepted value of 10 Sv (Gordon 2001)

but well within the uncertainty of the observational and model estimates (Godfrey 1996). The ITF waters at different depths follow different trajectories in the Indian Ocean (Song et al. 2004; Murtugudde et al. 1998). Only the upper layer transports (above ~150 m) are confined to 20°S and 8°S, with further significant influence on the mixed layer in the SWIO, as discussed below. Deeper ITF waters, especially below 500 m, mainly flow southward and circulate poleward to 15°S (Song et al. 2004). Therefore, in this study, we only focus on simulated ITF in the upper 150 meters, which is examined further below.

In the upper 150 meters, we calculated the potential density, the Ertel potential vorticity (EPV), which is defined as $\frac{(f + \zeta)}{\rho} \frac{\partial \theta}{\partial z}$ where f is the Coriolis parameter, ζ is the relative vorticity, ρ is the density, and θ is the potential temperature; and the zonal temperature advection, $-u \frac{\partial T}{\partial x}$, where u is the zonal velocity and T is the temperature. Associated with the strong westward velocities from July to September (Fig. 2.2.2a), the potential density σ_0 varies from 22.9 to 23.3 (Fig. 2.2.2b), the EPVs are smaller than 2×10^{-3} PVU ($1 \text{ PVU} = 10^{-6} \text{ K m}^2 \text{ kg}^{-1} \text{ s}^{-1}$, Fig. 2.2.2c), and the warm zonal advection occurs below the surface between 50 m to 100 m (Fig. 2.2.2d). The water mass ranging in potential density from 22.9 to 23.3 can be tracked from the SEIO to the SWIO as shown in the T - S diagram (cross signs in Fig. 2.2.3). To the east of 100°E, this water mass is not clearly separable from the ambient water (black and blue circles in Fig. 2.2.3), due to a strong mixing in the Indonesian seas (Meyers 1996; Murtugudde et al. 1998). To the west of 100°E, the ITF waters in the upper layer are distinguishable from the ambient Indian Ocean water. The density of the

water mass continues to increase during its westward journey due to mixing with the denser ambient Indian Ocean water (Fig. 2.2.3). The pathway of the water mass is qualitatively consistent with the Lagrangian trajectory of the upper-layer ITF water shown in Song et al. (2004).

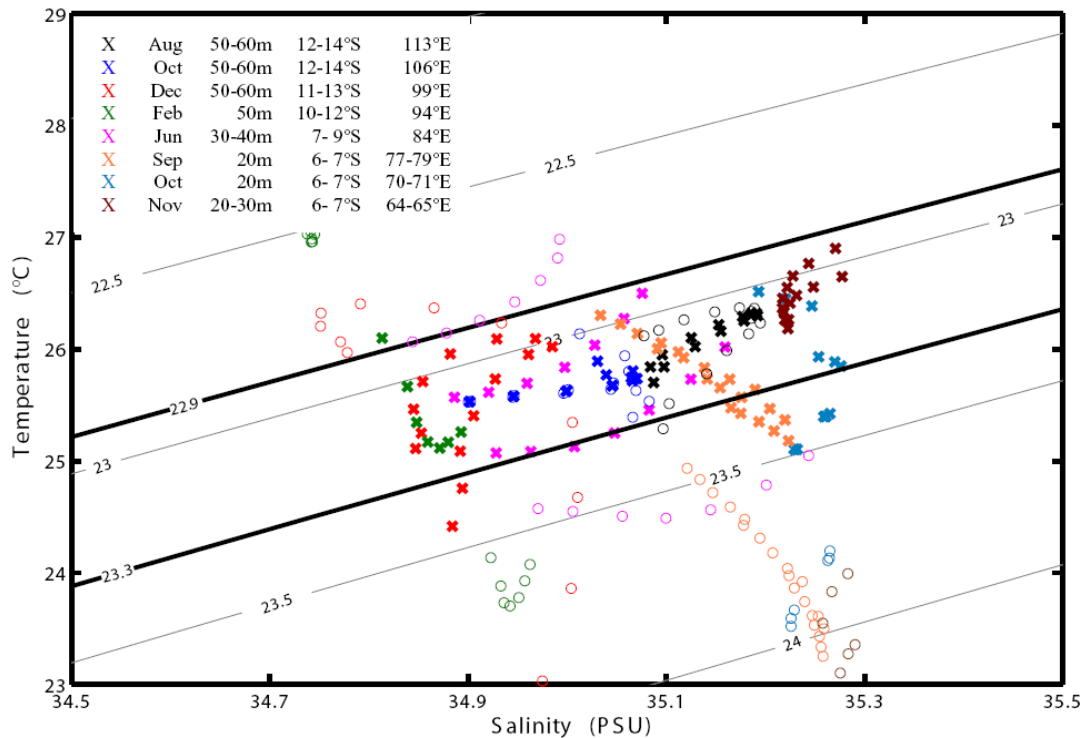


Figure 2.2.3 *T-S* diagram of the monthly 20-year mean model outputs. The circles represent the *T-S* at 20 meters below and above those represented by the crosses in the same color. Each symbol represents *T-S* at one specific depth, latitude, and longitude, as shown in the legend. For example, the twelve black crosses represent the *T-S* properties at two layers (50 m and 60 m), one longitude point (113°E), and six latitude points (from 12°S to 14°S with a latitudinal resolution of 1/3°).

2.2.3.2 Westward propagation of the ITF waters

Because the subsurface ITF waters are far from the surface and the lateral boundaries, there is no generation or destruction of potential vorticity once they enter the Indian Ocean. Therefore, projecting the EPV and the horizontal temperature advection onto the $\sigma_0 = 23.3$ surface and following the pathway shown in Fig. 2.2.3,

one can also track the small EPV ($< 2 \times 10^{-3}$ PVU) and warm advection associated with the ITF from the east to the west across the Indian Ocean basin. Since the ITF water does not propagate strictly westward especially between 80°E to 100°E (Fig. 2.2.3), to be more accurate, the horizontal temperature advection,

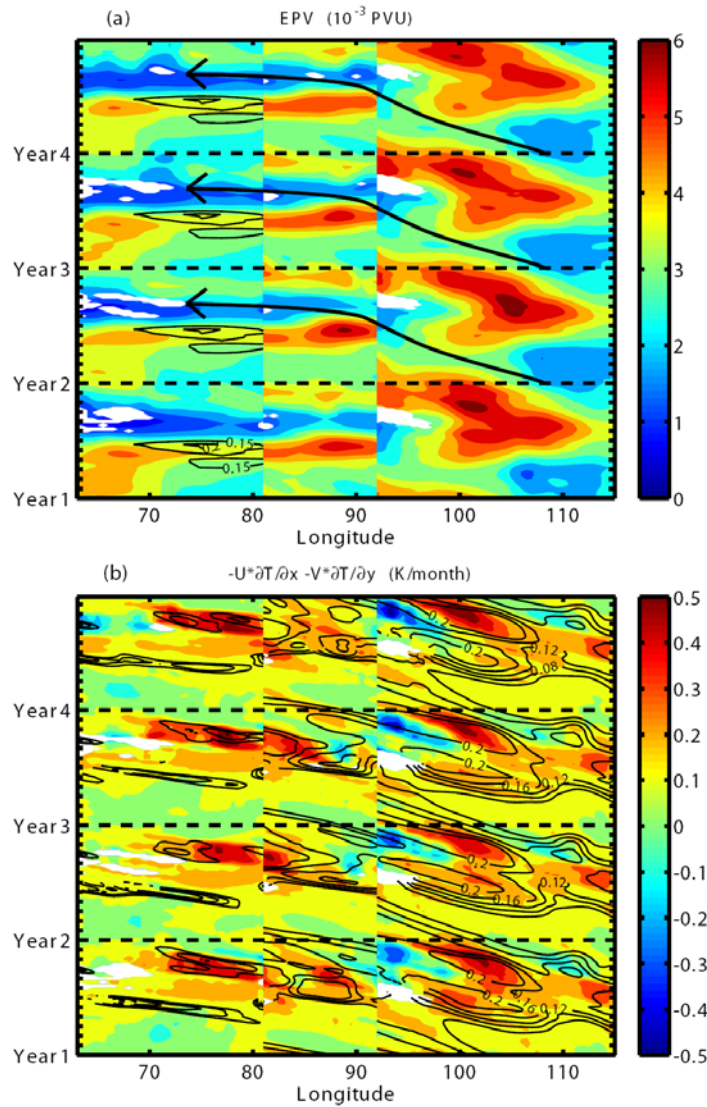


Figure 2.2.4 EPV (a) and horizontal temperature advection (b) projected onto the surface of $\sigma_0 = 23.3$ along 6°S from 63°E - 81°E , along 8°S from 81°E - 92°E , and along 12°S from 92°E - 115°E , which are smoothed with 5° zonal running mean. The latitude shift from 12°S to 6°S follows the spreading of ITF waters shown in Fig. 3. The contours in (a) are the wind stress curl (10^{-6} Pa m^{-1}) and the contours in (b) are the zonal velocities on the $\sigma_0 = 23.3$ surface in m s^{-1} .

$-u\partial T/\partial x - v\partial T/\partial y$ (where v is the meridional velocity), is shown in Fig. 2.2.4(b), although the zonal temperature advection, $-u\partial T/\partial x$, generally dominates. The warm ITF waters are carried westward by the south equatorial currents, as shown with the contours in Fig. 2.2.4b. The westward spreading rate of the ITF waters is about 20 cm s^{-1} in the SEIO, but slightly slower in the SWIO ($\sim 15 \text{ cm s}^{-1}$). The σ_0 at

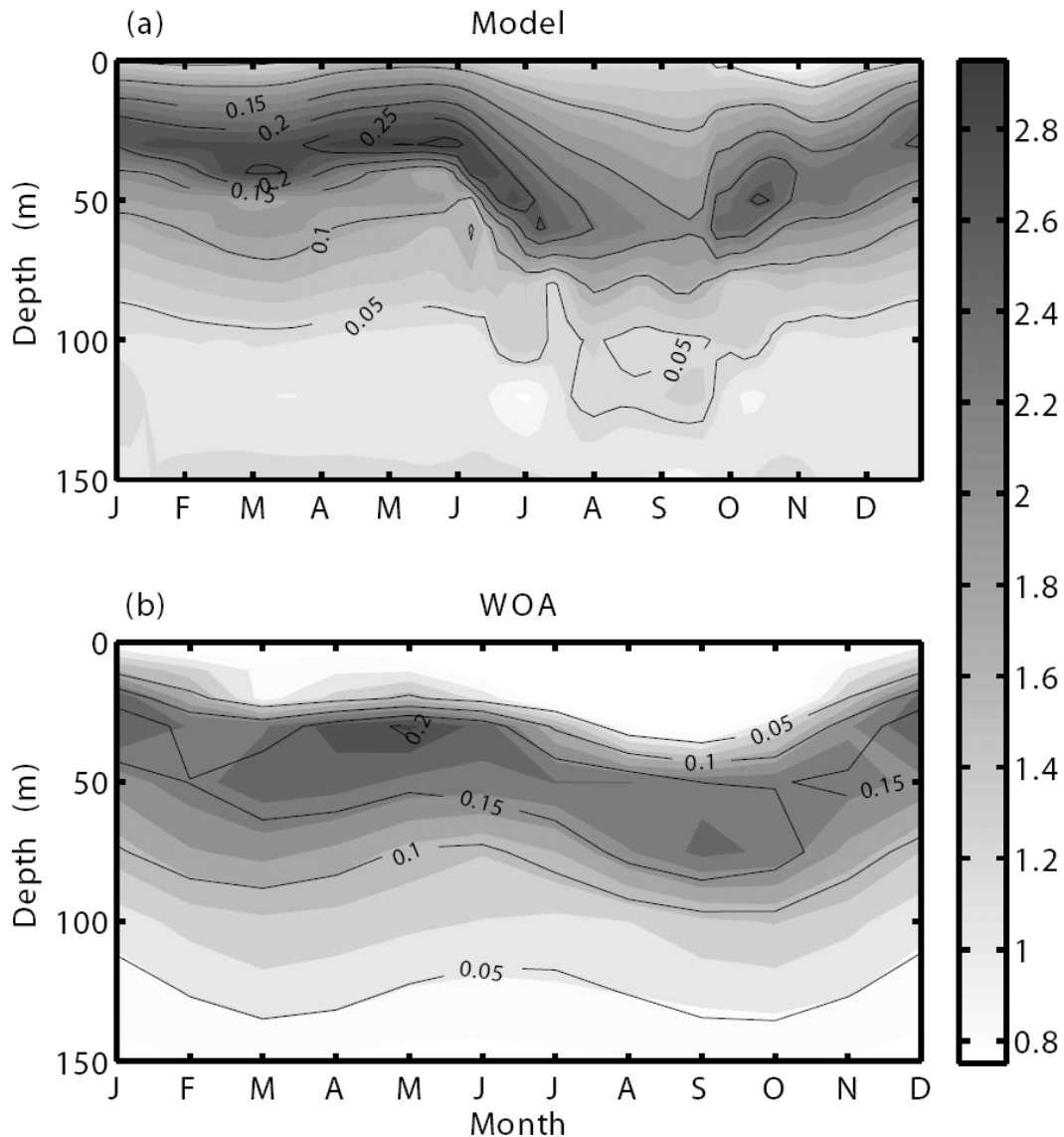


Figure 2.2.5 (a) Mean Brunt-Väisälä frequency (shades in 10^{-2} s^{-1}) and the vertical temperature gradient (contours in K m^{-1}) within a rectangular region 6°S - 7°S , 63°E - 73°E , calculated with the model outputs. (b) The same as (a), but calculated with the monthly high-resolution WOA.

the sea surface are larger than 23.3 in the blank regions between 63°E-73°E in Fig. 2.2.4, which imply very strong diapycnal mixing blurring the distinction between the ITF water and ambient Indian Ocean water (see Section 2.2.4). These regions are also where the warm horizontal advection carrying the ITF waters ends, which imply that the warm subsurface waters are entrained in to the surface mixed layer (see Section 2.2.5.1 for detailed discusses). The westward spreading of the ITF waters in the model is given in Fig. 2.2.4 and is discussed below.

2.2.3.3 The primary influence of the ITF waters in SWIO

There is a thermocline dome in the SWIO, which is maintained by the Ekman pumping. When the ITF waters reach this region, they significantly affect the vertical structure. Because the ITF waters are warmer and more buoyant than the ambient waters, they reduce the vertical stratification as well as the stability in the upper layer from August to December (Fig. 2.2.5a). The modification of the vertical structure is mainly attributable to the temperature effect of the ITF waters since the Brunt-Väisälä frequency (N) and the vertical temperature gradients are close to each other (Fig. 2.2.5a). Though the ITF waters are also fresher than the ambient waters, the salinity difference is so small that its effect on the vertical stratification is negligible (also see Hirst and Godfrey 1993). Vertical temperature gradients and N in the upper layer reach their minimum simultaneously in October and early November. Meanwhile, they become larger between the subsurface and the cold deep ocean waters due to warm advection. Vertical variation of N and the temperature gradients from August to the early December can also be detected in the monthly high-resolution ($1/4^\circ$) WOA (Conkright et al. 2002; Boyer et al. 2005), which is shown in Fig. 2.2.5b. In summary,

the primary influence of the ITF waters on the SWIO is to reduce the vertical stratification leading to significant impacts on the dynamics and thermodynamics in SWIO, which are discussed in the following two sections.

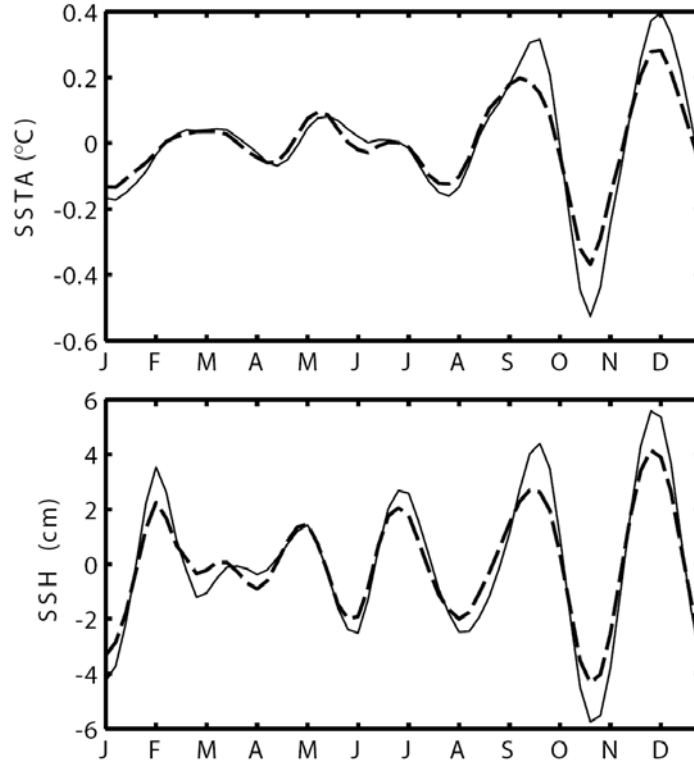


Figure 2.2.6 The intraseasonal SSTAs and SSHs averaged in the SWIO (6°S - 7°S , 63°E - 73°S) in the Java run (solid line) and in the control run (dash line).

In order to highlight the primary influence of the ITF on the SWIO, we made another test (which is referred to as the Java run) with the Karimata Strait open (the strait connecting the South China Sea and the Java Sea; identified with an oval in Fig. 2.2.1a) and rest of the model configuration unchanged. Correspondingly, the model run which we focused on in this paper is referred as the control run. As predicted in Gordon et al. (2003), in boreal winter, the intrusion of fresh surface waters from the Java Sea into the southern Makassar Strait lead to cool SSTs in the Indian Ocean, meanwhile, thermocline-intensification of the ITF is enhanced (Tozuka et al. 2007).

This seasonal variability is well resolved in the Java run. Thus, the contrast between the subsurface warm ITF water and upper Indian Ocean water is more distinct in the Java run, as is seen in the vertical profile of N (not shown). From July to December, the Brunt-Väisälä frequency in the Java run is smaller (larger) than it is in the control run above (below) the thermocline. Therefore, stability of the upper layer in boreal winter is reduced more in the Java run than it is in the control run. As a result, the intraseasonal variabilities of SSTs and SSHs in SWIO are stronger in the Java run than they are in the control run (Fig. 2.2.6) in boreal winter. These comparisons support the hypothesis that ITF exerts direct influence on the SWIO as discussed above.

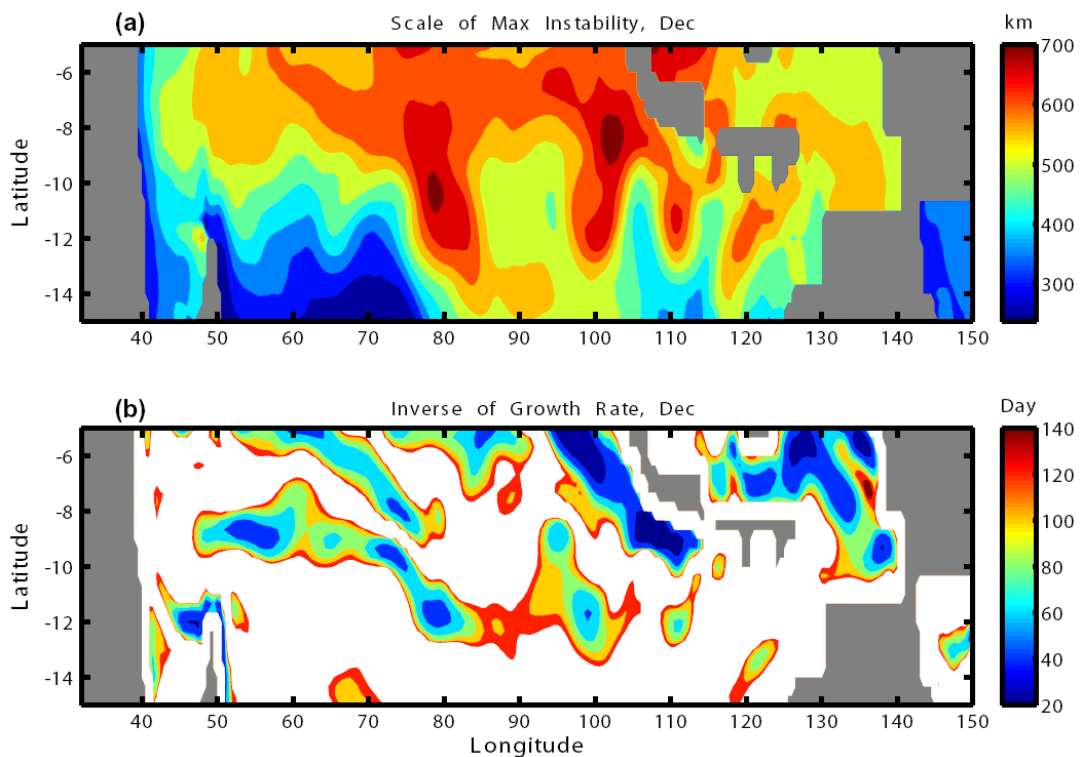


Figure 2.2.7 Wavelength of the maximum instability ($L_{max} = 3.9L_d$) in December (a) and the inverse of the corresponding maximum growth rate ($\sigma_{max} = 0.3U/ L_d$) in December (b).

2.2.4 Influence of ITF on the dynamics in the SWIO: Scale selection

In the SWIO, reduced vertical stratification by the ITF waters is in favor of the baroclinic instability. As a result, the baroclinic energy conversions and the OISVs are enhanced in boreal winter as shown in Section 2.1. Since the subsurface ITF waters are away from the boundaries, their potential vorticity is conserved during the westward propagation. Following the Eady model described in Vallis (2006, see the Appendix for details), the maximum growth rate of the baroclinically unstable wave is $\sigma_{\max} \approx 0.3U/L_d$, where U is the basic flow, L_d is the Rossby radius of deformation, the corresponding wavelength of the most unstable wave is $L_{\max} \approx 3.9L_d$. The L_{\max} and σ_{\max} are calculated with the model outputs and shown in Fig. 2.2.7. In the SWIO, the wavelength of the maximum instability is 500-600 km, which is very close to the wavelength of the OISVs in the SWIO (~650 km as shown in Section 2.1). The period corresponding to the maximum growth rate is mainly between 40 to 100 days, which is the typical intraseasonal band. Though the theoretical estimates are relatively simple and idealized, they reveal that the dynamical influence of the ITF waters in the SWIO is primarily to reinforce the baroclinic instability and the OISVs via reducing the stratification. Furthermore, the ITF-modified stratification determines the Rossby radius of deformation L_d (the Coriolis parameter and the water depth can be considered as invariable), and thereby determines the time-scale and length-scale of the OISVs in the SWIO.

2.2.5 Influence of ITF on the SSTs in SWIO

SST variability in the SWIO is dominated by net surface heat flux Q_{net} , as shown in Fig. 2.2.8. From April to September, the correlation between them is as high as

0.97. However, there are also obvious seasonally-dependent discrepancies between Q_{net} and the SST variability. From October to early December, SSTs warm faster while in late December and January, they warm slower than Q_{net} . The former difference can clearly be attributed to zonal advection and entrainment, which are significantly influenced by the ITF as discussed in Section 2.2.5.1, while the latter difference is assumed to have only indirect relations with the ITF, which is discussed in Section 2.2.5.2.

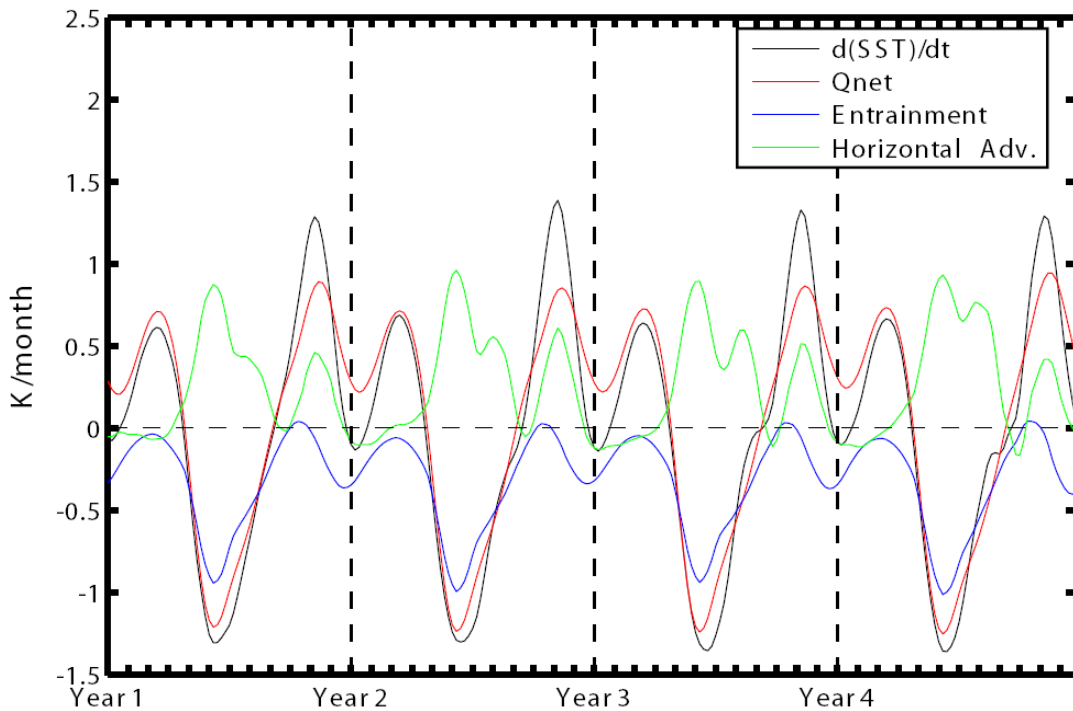


Figure 2.2.8 SST variation, net surface heat flux, entrainment, and horizontal temperature advection averaged within a rectangular region 6°S - 7°S , 63°E - 73°E , which are smoothed with the one-month running mean. Positive values mean that the upper mixed layer gain heat, while negative values mean that the upper mixed layer lose heat.

2.2.5.1 Fast warming SSTs from October to early December

Hirst and Godfrey (1993, 1994) concluded that only in regions with strong upwelling and convective mixing can SSTs be dramatically affected by subsurface

temperature perturbations generated by the ITF. The SWIO is just such a region. Due to Ekman pumping, it is an open-ocean upwelling region which is characterized by a shallow thermocline (Reverdin 1987; Murtugudde and Busalacchi 1999; Schott et al. 2002). Meanwhile, surface turbulent kinetic energy tends to deepen the mixed layer, leading to significant entrainment as a contribution to the mixed layer heat budget. The correlation between entrainment and SST variability is 0.8 (Fig. 2.2.8). In October after the warm ITF waters reach the SWIO, the water column from 30 m – 70 m (centered at ~55 m) which is just beneath the mixed layer bottom is significantly warmed (Fig. 2.2.9). Thus, rather non-intuitively, entrainment acts to warm the mixed layer rather than cool it (Fig. 2.2.8).

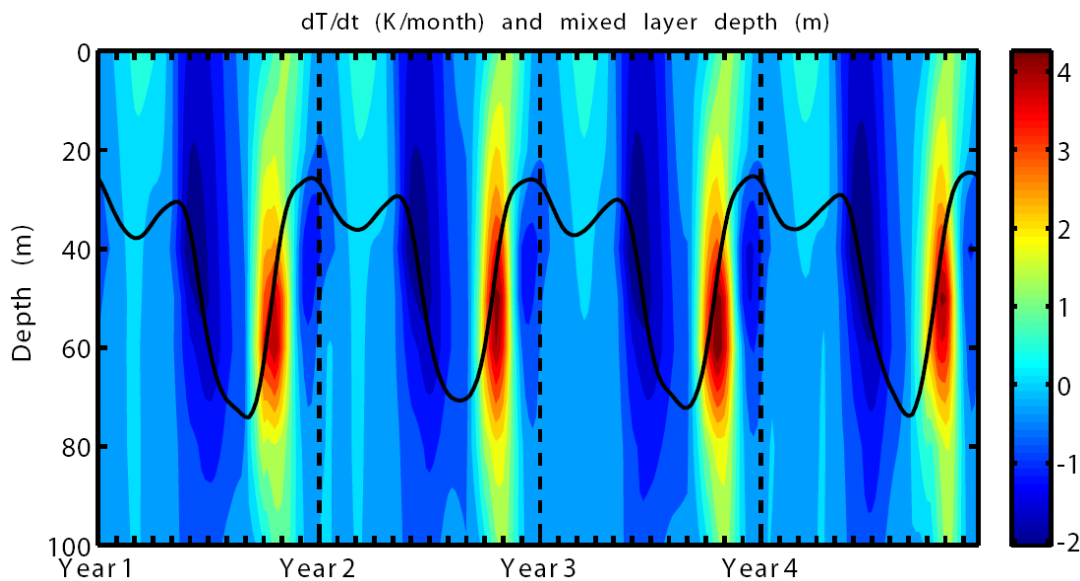


Figure 2.2.9 Temperature variations (color codes) and mixed layer depth (solid line), which are averaged in the region of 6°S-7°S, 63°E-73°E.

The anomalous warm entrainment is usually associated with a barrier layer structure, which is an isothermal layer below the density-stratified surface mixed layer (Lukas and Lindstrom 1991; Sprintall and Tomczak 1992) and serves to decouple the thermodynamics and the mixed layer dynamics. There are multiple

processes responsible for the barrier layer formation. For example, Schiller and Godfrey (2003) found that in the central and eastern tropical Indian Ocean, the barrier layer occurs due to the long-term fresh water gains at the surface. Meanwhile, the penetrative solar radiation heats the water below the shallow mixed layer during the clear and calm phase of an intraseasonal event. As a result, the vertical temperature inversion occurs, leading to the warm entrainment. We calculated the barrier layer according to the definition of Sprintall and Tomczak (1992) with the weekly model outputs. The large penetrative solar heating and the barrier layer formation are captured in the central and eastern tropical Indian Ocean (Fig. 2.2.10). However in SWIO, penetrative heating rates are smaller than 0.1 K month^{-1} in October. The mixed layer is quite deep and there is almost no barrier layer (also see Murtugudde and Busalacchi 1999), because the salinity effects on the stratification are negligible (Hirst and Godfrey 1993). Therefore, the genesis mechanism of warm entrainment in the SWIO is distinct from what was discussed in Schiller and Godfrey (2003). Rather than being heated by the solar penetration, the waters beneath the mixed layer in the SWIO are warmed by the warm ITF waters originating from the SEIO from October to early December (Fig. 2.2.9). Moreover, there are cyclonic eddies in the SWIO (ranging from 70°E to 60°E around 8°S), which lead to increased entrainment and SST disturbance (Fig. 2.2.11). Consequently, the subsurface warm waters are entrained into the surface mixed layer, leading to fast warming of SSTs. Dramatically reduced cooling at the subsurface and the weakening of the stratification tend to enhance the mixed layer deepening and entrainment. During this process, strong diapycnal mixing blends the ITF waters and the ambient Indian Ocean waters to the

extent that the ITF waters lose their T - S properties (blank regions in Fig. 2.2.4). Therefore, the influence of the ITF on SSTs in the SWIO depends on a subtle balance between the stratification and mixing.

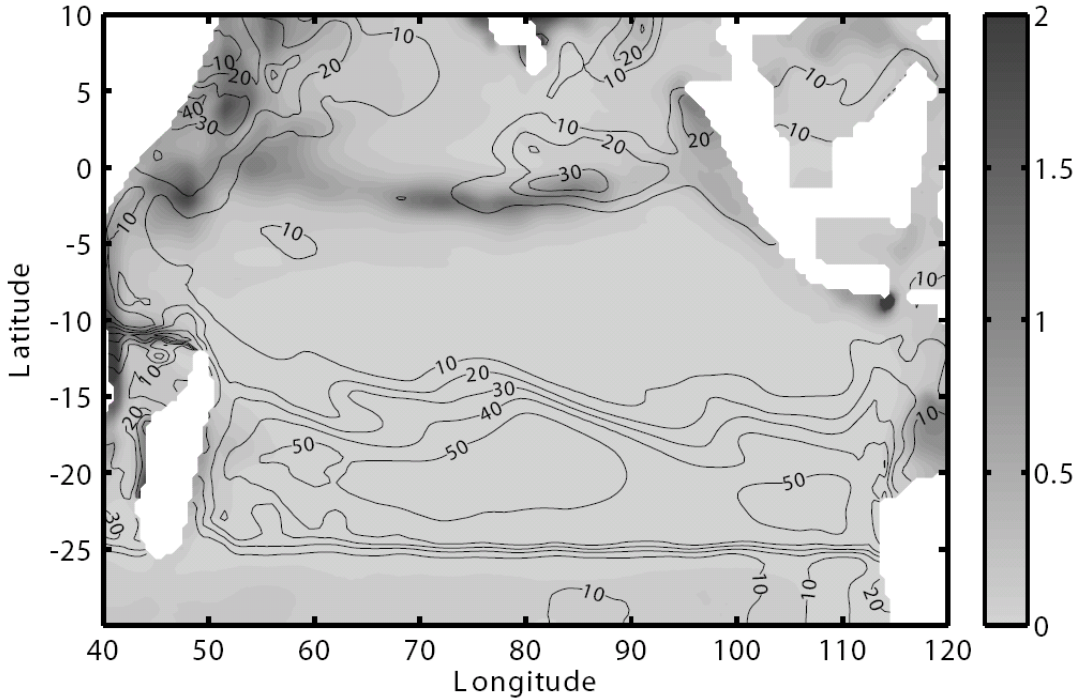


Figure 2.2.10 Solar radiation penetration heating rate (shades, in the unit of K/month) and the barrier layer depth (contours, in the unit of m) in October.

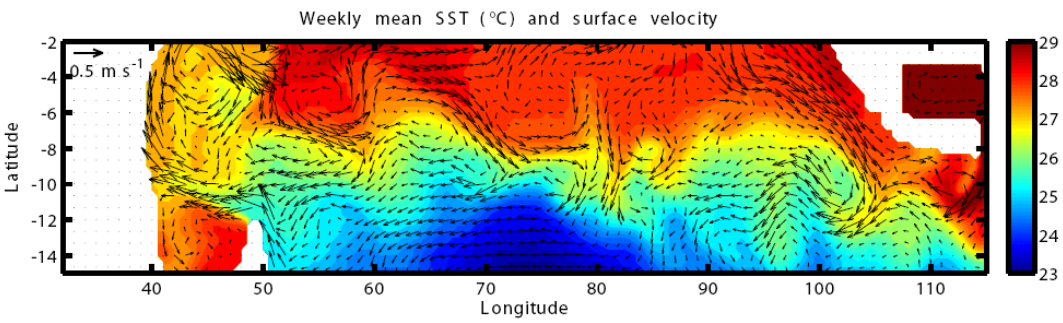


Figure 2.2.11 Weekly mean SSTs (color codes) and the surface velocities (vectors) from Nov. 16 to Nov. 21 of Year 7, when the warm entrainment reaches its maximum.

Please note that since the subsurface ITF waters are warmer than the Indian Ocean waters above, the temperature inversions do exist in the model outputs.

However, the inversions are too weak to initiate the vertical convection by themselves. Eddy kinetic energy (EKE, provided by the baroclinic instability) is still required to break the isopycnal surface and entrain the ITF waters into the upper mixed layer.

2.2.5.2 Slow warming SSTs in late December and January

The fast warming of SSTs from October to early December is thus attributable to the westward propagation of the warm ITF waters and the subsequent warm entrainment, as discussed above. The warming of SSTs is however slower than expected from Q_{net} from late December to January as seen in Fig. 2.2.8. This difference is attributed to the indirect influence of the injection of ITF waters on local vertical processes.

The ITF waters lose their warmer and fresher character during the strong diapycnal mixing from October to early December. Therefore, from late December into January, the subsurface waters significantly cool and the normal vertical stratification resumes (Fig. 2.2.9). However, the OISVs enhanced by the ITF-related baroclinic instability still persist during this time, albeit in their decaying phase (Section 2.1). Therefore, the remaining OISVs provide sufficient EKE to sustain the cold entrainment, which cools the SSTs, or alternatively, slows the rate of warming. After January, the OISVs dissipate completely and no EKE is available to drive entrainment which results in near-zero entrainment in February and March. Therefore, the slow warming of SSTs in SWIO in late December and January is

attributable to the vertical processes influenced by the intrusion of remote ITF waters into the region.

Pronounced cold entrainment from April to June is likely to be attributable to local Ekman pumping associated with the pronounced wind stress curl (contours in Fig. 2.2.4a). However, its influence on the upper layer heat budget is largely neutralized by the meridional warm temperature advection associated with the southward Ekman transport (note the large westward velocities at this time in Fig. 2.2.4b). Thus advection has no significant net impact on the SSTs and the SST variation is mainly controlled by Q_{net} (Fig. 2.2.8). The local processes at this time of the year are not directly related to the ITF, so the details of this cold entrainment are not discussed further here.

2.2.5.3 Relations between thermodynamics and dynamics in the intraseasonal band

ITF waters can influence both the dynamics and thermodynamics in the SWIO via modifying the vertical stratification as discussed above. Because the maximum growth rate of the unstable waves is in the intraseasonal band and the entrainment is partly sustained by the EKE generated by the baroclinic instability, intraseasonal entrainment and intraseasonal sea surface height anomalies (SSHAs) have high correlations, especially in boreal winter of each year. For example, at 8°S , 63°E , their correlation is 0.6 (Fig. 2.2.12). Actually, the correlation between the two is large both in SWIO and SEIO, where the OISVs and the entrainment are closely related to the ITF (Fig. 2.2.13, Du et al. 2005; Yu and Potemra 2006; Section 2.1). Therefore, in the SWIO, there is a close relation between the thermodynamics and the dynamics in the

intraseasonal band which is responsible for the relatively persistent Bjerknes feedback in this region (Annamalai et al. 2003, 2005). It should be possible to estimate the intraseasonal heat fluxes associated with these processes, which are not easily observed. But observed quantities such as the intraseasonal SSHAs may provide a useful entry into inverse calculations which is important for understanding the coupled climate interactions in the region which are of significant importance for the rim countries (for e.g., Xie et al. 2002).

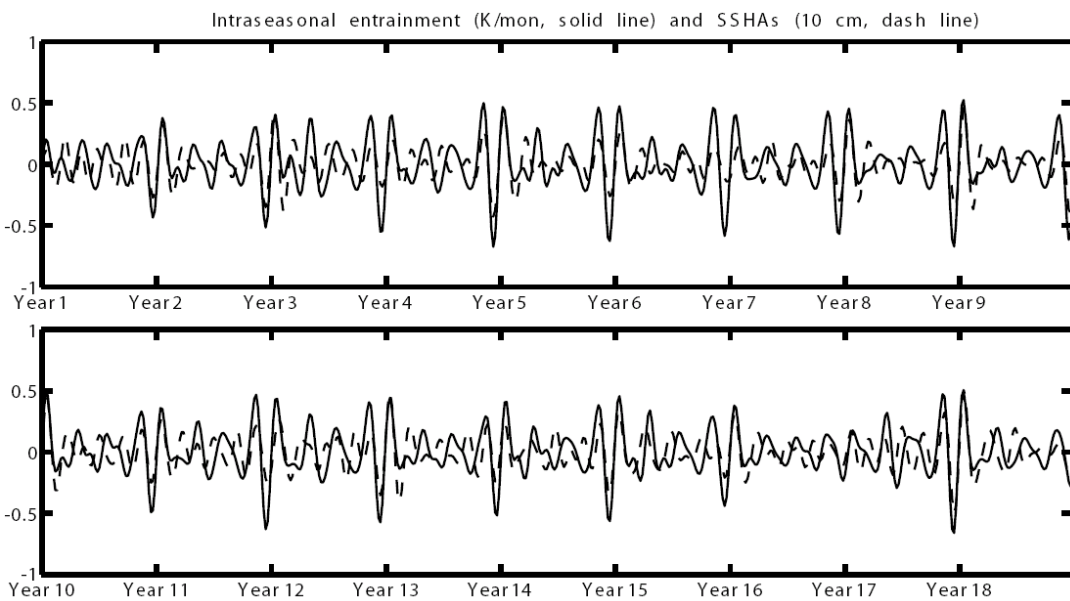


Figure 2.2.12 Intraseasonal entrainment and intraseasonal SSHAs at 8°S, 63°E for 18 years.

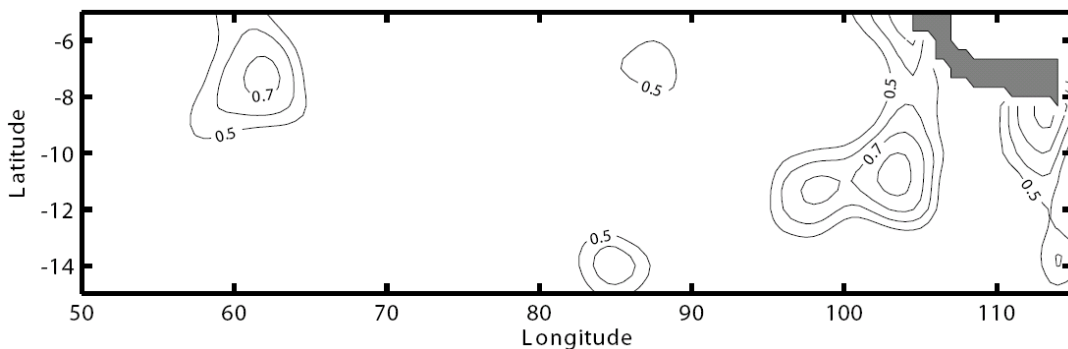


Figure 2.2.13 Correlations between the intraseasonal entrainment and the intraseasonal SSHAs, which are statistically significant at the 95% confidence level.

2.2.6 Discussion and conclusion

When the ITF waters reach the SWIO from August to early December, the primary influence is to reduce the vertical stratification, which is in favor of the baroclinic energy conversions. Consequently, the OISVs are enhanced (Section 2.1) and their temporal and spatial scales are determined by the ITF-modified stratification. The ITF also has a significant influence on the SSTs in SWIO. From October to early December, the warm ITF waters heat the subsurface waters leading to a reduction of cold entrainment which speeds up the SST warming. From late December to January, the warm ITF waters disappear due to the strong diapycnal mixing driven by the baroclinic instability and the subsurface waters become cool. However, the OISV activity still exists supplying the EKE to drive cold entrainment, leading to a relatively slow warming of the SSTs. These processes are attributable to the ITF impact on local processes.

In reality, we believe that the above influence of the ITF waters in SWIO can be even more pronounced if mixing rates are smaller (most models incur excess mixing) and eddies are resolved explicitly. Gordon et al. (2003) found that during boreal winter, cold water flows from the Java Sea into the southern Makassar Strait, preventing the warm Pacific water from entering the Indian Ocean and leading to cooler SSTs in the Indian Ocean. Therefore, the warm subsurface waters are more distinguishable against the ambient Indian Ocean water when they reach the SWIO. Moreover, the wind energy is mainly captured by the second baroclinic mode currents in the SEIO (Iskandar et al. 2006), which can supply more energy to the subsurface westward propagation of the ITF waters.

In summary, we propose that in reality, the southern Makassar Strait is like a valve, through which the cold waters from Java Sea flow into the southern Makassar Strait, making the subsurface warm advection of ITF more distinct compared with the relatively cool Indian Ocean SSTs. The winds over the SEIO are like a propeller, which supply energy to the subsurface warm advection in the ocean. The ITF is like a conveyor belt, which carries the variabilities from SEIO to SWIO and the SWIO is like a mixer during boreal winter, where the subsurface water is mixed up into the upper mixed layer and the SSTs are modulated. These processes are sketched in Fig. 2.2.14. Of course, these processes require more validation against observations and model simulations.

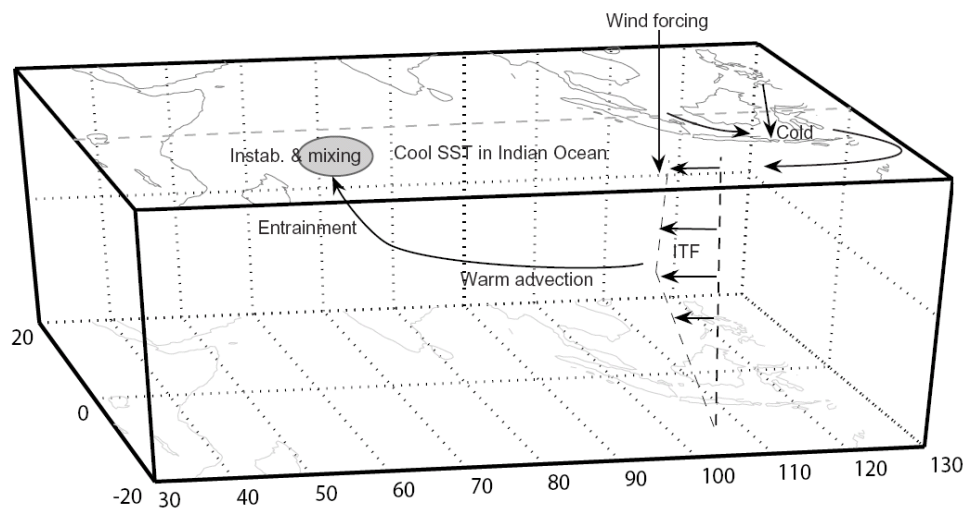


Figure 2.2.14 Sketch of the influence of ITF on the SWIO. See the text for detailed descriptions.

As shown in Song and Gordon (2004), the vertical structure of ITF has a significant impact on the stratification and surface heat flux in the Indian Ocean. Potemra et al. (2002) found that the vertical structure of the ITF has large temporal variability. This study argues that the spreading and mixing of the ITF water and its influence on the southern Indian Ocean have a significant seasonal variability. An

interesting question still unresolved now is whether the ITF leads to enhanced or diminished ocean heat gain (Song et al. 2004) from the atmosphere. Godfrey (1996) suggested less ocean heat gain assuming that the temperature of the upwelling water is increased when the ITF is open. While Vranes et al. (2002) suggested increased heat gain arguing that the transport-weighted temperature of the ITF tends to be cooler than the ambient Indian Ocean thermocline water. We do not intend to settle this issue by analyzing the present model outputs alone. Nonetheless based on the model results, it is very likely that the influence of the ITF on the ocean heat gain depends on the seasonal variability of the subtle balance between the stratification and the mixing. The SSTs warm relatively faster from October to December which should imply a reduced heat gain, while the SST warming is slower in late December into January, which should drive an enhanced heat gain. The role of these processes on the coupled climate variability remains to be explored.

2.2.7 Appendix

Because the subsurface ITF waters are away from the sea surface and the lateral boundaries, their potential vorticity are conserved after they enter the Indian Ocean until they are entrained into the upper mixed layer in the SWIO (Fig. 2.2.4a). Following Vallis (2006), the conservation equation of the potential vorticity is

$$\left(\frac{\partial}{\partial t} + U \frac{\partial}{\partial x} \right) \left(\nabla^2 \Psi + \frac{H^2}{L_d^2} \frac{\partial^2 \Psi}{\partial z^2} \right) = 0,$$

where U is the basic flow, Ψ is the stream function, H is the water depth, $L_d = NH / f$ is the Rossby radius of deformation, N is the Brunt-Väisälä frequency, and f is the Coriolis parameter. The boundary conditions are

$$\left(\frac{\partial U}{\partial z} z - c\right) \frac{\partial \Psi}{\partial z} - \frac{\partial U}{\partial z} \Psi = 0, \quad z = 0, H,$$

$$\Psi = 0, \quad y = 0, L.$$

Assuming the wave-like solution in both x- and y- directions

$$\Psi(x, y, z, t) = \psi(z) \sin ly e^{ik(x-ct)},$$

we obtain the dispersion relation of the Eady waves

$$c = \frac{U}{2} \pm \frac{U}{\mu} \left[\left(\coth \frac{\mu}{2} - \frac{\mu}{2} \right) \left(\frac{\mu}{2} - \tanh \frac{\mu}{2} \right) \right]^{1/2},$$

where $\mu = kL_d$. The instability occurs when $\mu > 2.4$. The corresponding growth rate is

$$\sigma = c_i k = \frac{U}{L_d} \left[\left(\coth \frac{\mu}{2} - \frac{\mu}{2} \right) \left(\frac{\mu}{2} - \tanh \frac{\mu}{2} \right) \right]^{1/2},$$

where c_i is the imaginary part of c . The meridional wave number is omitted in the growth rate because it is much smaller than k . The maximum growth rate occurs when $\mu_{\max} = 1.61$. Accordingly, the wavelength of the maximum instability is

$$L_{\max} = \frac{2\pi}{k} = \frac{2\pi L_d}{\mu_{\max}} \approx 3.9L_d \quad \text{and the corresponding maximum growth rate is}$$

$$\sigma_{\max} \approx 0.3U / L_d.$$

Chapter 3: Energy sources for Madden-Julian Oscillations

Abstract

The energy sources for the enhanced perturbed kinetic energy during Madden-Julian Oscillations (MJOs) are calculated with the NCEP/NCAR reanalysis. According to the energy equation, there are three main sources for the perturbed kinetic energy: perturbed potential energy, mean kinetic energy, and the energy source due to surface heat flux. In most MJO events, the energy is derived from the perturbed potential energy and the ocean can feedback to the atmosphere, prolonging the period of MJOs. Some MJO events are driven by a reinforced surface heat flux, which is caused by warm sea surface temperature anomalies induced by the internal oceanic variabilities. During the transition period between monsoon seasons, some MJO events can be triggered by the energy transferred from the mean kinetic energy. Although all MJO events are characterized as intraseasonal oscillations in the coupled climate system, they have various energy sources which should be considered carefully, not only for better understanding of MJOs but also for their simulations and predictions.

3.1 Introduction

The Madden-Julian Oscillations (MJOs) are the most dominant intraseasonal oscillations, originally thought to be an atmospheric phenomenon but now recognized to be part of the coupled climate system (Madden and Julian 1971, 1972, 1994, 2005). There have been many theories and model studies of MJOs thus far, as summarized in Wang (2005) and Slingo et al. (2005). However, until now, none of the existing

theories can explain all of the complex features of MJOs. Some theories have focused on the internal atmospheric dynamics. For example, the theory invoking the Convective Instability of the Second Kind, viz., the wave-CISK, can explain the convection associated with the MJOs (Lindzen 1974). Lau and Peng (1987) introduced the ‘mobile wave-CISK’, which favors a realistic large-scale convection, though the heating profile they used was larger than observations. Some theories emphasize the interactions between the large-scale circulation and small-scale convections, such as the discharge-recharge mechanism (Blade and Hartmann 1993; Hu and Randall 1995; Kemball-Cook and Weare 2001). The role of surface heat flux and sea surface temperatures (SSTs) in the development of MJOs has also received much attention (Sobel et al. 2008). A theory named ‘wind-induced surface heat exchange’ (WISHE) was proposed independently by Emanuel (1987) and Neelin et al. (1987). Some observations (e.g. Jones et al. 1998; Lau and Sui 1997; Zhang 1996) support the positive feedback hypothesis in which SST variations may modulate the amplitude and the speed of eastward propagation of the MJOs. With the reanalysis products, Sperber (2003) showed that favorable SST anomalies occur several days prior to the organization of deep convection. There is also a controversy about how much improvement could actually be achieved by including the oceanic influence in model simulations of MJOs. Some model experiments indicate that MJOs can be simulated in an atmosphere-only model (e.g. Hendon 2000; Shinoda et al. 1998), thus, leading to the conclusion that it is crucial to improve the atmospheric processes in the model for improving the MJO simulations, such as the convection scheme. Nevertheless, some model experiments show that resolving the oceanic feedbacks to

the atmosphere is also important for better MJO depiction (e.g. Jones et al. 1998; Waliser et al. 1999; Bellon et al. 2008; Pegion and Kirtman 2008a).

The diversity of conclusions, both from theoretical and modeling studies, indicates that the observed MJOs are probably a consequence of multiple-mechanisms. Benedict and Randall (2007) combined the discharge-recharge and frictional moisture convergence mechanisms, explaining many features of MJOs, but not quite all. In this study, we examine the development of MJOs from the point of view of energy conversions. Although all MJO events are represented by pronounced intraseasonal variations (ISVs) in the atmosphere, we will show that the energy sources for these ISVs vary from one event to another. The relative importance of various energy sources can shed light on how to apply appropriate theories and how to resolve appropriate processes to explain and better simulate different MJO events. This understanding is a critical step towards improving MJO predictions. The data and reanalysis products used in this study are introduced in Section 3.2. The energy conversions are presented in Section 3.3. A summary and some discussions are offered in Section 3.4.

3.2 Data and reanalysis products

Atmospheric variables such as wind velocities, air temperatures, geopotential heights, and specific humidity are obtained from daily NCEP/NCAR reanalysis (Kalnay et al. 1996). The SSTs are obtained from daily gridded AVHRR data (McClain et al. 1985). The MJO index is computed with the daily outgoing longwave radiation (OLR) from NOAA polar-orbiting series of satellites (Liebmann and Smith 1996) and zonal winds at 850 hPa and 200 hPa from daily NCEP/NCAR reanalysis

(Kalnay et al. 1996), following the method developed in Wheeler and Hendon (2004; referred as WH04 hereafter). The amplitudes of MJOs are determined with the sum of the squares of the first two leading principal components of the combined fields (i.e. $\text{MJO index} = \text{PC1}^2 + \text{PC2}^2$). A daily MJO index is used for this study. Significant MJO events are identified according to the following two criteria:

- (1) The MJO index larger than two lasts for more than 10 days;
- (2) Number of days with MJO index less than two is less than 3.

With this selection process, there are 54 MJO events in all from 1979 to 2006 satisfying both criteria, which are listed in Table 3.1. An MJO index larger than two indicates strong ISVs, which typically occur over the Indian and the western Pacific Oceans. The fundamental purpose of the first criterion is that the strong ISVs should last continuously for a sufficiently long period. The life times of the events in Table 3.1 are from 10 days to 58 days, with a mean time span of 20 days. In fact, the individual MJO events last longer than periods listed in Table 3.1, since the days during the decaying phase of the MJO events, when the ISVs are weak, are not included here. We do not intend to argue that the energetics during the MJO decaying phase is not important. Actually, MJOs have an influence on the climate anomalies in northern America (Yang et al. 2002), and the North Atlantic Oscillation (Cassou 2008, Lin et al. 2009), which are likely to be related to the energy spreading during the decaying phase of MJOs. However, since what we focus on in the paper is how the MJOs obtain energy, the energetics during the decaying phase is beyond the scope of this study. Because we use the daily MJO index, there are occasional breaks for one or two days during the strong ISVs. Therefore, the second criterion is necessary,

No.	Begin Date	End Date	No.	Begin Date	End Date	No.	Begin Date	End Date
1	01/12/79	01/24/79	19	01/09/89	01/19/89	37	08/20/00	08/29/00
2	05/25/79	06/05/79	20	01/13/90	01/24/90	38	01/20/01	02/06/01
3	08/02/79	08/14/79	21	02/27/90	03/23/90	39	02/09/01	03/01/01
4	08/18/79	09/01/79	22	05/08/90	05/17/90	40	01/15/02	01/27/02
5	09/24/79	10/07/79	23	05/15/91	05/24/91	41	05/02/02	05/30/02
6	03/01/81	04/10/81	24	09/06/91	09/16/91	42	06/09/02	06/18/02
7	08/04/84	08/14/84	25	12/31/92	02/07/93	43	06/29/02	07/17/02
8	10/29/84	11/14/84	26	10/26/93	11/07/93	44	11/03/02	12/01/02
9	01/21/85	02/22/85	27	02/10/94	02/25/94	45	12/16/02	12/29/02
10	10/23/85	11/06/85	28	05/10/94	05/22/94	46	05/11/03	05/28/03
11	12/31/85	01/20/86	29	09/19/94	09/30/94	47	12/11/03	12/29/03
12	03/06/86	03/24/86	30	03/16/96	03/30/96	48	01/05/04	02/09/04
13	08/05/86	08/15/86	31	11/06/96	11/20/96	49	03/12/04	03/31/04
14	10/28/86	11/10/86	32	12/22/96	01/04/97	50	06/27/04	07/15/04
15	11/06/87	11/15/87	33	02/11/97	04/02/97	51	03/23/05	05/12/05
16	01/18/88	01/27/88	34	05/16/97	06/16/97	52	09/04/05	09/14/05
17	02/17/88	04/14/88	35	06/26/97	07/06/97	53	01/19/06	02/08/06
18	09/22/88	10/08/88	36	05/09/98	05/23/98	54	09/26/06	10/18/06

Table 3.1 The MJO events defined based on the MJO index (Wheeler and Hendon 2004) and the two criteria in the main text.

so that a whole MJO event is not segmented into smaller pieces because of these occasional breaks. Hereafter, for convenience, each MJO event is labeled with a specific number in Table 3.1. The atmospheric intraseasonal oscillations were carefully categorized by Wang and Rui (1990; referred as WR90 hereafter). The above two criteria along with the WH04 MJO index only allow the eastward-propagating events. For example, event No. 9 (Table 3.1) is exactly the same as the one shown in WR90 (their Fig. 1). However, the independent northward-propagating events (e.g. Sep 18, 1984 – Oct 17, 1984; Fig. 6 in WR90) and the westward-propagating events (e.g. Aug 19, 1982 – Sep 12, 1982; Fig. 9 in WR90) are excluded.

3.3 Energy sources for the MJO events

Westerly wind bursts are a good indicator of the MJO events (Hendon et al. 1998; Kessler et al. 1995). Enhanced ISVs during MJO events can be regarded as perturbations to the background circulation of the atmosphere. The mean state of the atmosphere is represented by low-pass-filtered variables (such as wind velocities) with a cut-off period of 100 days, while the perturbations are represented by intraseasonal variables, which are obtained by band-pass filtering over 20-100 days. As shown in Fig. 3.1, during the MJO events listed in Table 3.1, the MJO index and the vertically averaged (from 1000 hPa to 250 hPa) perturbed kinetic energy have significant correlations, especially over the Indian Ocean, where the MJOs usually seem to originate and grow to the mature phase. Thus, we focus on the region between 0° - 10° S and 50° E- 100° E in the following discussion.

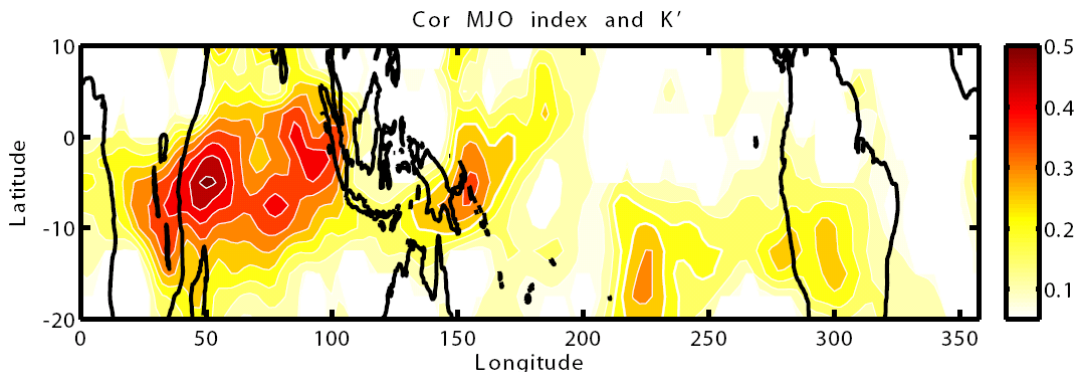


Figure 3.1 Correlations between the MJO index and the vertically averaged perturbed kinetic energy. Only the correlations statistically significant at a 95% confidence level are shown.

The zonal and meridional momentum equations in the log-pressure coordinate are (Holton 2004)

$$\begin{cases} \frac{\partial u}{\partial t} + u \frac{\partial u}{\partial x} + v \frac{\partial u}{\partial y} + w \frac{\partial u}{\partial z} - fv + \frac{\partial \Phi}{\partial x} = X & (3.1) \\ \frac{\partial v}{\partial t} + u \frac{\partial v}{\partial x} + v \frac{\partial v}{\partial y} + w \frac{\partial v}{\partial z} + fu + \frac{\partial \Phi}{\partial y} = Y & (3.2) \end{cases} ,$$

where u , v , w are the zonal, meridional and vertical velocities, f is the Coriolis parameter, Φ is the geopotential height, and X , Y represent the zonal and meridional drag components due to unresolved eddies. We decompose all variables into the mean state (the low-frequency variation in the atmosphere obtained by low-pass filtering with a cut-off period of 100 days) and the intraseasonal perturbation (obtained by band-pass filtering from 20 to 100 days). The intraseasonal component is much smaller than the mean state. For example, $u = \bar{u} + u'$ and $u' \ll \bar{u}$. Thus, Eq. (3.1) becomes

$$\begin{aligned} & \frac{\partial(\bar{u} + u')}{\partial t} + (\bar{u} + u') \frac{\partial(\bar{u} + u')}{\partial x} + (\bar{v} + v') \frac{\partial(\bar{u} + u')}{\partial y} + (\bar{w} + w') \frac{\partial(\bar{u} + u')}{\partial z} \\ & - f(\bar{v} + v') + \frac{\partial(\bar{\Phi} + \Phi')}{\partial x} = (\bar{X} + X') \end{aligned} \quad (3.3).$$

The meridional transport \bar{v} and the vertical fluxes $(\bar{w} + w') \partial(\bar{u} + u') / \partial z$ can be neglected (Holton 2004). Since $u' \ll \bar{u}$, $u' \partial \bar{u} / \partial x$ can also be neglected. Thus, the equation for u' can be written as

$$\left(\frac{\partial}{\partial t} + \bar{u} \frac{\partial}{\partial x} \right) u' - \left(f - \frac{\partial \bar{u}}{\partial y} \right) v' = - \frac{\partial \Phi'}{\partial x} + X' \quad (3.4).$$

Following a similar process, the equation for v' can be written as

$$\left(\frac{\partial}{\partial t} + \bar{u} \frac{\partial}{\partial x} \right) v' + fu' = - \frac{\partial \Phi'}{\partial y} + Y' \quad (3.5).$$

Spatially averaged perturbed kinetic energy is defined as $K' = \langle \rho_0(u'^2 + v'^2)/2 \rangle$, where

ρ_0 is the air density and $\langle \rangle = (DL)^{-1} \int_0^{\infty} \int_0^{DL} \int_0^{DL} () dx dy dz$. Taking the spatial average of

($\rho_0 u' \times \text{Eq. (3.4)} + \rho_0 v' \times \text{Eq. (3.5)}$), and considering the vertical momentum and the continuity equations, we can write the energy equation in a concise form for K' as

$$dK'/dt = P' \cdot K' + K' \cdot \bar{K} + R' + \varepsilon' \quad (3.6),$$

where K represents kinetic energy, P represents potential energy, R denotes energy sources or sinks due to surface heat flux, while ε corresponds to energy dissipation. The dot in the equation denotes the energy conversion and not a multiplication. Thus, positive $P' \cdot K'$ denotes the energy conversion from perturbed potential energy to perturbed kinetic energy and positive $K' \cdot \bar{K}$ is the energy conversion between perturbed kinetic energy and mean kinetic energy. Specifically, the energy source terms are (refer to Holton 2004 for more details);

$$P' \cdot K' = \left\langle \rho_0 w' \frac{\partial \Phi'}{\partial z} \right\rangle \quad (3.7),$$

$$K' \cdot \bar{K} = - \left\langle \rho_0 u' v' \frac{\partial \bar{u}}{\partial y} \right\rangle \quad (3.8),$$

$$R' = \left\langle \frac{\rho_0}{N^2} \frac{\kappa J'}{H} \frac{\partial \Phi'}{\partial z} \right\rangle \quad (3.9),$$

where N is the buoyancy frequency, H is a standard scale height, J is the heating rate due to the air-sea heat flux which is dominated by the latent heat flux, and $\kappa = 0.286$, is a constant. The above equations have the same mathematical form as the Lorenz energy cycle equations (Lorenz 1955; Holton 2004). However, the mean state and the

perturbations in the above equations are defined with respect to time, while the mean state and the perturbations are defined with respect to the Eulerian mean in the Lorenz energy cycle equations. In a review of the energy cycle, Plumb (1983) articulated that the mathematical expressions for the energy conversions are not unique. For example, he applied two schemes to calculate the energy budget. He emphasized that whether a mathematical combination of the terms in the energy equation is meaningful essentially depends on the physical interpretations. The mathematical results are physically significant, only when they can be reasonably interpreted and they are consistent with the cause-and-effect relation in the physical context. In this study, the energy conversions calculated with the energy equation are not the sole basis of support for our conclusions. More independent evidence in a time series is presented in the following. In order to maintain the consistency between the energy conversions and the other evidence, it is convenient to calculate the former also in terms of the temporal perturbations. Actually, the energy conversions calculated with the two methods are qualitatively consistent. The comparisons between the energy conversions obtained with the temporal perturbations and the ones obtained with the spatial perturbations are presented in the Appendix. Therefore, different averaging procedures do not lead to significantly different conclusions.

All variables are calculated with the NCEP/NCAR reanalysis. The latent heat flux in the reanalysis does not feel the SST feedbacks. However, Chou et al. (2004) and Feng and Li (2006) compared the latent heat flux in NCEP and Goddard Satellite-Based Surface Turbulent Fluxes, version 2 (GSSTF2, Chou et al. 2003), to point out that the large-scale patterns of surface heat flux of NCEP reanalysis are quite similar

to the observations, although some quantitative differences do exist. According to Chou et al. (2004), specifically, for the tropical Indian Ocean, which is the region we focus on, the differences of latent heat fluxes between NCEP and GSSTF2 are generally less than 15%. In addition, the standard deviations of differences in the tropical Indian Ocean are very small, which indicates that in this region, the NCEP latent heat fluxes are generally consistent with the observations.

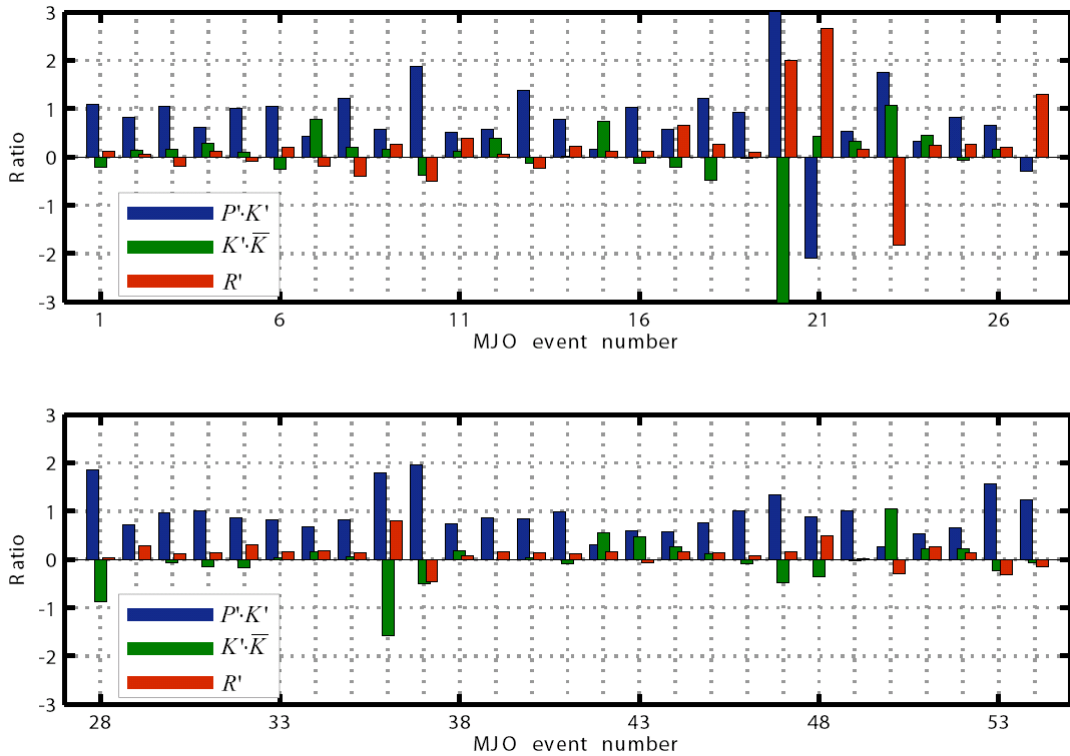


Figure 3.2 Ratios between $P' \cdot K'$ (blue bars), $K' \cdot \bar{K}$ (green bars), R' (red bars) and the total energy conversions TE for the MJO events listed in Table 3.1. For each event, the energy conversions are averaged between 50°E - 100°E and 0° - 10°S in the horizontal, from 1000 hPa to 250 hPa in the vertical, and from the beginning date to the end date (Table 3.1) in time.

The three terms, $P' \cdot K'$, $K' \cdot \bar{K}$, and R' act as energy sources to K' , while ε is usually an energy sink, which is hereby neglected in the following discussion. Adding the three possible energy sources together and defining,

$$TE = P' \cdot K' + K' \cdot \bar{K} + R' \quad (3.10),$$

the relative importance of these energy sources in each MJO event (Table 3.1) can be evaluated by calculating the ratio between each energy source term and TE . For each MJO event, the energy sources are averaged both in space and in time, viz., between 50°E-100°E and 0°-10°S in the horizontal, from 1000 hPa to 250 hPa in the vertical, and from the beginning date to the end date (Table 3.1) in time. The ratios are shown in Fig. 3.2. Averaging over all 54 MJO events listed in Table 3.1, $P' \cdot K'$ accounts for about 82% of the total energy source (TE) to the increase of K' , R' accounts for about 20% of the total energy source, while $K' \cdot \bar{K}$ is in fact a very weak sink of K' (about -2%) due to the negative viscosity (Starr 1968). Obviously, for most MJO events, $P' \cdot K'$ dominates, which indicates that the energy of the enhanced ISVs during these MJO events is derived dominantly from the perturbed potential energy. This is consistent with the observed energy cycle by Oort and Peixoto (1974) in which the main energy source of K' is that converted from P' . However, for a specific MJO event, the relative importance of the three energy sources varies significantly. There are some events in which $K' \cdot \bar{K}$ or R' is the dominant energy source. Each of the three cases is discussed in detail below with typical examples based on the selected MJO events in Table 3.1.

3.3.1 Events where $P' \cdot K'$ dominates

As discussed above, $P' \cdot K'$ overwhelms the other two energy sources in most MJO events. The spatially averaged (between 50°E-100°E and 0°-10°S in the horizontal, from 1000 hPa to 250 hPa in the vertical) energy conversions during the MJO events No. 9, 25, 44, and 48 from Table 3.1 are shown in Fig. 3.3. In the four

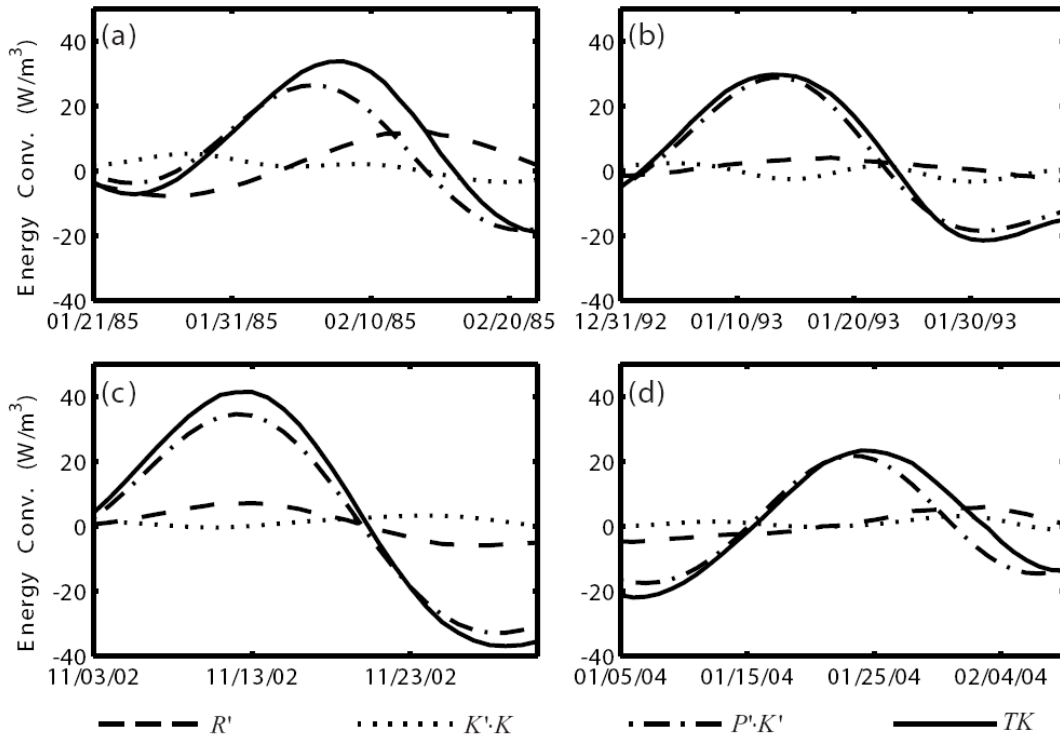


Figure 3.3 Energy conversions for four MJO events: No. 9 (a), No. 25 (b), No. 44 (c), and No. 48 (d). Dash lines: R' ; dot lines: $K'K$; dash-dot lines: $P'K'$; solid lines: TK . All terms are averaged between 50°E - 100°E and 0° - 10°S , and from 1000 hPa to 250 hPa. The units are 10^{-3} W m^{-3} .

examples, $K'\bar{K}$ is not significantly different from zero during the entire MJO periods considered, which means that the background circulation does not contribute to the enhancement of ISVs. The energy source due to surface heat flux, R' , is also smaller than $P'K'$. However, in some MJO events, such as event No. 9 (Fig. 3.3a), R' increases after the increase of $P'K'$. After Feb 5, 1985, R' becomes a significant energy source for K' , which turns out to be attributable to the increase of surface heat flux as a response to both enhanced wind forcing and warm SST anomalies. The total surface heat flux, which controls R' , is the sum of the net shortwave and longwave radiations, and the latent and sensible heat fluxes. The intraseasonal variations of the net shortwave radiation, latent heat flux, and the total surface heat flux, along with the intraseasonal SST anomalies are shown in Fig. 3.4. The negative heat fluxes are

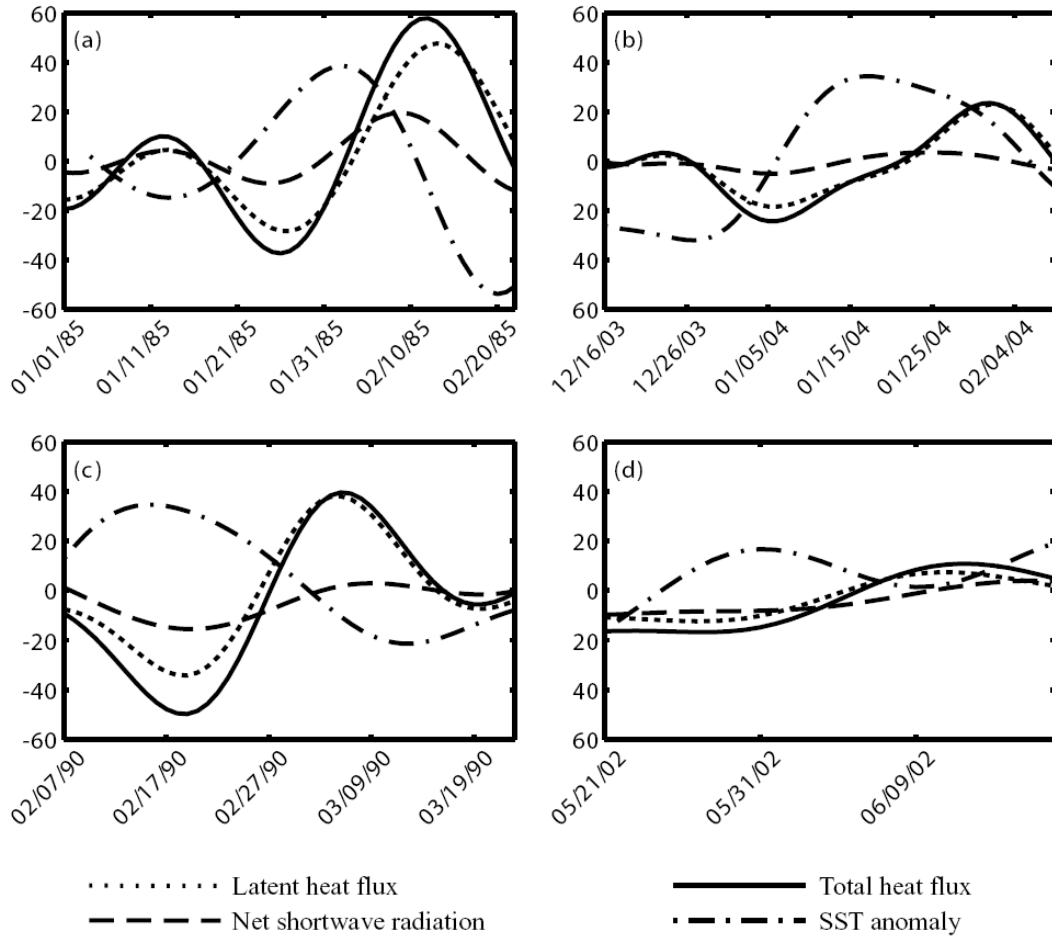


Figure 3.4 Latent heat fluxes (dot lines), net shortwave radiation at the sea surface (dash lines), total heat flux at the surface (solid lines), and SST anomalies (dash-dot lines) for four MJO events. The units of the energy fluxes are W m^{-2} and the unit for SST anomalies is 10^{-2} Kelvin. All variables are averaged between 50°E - 100°E , 0° - 10°S .

downward (from the atmosphere to the ocean) and the sea surface is warmed, while the positive heat fluxes are upward and the sea surface is cooled. The latent heat flux dominates the intraseasonal variation of the total surface heat flux. For the MJO event No. 9 (Fig. 3.4a), around Jan 25, 1985, the surface heat flux is negative, hence the ocean receives energy and becomes warmer. The peak of warm SST anomalies occurs on Feb 2, 1985, which is about 8 days after the negative peak in surface heat flux. The net shortwave radiation also contributes to the sea surface warming during

the suppressed phase of the MJO event, but it is smaller than the latent heat loss reduction. Then the latent heat increases and reaches a positive peak on Feb 12, 1985. Meanwhile, the SSTs decrease rapidly, primarily due to the increased latent heat loss and secondarily due to the reduction of net shortwave radiation during the active phase of the MJO event (Fig. 3.4a). The SST anomalies reach a minimum on Feb 20, 1985. Therefore, in this class of MJO events, the SST variation lags the surface heat flux by approximately 8 days (also see Fig. 3.4b for the MJO event No. 48), which indicates that the SST anomalies after the onset of MJO events are mainly a response to the atmospheric forcing (Jones et al. 1998).

3.3.1.1 Ocean-atmosphere feedbacks

An interesting question is whether these warm SST anomalies can feedback to the atmosphere. It has been shown above that the enhanced surface heat flux, of which the latent heat flux is the major component, can have a significant impact on the development of MJOs via providing energy to K' (the increase in R' in Figs. 3.3a and 3.3d). If the warm SST anomalies can influence the latent heat flux, they can have pronounced feedbacks to MJOs. The latent heat fluxes shown above (e.g. in Fig. 3.4) are directly obtained from NCEP/NCAR reanalysis. Alternatively, to a good approximation, they can be estimated with the method of Hendon and Glick (1997);

$$F_{LH} = \rho_0 C_d L V \Delta q \quad (3.11),$$

where $C_d = 1.3 \times 10^{-3}$ is the constant drag coefficient, $L = 2.5 \times 10^6 \text{ J kg}^{-1}$ is the latent heat of condensation, V is the surface wind speed (not a vector), and

$\Delta q = q_{SST} - q_{1000}$, q_{1000} is the specific humidity at 1000 hPa, q_{SST} is the saturation specific humidity at the SSTs which is calculated following Rogers and Yau (1989),

$$q_{SST} \approx \varepsilon e_s(T) / p = \varepsilon A e^{-B/T} / p \quad (3.12),$$

where e_s is the saturation vapor pressure at temperature T , $\varepsilon = 0.622$, $A = 2.53 \times 10^9$ hPa, $B = 5.42 \times 10^3$ K, $p = 1000$ hPa is the sea level pressure, and T is the SST. Obviously, both winds and SSTs can influence F_{LH} . In order to quantitatively determine the contributions of winds and SSTs to the changes of F_{LH} , these variables are also separated into the mean and the perturbation (intraseasonal) parts, i.e. $V = \bar{V} + V'$, $T = \bar{T} + T'$, and $q_{1000} = \bar{q}_{1000} + q'_{1000}$. Replacing q_{SST} with Eq. (3.12), Eq. (3.11) can be rewritten as,

$$\begin{aligned} F_{LH} &= \rho_0 C_d L (\bar{V} + V') \left[\frac{\varepsilon}{p} A e^{-B/(\bar{T}+T')} - (\bar{q}_{1000} + q'_{1000}) \right] \\ &\approx \rho_0 C_d L (\bar{V} + V') \left[\frac{\varepsilon}{p} A e^{-B/\bar{T} \cdot (1-T'/\bar{T})} - (\bar{q}_{1000} + q'_{1000}) \right] \\ &\approx \rho_0 C_d L (\bar{V} + V') \left[\frac{\varepsilon}{p} A e^{-B/\bar{T}} \left(1 + \frac{BT'}{\bar{T}^2} \right) - (\bar{q}_{1000} + q'_{1000}) \right] \quad (3.13) \\ &= \rho_0 C_d L \times [\bar{V} \left(\frac{\varepsilon}{p} A e^{-B/\bar{T}} - \bar{q}_{1000} \right) \quad \text{(I)} \\ &\quad + \bar{V} \left(\frac{\varepsilon}{p} A e^{-B/\bar{T}} \cdot \frac{BT'}{\bar{T}^2} - q'_{1000} \right) \quad \text{(II)} \\ &\quad + V' \left(\frac{\varepsilon}{p} A e^{-B/\bar{T}} - \bar{q}_{1000} \right) \quad \text{(III)} \\ &\quad + V' \left(\frac{\varepsilon}{p} A e^{-B/\bar{T}} \cdot \frac{BT'}{\bar{T}^2} - q'_{1000} \right) \quad \text{(IV)}] \end{aligned}$$

Term (I) in Eq. (3.13) only contains the mean states, thus it represents the background latent heat flux and does not change significantly in the intraseasonal period. Term (IV) is the product of perturbations, thus it is much smaller than other terms (not

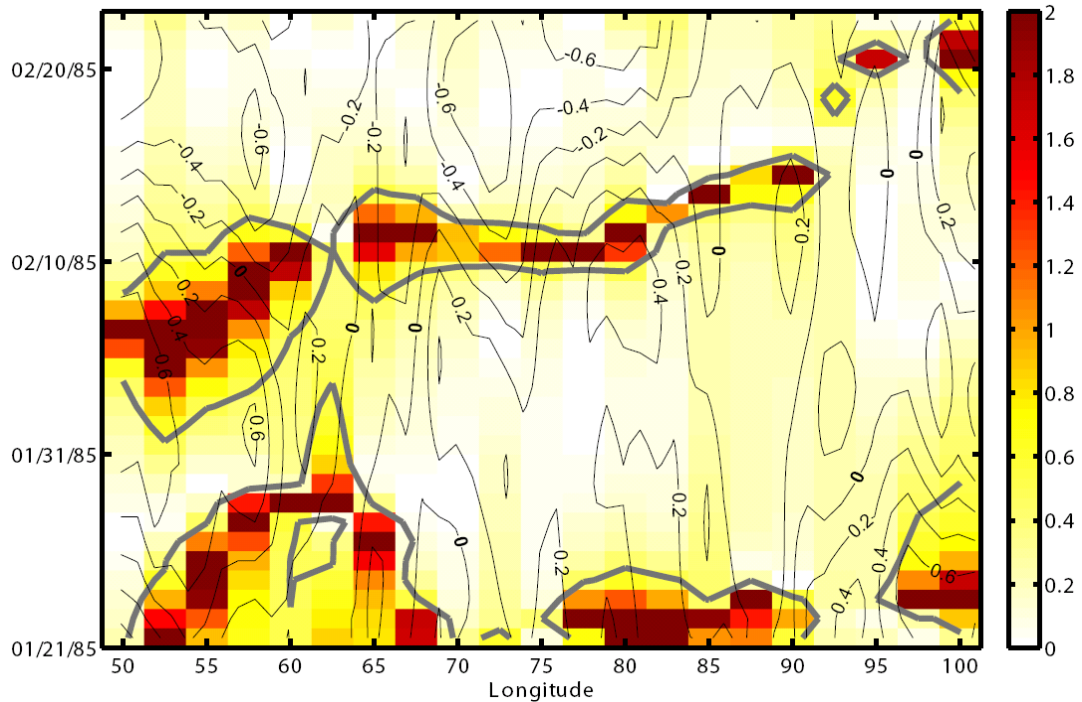


Figure 3.5 The ratio between Term II and Term III in Eq. (3.13) during the MJO event No. 9. The thick gray contour corresponds to a value of 0.5. Intraseasonal SST anomalies are superimposed with the thin contours. The unit of SST anomalies is Kelvin. All variables are averaged between 0° and 10°S.

shown) and is neglected hereafter. Term (III) is the combination of perturbed winds and mean SSTs, which embodies the principle of WISHE (Emanuel 1987; Neelin et al. 1987), viz. the enhanced winds increase the latent heat flux. Term (II) is the combination of mean wind speeds and perturbed SSTs, which represents the influence of intraseasonal oceanic variabilities on the surface heat flux. The ratio between Term (II) and Term (III) (i.e., Term II / Term III) for the MJO event No. 9 is shown in Fig. 3.5, superimposed on the intraseasonal SST anomalies. During most of this MJO event, Term (III) dominates, since the ratios are much smaller than 1. Therefore, the WISHE mechanism operates for enhancing surface heat flux. However, over some warm SST anomalies, Term (II) can be considerably large, as marked with gray thick contours in Fig. 3.5. Especially, centered on Feb 10, 1985, the latitudinal belt with

large ratios extends eastwards, along with the warm SST anomalies. Since warm SST anomalies barely exist to the east of 92°E, the belt with large ratios also ends at this longitude. Therefore, the increase of R' (Fig. 3.3a) is attributable to the increased surface heat flux as a response to both the enhanced wind forcing and warm SST anomalies and R' captures both the atmosphere driven and the ocean driven fluxes.

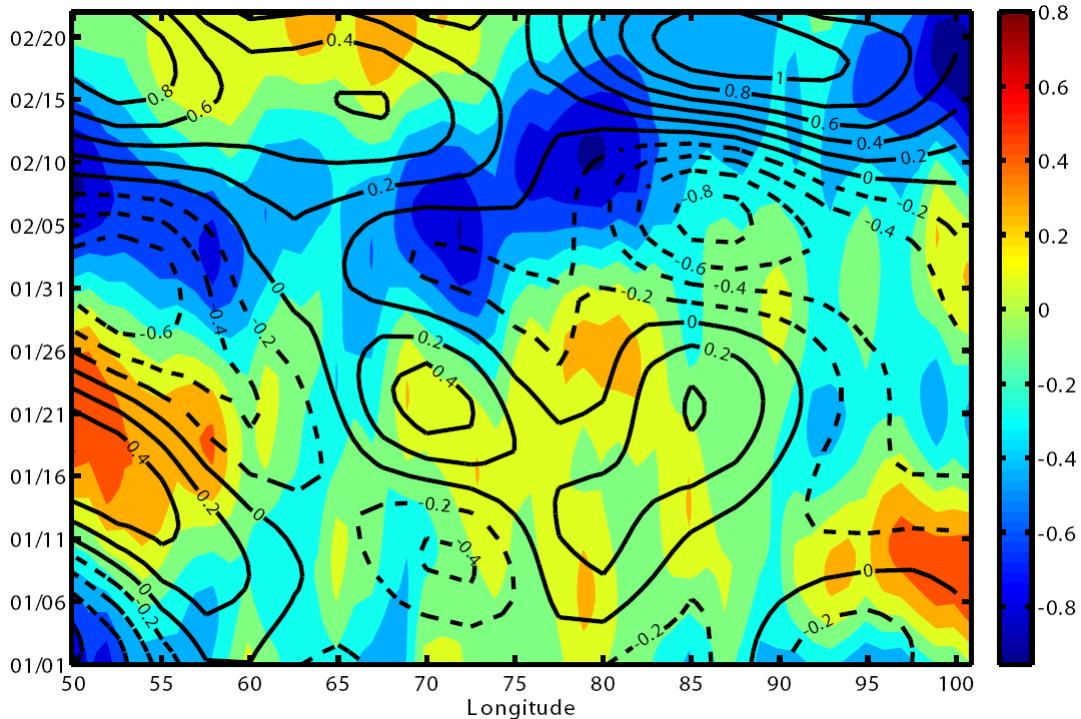


Figure 3.6 Intraseasonal SSTAs from Jan 1, 1985 to Jan 22, 1985, with a unit of Kelvin (color shades). The intraseasonal vorticity of surface winds averaged between the equator and 10°S are superimposed (black contours) with a unit of 10^{-5} s^{-1} .

The forcing-response relation between the winds and the ocean can also be determined from the relationship between the wind stress curl and the SST anomalies, as discussed in Peña et al. (2003). If the atmosphere drives the ocean, cyclones are over the cold water, because cyclones drive enhanced supply of cool subsurface water by Ekman pumping, typically leading to negative SST anomalies by entrainment when turbulent kinetic energy can deepen the mixed layer. Equivalently, if the

atmosphere drives the ocean, anti-cyclones are over the warm water due to the enhanced downward radiation and detrainment. Moreover, if horizontal advection needs to be considered, for a cyclone, equatorward cold (poleward warm) air induces cold (warm) SSTs to the west (east) of the cyclone. As shown in Fig. 3.6, at the beginning or even several days prior (around Jan 21, 1985) to event No. 9, anti-cyclones are found over warm SST anomalies in the western and central Indian Ocean. About 15 days later (on Feb 5, 1985), when horizontal advection becomes important due to increased wind speeds, one can find cold SST anomalies to the west of a strong cyclone in the central Indian Ocean. Note that in the southern hemisphere, a cyclone has a negative vorticity and an anti-cyclone has a positive vorticity.

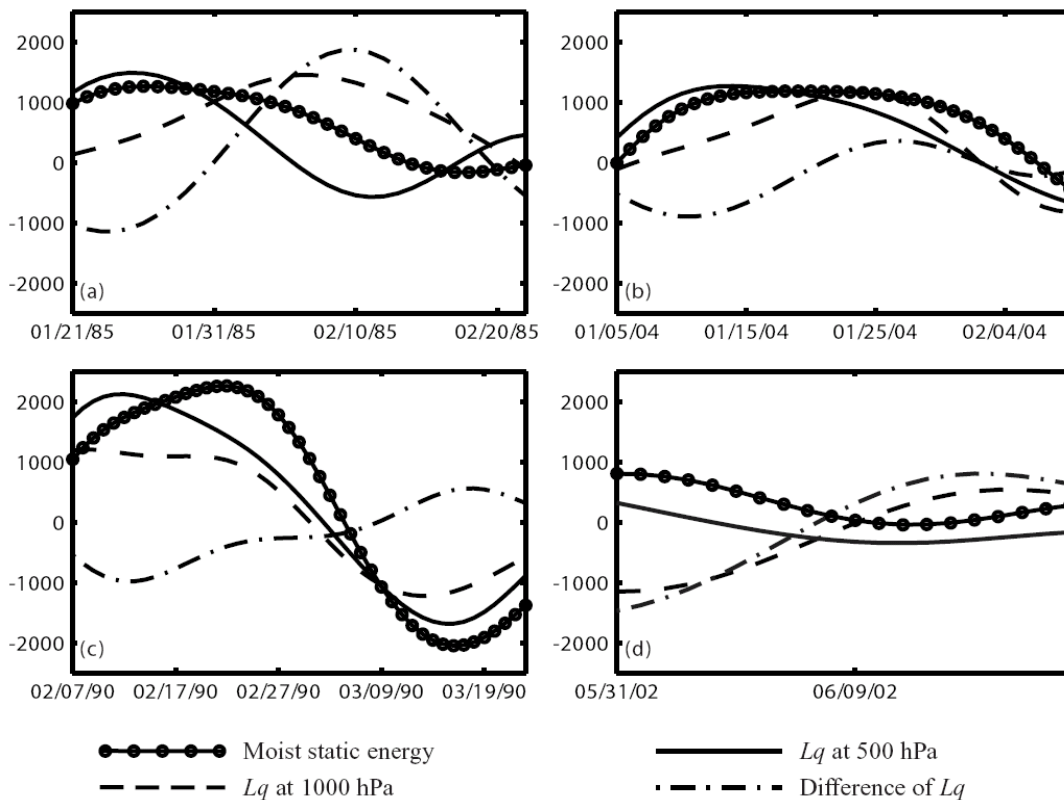


Figure 3.7 Moist static energy (solid lines with cycles), Lq at 1000 hPa (dash lines) and 500 hPa (dash-dot lines), and the difference of Lq at the two pressure levels (solid lines) during four MJO events. The units are J kg^{-1} .

3.3.1.2 Role of the Moist Static Energy

It has been shown that the atmospheric internal instability is usually necessary for the onset of MJOs by examining the moist static energy h (Kemball-Cook and Weare 2001), which is defined as $h = C_p T + Lq + gz$, where $C_p = 1005 \text{ J kg}^{-1} \text{ K}^{-1}$ is the specific heat of the air, T is the air temperature, q is the specific humidity, g is the gravitational acceleration, and z is the geopotential height. The difference between $h(1000 \text{ hPa})$ and $h(500 \text{ hPa})$ is a good index for the atmospheric instability (Kemball-Cook and Weare 2001). Defining $\Delta MSE = h(1000 \text{ hPa}) - h(500 \text{ hPa})$, positive ΔMSE implies an unstable atmosphere, while negative ΔMSE implies a stable atmosphere. Fig. 3.7a and 3.7b show the moist static energy during the MJO events No. 9 and No. 48. The latent heat release (Lq) controls the large positive ΔMSE , leading to an atmospheric instability, especially during the first 10–15 days of these events. These MJO events start with a considerable negative Lq at the upper level (500 hPa). Meanwhile, Lq at the lower level (1000 hPa) does not significantly differ from zero during the onset of the events. The Lq at both levels increases with time. The increase of Lq at the upper level reduces the moist static energy and tends to stabilize the air column, while the increase of near-surface Lq tends to sustain positive ΔMSE , i.e. the instability of the atmosphere, and thereby prolonging the MJO events. In Fig. 3.7a, the increase of Lq near the surface is weaker than it is in the upper level, thus ΔMSE drops below zero in about 20 days. But in Fig. 3.7b, the increase of Lq at 1000 hPa is comparable with that at 500 hPa, leading to a positive ΔMSE that lasts for almost 30 days. In the model simulations, one major deficiency is that the simulated periodicity is generally 25-30 days, which is slightly shorter than observations (Sperber et al.

1997). It has been shown by some model experiments (e.g. Waliser et al. 1999) that including oceanic feedbacks can extend the period of simulated MJOs, which is consistent with our results derived from the reanalysis products. Thus, this class of MJO events is mainly controlled by the atmospheric instabilities and the ocean only has a secondary influence on the MJOs as a feedback to the atmospheric forcing in extending the life-span of the events.

3.3.2 The events with dominant R'

In a few of the MJO events, the energy source R' due to surface heat flux dominates (Fig. 3.2). An example is the MJO event from Feb 27, 1990 to Mar 23, 1990 (No. 21 in Table 3.1). The three components of the energy sources with respect to time are shown in Fig. 3.8a. At the beginning of this event, all energy sources are relatively small. Then, R' increases significantly in the following 10 days, while $P'K'$ and $K'\bar{K}$ remain nearly unchanged. Correspondingly, the perturbed kinetic energy K' increases and reaches a maximum around Mar 4, 1990 (Fig 3.8b). After Mar. 4, 1990, along with the decrease of R' , K' also decreases. The variations of surface heat fluxes along with the SST anomalies are shown in Fig. 3.4c. On Feb 7, 1990, which is 20 days before the onset of this MJO event, all surface fluxes are small. However, there is a noticeable warm SST anomaly, which reaches a peak on Feb 15, 1990, about 5 days before the negative maximum of surface fluxes, which is consistent with the lead time of warm SSTs before the organization of deep convection shown in Sperber (2003) and Pegion and Kirtman (2008b). Therefore, the warm SST anomalies before this MJO event are not attributable to surface heat flux, and thereby can only be attributable to the internal ocean dynamics and

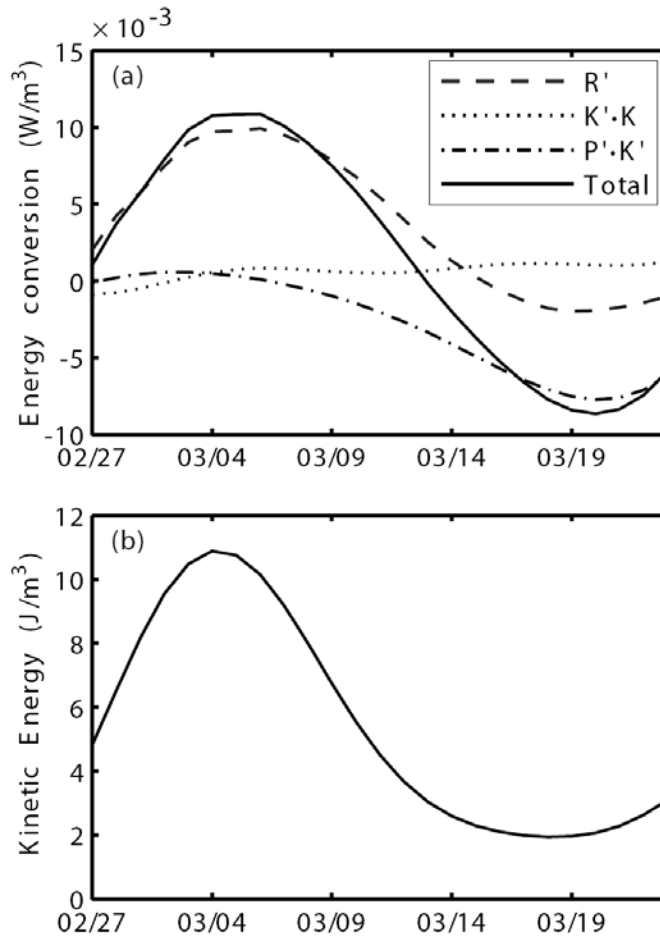


Figure 3.8 (a) Energy conversions for the MJO event from Feb 27, 1990 to Mar 23, 1990. (b) The corresponding perturbed kinetic energy. All variables are averaged between $50^\circ E$ - $100^\circ E$, 0° - $10^\circ S$ and from 1000 hPa to 250 hPa.

thermodynamics (Jochum and Murtugudde 2005; Hermes and Reason 2008; Zhou et al. 2008a, b; also see Chapter 2). From the ratio between Term (II) and Term (III) in Eq. (3.13), one can also see the warm SST anomalies are important for the enhancement of surface heat flux from Feb 7 to Feb 17, 1990 in the western Indian Ocean before the strong convection organizes itself (Fig. 3.9), which is further evidence that the ocean drives the atmosphere prior to this MJO event. However, after the onset of this MJO event, the SST anomalies are mainly controlled by the relatively large surface heat fluxes (Fig. 3.4c). The maximum heat fluxes occur on

Mar 5, 1990, while the lowest SST anomaly occurs about 7 days later, on Mar 12, 1990, which is similar to the relations shown in Figs. 3.4a and 3.4b.

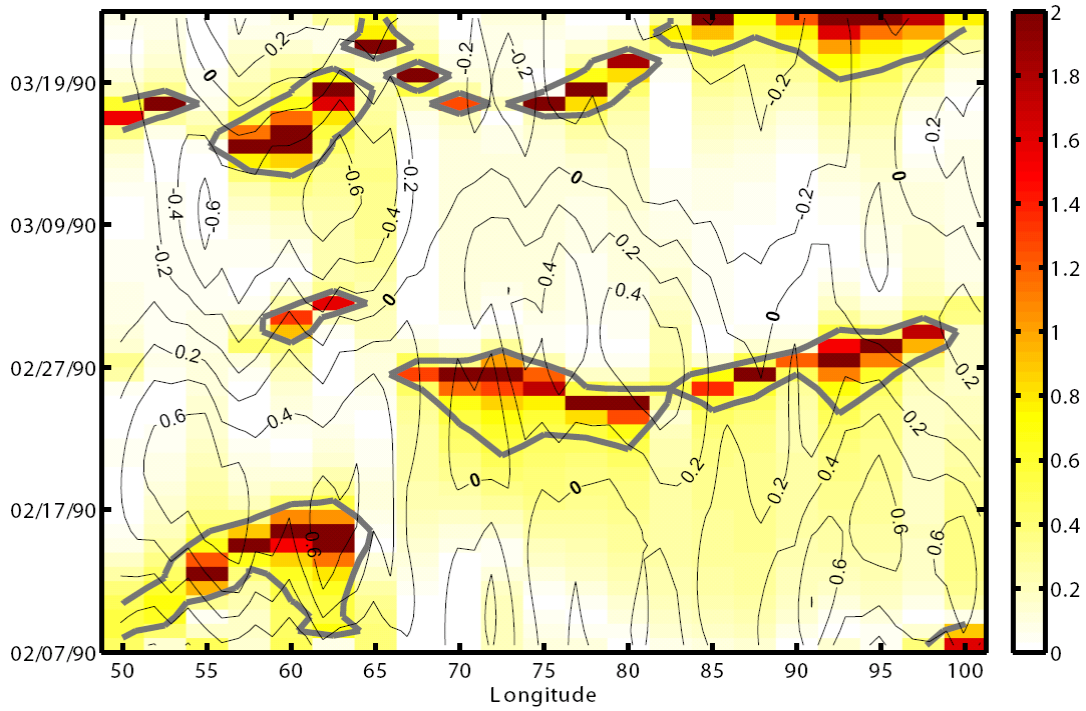


Figure 3.9 The ratio between Term II and Term III in Eq. (3.13) during the MJO event No. 21. The thick gray contour represents a value of 0.5. Intraseasonal SST anomalies are superimposed with the thin contours. The unit of SST anomalies is Kelvin. All variables are averaged between 0° and 10° S.

3.3.2.1 Variation of moist static energy

The variation of moist static energy (h) during this MJO event is shown in Fig. 3.7c. The ΔMSE begins to increase around Feb 7, 1990 and reaches a maximum on Feb 21, 1990. Prior to the MJO event, significantly positive Lq at 1000 hPa leads to relatively high h at the lower level and thereby destabilizing the atmosphere. Meanwhile, Lq at 500 hPa increases only moderately during the life-cycle of the MJO event. The rise of surface heat flux is partly attributable to warm SST anomalies (Fig. 3.9), which begin to occur as early as Feb 7, 1990 in the central and western Indian Ocean, reach a peak about 7 days prior to the peak of ΔMSE . In addition, that a

cyclone (negative vorticity in the southern hemisphere) lies to the east of the warm SSTAs and cool SSTAs (Fig. 3.10) occur prior to this MJO event, also reaffirm that the ocean is driving the atmosphere, with a background horizontal advection underneath (Peña et al. 2003). Therefore, before the onset of this MJO event, warm SSTs lead to an increase in near-surface specific humidity and an increase of latent heat release, which destabilize the atmosphere and enhance the intraseasonal wind anomalies. After the onset of this MJO event, the SST anomalies return to a cool phase, because of the large latent heat loss (Fig. 3.4c). Consequently, the low level Lq decreases rapidly (Fig. 3.7c), hence h also decreases relatively fast and the atmosphere becomes stable. As a result, the perturbed kinetic energy is reduced (Fig. 3.8b). In this class of MJO events, the ocean feeds back to the atmosphere actively, rather than as a response with secondary impact.

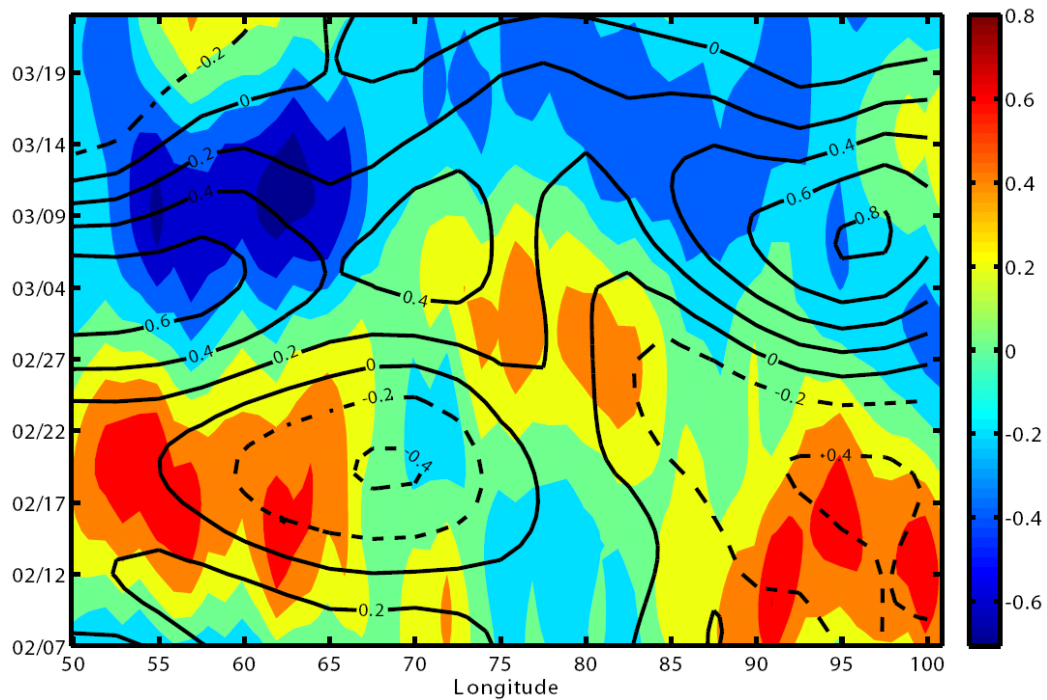


Figure 3.10 Intraseasonal SSTAs from Feb 7, 1990 to Mar 23, 1990, with a unit of Kelvin (color shades). The intraseasonal vorticity of surface winds averaged between the equator and 10°S are superimposed (black contours) with a unit of 10^{-5} s^{-1} .

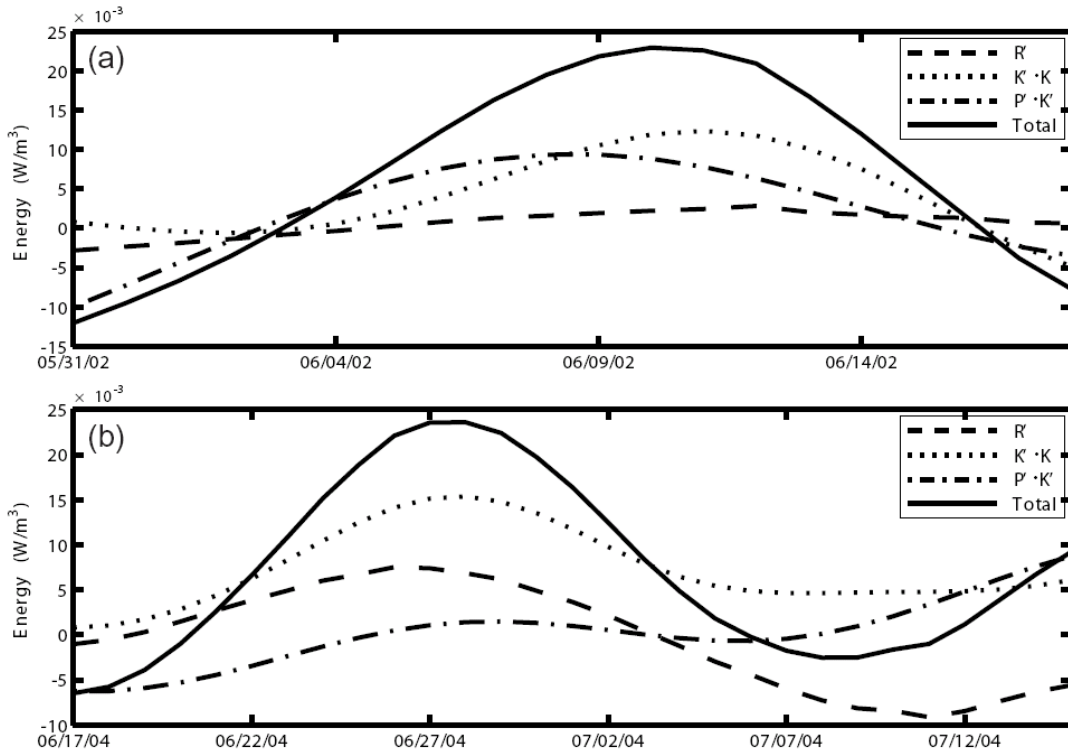


Figure 3.11 Energy conversions for two MJO events. All variables are averaged between 50°E - 100°E , 0° - 10°S and from 1000 hPa to 250 hPa.

3.3.3 The events where $K'\bar{K}$ dominates

As shown in Fig. 3.2, the energy for some of the MJOs is extracted from the mean kinetic energy. The energy sources for two examples of such MJO events, viz., No. 42 and 50, are given in Fig. 3.11. The surface heat fluxes and the SST anomalies during the MJO event No. 42 (Fig. 3.4d) are smaller than those in the previous two classes of MJOs, which implies that the air-sea heat exchange is not a primary driver for this class of MJO events. The moist static energy during the MJO event from May 31, 2002 to June 18, 2002 is shown in Fig. 3.7d. The specific humidity at 1000 hPa and 500 hPa are similar to each other and vary synchronously, which implies an approximately barotropic structure. Therefore, the difference of Lq between the two levels is small and only contributes to less than half to the ΔMSE during this MJO

event. Actually, since moist static energy is a convenient measure of convective available potential energy, small ΔMSE (especially after Jun 9, 2002) is also evidence that the energy conversion from the potential energy is not the dominant mechanism for this MJO event. Usually, a pronounced $K' \cdot \bar{K}$ conversion is driven by barotropic instability. The necessary condition for barotropic instability is that $dq/dy = \beta - \partial^2 \bar{u} / \partial y^2$, where q is the quasi-geostrophic potential vorticity (QG PV), β is the meridional gradient of the Coriolis parameter, and \bar{u} is the basic flow; should change sign in the study area. One can see alternatively positive and negative dq/dy during the MJO event from Jun 9, 2002 to Jun 18, 2002, as shown in Fig. 3.12a. A snapshot of dq/dy on Jun 9, 2002 is shown in Fig. 3.12c, in which the positive and negative dq/dy have comparable amplitudes and areas. Therefore, the necessary condition for barotropic instability is satisfied in this region. In comparison, dq/dy during MJO event No. 9 (which is discussed in Section 3.3.1) is shown in Fig. 3.12b and a snapshot on Jan 21, 1985 is shown in Fig. 3.12d. Positive dq/dy dominates over most of the region and during most of the time for the latter MJO event, indicating that the meridional gradient of zonal winds is not large enough to overcome β and thus, barotropic instability cannot be triggered. For this class of MJO events, since the energy is mainly obtained from the mean kinetic energy, large gradients of horizontal winds are a necessary ingredient. Thus, they typically occur during the transition periods between monsoon seasons, when the wind direction is changing.

MJOs have a distinct seasonality, viz. there are more MJO events in boreal winter than in boreal summer. Nevertheless, the MJO events in this class usually occur

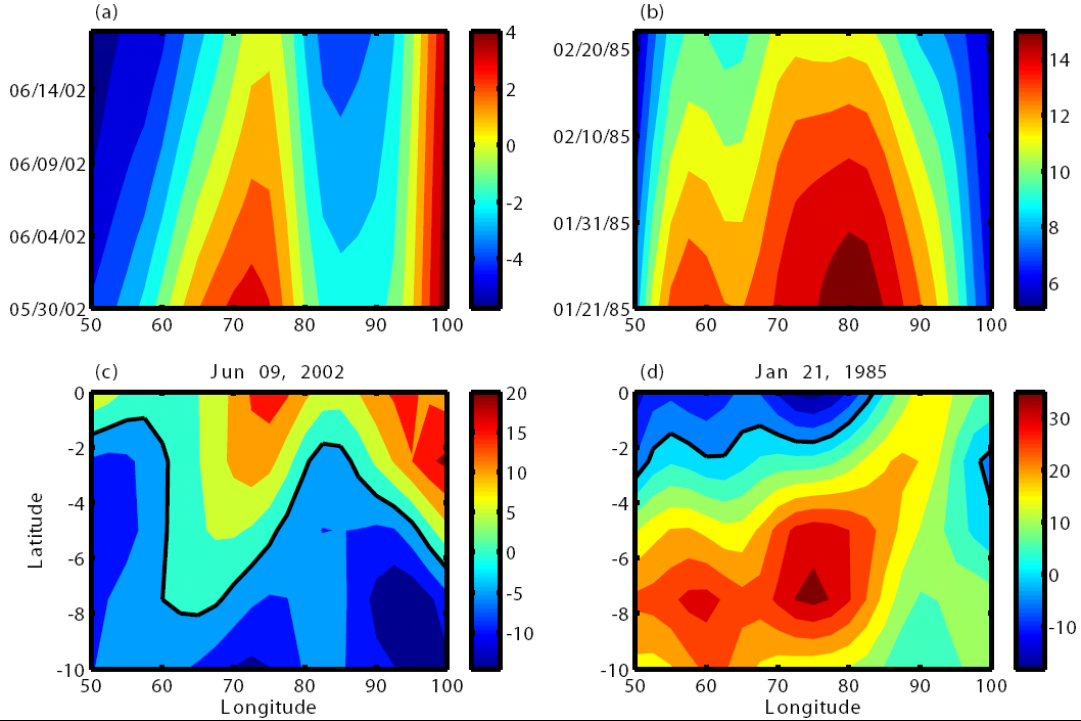


Figure 3.12 dq/dy averaged between 0° and 10°S during the MJO event No. 42 (a) and No. 9 (b). (c) and (d) are two snapshots of dq/dy on two days. The black contours in (c) and (d) are the zero contours. The units are $10^{-12} \text{ m}^{-1} \text{ s}^{-1}$.

during boreal summer. Thus, the energy sources, i.e., $P'K'$, $K'\bar{K}$, and R' , are also averaged from 10°S to 10°N , including variations in the northern hemisphere. The relative importance of the three energy sources for four MJO events (No. 3, 7, 29, and 50), which all occur in boreal summer, are shown in Fig. 3.13, along with the counterparts averaged between 10°S and the equator (also see Fig. 3.2). The results obtained in the two latitude regions are similar. Especially, the dominant energy source for each MJO event does not change. Therefore, even for MJO events in boreal summer, the results shown in Fig. 3.2 are still valid.

3.4 Conclusions and discussion

Madden-Julian Oscillations, which are the major intraseasonal oscillations in the climate system, can be regarded as perturbations to the background circulation in the

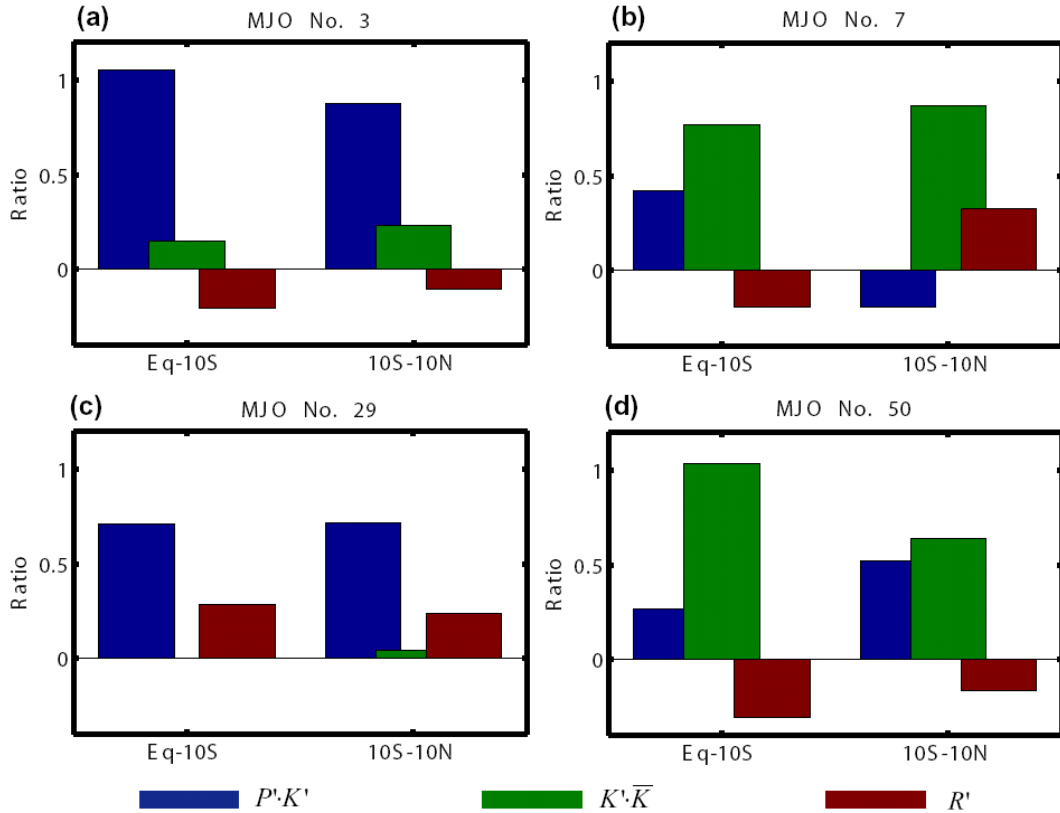


Figure 3.13 Ratios between $P' \cdot K'$ (blue bars), $K' \cdot \bar{K}$ (green bars), R' (red bars) and the total energy conversions TE for four MJO events in boreal summer. The energy conversions are averaged between the equator and 10°S for the left group in each panel (the same as Fig. 2), while they are averaged between 10°S and 10°N for the right group in each panel.

atmosphere. Usually, they are accompanied by enhanced perturbed kinetic energy. Thus their energy sources are explored with the energy budget of the perturbed kinetic energy with respect to the intraseasonal perturbations. There are three sources for the perturbed kinetic energy: the energy conversion from perturbed potential energy, the energy source due to surface heat flux, and the energy conversion from mean kinetic energy. Among the 54 MJO events defined based on the MJO index (WH04), most events gain their kinetic energy from the perturbed potential energy. At the beginning of this class of MJO events, the specific humidity drops at the upper level, which is known as the suppressed phase of MJO (e.g. Kemball-Cook and

Weare 2001; Shinoda et al. 1998; Woolnough et al. 2007). As a result, the atmosphere becomes unstable, and the available potential energy is released. Meanwhile, as a response to the atmospheric forcing, the sea surface is heated, leading to warm SST anomalies, which consequently feedback to latent heat flux, raise the specific humidity in the lower atmosphere, and sustain the instability. Therefore, the MJO events can last longer with oceanic feedbacks than only with atmospheric instabilities. This conclusion can explain why in many numerical models, including the oceanic feedbacks can improve the simulation of the MJO period. There are three MJO events, in which the kinetic energy increases mainly due to enhanced surface heat flux. The warm SST anomalies, which are induced by the ocean dynamic and thermodynamic processes (Jochum and Murtugudde 2005; Hermes and Reason 2008; Chapter 2) before the onset of the MJO events, lead to low-level convergence and unstable conditions in the atmosphere, providing an important ingredient for the onset of MJOs. In this case, the ocean drives the atmosphere actively. Therefore, if one wants to capture this type of MJO events in a model, an ocean-atmosphere coupled model would seem essential. Lastly, during the transition between monsoon seasons, barotropic instability in the atmosphere can be triggered, because the gradients of horizontal winds become large enough to overcome the meridional gradient of the Coriolis parameter, β . Thus, the intraseasonal variabilities can draw energy from the mean kinetic energy. The period of this flavor of MJO events is shorter than the other two types, likely because the energy is not organized into baroclinic instability in the atmosphere and thereby the convection is weaker.

Our analysis indicates that although all MJO events have a similar period ranging between 30-60 days, their energy sources are different. For a specific MJO event, its energy can come from perturbed potential energy (which is the most important energy source), surface heat flux, and mean kinetic energy, due to different mechanisms. In order to highlight the role of each of the three possible energy sources for MJOs, typical examples are selected and analyzed. However, the three energy sources cannot always be completely separated. In some events, two energy sources may be comparable and both can be important. In several of the events, all three energy sources are non-negligible (e.g. No. 24). Therefore, appropriate mechanism or combination of mechanisms should be studied carefully in order to understand a specific MJO event. This is also true for model simulations and predictions. With an atmosphere-only model, acceptable simulations can probably be expected for only the MJO events in which only $P'K'$ dominates, but with a shorter time period in models. For the MJO events in which R' dominates, an atmosphere-only model would likely be inadequate; requiring an ocean-atmosphere coupled model instead.

The composite MJO event is usually created in a numerical experiment which is conducted to examine the oceanic impact on the simulation or prediction of MJO events. However, based on the relative importance of energy sources shown in Fig. 3.2, if an average over many randomly-chosen MJO events is taken, it is very likely that most energy of the composite MJO event comes from the atmospheric internal variability, while a small part of energy is derived from the ocean-atmosphere interactions. Therefore, even if the oceanic processes are resolved and well simulated in a numerical model, one cannot expect dramatic improvements in the simulation of

a composite MJO event. This could be an important reason why no significant or systematic oceanic influences were found in many previous numerical experiments (e.g. Hendon 2000; Zhang et al. 2006). Nevertheless, it is shown in this study that each of the MJO events is quite distinct, at least in terms of the energy sources. Thus, compositing MJO events should be done carefully, so that conclusions could be really robust and highlight the common properties of the events in the composite.

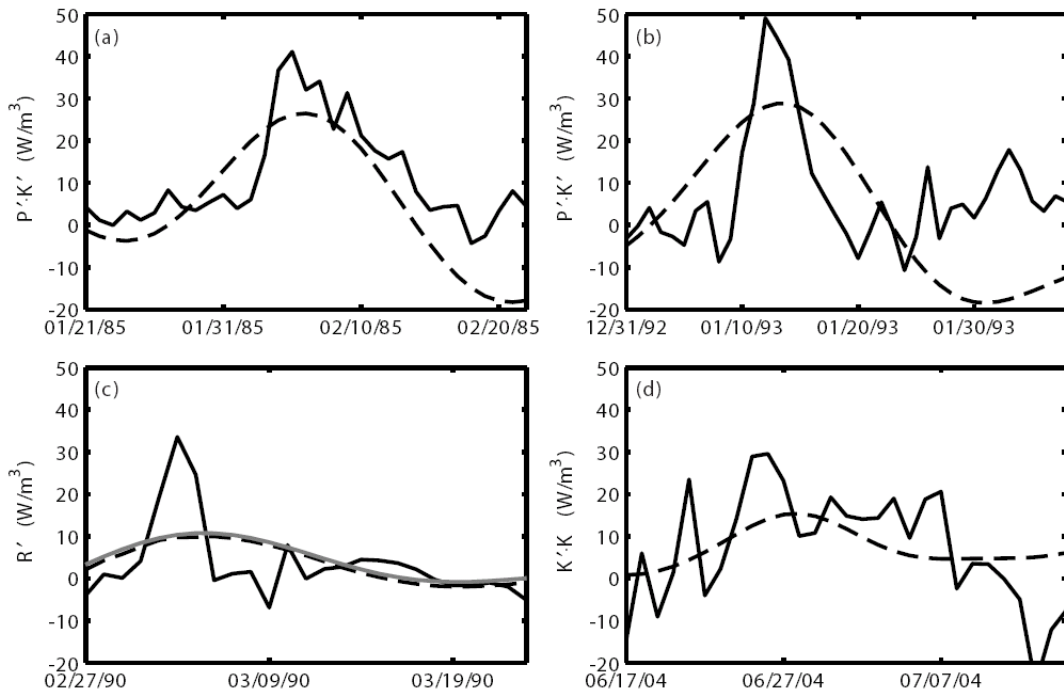


Figure 3.14 Comparisons between the three energy sources calculated with the Lorenz energy cycle equations (solid lines) and with the temporal perturbations (dash lines) during 4 typical MJO events. For clearance, only the dominant energy sources in each MJO event are shown. The gray solid line in (c) is the intraseasonal part (obtained with band-pass filtering between 20 and 100 days) of the corresponding black solid line. The units are 10^{-3} W m^{-3} .

3.5 Appendix

The Lorenz energy cycle, which applies the Eulerian mean in the zonal direction, is a classic method to calculate the energy transfers. However, in this study, we

calculate the energy conversions with the temporal perturbations. As emphasized in Plumb (1983), the combinations of the terms in the energy equations are not unique. Thus, multiple and consistent evidences are necessary to support the physical interpretation of the terms in the energy equations. Because all other independent evidences are inter-twined in a time series and it is not easy to determine whether the temporal perturbations and the spatial perturbations are equivalent, we choose to calculate energy transfers with temporal perturbations.

The three energy sources calculated with the two methods are compared in Fig. 3.14. The black solid lines in Fig. 3.14 are obtained with the Lorenz energy cycle equations. The mean part is the Eulerian mean and the perturbation part is the deviation from the Eulerian mean. The dashed lines in Fig. 3.14 are obtained with temporal perturbations, which are analyzed in this study. The mean part is the low-frequency variation with a period longer than 100 days and the perturbation is the intraseasonal part with a period between 20 and 100 days. The two results are qualitatively consistent. Especially, after a band-pass filtering with cut-off periods between 20 and 100 days, the two results for R' are quantitatively almost the same (Fig. 3.14c). Actually, it is hard to determine whether the differences are significant or they are within the range of model errors, because the small scale processes are not explicitly resolved in the NCEP reanalysis.

Chapter 4: Ocean-Atmosphere coupling on distinct scales

4.1 Ocean-atmosphere coupling on different spatio-temporal scales: A mechanism for intraseasonal instabilities

Abstract

The possibility of interactions between oceanic and atmospheric oscillations with different temporal and spatial scales is examined with analytical solutions to idealized linear governing equations. With a reasonable choice for relevant parameters, the meso-scale oceanic features and the large-scale atmospheric oscillations can interact with each other and lead to unstable waves in the intraseasonal band in the specific coupled model presented in this study. This mechanism is different from the resonance mechanism, which requires similar temporal or spatial scales in the two media. Instead, this mechanism indicates that even in the cases when the temporal and spatial scales are different, but the dispersion relations (i.e. functions of frequency and wavenumber) of the oceanic and atmospheric oscillations are proximal, instabilities can still be generated due to the ocean-atmosphere coupling.

4.1.1 Introduction

4.1.1.1 Motivation

Interactions between the ocean and the atmosphere are important for driving many phenomena in the climate system, such as El Niño-Southern Oscillation (ENSO, see the review in Neelin et al. 1998). In a linear framework, it is usually assumed *a priori* that the oceanic and the atmospheric components which interact with each other should be of similar temporal and spatial scales. For example, most

recently, Han et al. (2008) concluded that the intraseasonal (with a period of about 2 weeks) wind forcing is critical for the generation of the intraseasonal variabilities in the tropical Atlantic Ocean. However, some mismatches have been found between the oceanic and atmospheric variabilities in the coupled system. For example, the Kelvin waves which are generated by the Madden-Julian Oscillations (MJOs) in the Pacific Ocean are found to have a longer period (~ 70 days) than that of the MJOs (30-60 days, Kessler et al. 1995). Hendon et al. (1998) attributed this inconsistency to changes of the temporal and spatial characteristics of the MJO forcing over the eastern Pacific. They emphasized that, due to resonance, the relatively weak forcing around a period of 70 days resulted in significant Kelvin waves with a similar period. Roundy and Kiladis (2006) and Shinoda et al. (2008) also attributed this discrepancy to the time-varying intraseasonal forcing over the central and eastern tropical Pacific Ocean. Another example of such inconsistency is the interaction between sea surface temperatures (SSTs) and MJOs. Both observations (Jones et al. 1998; Lau and Sui 1997; Zhang 1996) and modeling studies (Sperber et al. 1997; Waliser et al. 1999) provide support for a positive feedback between SSTs and MJOs. However, because the spatial scale of the SSTAs is only on the order of a hundred kilometers (Section 2.1) while that of MJOs is on the order of a thousand kilometers (see the review by Madden and Julian 1994), there is a clear discrepancy in the spatial scales of the two processes. In this study, we propose a possibility that oscillations with different temporal and spatial scales are able to interact with each other under certain conditions. This hypothesis is examined with a simple theoretical ocean-atmosphere coupled model and the corresponding analytical solutions. In this model, the ocean

and the atmosphere only interact with one degree of freedom. The advantages and the limitations of the idealized coupled system are discussed in Section 4.1.3.

4.1.1.2 Review of the uncoupled solutions

In order to favor comparisons with the solutions to the following coupled model in Section 4.1.2, the uncoupled oceanic and atmospheric models, which are the bases of the coupled model, are briefly described.

For the barotropic, tropical ocean, the linear inviscid governing equations with no atmospheric forcing are adopted from Gill (1982);

$$\begin{cases} \frac{\partial u}{\partial t} - \beta y v = -g \frac{\partial \eta}{\partial x} & (4.1.1a), \\ \frac{\partial v}{\partial t} + \beta y u = -g \frac{\partial \eta}{\partial y} & (4.1.1b), \\ \frac{\partial u}{\partial x} + \frac{\partial v}{\partial y} = -\frac{1}{H} \frac{\partial \eta}{\partial t} & (4.1.1c), \end{cases}$$

where u , v are the zonal and meridional velocities in the ocean, respectively; β is the meridional gradient of Coriolis parameter f ; g is the gravitational acceleration; η is the sea surface height (SSH) anomaly; and H is the water column depth. For the barotropic atmosphere in the tropics, the governing equations without oceanic feedbacks are applied following Anderson and McCreary (1985),

$$\begin{cases} \frac{\partial U}{\partial t} - \beta y V = -\frac{\partial P}{\partial x} - rU & (4.1.2a), \\ \frac{\partial V}{\partial t} + \beta y U = -\frac{\partial P}{\partial y} - rV & (4.1.2b), \\ \frac{\partial U}{\partial x} + \frac{\partial V}{\partial y} = -r \frac{P}{c^2} & (4.1.2c), \end{cases}$$

where U and V are the zonal and meridional winds, P is the pressure at the bottom of the modeled column of barotropic atmosphere, r is a damping coefficient, and c is the phase speed of Kelvin waves. Since we focus on the deep tropics, the Coriolis parameter f in both the ocean and the atmosphere is consistently replaced with βy . The SSH gradient in Eq. (4.1.1) and the air pressure gradient in Eq. (4.1.2) are not generated by the ocean-atmosphere coupling. They are free oscillations which are balanced by other dynamical variables in the uncoupled systems.

For the ocean, by assuming a wavelike solution, $v = v_0 \exp\left(-\frac{\beta y^2}{2c}\right) e^{i(kx - \omega t)}$, we obtain the dispersion relation for the Mixed-Rossby-Gravity waves (MRG waves, see the derivations in Gill 1982) from Eq. (4.1.1)

$$\frac{\omega^3}{c^2} - \left(k^2 + \frac{\beta}{c}\right)\omega - \beta k = 0 \quad (4.1.3).$$

The discriminant of the cubic equation (3) is $\Delta = 4\left(k^2 + \frac{\beta}{c}\right)^3 - 27\frac{(\beta k)^2}{c^2}$, which has a minimum value of 0 when $k^2 = \frac{\beta}{2c} = R_D^{-2}$, where R_D is the equatorial Rossby radius of deformation. Because the discriminant is always positive or zero, Eq. (4.1.3) always has three real roots, which indicates that the free MRG waves are always stable. For the atmosphere, also assuming a wave form solution for U with $U = U_0 e^{i(kx + ly - \omega t)}$, Eq. (4.1.2) becomes

$$-ik\left[\omega^2 - c^2 k^2 - r^2 - (\beta y)^2\right]U_0 + \frac{\omega k}{r}\left[c^2 k^2 + 2r^2\right]U_0 = 0 \quad (4.1.4),$$

which describes an inertial-gravity wave in the atmosphere with a dispersion relation given by,

$$\omega^2 - c^2 k^2 - r^2 - (\beta y)^2 = 0 \quad (4.1.5).$$

Obviously, Eq. (4.1.5) always has two real solutions, one of which propagates westward while the other one propagates eastward. Therefore, without ocean-atmosphere coupling, the free systems described by Eqs. (4.1.1) and (4.1.2) are stable, and the unstable waves examined below are only attributable to the ocean-atmosphere interactions.

In this study, the possibility of ocean-atmosphere interactions between processes with different scales in a linear framework is examined with idealized dynamic equations which are based on Eqs. (4.1.1) and (4.1.2) and their analytical solutions. The coupled system is studied in Section 4.1.2. The equations are presented in Section 4.1.2.1. In Section 4.1.2.2, they are solved under the traditional assumption that the spatial and temporal scales in the two media are the same. In Section 4.1.2.3, they are solved by assuming different scales in the ocean and the atmosphere. The validation of the approximations used in this study is discussed in Section 4.1.3 and the conclusions are presented in Section 4.1.4.

4.1.2 Coupled system

4.1.2.1 Coupled equations

The ocean and the atmosphere are now coupled together, in order to explore whether the processes with different scales can interact with each other and generate unstable waves. The key atmospheric variable that drives the ocean is the zonal wind stress (τ_x), or the zonal wind (U) and the key variable for the oceanic feedback to the

atmosphere is SST (T). Hence, the atmospheric forcing on the ocean is expressed as a function of U and the oceanic feedback to the atmosphere is expressed as a function of T .

The coupled equations for the tropical ocean are expressed as

$$\begin{cases} \frac{\partial u}{\partial t} - \beta y v = -g \frac{\partial \eta}{\partial x} + \frac{\tau_x}{\rho_0 H}, \\ \frac{\partial v}{\partial t} + \beta y u = -g \frac{\partial \eta}{\partial y}, \\ \frac{\partial u}{\partial x} + \frac{\partial v}{\partial y} = -\frac{1}{H} \frac{\partial \eta}{\partial t}, \end{cases} \quad (4.1.6)$$

where ρ_0 is water density. For simplicity, the meridional wind stress is neglected, because the zonal wind speeds are significantly larger than the meridional ones over most tropical oceans (especially the Pacific and the Atlantic, Fig. 4.1.1). Applying the ‘Moore’s maneuver’ (Gill 1982) and assuming $\tau_x = \gamma U$, we have

$$\frac{\partial^3 v}{c^2 \partial t^3} + \frac{(\beta y)^2}{c^2} \frac{\partial v}{\partial t} - \frac{\partial(\nabla^2 v)}{\partial t} - \beta \frac{\partial v}{\partial x} = \frac{\gamma}{\rho_0 H} \left(-\frac{\beta y}{c^2} \frac{\partial U}{\partial t} + \frac{\partial^2 U}{\partial x \partial y} \right) \quad (4.1.7),$$

where $c = \sqrt{gH}$. For the intraseasonal (~ 40 days) and meso-scale ($\sim 10^2$ km)

oscillations in the tropics, $\frac{\beta y}{c^2} \frac{\partial}{\partial t} \sim 2 \times 10^{-13} \text{ m}^{-2}$, while $\frac{\partial^2}{\partial x \partial y} \sim 1 \times 10^{-10} \text{ m}^{-2}$.

Therefore, the first term on the right hand side of Eq. (4.1.7) is neglected and Eq.

(4.1.7) becomes

$$\frac{\partial^3 v}{c^2 \partial t^3} + \frac{(\beta y)^2}{c^2} \frac{\partial v}{\partial t} - \frac{\partial(\nabla^2 v)}{\partial t} - \beta \frac{\partial v}{\partial x} = \frac{\gamma}{\rho_0 H} \frac{\partial^2 U}{\partial x \partial y} \quad (4.1.8).$$

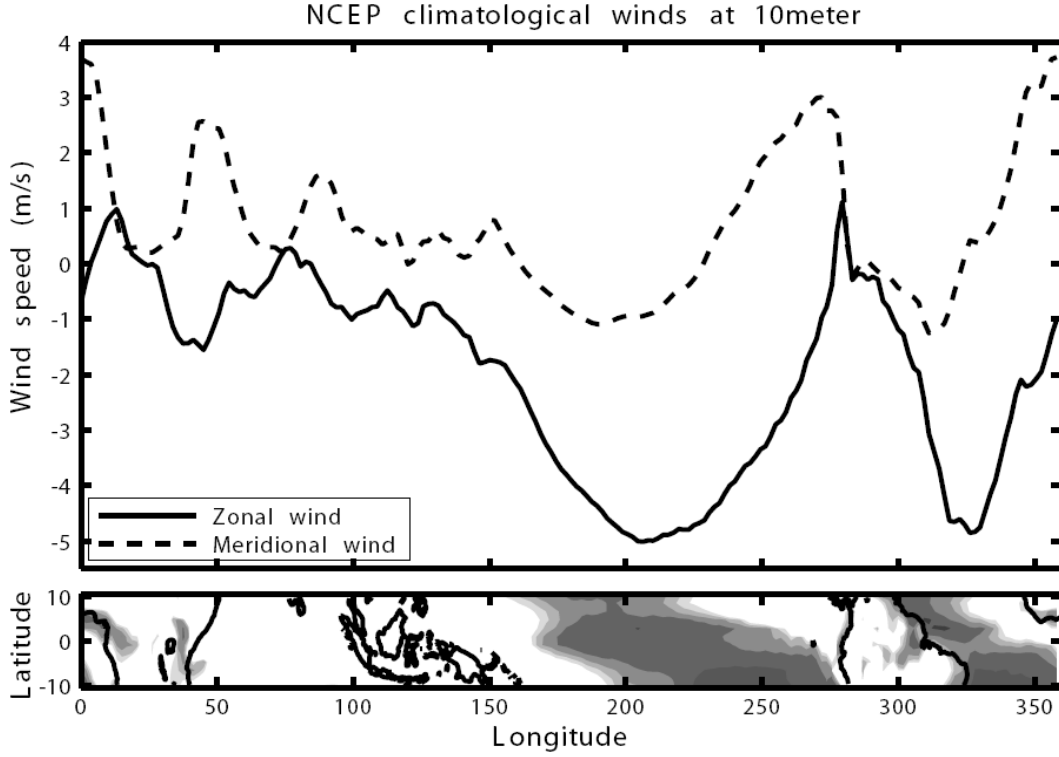


Figure 4.1.1 Climatological NCEP winds at 10-meter (Kalnay et al. 1996) averaged from 10°N to 10°S. The gray scales in the lower panel show the ratio between the standard deviation and the climatological mean of the zonal NCEP winds at 10-meter. The contours are from 0.1 to 0.5, with an interval of 0.1.

The coupled equations for the atmosphere are

$$\begin{cases} \frac{\partial U}{\partial t} - \beta y V = -\frac{\partial P}{\partial x} - rU, \\ \frac{\partial V}{\partial t} + \beta y U = -\frac{\partial P}{\partial y} - rV, \\ \frac{\partial U}{\partial x} + \frac{\partial V}{\partial y} = -r\frac{P}{c^2} + \frac{Q}{c^2}, \end{cases} \quad (4.1.9)$$

where Q is the net surface heat flux. These equations have been used widely in previous studies in the ocean-atmosphere coupling (e.g. Anderson and McCreary 1985; Hirst 1986). Assuming Q is linearly proportional to SST, i.e. $Q = \alpha T$, after similar processes as above, we have

$$\left[\left(\frac{\partial}{\partial t} + r \right)^2 + (\beta y)^2 \right] \frac{\partial U}{\partial x} - \frac{c^2}{r} \left(\frac{\partial}{\partial t} + r \right) \nabla^2 \frac{\partial U}{\partial x} = -\nabla^2 Q = -\alpha \nabla^2 T \quad (4.1.10).$$

4.1.2.2 Solutions with same ω and k in the ocean and the atmosphere

The wavelike solutions of the form $v = v_0 \exp\left(-\frac{\beta y^2}{2c}\right) e^{i(kx - \omega t)}$ and $U = U_0 e^{i(kx + ly - \omega t)}$ are assumed again. Note that these assumptions follow the traditional point of view of the ocean-atmosphere interaction, i.e. the frequency (ω) and wavenumber (k) are the same in the ocean and the atmosphere. An approximate relation between the meridional velocity (v) in the ocean and SST (T) is needed to obtain the following analytical solutions. Replacing v with the geostrophic approximation, $v = \frac{g}{f} \frac{\partial \eta}{\partial x}$, and assuming that η is proportional to SST, i.e. $T = m\eta$ (m is a constant coefficient but not explicitly used in the calculations below), we have an approximation, $v = \frac{g}{mf} \frac{\partial T}{\partial x} = \lambda \frac{\partial T}{\partial x}$ and $v_0 = ik\lambda T_0$. Substituting the roughly linear approximation between v_0 and T_0 , as well as the wavelike solutions above into Eqs. (4.1.8) and (4.1.10), we obtain

$$\begin{cases} \left[\frac{\omega^3}{c^2} - \left(k^2 + \frac{\beta}{c} \right) \omega - \beta k \right] k\lambda T_0 = \frac{kly}{\rho_0 H} U_0, \\ -ik \left[\omega^2 - c^2 k^2 - r^2 - (\beta y)^2 \right] U_0 + \frac{\omega k}{r} \left[c^2 k^2 + 2r^2 \right] U_0 = \alpha (k^2 + l^2) T_0. \end{cases} \quad (4.1.11)$$

In order to have non-trivial solutions, it is required that

$$\left[\begin{array}{cc} \left[\frac{\omega^3}{c^2} - \left(k^2 + \frac{\beta}{c} \right) \omega - \beta k \right] k \lambda & -\frac{k l \gamma}{\rho_0 H} \\ -\alpha (k^2 + l^2) & -i k \left[\omega^2 - c^2 k^2 - r^2 - (\beta y)^2 \right] + \frac{\omega k}{r} \left[c^2 k^2 + 2r^2 \right] \end{array} \right] = 0 \quad (4.1.12).$$

From the imaginary part, one can obtain stable MRG waves and stable inertial-gravity waves again. From the real part, the following condition must be satisfied;

$$\frac{\omega^4}{c^2} - \left(k^2 + \frac{\beta}{c} \right) \omega^2 - \beta k \omega - \frac{\alpha r \gamma}{\rho_0 H \lambda} \frac{(k^2 + l^2)}{c^2 k^2 + 2r^2} = 0 \quad (4.1.13),$$

which is a depressed quartic equation and can be solved in the following manner. Let

$$C_\alpha = -c^2 \left(k^2 + \frac{\beta}{c} \right), \quad C_\beta = -c^2 \beta k, \quad C_\gamma = -\frac{c^2 \alpha r \gamma}{\rho_0 H \lambda} \frac{(k^2 + l^2)}{c^2 k^2 + 2r^2}, \quad \text{and Eq. (4.1.13)}$$

becomes

$$\omega^4 + C_\alpha \omega^2 + C_\beta \omega + C_\gamma = 0 \quad (4.1.14).$$

Following the Ferrari's solution (Tignol 2001, Chapter 3), let

$$P = -\frac{C_\alpha^2}{12} - C_\gamma, \quad Q = -\frac{C_\alpha^3}{108} + \frac{C_\alpha C_\gamma}{3} - \frac{C_\beta^2}{8},$$

$$R = \frac{Q}{2} \pm \sqrt{\frac{Q^2}{4} + \frac{P^3}{27}}, \quad U = \sqrt[3]{R},$$

$$Y = -\frac{5}{6} C_\alpha - U + \begin{cases} U, & U = 0 \\ \frac{P}{3U}, & U \neq 0 \end{cases}, \quad W = \sqrt{C_\alpha + 2Y},$$

and we have the following solutions to Eq. (4.1.14)

$$\left\{ \begin{array}{l} \omega_1 = \frac{W + \sqrt{-\left(3C_\alpha + 2Y + \frac{2C_\beta}{W}\right)}}{2}, \\ \omega_2 = \frac{W - \sqrt{-\left(3C_\alpha + 2Y + \frac{2C_\beta}{W}\right)}}{2}, \\ \omega_3 = \frac{-W + \sqrt{-\left(3C_\alpha + 2Y - \frac{2C_\beta}{W}\right)}}{2}, \\ \omega_4 = \frac{-W - \sqrt{-\left(3C_\alpha + 2Y - \frac{2C_\beta}{W}\right)}}{2}. \end{array} \right. \quad (4.1.15)$$

The dispersion relation, calculated with the parameters based on Anderson and McCreary (1985), as listed in Table 4.1.1, is shown in Fig. 4.1.2. The first two roots are real, which represent stable waves (Fig. 4.1.2a). For long waves, the phase speeds are very large, but the group velocities are small, while for short waves, both phase speeds and group velocities approach twice those of Kelvin waves (Fig. 4.1.2c). The solutions ω_3 and ω_4 are conjugate imaginary parts; ω_3 has a logarithmically increasing rate and ω_4 has the contrasting damping rate. The real parts of ω_3 and ω_4 are very close to a Rossby wave (Fig. 4.1.2b), which always has a westward phase speed and has a westward group velocity for long waves but an eastward group velocity for short waves (Fig. 4.1.2d). Note that for the imaginary solutions, the group

Parameter (unit)	α (m ² /s ³)	r (1/s)	γ (kg/m ² /s)	ρ_0 (kg/m ³)	H (m)	λ (m ² /K/s)
Value	0.05	5×10^{-5}	0.012	1000	100	10^5

Table 4.1.1 Parameters used in the analytical solutions. They are selected based on Anderson and McCreary (1985).

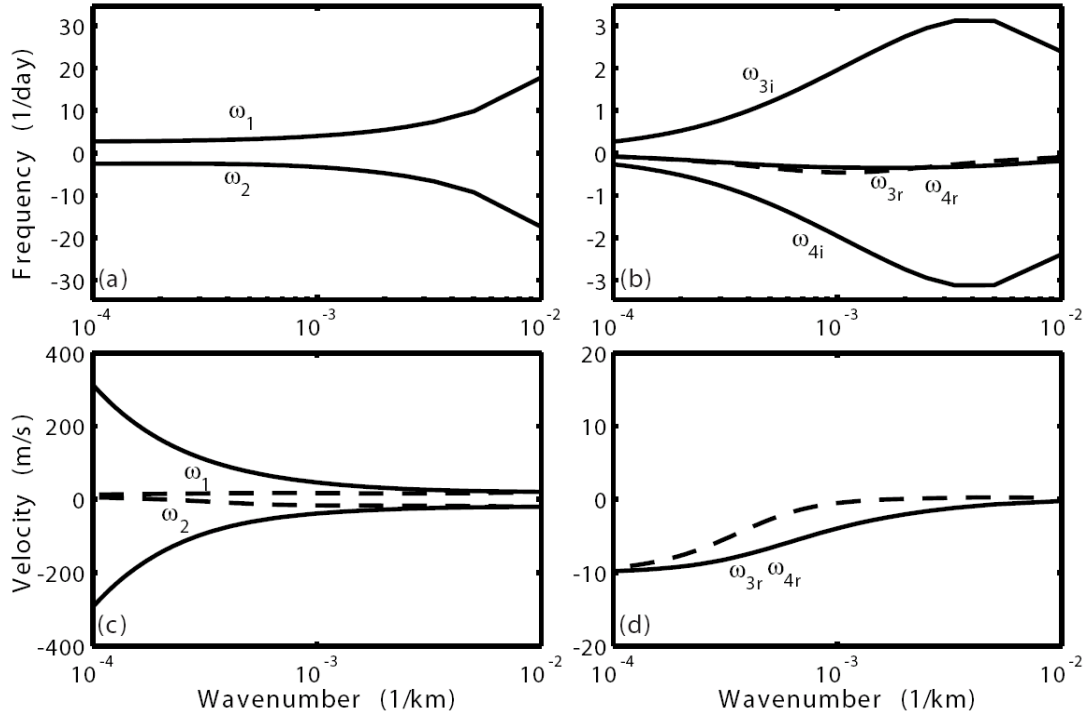


Figure 4.1.2 (a) Dispersion relations of the solutions ω_1 and ω_2 to Eq. (4.1.13). (b) Dispersion relations of the solutions ω_3 and ω_4 . The dashed line is the dispersion relation of the theoretical Rossby waves. (c) and (d) show the phase speeds (solid lines) and group velocities (dashed lines) of the corresponding solutions. The subscript r stands for the real parts of the solutions and the subscript i stands for the imaginary parts of the solutions.

velocity is $\partial\omega_r/\partial k$, where ω_r is the real part of ω . We should note here that the form of dispersion relations in Wheeler and Kiladis (1999, WK99 hereafter), which showed positive ω versus positive and negative k , has been widely used. In fact, the dispersion relation form shown in Figs. 4.1.2a and 4.1.2b is equivalent to those of WK99. Suppose $(+k, -\omega)$ is a solution to Eq. (4.1.13), it is obvious that $(-k, +\omega)$ is also a solution. Therefore, one can easily compare the dispersion relations in Fig. 4.1.2 and those of WK99, via rotating the $(+k, -\omega)$ part by 180° with respect to the origin (not shown). This is also true for the dispersion relations shown below. The Hovemueller diagrams of the solutions with an initial unit amplitude and a

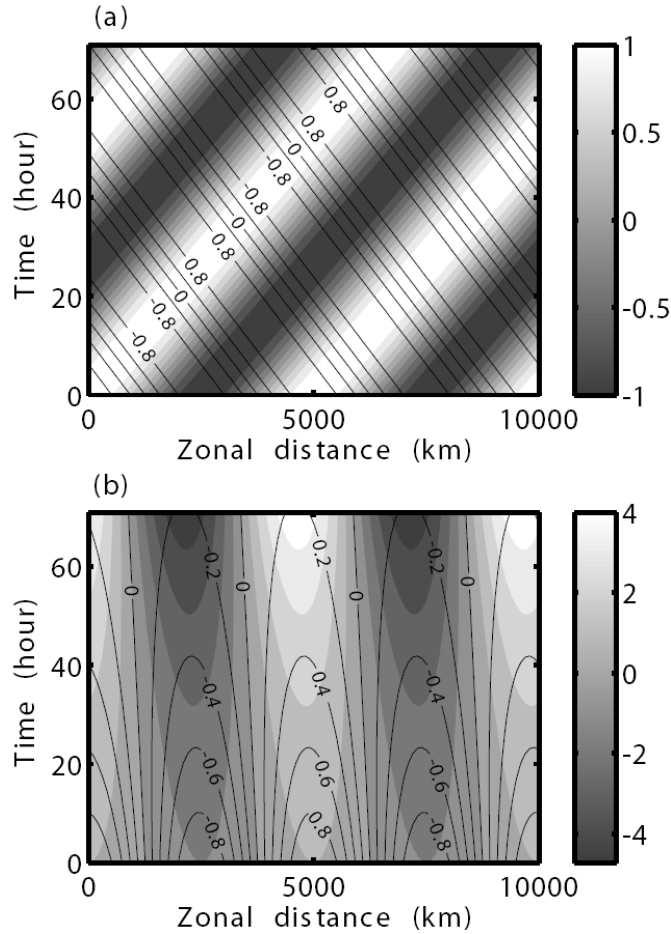


Figure 4.1.3 Hovemueller diagram of the solutions to Eq. (4.1.13) with an initial unit amplitude and a wavelength of 5000 km at the equator ($y = 0$). (a) ω_1 (gray scale) and ω_2 (contour). (b) ω_3 (gray scale) and ω_4 (contour).

wavelength of 5000 km at the equator ($y = 0$) are shown in Fig. 4.1.3. The initial unit amplitude is also used in the following Hovemueller diagrams. The stable solution ω_1 (ω_2) propagates eastward (westward) with unchanged amplitudes (Fig. 4.1.3a). As shown in Fig. 4.1.3b, the phase speeds and the group velocities of the other two solutions are westward and the group velocities are much slower than the phase speeds. The amplitude of the unstable solution ω_3 increases logarithmically, while that of ω_4 decreases logarithmically. Because the solutions are obtained under the assumption that the spatial and temporal scales in the ocean and the atmosphere are

the same, the oceanic and the atmospheric oscillations travel at the same speed. Moreover, the westward group velocities are much smaller than the eastward ones, thus the ocean and the atmosphere have enough time to interact with each other. All of these favor the resonance. As a result, both the ocean and the atmosphere become unstable.

4.1.2.3 Solutions with different ω and k in the ocean and the atmosphere

Next, we examine what happens if the oscillations in the ocean and the atmosphere have different periods and wavelengths. Representing the wave properties in the ocean with a subscript o , i.e., ω_o and k_o , and the wave properties in the atmosphere with a subscript a , i.e., ω_a and k_a . Eq. (4.1.11) is re-written as

$$\begin{cases} \left[\frac{\omega_o^3}{c^2} - \left(k_o^2 + \frac{\beta}{c} \right) \omega_o - \beta k_o \right] k_o \lambda T_0 = \frac{k_a^2 \gamma}{\rho_0 H} U_0, \\ -i k_a \left[\omega_a^2 - c^2 k_a^2 - r^2 - (\beta y)^2 \right] U_0 + \frac{\omega_a k_a}{r} \left[c^2 k_a^2 + 2r^2 \right] U_0 = \alpha (k_o^2 + l_o^2) \Gamma_0. \end{cases} \quad (4.1.16)$$

Again, similar to Eq. (4.1.12), in order to have non-trivial solutions, the following condition has to be satisfied;

$$\begin{cases} \frac{\omega_o^3}{c^2} - \left(k_o^2 + \frac{\beta}{c} \right) \omega_o - \beta k_o - \frac{\alpha r \gamma k_a}{\omega_a \rho_0 H \lambda (c^2 k_a^2 + 2r^2)} \frac{(k_o^2 + l_o^2)}{k_o} = 0 & (4.1.17a), \\ \omega_a^2 - c^2 k_a^2 - r^2 - (\beta y)^2 = 0 & (4.1.17b). \end{cases}$$

Comparing Eqs. (4.1.17a) and (4.1.3), the only difference is the last term on the left hand side of Eq. (4.1.17a), which contains all the coupling parameters and the atmospheric properties. Note that c in the ocean and the atmosphere is assumed the same. Actually, the phase speed in the atmosphere only appear in the term

$(c^2 k_a^2 + 2r^2)$ and $2r^2$ is larger than $c^2 k_a^2$, because k_a is small (a long wavelength is assumed in the atmosphere). Thus, using different c for the atmosphere does not change the denominator significantly and the following analyses of Eq. (4.1.17a) are still valid. If we neglect l_o and define $\beta_c = \frac{\alpha r \gamma k_a}{\omega_a \rho_0 H \lambda (c^2 k_a^2 + 2r^2)}$, Eq. (4.1.17a) can be re-written as

$$\frac{\omega_o^3}{c^2} - \left(k_o^2 + \frac{\beta}{c} \right) \omega_o - (\beta + \beta_c) k_o = 0 \quad (4.1.18),$$

which has the same form as Eq. (4.1.3). Now the discriminant of Eq. (4.1.18) becomes $\Delta = 4 \left(k_o^2 + \frac{\beta}{c} \right)^3 - 27 \frac{[(\beta + \beta_c) k_o]^2}{c^2}$. The sign of β_c is determined by the sign of ω_a , since all other terms are positive. Because the discriminant for Eq. (4.1.3) is always positive if β_c is negative, i.e. $\omega_a < 0$, the discriminant of Eq. (4.1.18) remains positive. As a result, the solutions to Eq. (4.1.18) are all real, which means no unstable waves occur. Therefore, eastward waves in the atmosphere ($\omega_a > 0$) are required to have unstable waves in the coupled system. As discussed above, the discriminant Δ around $k_o = R_D^{-1}$ easily goes negative, so that the solutions can easily become imaginary, which physically indicates that the oceanic oscillations with a wavelength similar to R_D are more prone to go unstable. The variation in β_c with respect to k_a is shown in Fig. 4.1.4. For short waves in the atmosphere, β_c is comparable with β , while for long waves, β_c is much smaller than β . Therefore, at a given k_o , it is easier for short atmospheric waves to lead to a negative discriminant, which indicates imaginary solutions and unstable waves. Note that this conclusion

cannot be extended to its limit, because for very short waves in the atmosphere, Eq. (4.1.9) is not applicable, e.g. the Coriolis force becomes less important and horizontal advection needs to be considered.

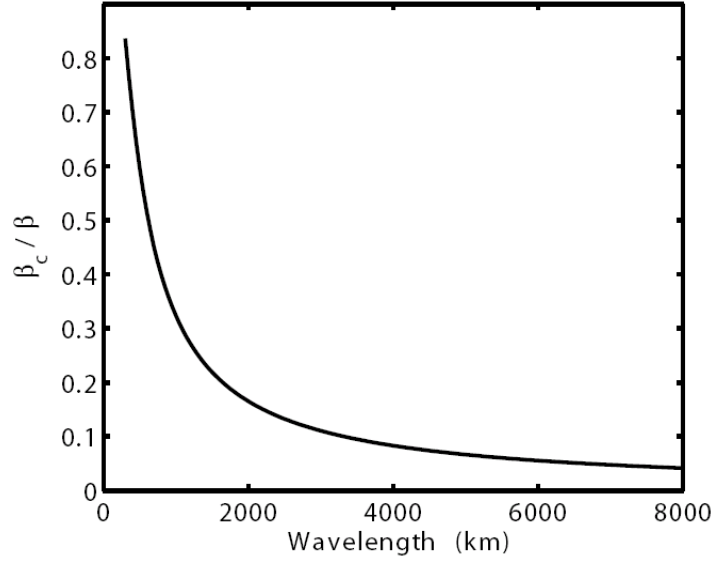


Figure 4.1.4 Ratio between β_c and β , with respect to the wavelength in the atmosphere.

Eq. (4.1.18) can be solved analytically. Let

$$A = \frac{1}{c^2}, B=0, C = -\left(k_o^2 + \frac{\beta}{c}\right), D = -\beta k_o - \frac{\alpha r \gamma k_a}{\omega_a \rho_0 H \lambda k_o} \frac{(k_o^2 + l_o^2)}{c^2 k_a^2 + 2r^2},$$

the depressed cubic equation,

$$A\omega_o^3 + C\omega_o + D = 0 \dots (4.1.19),$$

can be solved as follows (Tignol 2001, Chapter 2). Let $Q = \frac{C}{3A}$, $R = -\frac{D}{2A}$,

$s = \sqrt[3]{R + \sqrt{Q^3 + R^2}}$, and $t = \sqrt[3]{R - \sqrt{Q^3 + R^2}}$, the solutions to Eq. (4.1.19) are

$$\begin{cases} \omega_{o1} = s + t - \frac{B}{3A}, \\ \omega_{o2} = -\frac{1}{2}(s+t) - \frac{B}{3A} + \frac{\sqrt{3}}{2}(s-t)i, \\ \omega_{o3} = -\frac{1}{2}(s+t) - \frac{B}{3A} - \frac{\sqrt{3}}{2}(s-t)i. \end{cases} \quad (4.1.20)$$

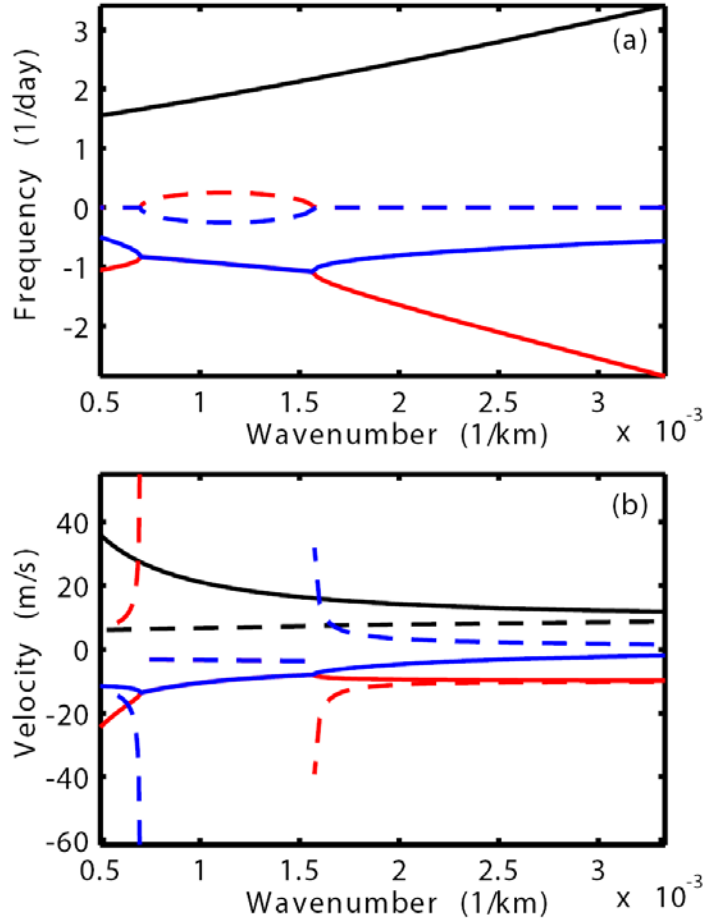


Figure 4.1.5 (a) Dispersion relations of the solutions to Eq. (4.1.18) with the wavelength of 6000 km in the atmosphere. Solid lines represent the real parts and dashed lines represent the imaginary parts. (b) The corresponding phase speeds and group velocities, solid lines for phase speeds and dashed lines for group velocities. Black lines are for ω_{o1} , red lines are for ω_{o2} , and blue lines are for ω_{o3} .

Applying the same parameters listed in Table 4.1.1, one real root and two conjugate imaginary roots are obtained. The dispersion relations and the corresponding phase speeds and group velocities are shown in Fig. 4.1.5. ω_{o1} is a real solution and

represents a stable wave. It propagates eastward, in the same direction as the atmospheric waves (as discussed above, ω_a has to be positive). The other two solutions are imaginary, ω_{o2} increases with time, while ω_{o3} decreases with time.

Because $B = 0$ and Eq. (4.1.19) is a depressed cubic equation, adding the three solutions of Eq. (4.1.20), one has the following relation

$$\omega_{o1} + \omega_{o2} + \omega_{o3} = 0 \quad (4.1.21).$$

Dividing this equation with k_o and taking a derivative with respect to k_o , one obtains that the sum of the phase speeds and the group velocities of the three solutions are also zero. These balances (especially the last one) imply that there is energy transfer among the three oceanic waves. As shown in Fig. 4.1.6, the amplitude of wave ω_{o1} does not change with time, thus it is not clearly seen in terms of energy transfer. However, it is still not negligible for the validity of the above balances. In addition, it is the only one in the three solutions that propagates eastward, which can exchange energy directly with the eastward-propagating atmospheric waves. The other two solutions propagate westward at the same phase speed and group velocity. The energy is transferred from one wave to the other. As a result, one wave grows exponentially while the other one decays exponentially. The amplitude of wave ω_{o2} increases during its westward propagation. Therefore, it is able to lead to detectable instabilities with large amplitudes in the western part of an ocean basin. This is qualitatively similar to the westward-propagating waves in the Indian Ocean, which lead to instabilities in the western Indian Ocean (Xie et al. 2002; Section 2.2). The period of $2\pi/\omega_{o2i}$, where ω_{o2i} is the imaginary part of the imaginary root, with respect to the wavelengths in the ocean and the atmosphere is shown in Fig. 4.1.7. As described

above, the imaginary solutions (i.e. unstable waves) are centered on R_D in the ocean. At any given oceanic wavenumber (k_o), the short atmospheric oscillations more easily lead to unstable waves (blank region in Fig. 4.1.7). One can see that the oscillations in the two media with similar wavelengths ($\sim 10^3$ km) can interact with each other and lead to instability. But what's interesting is that the large-scale oscillations (\sim thousands of kilometers) in the atmosphere can interact with the relatively small-scale oscillations (\sim hundreds of kilometers) in the ocean and lead to unstable waves in the intraseasonal band.

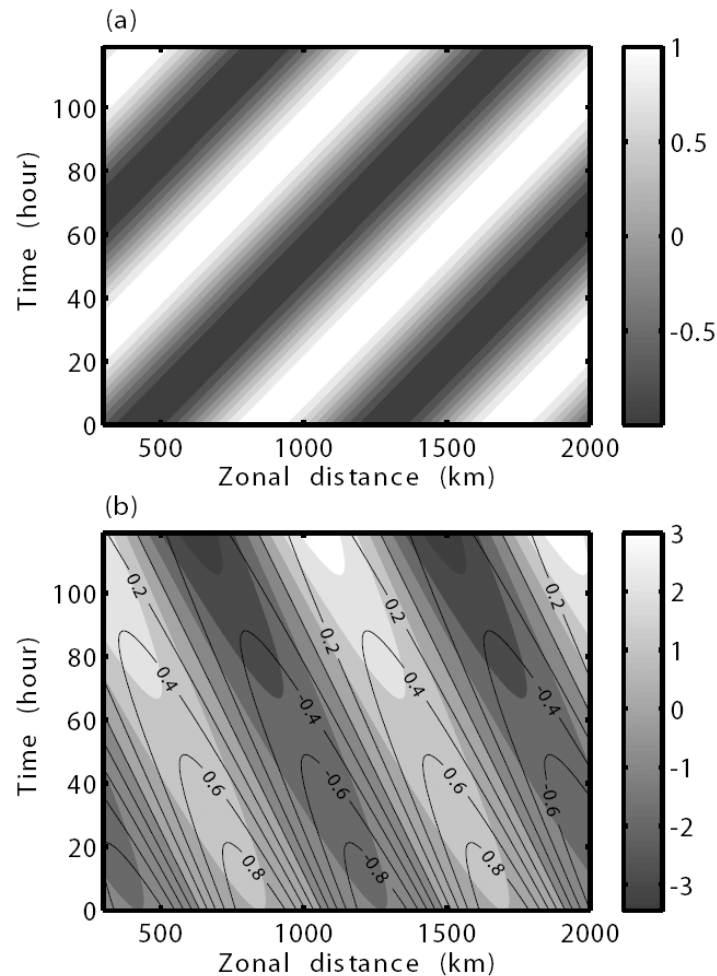


Figure 4.1.6 Hovemueller diagram of the solutions to Eq. (4.1.18) with an initial unit amplitude at the equator ($y = 0$). The wavelength in the atmosphere is 6000 km and that in the ocean is 850 km. (a) ω_{o1} , (b) ω_{o2} (gray scale) and ω_{o3} (contour).

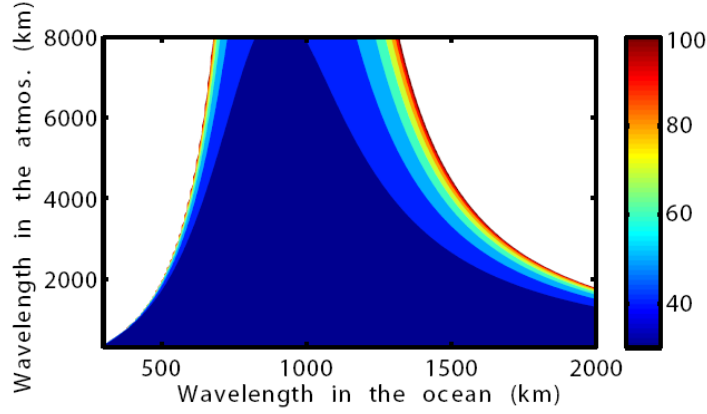


Figure 4.1.7 Period of $2\pi/\omega_{o2i}$ with the unit of day. The blank region represents that $\omega_{o2i} = 0$, i.e. the solution ω_{o2} is a real solution with these parameters.

Substituting Eq. (4.1.17b), $c^2 k_a^2 = \omega_a^2 - r^2 - (\beta y)^2$, into Eq. (4.1.17a), we have

$$\omega_a^3 + \left[r^2 - (\beta y)^2 \right] \omega_a - \frac{\alpha r \gamma k_a}{\rho_0 H \lambda k_o} \frac{(k_o^2 + l_o^2)}{\frac{\omega_o^3}{c^2} - \left(k_o^2 + \frac{\beta}{c} \right) \omega_o - \beta k_o} = 0 \quad (4.1.22).$$

Let $A=1$, $B=0$, $C = r^2 - (\beta y)^2$, and $D = -\frac{\alpha r \gamma k_a}{\rho_0 H \lambda k_o} \frac{(k_o^2 + l_o^2)}{\frac{\omega_o^3}{c^2} - \left(k_o^2 + \frac{\beta}{c} \right) \omega_o - \beta k_o}$, the

depressed cubic equation $A\omega_a^3 + C\omega_a + D = 0$ can be solved in the same way with the same parameters as above. Note that all c in Eq. (4.1.22) are the phase speed in the ocean. Thus using different c in the atmosphere has no influence on the following analyses on Eq. (4.1.22). The dispersion relations and the corresponding phase speeds and group velocities are shown in Fig. 4.1.8. All three solutions are imaginary. The atmospheric wave ω_{a1} (black lines in Fig. 4.1.8, note that the subscript is a , not o) propagates eastward and grows with time, the wave ω_{a2} (red lines in Fig. 4.1.8) also propagates eastward but decays with time, and the wave ω_{a3} (blue lines in Fig. 4.1.8) propagates westward and decays at a much slower rate. Because Eq. (4.1.22) is also a

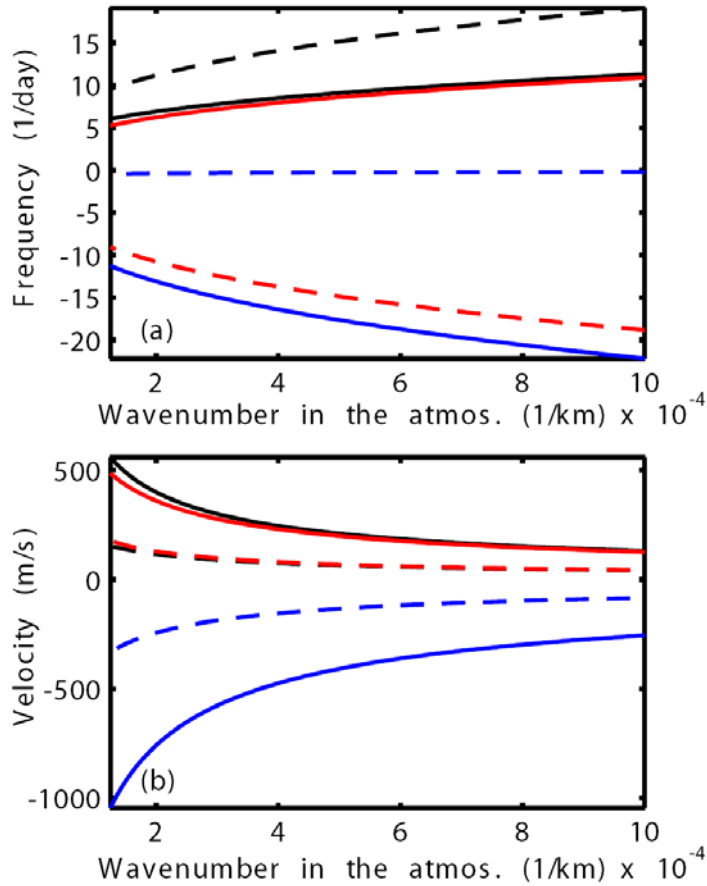


Figure 4.1.8 (a) Dispersion relations of the solutions to Eq. (4.1.22) with the wavelength of 850 km in the ocean. Solid lines represent the real parts and dashed lines represent the imaginary parts. (b) The corresponding phase speeds and group velocities, solid lines for phase speeds and dashed lines for group velocities. Black lines are for ω_{a1} , red lines are for ω_{a2} , and blue lines are for ω_{a3} .

depressed cubic equation, the above balances for the oceanic waves are also valid for the three atmospheric waves. Therefore, as shown in the Hovemueller diagrams in Fig. 4.1.9, energy is mainly transferred between two eastward-propagating waves (ω_{a1} and ω_{a2}). The westward-propagating wave (ω_{a3}) also provides small amount of energy to the growing wave ω_{a1} , since it decays very slowly (dashed blue line in Fig. 4.1.8a). Note however that ω_{a1} grows too fast (Fig. 4.1.9b). Such fast growing waves cannot be well described with the linear equations used in this study. As for wave

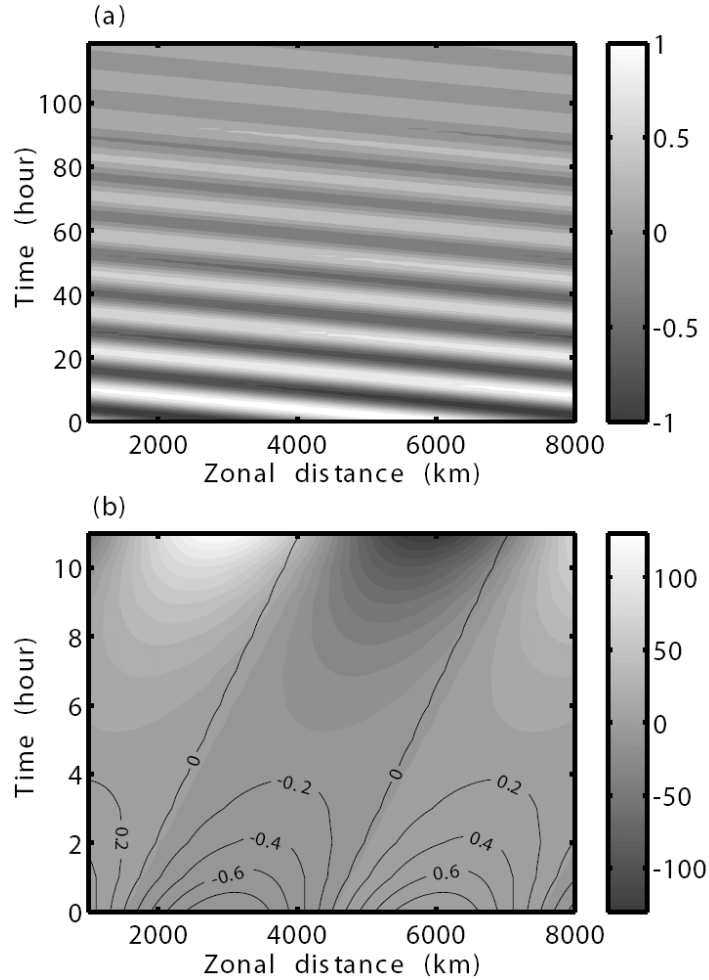


Figure 4.1.9 Hovemueller diagram of the solutions to Eq. (4.1.22) with an initial unit amplitude at the equator ($y = 0$). The wavelength in the atmosphere is 6000 km and that in the ocean is 850 km. (a) ω_{a3} , (b) ω_{a1} (gray scale) and ω_{a2} (contour).

ω_{a3} , it propagates westward and decays in the intraseasonal time scale due to downscale or upscale energy transfer (Biello and Majda 2005). It is qualitatively similar to the behavior of MJOs in the tropical regions. Similar to Fig. 4.1.7, the period of $2\pi/\omega_{a3i}$, where ω_{a3i} is the imaginary part of the imaginary root, is shown in Fig. 4.1.10 as a function of the wavelengths in the ocean and the atmosphere. The oceanic oscillations can feedback to the atmospheric counterparts with a similar scale ($\sim 10^3$ km). It is also clear and more striking that the meso-scale oceanic variabilities

with a wavelength of hundreds of kilometers can feedback to the large-scale atmospheric variabilities with a wavelength of thousands of kilometers, leading to intraseasonal oscillations in the atmosphere.

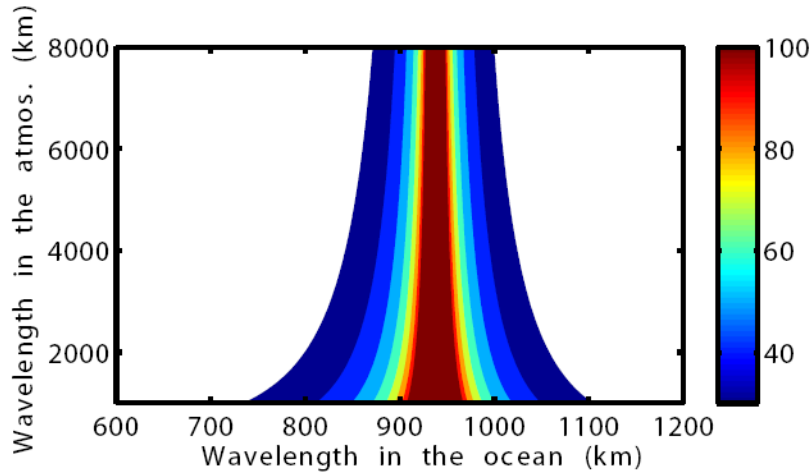


Figure 4.1.10 Period of $2\pi / \omega_{a3i}$ with the unit of day.

4.1.3 Discussion on the approximations

Simple oceanic and atmospheric model assumptions are applied in this study to understand potential coupling at intraseasonal time-scales. Although these are probably not the only choices, they are suitable for testing our hypothesis that scale similarity is not necessary for the ocean-atmosphere coupling. In the present model, no boundaries are considered. Actually, the size of the ocean basin can also influence the period and spatial pattern of the ocean-atmosphere coupled mode (Zebiak 1993).

In order to obtain the analytical solutions, many approximations are made above. However, they are chosen carefully based on previous works and scale analysis, so that they support the validity of the extension of these results. Because the purpose of this paper is to examine whether oceanic and atmospheric processes with different scales can interact with each other in a linear framework, the whole dynamical set of

equations are linearized by applying some approximations, such as $Q = \alpha T$ and $T = m\eta$, which were used in previous theoretical studies on ocean-atmosphere interactions (e.g. Hirst 1986). For wind stress, the linear relation of $\tau_x = \gamma U$ is used, which is similar to what was used by Anderson and McCreary (1985). This equation can be regarded as a linear approximation of the nonlinear bulk formula $\bar{\tau} = \rho_a C_D |\bar{U}| \bar{U}$. As shown with the shades in Fig. 4.1.1, in the tropical Pacific and the Atlantic Oceans, the variability (represented with standard deviations) of the surface zonal winds is significantly smaller than the climatological mean, which implies that the above linearization (replacing one \bar{U} with its climatological mean in the bulk formula) do not lead to dramatic errors. Another notable approximation is the geostrophic balance between v and η . For Eq. (4.1.1a), in the tropics, $f = f_0 + \beta y \approx \beta y$ is much larger than the $\partial/\partial t$ term at intraseasonal time scales (~ 30 -60 days). Therefore, this approximation is justifiably applicable for the intraseasonal oscillations in the tropics.

The parameters (Table 4.1.1) used in this study are chosen based on Anderson and McCreary (1985). In Eqs. (4.1.13, 4.1.17, and 4.1.22), the combination of the parameters are all in a form of $X = \frac{\alpha r \gamma}{H \lambda}$. The three equations are also solved with a

50% change in X . We increase α , r , γ by 10% and reduce H , λ by 10%, thus

$$X' = \frac{\alpha r \gamma (1 + 0.1)^3}{H \lambda (1 - 0.1)^2} \approx (1 + 0.5)X. \text{ We also reduce } \alpha, r, \gamma \text{ by 10\% and increase } H, \lambda$$

by 10%, thus $X'' \approx (1 - 0.5)X$. In both cases, the similar solutions are obtained (not

shown) and the same conclusions can be drawn. Therefore, the above solutions are not sensitive to the choice of these parameters.

Since the coupled equations are homogeneous equations, only the dispersion relations can be derived and the amplitudes of the variables cannot be determined. In reality, there are oscillations with various spatial and temporal scales in the ocean and the atmosphere, thus much more complicated ocean-atmosphere coupling may be expected even in the linear framework. Although the model is idealized and the analytical solutions are subject to many approximations, it demonstrates that the possibility of ocean-atmosphere coupling between processes with different scales cannot be excluded before further careful studies.

4.1.4 Conclusions

It is well known that the oscillations with various frequencies and wavenumbers can interact via some nonlinear mechanisms, such as the resonant interaction (Pedlosky 1987). The question proposed in the introduction is whether oscillations with different temporal and spatial scales can interact with each other and lead to instabilities in both the ocean and the atmosphere in a linear framework. With simple but widely used dynamic equations in the ocean and the atmosphere, the possibility is examined. The uncoupled ocean and atmosphere are stable as briefly introduced with the dispersion relations in Eqs. (4.1.3) and (4.1.4). When the ocean and the atmosphere are coupled, instabilities evolve. If the periods and wavelengths are required to be the same, unstable waves are generated due to resonance. When the requirement of similar scales is relaxed, as shown in Figs. 4.1.7 and 4.1.10, one can also see interactions with comparable scales. However, the interesting results are the

interactions between different scales. As a response to large-scale eastward-propagating atmospheric waves, there are meso-scale oceanic waves, one propagating eastward and two westward. One of the westward-propagating oceanic waves grows during its propagation and is expected to lead to instabilities in the western part of an ocean basin. These meso-scale oceanic waves can also feedback to large-scale atmospheric waves. There is one eastward-propagating wave, which decays at intraseasonal time scales. For the latter mechanism, variabilities internal to the ocean and the atmosphere are also critical processes for the ocean-atmosphere interactions. Such a coupling pattern is qualitatively comparable to the SST-MJO interaction, in which the large-scale MJOs propagate eastward in the atmosphere decaying over the eastern Pacific Ocean (Madden and Julian 1994) and the meso-scale oceanic properties propagate westward leading to instabilities in the western Indian Ocean (Xie et al. 2002; Section 2.2). Of course, the analytical solutions cannot simulate the real SST-MJO interactions and they cannot be quantitatively compared with the observations, because, for example, the vertical structure of MJOs is dominated by the first baroclinic mode, while the model in this study is only a barotropic one and the interactions via meridional transports are excluded. Thus, more detailed and realistic model experiments are needed for further test of the application of this mechanism in the future.

We propose that there are probably two types of ocean-atmosphere interactions. One, the traditional one, is like a piston interaction, as sketched in Fig. 4.1.11a. The spatial and temporal scales of the oscillations both in the ocean and the atmosphere are nearly the same. Instabilities are mainly triggered by the resonance, viz. the equal

of the forcing scales and the intrinsic scales. The other one, which is discussed in this study, is like a gear interaction, as sketched in Fig. 4.1.11b. The spatial and temporal scales of the oscillations in the ocean and the atmosphere are distinct from each other. However, instabilities can be triggered when the combination of the temporal and

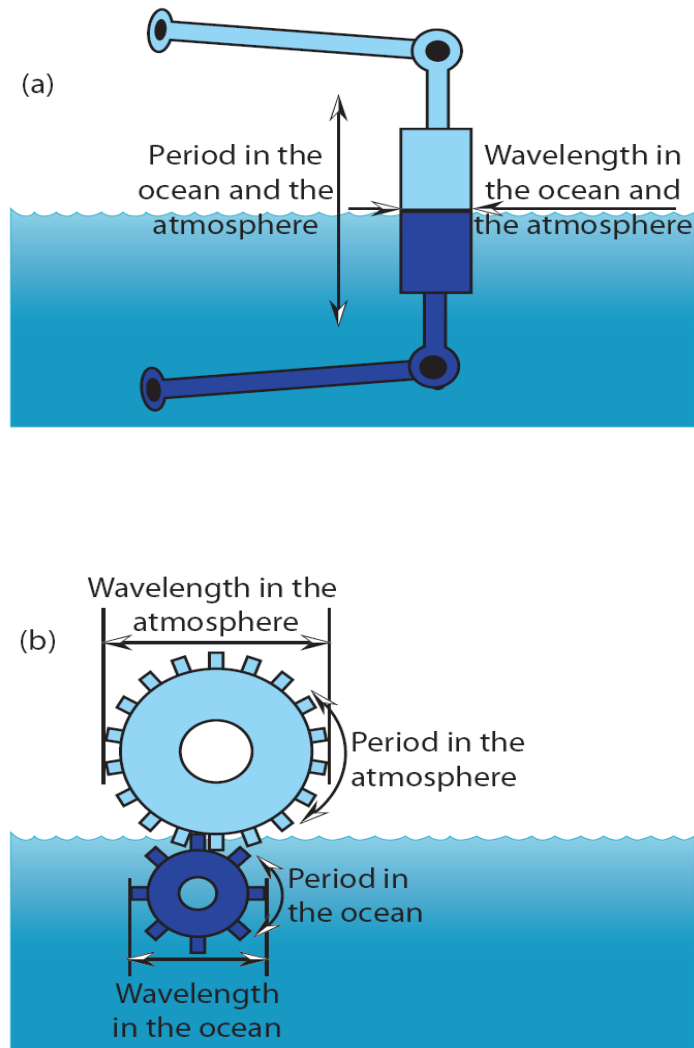


Figure 4.1.11 Sketches of the proposed two types of ocean-atmosphere interactions. (a) Piston-like coupling, in which the oceanic and atmospheric oscillations have similar temporal and spatial scales. (b) Gear-like coupling, in which the oceanic and atmospheric oscillations have different temporal and spatial scales.

spatial scales of the forcing matches the combination of the intrinsic oscillations, viz. when the dispersion relation of the oceanic and the atmospheric oscillations match each other.

4.2 Frequency shifts in the ocean and the atmosphere in response to small forcing changes

Abstract

The response of the ocean and an atmosphere system to small external forcing is studied with theoretical and numerical models. The external forcing is prescribed to be so small that the oscillation periods of response are not completely controlled by the period of external forcing, and thus the intrinsic properties of the system cannot be neglected. It is found that a small forcing can generate two kinds of deviations from the intrinsic oscillations in the ocean and the atmosphere. One is a frequency shift, which is continuously dependent on continuous forcing changes. The other one is an appearance of new oscillations or the disappearance of existing oscillations, which is the discontinuous response to continuous forcing. The two responses are determined by the intrinsic properties of the ocean and the atmosphere, which is represented with a function $F(\omega; k)$, defined in this study. Specifically, the amplitude of frequency shift is influenced by $\partial F(\omega; k)/\partial \omega$. The period of the discontinuous response is determined by the position of its turning point ω_p and the possibility that the discontinuous response can occur is determined by the distance between $F(\omega_p; k)$ and zero. Both continuous and discontinuous responses to small external forcing are able to cause irregularity in the oceanic and the atmospheric oscillations, even in a linear framework. Thus, this study provides an alternative way to examine the irregularity in the natural oscillations, in contrast to previous studies that invoke

nonlinear and stochastic effects. These findings have implications for a range of observed phenomena including ENSO and the Madden-Julian Oscillations.

4.2.1 Introduction

4.2.1.1 Motivation

Many natural phenomena in the coupled ocean-atmosphere system span a wide range in the frequency domain. For example, the period of ENSO is about 2-7 years (Jiang et al. 1995) and the period of Madden-Julian Oscillations (MJOs) is 30-60 days (Madden and Julian 1971, 1972, 1994, 2005). These frequency bands have been well documented with observations. Usually, the frequency variations from one event to the other are regarded as an important factor in the irregularity of these oscillations. There have been many studies on this topic addressing the difficulty in simulating these irregularities in the ocean-atmosphere GCMs (Neelin et al. 1998; Slingo et al. 1996). As a result, potential predictability levels at both weather and climate time-scales are often not achieved by the models (Chen et al. 2004; Waliser 2005). Numerous studies have focused on better understanding the irregularities by examining the stochastic and nonlinear effects (e.g. Roulston and Neelin 2000; Moore and Kleeman 1998; Sardeshmukh and Sura 2007; Kleeman 2008). Jin et al. (1994) and Tziperman et al. (1994) studied a nonlinear, theoretical model to explain irregularity in the frequency of ENSO by low-order deterministic chaos. This hypothesis was tested with an intermediate ENSO prediction model (Zebiak and Cane 1987) and it was found that the irregularity of model ENSO events was attributable to the chaos driven by the seasonal cycle when the nonlinearity in the model was large enough (Tziperman et al. 1995). Kleeman and Moore (1997) studied a linear

stochastic differential equation and argued that irregularity of ENSO was due to the stochastic transients in zonal wind stresses. With an intermediate coupled model, Flügel et al. (2004) also revealed that the ENSO predictability was related to the spatial structures of the uncoupled atmospheric noise in wind stresses. However, by conducting retrospective forecast experiments with an intermediate coupled model, Chen et al. (2004) claimed that the self-sustaining internal dynamics, rather than the stochastic forcing or the atmospheric noise, were of the most importance for the predictability of ENSO events. For MJOs, there are still substantial deficiencies in model simulations, such as a shorter periodicity and a more regular seasonality in the model than in observations (Sperber et al. 1997; Slingo et al. 1996; Lin et al. 2006). Therefore, it is believed that there is significant scope for improving the MJO simulations via a better understanding and resolving the irregularity of MJOs (Waliser et al. 2003b; Zhang 2005). Nonlinearity and stochasticity are also supposed to be the major contributors to the irregularity of MJOs. For example, the theories of nonlinear wave-CISK (Lau and Peng 1987) and nonlinear WISHE (wind induced surface heat exchange; Xie et al. 1993; Maloney and Sobel 2004) have been proposed, while Biello and Majda (2005) built a multi-scale MJO model with stochastic parameters, and Jones (2009) established an empirical stochastic model to simulate the irregularity of MJOs.

With an idealized coupled ocean-atmosphere model, we showed that the oceanic and the atmospheric oscillations with different temporal and spatial scales can interact with each other in a linear framework (Section 4.1; Zhou and Murtugudde 2009). With no nonlinearity and stochastic forcing, the idealized theoretical coupled system

produced unstable oscillations in the intraseasonal band (30-60 days). This finding provides a different point of view for studying the irregular oscillations in contrast to the earlier ideas on the role of stochastic and nonlinear effects. If, for example, the variations at other frequencies can influence the intraseasonal time-scale in a linear and deterministic system, they can possibly contribute to the frequency differences from one MJO event to another. As a result, we may have oscillations spanning a large frequency band even without strong nonlinear or stochastic effects; some irregularities may be attributable solely to linear dynamics. This is the motivation for the current study, keeping in mind the significant implications for the understanding of processes and predictability of these observed phenomena.

4.2.1.2 A brief review of the simplest forced ocean system: Inertial oscillation

Our hypothesis is first examined by an analysis of the equation for forced inertial oscillations. The inertial oscillation due to Earth's rotation can be expressed as $d^2u/dt^2 + f^2u = 0$ (Gill 1982), where u is the zonal velocity and f is the Coriolis parameter, i.e., the intrinsic frequency of Earth's rotation. Assume there is a forcing $E(t)e^{i\sigma t}$, which includes both external forcing and friction (the specific forms of the forces are not important in our study, thus the external forcing and friction are represented with a combined format, see more discussion of this in Section 4.2.2.1). The general solution to the forced equation is

$$u = Ae^{ift} + Be^{-ift} + \frac{E}{f^2 - \sigma^2} e^{i\sigma t} \quad (4.2.1),$$

where A and B are arbitrary amplitudes of the internal oscillations. For a very strong forcing, viz. the amplitude of forcing (E) much larger than those of internal oscillations (A and B), the frequency of the forced motion is controlled by the frequency of the forcing σ . In the special case where $\sigma = f$, a resonance occurs. However, what we focus on in this study is a small forcing (E is smaller than A or B) to the internal oscillations, which is relatively common in nature. In this case, the internal oscillations (Ae^{ift} and Be^{-ift}) dominate the forced motion and the external forcing leads to a moderate adjustment. Therefore, we can assume a slowly-varying solution $u = U(t)e^{i\omega t}$, which satisfies $|dU/dt| \ll |U|$ and $|d^2U/dt^2| \ll |U|$. Applying the WKB approximation (Garrett 2001; Pedlosky 2003), we obtain the dispersion relation $\omega^2 = f^2 - \varepsilon$, where $\varepsilon = Ee^{i(\sigma-\omega)t}/U$ is a small term due to the weak external forcing. It is obvious that the response frequency ω is distinct from the intrinsic frequency f of the system, although the deviation is relatively small. We do not intend to argue that the above small deviation is the major mechanism for the well-observed, near-inertial oscillations in the deep ocean, which actually have many more complex processes involved, such as the equatorward propagation and the β -effect as summarized in Garrett (2001). Nevertheless, a brief review of this very simple forced oscillatory system leads to a justifiable assumption that, with a small perturbation, the response frequency can be clearly distinct from the intrinsic frequency or the forcing frequency, due to the modification by the external forcing. Actually, in a more complex system, this assumption can be extended to the dispersion relation, which is a combination of frequency and wavenumber.

In Section 4.2.2.1, this assumption is shown to be justifiable with an idealized theoretical model. Then it is tested in an ocean model with very simple and idealized configurations in Section 4.2.2.2. For demonstration purposes, possible complications which may be caused by details such as nonlinearities, baroclinic and boundary effects, and large gradients in ocean fronts, are avoided. Thus the ocean model results can be compared with the analytical solutions in Section 4.2.2.1 and clearly support the assumption. Nevertheless, they cannot be directly compared with any observations. In Section 4.2.3, this assumption is tested in both the ocean model and the atmosphere model with much more realistic configurations, in order to show its possible realistic application. The influence of intraseasonal wind stress anomalies (similar to MJOs) on the tropical Pacific Ocean is used as an example for the oceanic response to the atmospheric forcing, while the influence of meso-scale sea surface temperature (SST) anomalies in the Indian Ocean on two MJO events is used as an example for elucidating the atmospheric response. Since the model configurations in this section are pretty realistic, the simulated oceanic and atmospheric responses can be qualitatively compared against observations. We are aware that these model results cannot be totally attributed to the proposed mechanism, because the nonlinearity and processes such as the vertical convection are included in the model configurations (but there is no stochastic effect). However, since we only alter the external forcing in different model runs, viz., the intraseasonal wind stress anomalies and the meso-scale SST anomalies, we believe the proposed mechanism is a major contributor to the model results discussed below. Conclusions and some discussion are presented in Section 4.2.4.

4.2.2 Theory

4.2.2.1 Theoretical model

A set of dynamic equations and the corresponding analytical solutions are used to illustrate the theory. Consider the linear and inviscid governing equations with no atmospheric forcing for the tropical ocean (Gill 1982),

$$\frac{\partial u}{\partial t} - \beta y v = -g \frac{\partial \eta}{\partial x} \quad (4.2.2a),$$

$$\frac{\partial v}{\partial t} + \beta y u = -g \frac{\partial \eta}{\partial y} \quad (4.2.2b),$$

$$\frac{\partial u}{\partial x} + \frac{\partial v}{\partial y} = -\frac{1}{H} \frac{\partial \eta}{\partial t} \quad (4.2.2c),$$

where u , v are the zonal and meridional velocities in the ocean, respectively; β is the meridional gradient of Coriolis parameter f ; g is the gravitational acceleration; η is the sea surface height (SSH) anomaly; and H is the water column depth. An equation with a single variable v can be obtained (Gill 1982; also see Section 4.1),

$$\frac{\partial^3 v}{c^2 \partial t^3} + \frac{(\beta y)^2}{c^2} \frac{\partial v}{\partial t} - \frac{\partial}{\partial t} \left(\frac{\partial^2 v}{\partial x^2} + \frac{\partial^2 v}{\partial y^2} \right) - \beta \frac{\partial v}{\partial x} = 0 \quad (4.2.3).$$

Assuming a wavelike solution, $v = v_0 \exp\left(-\frac{\beta y^2}{2c}\right) e^{i(kx - \omega t)}$, where k is the wavenumber and ω is the frequency, we obtain the dispersion relation

$$\frac{\omega^3}{c^2} - \left(k^2 + \frac{\beta}{c}\right) \omega - \beta k = 0 \quad (4.2.4).$$

Define a function,

$$F(\omega, k) = \frac{\omega^3}{c^2} - \left(k^2 + \frac{\beta}{c}\right) \omega - \beta k \quad (4.2.5),$$

where k is treated as a parameter. It is obvious that the above dispersion relation in Eq. (4.2.4) is the implicit form of the solution to $F(\omega; k) = 0$. Traditionally, when

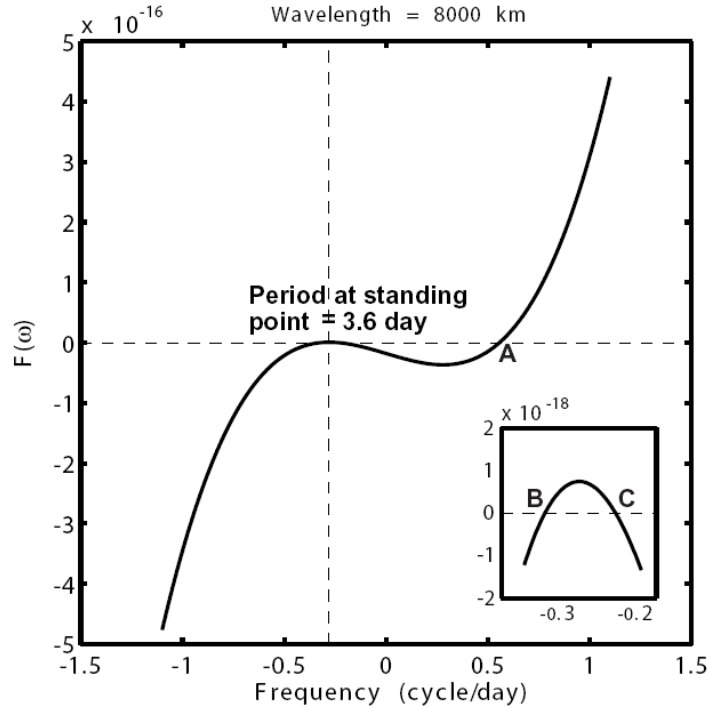


Figure 4.2.1 $F(\omega; k)$ with a wavelength of 8000 km. The embedded figure is zoomed-in around the turning point. Points A, B, and C represent the three zero-crossing points of the curve, i.e. three solutions to $F(\omega; k) = 0$. See text for the definition of $F(\omega; k)$.

studying free oscillations in the ocean, only the dispersion relation is considered. However, we will show below that when discussing the oceanic responses to moderate wind forcing, we must have a complete understanding of $F(\omega; k)$, rather than the dispersion relation, $F(\omega; k) = 0$, alone. Figure 4.2.1 shows $F(\omega; k)$ for a wavelength of 8000 km. There is one zero-crossing point, i.e., a solution, at $\omega = 0.56$ cycle day⁻¹ (Point A in Fig. 4.2.1). The turning point of $F(\omega; k)$ in Fig. 4.2.1 is at $\omega_{tp} = -0.28$ cycle day⁻¹ (a period of 3.6 days), where the subscript tp stands for the turning point. As shown in the embedded zoom-in figure, one can see that $F(\omega_{tp}; k)$

is slightly larger than zero and there is one real solution to $F(\omega; k) = 0$ (Points B and C) on each side of the turning point. Thus, there are two oscillations with relatively similar periods and thereby one can expect two peaks close to each other in the power spectrum, which can be illustrated with the following model outputs.

If the ocean system is perturbed by surface winds, the corresponding terms should be on the right hand side (RHS) of Eq. (4.2.4). For example, following Gill (1982), if a forcing term, $\tau_x / \rho H$ is added to Eq. (4.2.2a) and a forcing term, $\tau_y / \rho H$ is added to Eq. (4.2.2b), where τ_x and τ_y are the zonal and meridional wind stress, ρ is the water density, then we have a net forcing term,

$$\frac{1}{\rho H} \left[\frac{1}{c^2} \frac{\partial}{\partial t} \left(\frac{\partial \tau_y}{\partial t} - f \tau_x \right) - \frac{\partial}{\partial x} \left(\frac{\partial \tau_y}{\partial x} - \frac{\partial \tau_x}{\partial y} \right) \right],$$

on the RHS of Eq. (4.2.4). If there are frictional terms F_x and F_y on the RHS of Eq. (4.2.2a) and Eq. (4.2.2b), respectively,

$$\text{one can find a similar term, } \frac{1}{c^2} \frac{\partial}{\partial t} \left(\frac{\partial F_y}{\partial t} - f F_x \right) - \frac{\partial}{\partial x} \left(\frac{\partial F_y}{\partial x} - \frac{\partial F_x}{\partial y} \right),$$

on the RHS of Eq. (4.2.4). Of course, the specific form varies according to the structure of the wind forcing and the friction, but the detailed wind and friction pattern is not the focus for the small forcing we are interested in here. What is important is that there is a small non-zero term on the RHS of Eq. (4.2.4) in the forced system and the forced system can be mathematically represented by $F(\omega; k) = \varepsilon$ (also refer to the small term ε in the Introduction). If ε is positive, the net effect of the wind perturbation drags the curve of $F(\omega; k)$ in Fig. 4.2.1 continuously downward, the periods of the two oscillations at Points B and C will come closer and closer and finally merge, becoming a single oscillation. Correspondingly, in the spectrum, the two adjacent

peaks will also approach each other until only one peak can be detected. These processes are shown with the model simulations below. Mathematically, only when the curve of $F(\omega; k)$ is tangential to the zero line at the turning point can the two solutions coincide. Nevertheless, in reality, it is not necessary to satisfy this stringent condition to have a coincident peak in the spectrum due to the finite sampling frequency of both observations and model simulations. Suppose the curve of $F(\omega; k)$ in Fig. 4.2.1 is continuously dragged downward by the wind forcing, if the turning point is below zero, the oscillations around the turning point will disappear. Physically, this indicates the disappearance of a previously existing oscillation, as a result of the oceanic response to moderate wind forcing variations. Therefore, although the function $F(\omega; k)$ is continuous and smooth, the ocean is able to respond discontinuously in frequency space to the wind forcing. All processes around the turning point discussed above can be naturally reversed; i.e., if the turning point is originally below zero and the wind forcing happens to pull the curve upward (via a negative ε), a new oscillation can be expected to appear in the ocean as its response to this wind change. Furthermore, if the wind forcing keeps on pulling the curve upward, the two coincident oscillations will become two distinguishably distinct ones. Correspondingly, in the power spectrum, one can see one peak split into two adjacent ones.

It is clear that the difficulty in predicting the appearance or disappearance of oscillations in the oceanic responses to wind forcing depends on the distance between $F(\omega_p; k)$ and zero. It turns out that the requirement for the discontinuous response is

not high, at least for this simple system. Mathematically, because $c^2 > 0$, the turning point of $F(\omega; k)$ satisfies

$$\frac{\partial F}{\partial \omega} = \frac{3\omega^2}{c^2} - \left(k^2 + \frac{\beta}{c} \right) = 0 \quad (4.2.6)$$

and

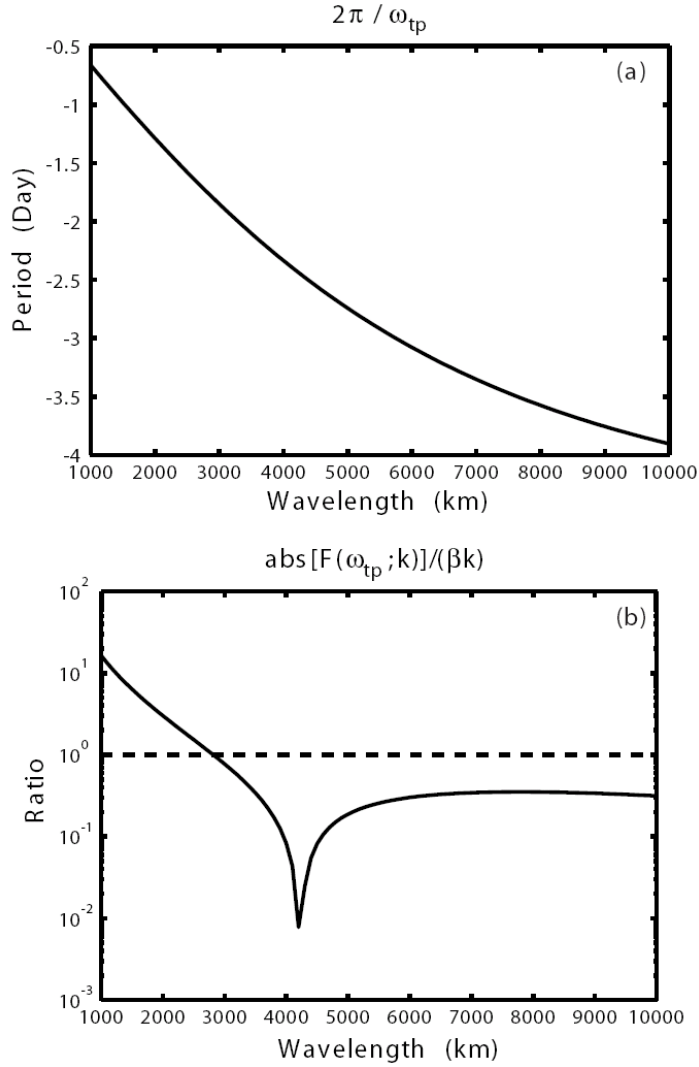


Figure 4.2.2 (a) $2\pi / \omega_{tp}$, where ω_{tp} is obtained from Eq. (4.2.8). (b) Absolute values of $F(\omega_{tp}; k)$ normalized by βk .

$$\frac{\partial^2 F}{\partial \omega^2} = \frac{6\omega}{c^2} < 0 \quad (4.2.7).$$

Therefore,

$$\omega_{tp} = -c\sqrt{k^2 + L_D^{-2}}/\sqrt{3} \quad (4.2.8),$$

where $L_D = \sqrt{c/\beta}$ is the equatorial Rossby radius of deformation. The periods at the turning point ω_{tp} , with respect to wavelengths are shown in Fig. 4.2.2a. In order to highlight how far the distance between $F(\omega_{tp}; k)$ and zero is, $F(\omega_{tp}; k)$ is normalized by βk , which represents the typical magnitudes of the terms in $F(\omega; k)$ shown in Eq. (4.2.5). As shown in Fig. 4.2.2b, for wavelengths longer than 3000 km, the normalized $F(\omega_{tp}; k)$ is smaller than 1, which means that, compared with the major dynamic mechanism (i.e., the β -effect) in the system, the distance between $F(\omega_{tp}; k)$ and zero is considerably small. Therefore, mathematically, it is possible to diminish oscillatory solutions to $F(\omega; k)$ by adding only a small perturbation term to the RHS of Eq. (4.2.4). Physically, a small wind forcing (compared with the β -effect) is capable of generating a completely different oscillation in the ocean. Note that the wind forcing is not required to have the same period as the period at the turning point. In conclusion, although the function $F(\omega; k)$ is continuous and smooth, its zero-crossing points (viz. the solutions) are not continuously dependent on external perturbations; thereby the ocean system is able to have discontinuous responses to moderate wind variations. Since the turning point is a mathematical property of $F(\omega; k)$ which is a description of the ocean system, the discontinuous response is also an intrinsic property of the system and is actually independent of the small external forcing. In a free ocean system, only the properties represented by $F(\omega; k) = 0$ are explicitly displayed and other properties are generally not apparent. In a forced

system, $F(\omega; k)$ does not change, when the external forcing is small. However, the properties represented by $F(\omega; k) = \varepsilon$ are experienced by the system, with potentially discontinuous deviations from $F(\omega; k) = 0$.

Besides the discontinuous oceanic responses, the frequency shift due to wind forcing is also physically interesting. Assume $F(\omega; k)$ undergoes a small change and becomes $\tilde{F}(\omega; k) = F(\omega; k) - \varepsilon$, due to a small external forcing which is represented by ε . Note that the ε here has fundamentally the same function as the ε defined in the Introduction. Thus, although the specific forms of these two ε are different, we use the same notation. Suppose ω_0 is the solution to $F(\omega; k)$, i.e. the frequency of an oceanic oscillation without the perturbation wind forcing, while $\tilde{\omega}$ is the solution to $\tilde{F}(\omega; k)$, i.e. the oceanic oscillation with the perturbation wind forcing. The difference between ω_0 and $\tilde{\omega}$ (viz. the frequency shift due to small wind forcing) can be estimated in the following way.

$$\begin{aligned} F(\omega_0) - \tilde{F}(\tilde{\omega}) &= \frac{\omega_0^3 - \tilde{\omega}^3}{c^2} - \left(k^2 + \frac{\beta}{c}\right)(\omega_0 - \tilde{\omega}) + \varepsilon \\ &= \left[\frac{\omega_0^2 + \omega_0\tilde{\omega} + \tilde{\omega}^2}{c^2} - \left(k^2 + \frac{\beta}{c}\right) \right] (\omega_0 - \tilde{\omega}) + \varepsilon \\ &= 0. \quad (4.2.9) \end{aligned}$$

The term in the squared bracket is approximately equal to $\partial F(\omega_0; k) / \partial \omega$, as shown in Eq. (4.2.6), if $\tilde{\omega}$ is not far from ω_0 . Therefore, Eq. (4.2.9) can be rewritten as

$$\Delta\omega = |\omega_0 - \tilde{\omega}| = \frac{|\varepsilon|}{|\partial F(\omega_0; k) / \partial \omega|} \quad (4.2.10).$$

Note that the amplitude of the frequency shift does not only depend on the time-characteristic of $F(\omega; k)$, but also on its spatial structure which is represented by the parameter k . Obviously, when the gradient in the denominator is small, the frequency shift of the oceanic response could be significantly large, even if the wind forcing is weak. If this conclusion obtained from the simple theoretical analysis can be applied to the real world, it is expected that the moderate external forcing, which always exists, can lead to frequency shifts of natural oscillations, which are qualitatively similar to the irregularity of the natural oscillations as introduced above. Thus, this finding provides a useful way to study and predict the irregularity in the ocean-atmosphere system (such as ENSO and MJOs), which has been a major hindrance to achieving theoretical predictability in models as discussed in the Introduction. Possible realistic applications of this frequency shift are illustrated with numerical models and are discussed in detail in Section 4.2.3.

4.2.2.2 Idealized numerical model

The above theory is tested in an ocean GCM – Regional Ocean Model Systems (ROMS) with simple and idealized configurations. ROMS is a free-surface, incompressible, hydrostatic, primitive equations ocean model with a staggered Arakawa C-grid (Shchepetkin and McWilliams 2003, 2005). The advection terms are excluded here, in order to minimize the nonlinearity in the model. The vertical eddy diffusivity is uniformly set to $4 \times 10^{-3} \text{ m}^2 \text{ s}^{-1}$. The water depth is prescribed in the form $h = h_{\max} \times [0.08 + 0.92 \times (1 - y^2 / Y^2)]$, where $h_{\max} = 150 \text{ m}$ is the maximum depth (this depth is unrealistic, but the model in Section 4.2.3.1 uses the realistic bottom

topography), $Y = 30^\circ$ latitude marks the northern and southern boundaries of the model domain, and y is the latitude between $\pm Y$. Thus, the water depth is uniform in the zonal direction, but changes from 150 m at the equator to a minimum of 12 m at the zonal boundaries. This structure is an approximate imitation of the meridional structure of the main thermocline in the tropical–subtropical ocean. However, the following model results are not sensitive to this idealized, curved bottom topography. The horizontal resolution is $1/2^\circ \times 1/2^\circ$. The boundary conditions at $y = \pm Y$ are the zero gradient condition, so that no waves are reflected back to the interior from the northern and the southern boundaries. In the zonal direction, periodic boundaries are assumed, thus the model is zonally symmetric and there is neither zonal gradient nor zonal wave propagation in the model. As a result, only the model outputs along one longitude are shown below, but they are the same for all other longitudes. At the bottom, a quadratic friction is used, which has a form of $C_{bf} \vec{U}_{bottom} |\vec{U}_{bottom}|$, where $C_{bf} = 3 \times 10^{-3}$ is the quadratic bottom drag coefficient and \vec{U}_{bottom} is the ocean current vector at the bottom. There are no temperature and salinity fluxes at the bottom. For simplicity, the temperature is specified to be uniformly 20°C over the model domain, thus no thermodynamics or baroclinic effects are considered.

The purpose of the idealized model experiments in this section is to compare with the conclusions of the barotropic theoretical model presented in Section 4.2.2.1. However, the Ekman pumping due to the bottom stress prevents a pure barotropic mode in ROMS (there is no surface Ekman pumping, because, as will show below, there is no curl in the prescribed surface wind stress). We use 15 vertical layers to separate the sea surface from the bottom Ekman layer. Comparing the outputs with 15

layers and fewer layers (5 layers and 3 layers), the vertical velocity at the bottom of the top layer is much weaker and the vertical shear of the horizontal velocity between the first two top layers is much smaller in the former case (not shown). In addition, the vertical velocity and the vertical shear of the horizontal velocity at the top are quite similar when we use 15 layers and 20 layers in the vertical (not shown). Thus, 15 vertical layers are a reasonable choice and the top layer is much like a barotropic layer in this case. The model results are stored every 6 hours for 100 days, after spinning up for 200 days, which is long enough for the barotropic mode to reach a steady state.

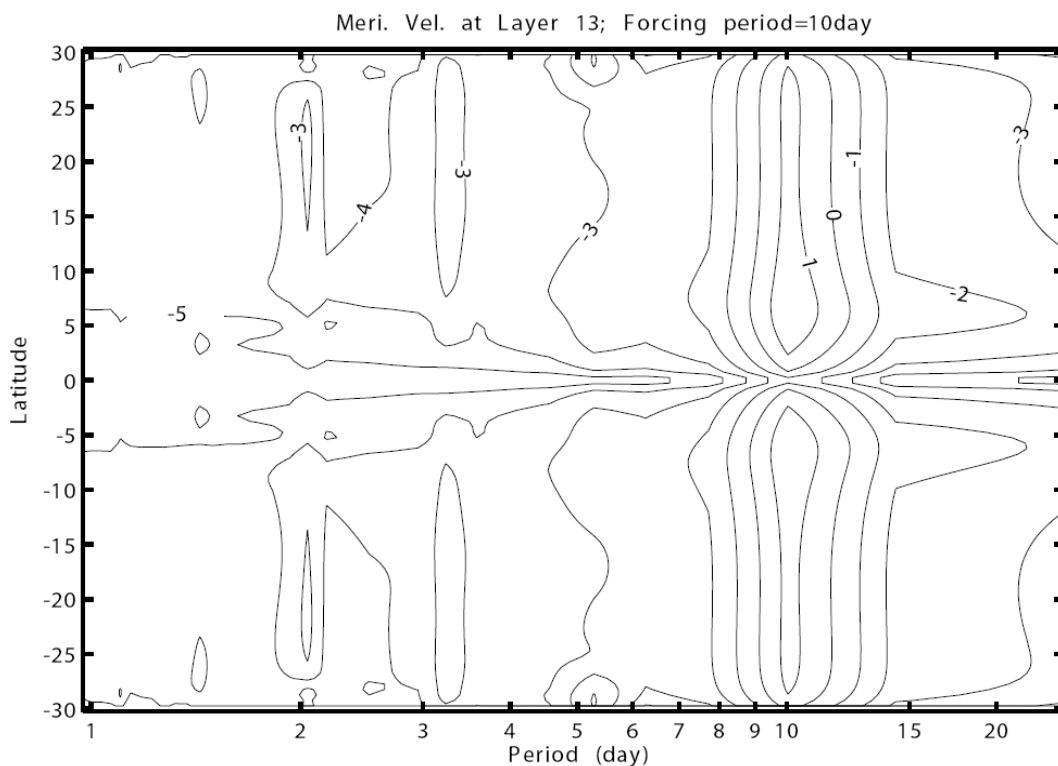


Figure 4.2.3 Power spectra of meridional velocities in the 10-day run. The contours show the logarithm of the spectrum values.

The wind stress used to drive the model is purely zonal and periodic, with a form of $\tau_x = W \sin(\omega_w t)$ and $\tau_y = 0$, where $W = 0.1 \text{ N m}^{-2}$, which is the order of the

climatological mean surface wind stress, and ω_w is the wind frequency. The wind stress is horizontally uniform over the whole model domain and only changes with time. It is well known that the wind stress curl is important for driving the equatorial Rossby waves, but purposely, we apply the wind stress with no curl. As argued above, we intend to keep the numerical model barotropic, so that the results can be compared with analytical results in Section 4.2.2.1. With no wind stress curl, there is no surface Ekman pumping nor the associated vertical velocity. In addition, because of the periodic east-west boundary condition, there is no zonal gradient. Hence, there is no zonal wave propagation and we will only examine the local variations with respect to time in the following of this section. Three model runs are compared below, in which the wind stress has a period of 9 days, 10 days, and 11 days, respectively. They are referred to as 9-day, 10-day, and 11-day run hereafter. Wind stresses with longer periods (e.g., 14 days, a biweekly wind anomaly) were also applied to drive the model but yielded results that were fundamentally the same as those shown below, hence they are not displayed. Since the theoretical analyses are based on the equation in terms of the meridional velocity (Eq. 4.2.3), the model analysis also focuses on the meridional velocities. But one can also reach similar conclusions with other dynamical variables.

The power spectrum of the meridional velocities along one longitude in the 10-day run is shown in Fig. 4.2.3. Since the model configuration is zonally symmetric, the spectra along other longitudes are exactly the same as the one shown in Fig. 4.2.3. The highest energy lies in the oscillations with a period of 10 days, since they are directly driven by the wind forcing. There are two other frequency bands with high

spectral peaks: one is around 2 days and the other is around 3.2 days. In Fig. 4.2.3, we show that the spectral structures are quite similar at different latitudes, although due to the latitudinal variations of water depths and Coriolis parameters, they are not exactly the same. Therefore, the following conclusions which are drawn based on the power spectra at 10° latitude are actually robust at other latitudes.

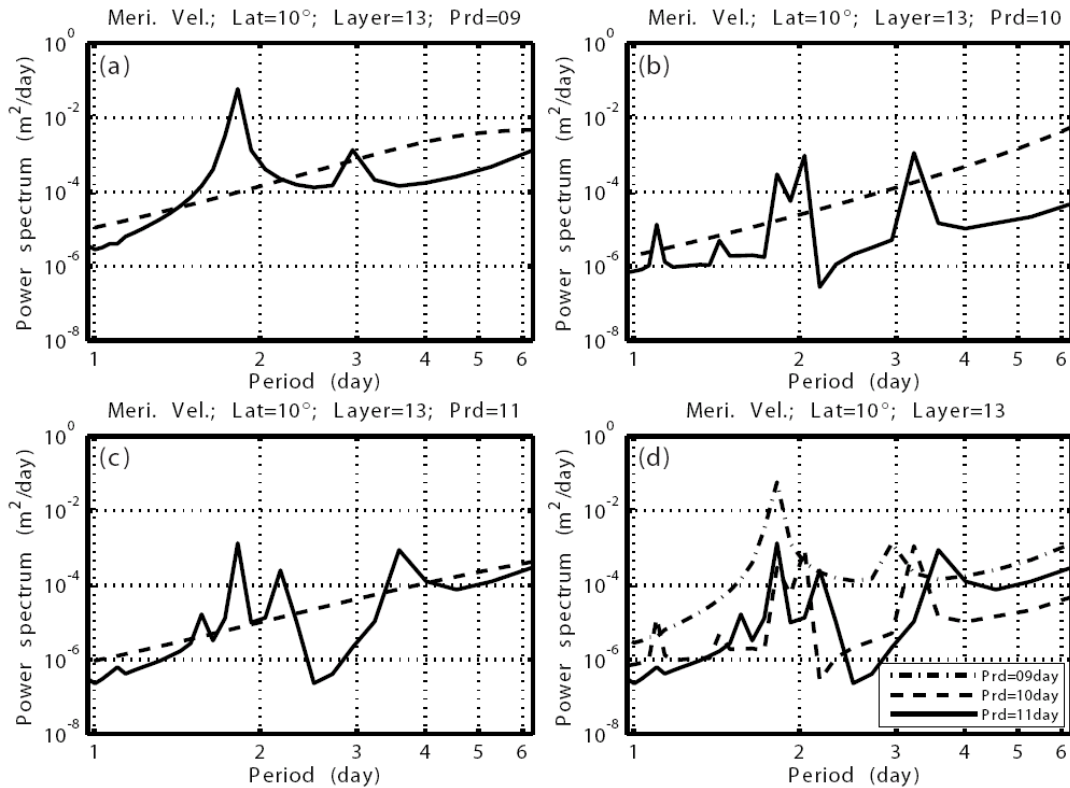


Figure 4.2.4 Power spectra of meridional velocities at 10° latitude in the (a) 9-day run, (b) 10-day run, and (c) 11-day run. The dash lines show the 95% confidence limits. (d) The power spectra in the three model runs are shown together to favor the inter-comparisons.

The detailed spectra at 10° latitude in the three model runs are shown in Fig. 4.2.4. In order to highlight the oceanic responses, the peak at the period of wind forcing is not included. In the 9-day run, one distinguishable peak is at 1.8 days. Another peak at 2.9 days just passes the 95% confidence limit. In the 10-day run, there are two adjacent peaks around 2 days and another pronounced peak at 3.24

days. Especially, there is a peak at 1.1 days, which is not found in other two model runs. In the 11-day run, there are also two adjacent peaks around 2 days and a peak at 3.6 days. In addition, there is a small peak at 1.6 days, which just passes the 95% confidence limit. The spectral peaks in the three model runs can be categorized into three groups.

- (1) The oscillations around 3 days shift from 2.9 days in the 9-day run to 3.6 days in the 11-day run. This resembles the behavior of the zero-crossing point A in Fig. 4.2.1. These oscillations are continuously dependent on the continuous variation of the wind forcing.
- (2) There is only one peak for oscillations around 2 days in the 9-day run, while there are two adjacent peaks in the other two runs. Moreover, the frequency difference between the two peaks is slightly smaller in the 10-day run than it is in the 11-day run. This is quite similar to the behavior of the two oscillations (Points B and C) which straddle the turning point in Fig. 4.2.1.
- (3) The peak at 1.1 days in the 10-day run is unique, which displays the discontinuity of the oceanic response to the small change in the wind forcing.

With these simple configurations, the model is an approximate simulation of the barotropic theoretical model developed in Section 4.2.2.1. The peaks have similar periods as the zero-crossing points in Fig. 4.2.1, albeit not exactly the same. Although it is almost impossible to display all possibilities that the theoretical analysis implies with only one simple ocean model, the essentials of the proposed behavior of the oceanic responses to small wind forcing are supported.

In the above ocean model, all baroclinic oceanic responses to the wind forcing are removed *a priori* and only fast barotropic mode responses are resolved. As a result, the oscillations shown in Fig. 4.2.4 have much shorter periods than most observations, since the barotropic waves are too fast to be captured in most observations (Chelton and Schlax 1996). Although the fast barotropic responses are less physically significant than the slow baroclinic ones, the purpose of this numerical model is to verify the conclusions obtained from the theoretical analysis, which is also based on barotropic equations (Eq. 4.2.2). Therefore, we believe that using the barotropic model configuration is appropriate and instructive for illustrating our conclusions clearly. Actually, although the oceanic waves propagate much more slowly in a baroclinic system than the barotropic waves, the two influences of wind forcing variations on the ocean system hypothesized in this study can also be significant. For example, following Pedlosky (1987), we can define the intrinsic function of baroclinic Rossby waves in a stratified ocean as

$$F(\omega; k, l) = \omega - \frac{\beta k}{k^2 + l^2 + L_D^2} \quad (4.2.11),$$

where k and l are the zonal and meridional wave numbers, respectively. Although the frequency of a baroclinic Rossby wave (i.e. the solution ω_0 to $F(\omega; k, l) = 0$) is low, the term $\partial F(\omega_0; k) / \partial \omega$ equals one and is independent of frequencies. Hence, similar to Eq. (4.2.10), the frequency shift of the baroclinic Rossby waves due to wind forcing is likely to be non-negligible.

4.2.3 Model experiments with realistic configurations

In this section, the possible applications of our hypothesis are tested with two sets of model experiments, both of which have much more realistic configurations than the ones in Section 4.2.2.2. The oceanic responses in the tropic Pacific Ocean to the intraseasonal wind stress variations are tested with ROMS and the atmospheric responses to the meso-scale SST anomalies in the Indian Ocean are tested with a regional atmospheric model – the Experimental Climate Predictions Center (ECPC) Regional Spectrum Model (RSM).

4.2.3.1 Oceanic response to atmospheric forcing

MJOs have been shown to be the main enforcers of the oceanic intraseasonal variabilities (ISVs). During the TOGA program, Kessler et al. (1995) found that ISVs in the tropical Pacific are consistent with the MJOs. The relationship between the Kelvin waves and MJOs were fully described by Hendon et al. (1998) and were confirmed again with altimeter data by Edwards et al. (2006). The oceanic responses to the intraseasonal wind stress anomalies are simulated with ROMS here. The model domain extends from 160°E to 60°W and from 30°N to 30°S, with a horizontal resolution of $1^\circ \times 1^\circ$. There are 20 vertical layers from the sea surface to the bottom. The bottom topography is adopted from the ETOPO2v2 database (National Oceanic and Atmospheric Administration, National Geophysical Data Center, 2006), which are then smoothed with a Hanning filter. As a result, isolated seamounts in the deep ocean and the fine-scale noises in the bottom topography are removed. Maximum depth at the shore is set to 150 m, which limits the generation of excessively big walls

along the shore. The above smoothing of the bottom topography prevents unstable numerical waves from originating at the bottom or near the shore. A quadratic friction is used again and the vertical eddy diffusivity is uniformly set to $4 \times 10^{-3} \text{ m}^2 \text{ s}^{-1}$. The horizontal boundaries are nudged to the 5-day SODA reanalysis (Carton and Giese 2008, Carton et al. 2000a, b). A sponge layer is used, so that the influence of wave reflection from the horizontal boundaries is small. The atmospheric forcing, including the surface wind stresses, the net surface heat and freshwater fluxes, are obtained from ERA-40 (Simmons and Gibson 2000), after a low-pass filtering with a cut-off period of 100 days. Initial structure is initiated from the climatological SODA averaged from 1975-2005. Outputs are stored every 5 days for 3 years after spinning up for 3 years. This is referred to as the control run hereafter. The mean zonal currents over the 3 years are shown in Fig. 4.2.5. The major climatological and large-scale equatorial currents are well captured, such as the westward equatorial current with northern and southern maxima, as well as the eastward equatorial countercurrent and the equatorial undercurrent. With the limitation of the low-pass-filtered atmospheric forcing and the horizontal resolution of 1° , the meso-scale features (such as the tropical instability waves), which are not the focus of this study, are not resolved in the control run.

The intraseasonal zonal wind stresses are added to the low-pass-filtered wind stresses, in the form of $A_w \exp(y^2 / L_y^2) \cos[2\pi(kx - \omega_w t)]$, where $A_w = 0.05 \text{ N m}^{-2}$, which is the order of the intraseasonal wind stress anomalies, L_y is 5 degree in latitude which is the Rossby radius of deformation in the y direction, $\omega_w = ck$ which satisfies the dispersion relation of Kelvin waves, $c = 5 \text{ m s}^{-1}$ which is the typical eastward

speed of MJOs (Zhang 2005). All the other atmospheric forcing and model configurations remain the same as those in the control run. We conducted four model experiments (each for 3 years) with $\omega_w = 1/30, 1/40, 1/50,$ and $1/60 \text{ day}^{-1}$, which cover the whole period span of MJOs. Hereafter, these model runs are referred to as R30, R40, R50, and R60, respectively.

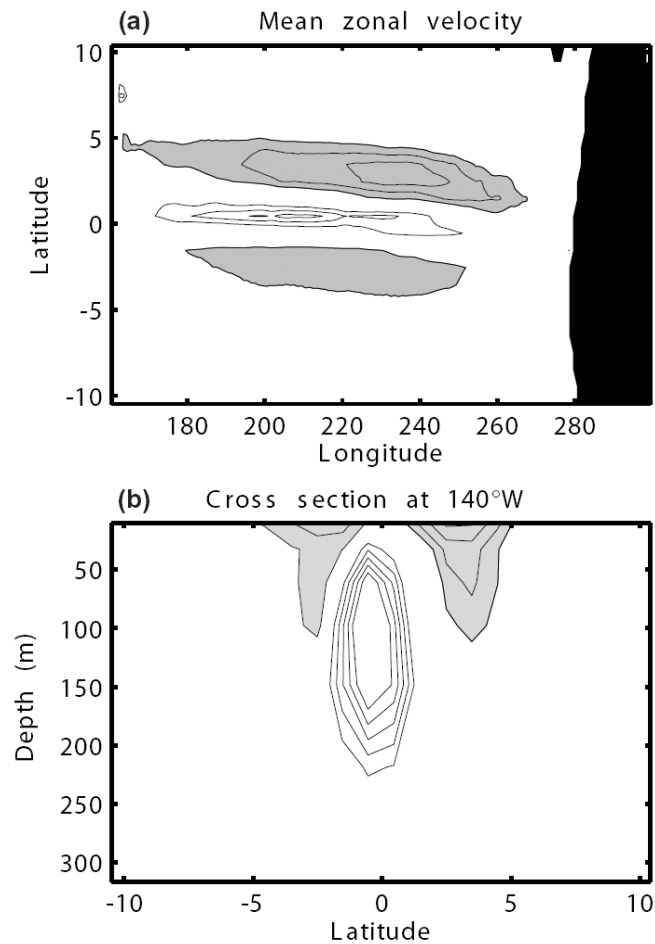


Figure 4.2.5 (a) Mean zonal current at the surface and (b) mean zonal current at 140°W with respect to depth. The westward currents are shaded. The contours for eastward currents start from 0.2 m s^{-1} and the contours for westward currents start from -0.2 m s^{-1} . The contour interval is 0.1 m s^{-1} . The black region is the continent.

The power spectra of the zonal currents at four different places are shown in Fig. 4.2.6. For comparison, the corresponding spectra in the control run are also shown

with dash gray lines. The four locations represent the major large-scale ocean currents. Figs. 4.2.6a and 4.2.6b show the spectra within the northern and southern maxima in the equatorial currents, Fig. 4.2.6c is in the equatorial countercurrents, and Fig. 4.2.6d is in the equatorial undercurrent. The frequency shifts and spectral discontinuities are obvious in all spectra. In Fig. 4.2.6a, the highest peak is the one at 34-day in the R60 run (the green line), although the corresponding forcing period is 60 days. In contrast, the peak around 60-days just passes the 95% confidence limit. For the R50 run (the black line), the largest peak is at 30-days and the spectrum from 30-days to 47-days is quite flat. The peak in the R40 run is at 37-day (the red line), which is also clearly shifted from the forcing period. There are two spectral peaks at 31-days and 39-days in the R30 run (the blue line), which seem to straddle the peak at 34-days in the R60 run. The control run has a significant peak around 33 days (dashed line in Fig. 4.2.6a), thus the responses tend to have peaks around the intrinsic period but with small shifts. The pattern of the spectrum in Fig. 4.2.6b is qualitatively similar to the one in Fig. 4.2.6a. One notable feature in Fig. 4.2.6b is that the R60 run does not have a significant peak around 60-days (the green line). At the equator, the intraseasonal oscillations are generally consistent with the periods of the atmospheric forcing. However, the peaks in the spectra at 32-days in the R60 run and at 35-days in the 50-days are also statistically significant. At a depth of 120 m at the equator, the frequency shift is also clear (Fig 4.2.6d). The peak at 35-days in the R60 run and the peak at 29-days in the R50 run are obvious. For the R40 run, the spectrum between 37-days and 47-days is flat and statistically significant. For the R30 run, other than the peak at 30-days, there is another one at 53-days, which is slightly above the 95%

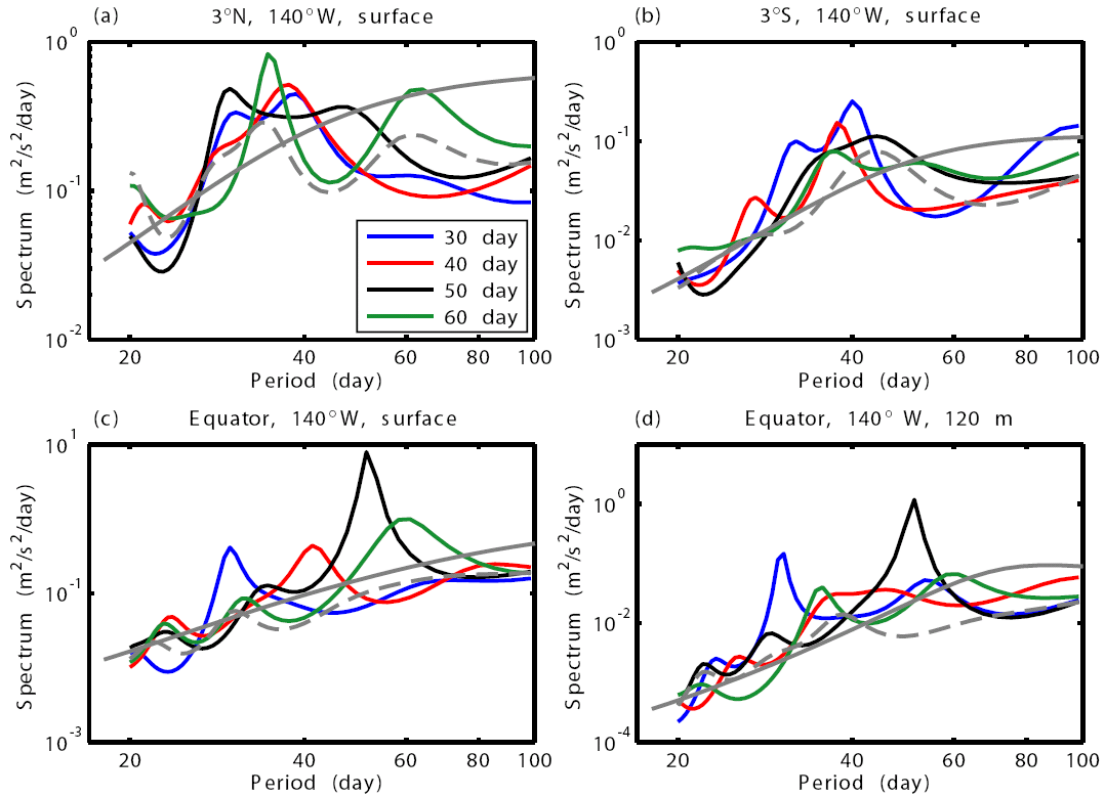


Figure 4.2.6 Power spectra of zonal currents at four different locations in the four scenarios and the control run (with dashed gray lines). The gray line shows the 95% confidence limits. See texts in Section 4.2.3.1 for detailed descriptions.

confidence limit. Therefore, although the intraseasonal variation in the atmospheric forcing only has one deterministic period in each model experiment, the oceanic responses have periods clearly distinct from the forcing periods almost everywhere.

Since the model configurations are quite realistic, nonlinearity is not avoidable (but there is no stochastic forcing), thus the frequency shifts may not be solely due to the mechanism proposed in this study. The periods of wind stress anomalies are from 30 to 60 days, which are the time scale of MJOs. Meanwhile, the range of periods is also consistent with the periods of oceanic responses. As clearly shown in Fig. 4.2.6, the responses around the forcing periods can be either (1) dominant (Fig. 4.2.6c), or (2) statistically significant but not dominant (the green line in Fig. 4.2.6a and the blue

line in Fig. 4.2.6b), or (3) detectable but not statistically significant at the 95% confidence limit (the green line in Fig. 4.2.6b). Thus, due to the overlap of the period of the forcing and the responses, it is hard to ascertain whether the responses near the forcing periods are directly due to external forcing or due to the processes hypothesized in this study. But one notable result is that the responses do not necessarily occur at exactly the same periods as the forcing; instead there are small frequency shifts (see detailed descriptions above). In summary, since the frequency shifts are quite obvious and the only difference between the four scenarios lies in the different periods of intraseasonal wind stresses, we believe that our hypothesis does largely explain the frequency shifts shown in Fig. 4.2.6.

4.2.3.2 Atmospheric response to oceanic forcing

The influence of oceanic feedbacks to MJOs is still not well understood, although many model studies have reported a role for the ocean. For example, Waliser et al. (1999) coupled a slab ocean mixed layer to an AGCM, producing MJOs with more realistic amplitudes, time-scale, eastward phase speed, and seasonal variability. By analyzing the model outputs with five ensembles of different initial and boundary conditions, Reichler and Roads (2005) reported that it was important to couple an interactive ocean model to an AGCM, in order to achieve a long-range predictability of MJOs. With a simple coupled model, Bellon et al. (2008) showed that the ocean-atmosphere coupling produced an MJO period which was closer to observations. Kim et al. (2008) showed that higher frequency SSTs (from monthly to daily) also improved the MJO simulations, and Pegion and Kirtman (2008a) claimed that the

intraseasonal SSTAs were a key factor to a better prediction of MJOs with the operational NCEP Climate Forecast System. The energy sources for the MJO events were analyzed in Chapter 3, showing that the oceanic forcing was important for the onset of two MJO events. One is from Feb 27, 1990 to Mar 23, 1990 and the other one is from Feb 10, 1994 to Feb 25, 1994. Hence, we test the hypothesis that the oscillations with different scales can interact with each other via simulating these two MJO events with the RSM, which is a hydrostatic, primitive equation model. In the horizontal, the double sine-cosine series are used for base functions when converting the variables to the spectral space. A terrain-following sigma coordinate is used in the vertical. The detailed model physics is described in Kanamitsu et al. (2002). The model covers the Indian Ocean region from 30°E to 150°E and from 30°N to 30°S. It has a horizontal resolution of $1^\circ \times 1^\circ$ and a terrain-following sigma coordinate system with 28 levels in the vertical. The model is initiated with NCEP reanalysis on Jan 1 and run for one year from Jan 1 to Dec 31 for each of the two MJO events. The outputs are stored every 6 hours.

In the Indian Ocean, mesoscale warm SST anomalies originate from the southeastern Indian Ocean, with a spatial scale of about 600 km – 900 km (Feng and Wijffels 2002). Then they propagate westward as Rossby waves (Xie et al. 2002; Zhou et al. 2008b; Section 2.2), which are assumed to have an impact on the atmosphere. As an example, a snapshot of the intraseasonal SST anomalies (band-pass filtered with the cut-off periods of 20 and 100 days) obtained from the AVHRR gridded data (McClain et al. 1985) on Feb 17, 1990, which is 10 days before the onset of the MJO event in 1990, is shown in Fig. 4.2.7a (gray shades). First, we make a

control run with low-pass filtered AVHRR SSTs (the cut-off period is 100 days), in which there are no intraseasonal oceanic boundary forcing of the atmosphere. Then, the total AVHRR SSTs (including the high-frequency component) are used to drive the model (referred to as the total-SST run hereafter). The mean zonal winds at 850 hPa averaged from the equator to 5°S (which are usually analyzed in MJO studies, e.g., Hendon et al. 1998; Kessler et al. 1995) in these two runs are shown in Figs.

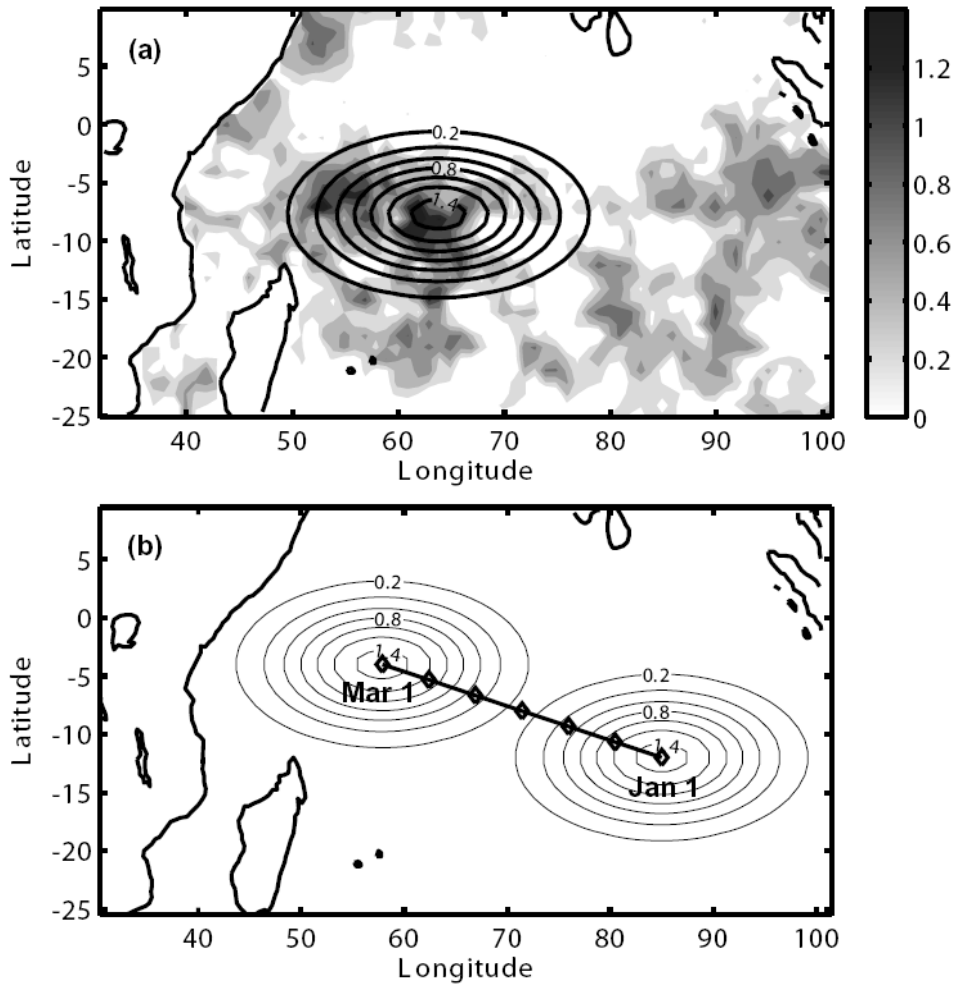


Figure 4.2.7 (a) Intraseasonal SST anomalies on Feb 17, 1990. Gray scales show the high-pass-filtered SSTs from AVHRR data with cut-off periods of 20 and 100 days. The contours show the analytical SST anomalies with a zonal wavelength of 1000 km. (b) Analytical SST anomalies with a zonal wavelength of 1000 km. The centers of SST anomalies are marked with diamonds at every ten day intervals. For clarity, the SST anomaly fields are only shown on Jan 1 and Mar 1. The unit for SST is °C and the contour interval is 0.2°C.

4.2.8b and 4.2.8c respectively. Both simulations are similar to NCEP reanalysis (Fig. 4.2.8a), indicating that the model can capture the background state of the atmosphere. Especially, the westerly wind burst on Feb 27, 1990, marks the beginning of the MJO event. The differences between these two model runs (total-SST run – control run) are shown in Fig. 4.2.8d. It is clear that the westerly winds are reinforced due to the intraseasonal SST anomalies, which indicates that the oceanic impact is significant in the development of this MJO event (Chapter 3). Since a scale selective spectral nudging is used, as recommended by Kanamaru and Kanamitsu (2007), the large-scale structure of the two model runs are constrained. However, what are interesting are the differences shown in Fig. 4.2.8d, which indicate that the intraseasonal SST anomalies indeed have significant impacts on the atmospheric variability.

In order to test the atmospheric responses to small oceanic variations, the SST anomalies represented with a 2D Gaussian form of $A_{SST}e^{-(x-x_0)^2/2L_x^2}e^{-(y-y_0)^2/2L_y^2}$ are added to the low-pass-filtered SSTs, where $A_{SST} = 1.5^\circ\text{C}$ is consistent with the observation (Fig. 4.2.7a), L_x is 10 degree in longitude and L_y is 5 degree in latitude, which are approximately the Rossby radius of deformation. The zonal center x_0 of the SST anomalies propagate westward at the phase speed of Rossby wave, i.e., $x_0 = x_{ini} + ct$, where $x_{ini} = 85^\circ\text{E}$ on Jan 1, $c = \omega_R/k_R$ is the phase speed of Rossby wave, and $\omega_R = -\beta k_R/(k_R^2 + L_x^{-2})$. In reality, the Rossby waves also propagate slightly northward during the westward propagation, thus the meridional center y_0 moves linearly with time from 12°S on Jan 1 at a speed of $1/8$ degree latitude per day. The same analytical SST anomalies are applied to both 1990 and 1994, but the

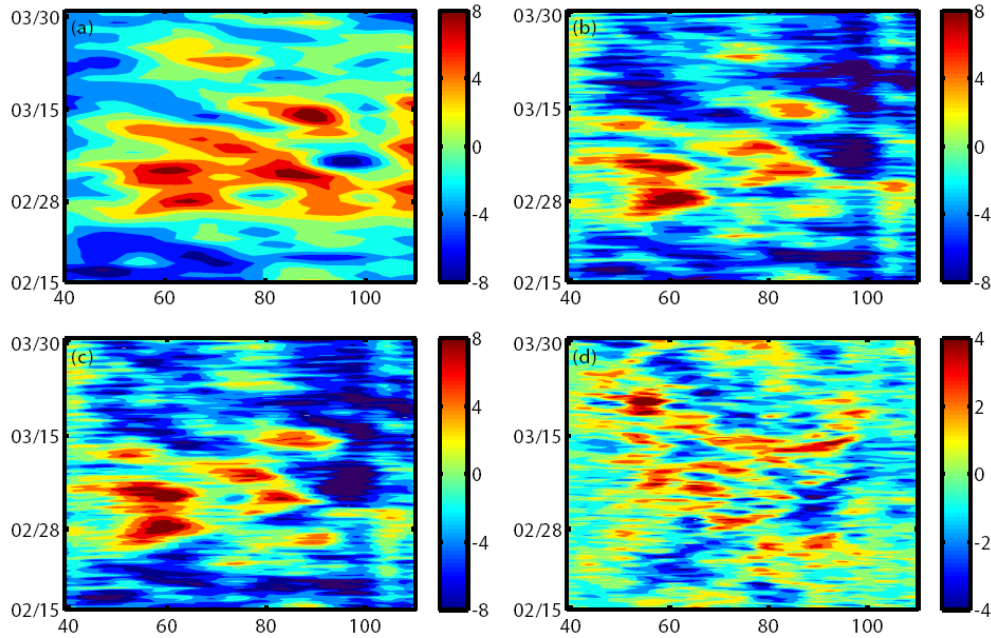


Figure 4.2.8 Zonal winds at 850 hPa averaged between the equator and 5°S from Feb 15, 1990 to Mar 31, 1990. (a) NCEP/NCAR reanalysis, (b) control run, (c) total-SST run, and (d) the difference between (c) and (b) (the former minus the latter). The units are m s^{-1} . Note that the color scales in (d) are different from the other panels.

background SSTs obtained from AVHRR data correspond to the two different years. Four scenarios are conducted with the zonal wavelengths of 800 km, 900 km, 1000 km, and 1100 km, respectively. The corresponding periods are 26.7 days, 24.2 days, 22.1 days, and 20.5 days, respectively. Note that the zonal wavelengths used here are a little larger than observations (Feng and Wijffels 2002) and the corresponding periods are slightly smaller. It is shown later with the model results that the small discrepancies between the analytical setup and observations allow a frequency separation between the SST forcing and the atmospheric responses. Hence, the responses with periods between 40 to 80 days, which are discussed in detail below, have no direct relation with the SST forcing. This frequency separation between the forcing and responses is in contrast to the situation with a frequency overlap discussed at the end of Section 4.2.3.1. Hereafter, the four model runs are referred to

as R800, R900, R1000, and R1100, respectively. Take the wavelength of 1000 km for instance, the snapshot of the analytical SST anomalies on Feb 17, 1990 is superimposed in Fig. 4.2.7a (contours). The northwestward propagation of the SST anomalies is shown in Fig. 4.2.7b. The centers of the SST anomalies are marked with diamonds every 10 days. For clarity of presentation, only the SST anomaly fields on Jan 1 and Mar 1 are shown explicitly.

For the RSM experiments in 1990, after removing the seasonal cycle, the mean and the standard deviation (STD) of the differences in the zonal winds at 850 hPa between the R1100 run and the R800 run (R1100-R800) are shown in Figs. 4.2.9a and 4.2.9b, respectively. For comparison, the mean and STD of the zonal winds at 850 hPa in the R800 run are shown in Figs. 4.2.9c and 4.2.9d. The mean of the differences between the two runs are much smaller than the mean of either of them

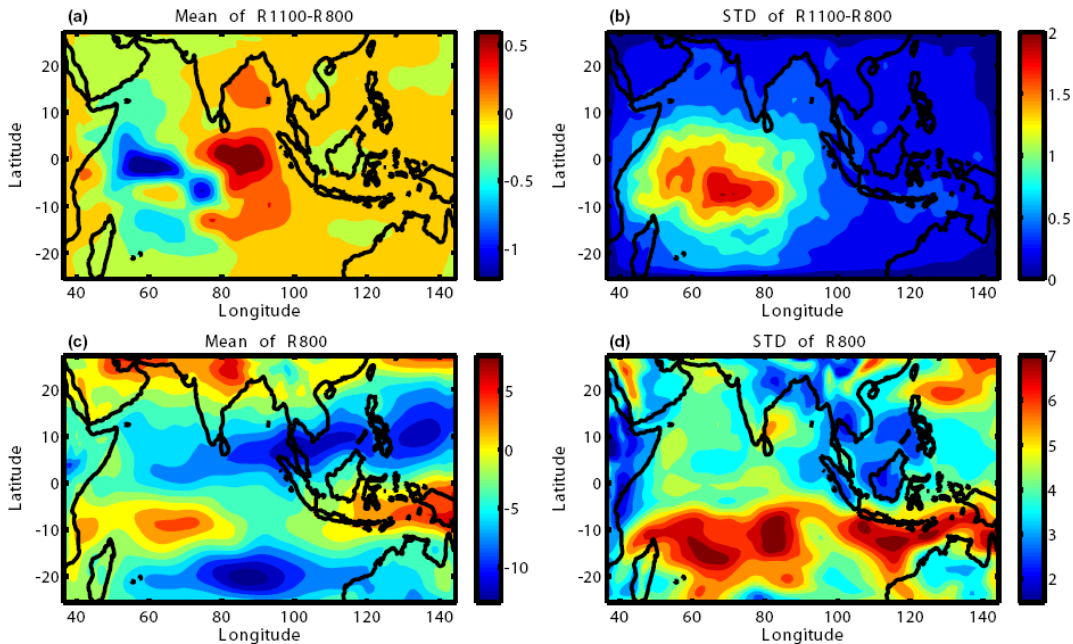


Figure 4.2.9 Mean (a) and STD (b) of differences in zonal winds at 850 hPa between the R1100 run and the R800 run. Mean (c) and STD (d) of the zonal winds at 850 hPa in R800 run. The model runs are conducted in 1990. The seasonal cycle is removed. The unit is m s^{-1} .

(note the color scales in Fig. 4.2.9a and 4.2.9c are different), which indicates that there are no dramatic deviations between the background state in the two runs. This is understandable, because only different meso-scale and intraseasonal SST anomalies are applied in the two experiments and thereby the major differences also reside in the intraseasonal variation. However, the STD of the differences between the two runs is comparable to the STD of the individual runs in the western and central Indian Ocean between the equator and 10°S. Since the background states in the two runs are similar, the large STDs in the tropical Indian Ocean are attributable to the differences in the meso-scale and intraseasonal perturbations, which are caused by different meso-scale SST anomalies. Therefore, the variations caused by the SST anomalies with different spatial scales are pronounced.

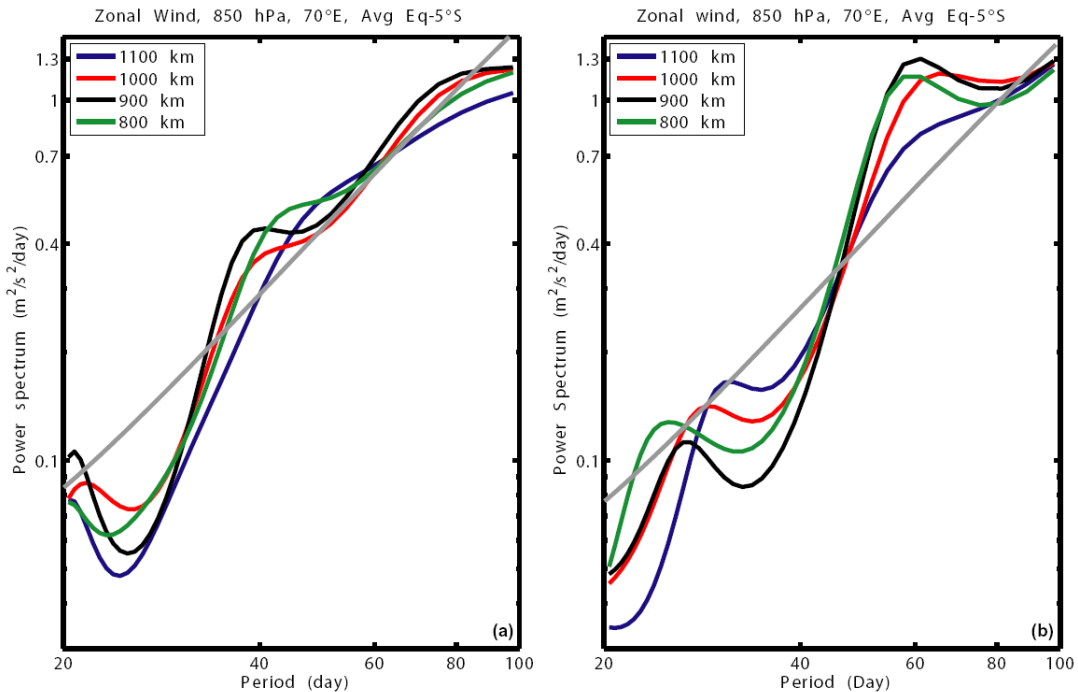


Figure 4.2.10 Power spectra of the zonal winds at 70°E in four atmospheric model runs for the MJO events in 1990 (a) and in 1994 (b). The gray line shows the 95% confidence limits.

Since all zonal winds analyzed below are averaged between the equator and 5°S at 850 hPa, for the conciseness of description, the zonal winds mentioned hereafter are these latitudinal averages. The power spectra of the zonal winds at 70°E in the four model runs are shown in Fig. 4.2.10. For the MJO event in 1990 (Fig. 4.2.10a), there are differences between 20-30 days, which is the range of periods of the prescribed external forcing. However, the spectra in this band are not significant at the 95% confidence level. Significant peaks are found between 40 and 80 days, which is the typical band for MJOs. Moreover, there is only one peak in the R1100 run, but there are two peaks in R1000 and R900 runs which straddle the peak in the R1100 run. This pattern is qualitatively similar to the one in Fig. 4.2.4. But the variations in the four model runs are not as continuous as those in the idealized ocean model (Section 4.2.2.2). For the MJO event in 1994 (Fig. 4.2.10b), the spectral peaks in the range of the external forcing are slightly significant. But the corresponding periods, which are 30.5 days, 28.7 days, 27.2 days, and 25.1 days respectively, are shifted from the forcing periods. The most pronounced peaks in the scenarios for 1994 are around 60 days, which are again completely separated from the forcing periods.

Statistically, an MJO event is not a stationary process, thus the power spectrum analysis based on Fourier transform is not the best tool to show the frequency shift quantitatively. This is an important reason why the spectral peaks in Fig. 4.2.10 are not very distinct and the variations are not strictly continuous. Therefore, we apply the wavelet spectrum with the Morlet wavelet with respect to time, which has been shown to be suitable for such analysis (Meyers et al. 1993; Torrence and Compo 1998). The differences of the wavelet spectra of the zonal winds between R1100 run

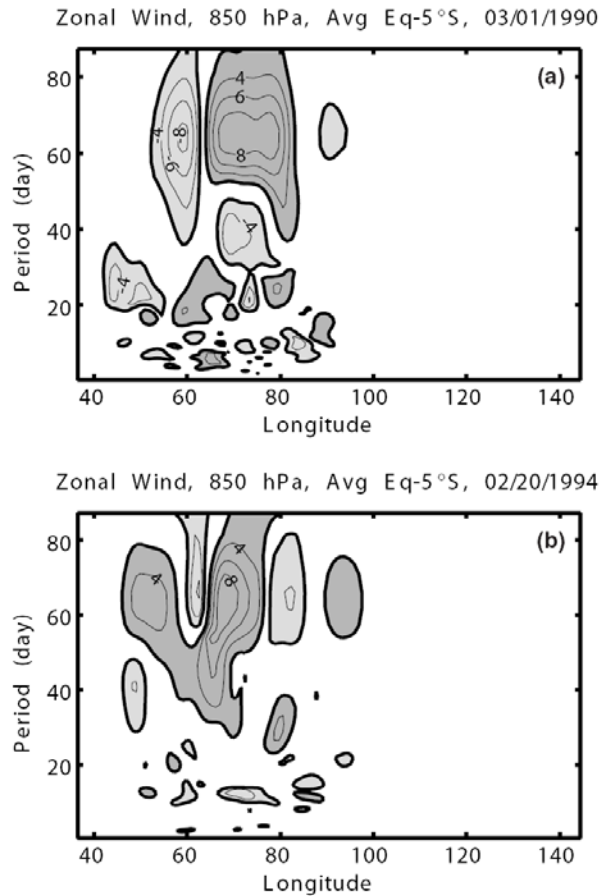


Figure 4.2.11 (a) Differences between wavelet spectra of the zonal winds on Mar 1, 1990 in the R1100 run and R800 run (R1100 – R800). (b) is the same as (a), but on Feb 20, 1994. The unit is $\text{m}^2 \text{s}^{-2}$. The dark gray areas are larger than $2 \text{ m}^2 \text{ s}^{-2}$, while the light gray areas are smaller than $-2 \text{ m}^2 \text{ s}^{-2}$.

and R800 run on Mar 1, 1990 and on Feb 20, 1994 are shown in Fig. 4.2.11. Similar to the power spectrum in Fig. 4.2.10, there are some differences in the band between 20 and 30 days, which is the range of external forcing. But the major differences reside from 40 days to 80 days, which is longer than the forcing period. Spatially, the major differences range from 55°E and 90°E , which is larger than the spatial scale of the analytical SST anomalies (Fig. 4.2.7). Further details can be detected by examining the cross section along 70°E , as shown in Fig. 4.2.12. The spectra for the MJO events in 1990 (Fig. 4.2.12a) and in 1994 (Fig. 4.2.12b) are qualitatively similar. Generally, there are two energetic period bands between 30 days and 80 days. One is

around 40 days in Fig. 4.2.12a and around 35 days in Fig. 4.2.12b, while the other one is around 65 days in both MJO events. In all scenarios, the former peak dominates and the latter one is relatively weaker. For the MJO event in 1990, along with the increase of the perturbation wavelength, the peak around 40 days weakens while the peak around 65 days strengthens continuously, which physically indicates that the energy of the westerly winds shifts from ~ 40 days to ~ 65 days. On the contrary, for the MJO event in 1994, along with the increase of the perturbation wavelength, the peak around 35 days increases while the peak around 65 days diminishes continuously, which physically indicates that the westerly wind energy shifts to the shorter period. Therefore, for both MJO events, moderate changes in the SST anomalies lead to considerable frequency changes of the atmospheric oscillations, which are regarded as the irregularity of MJOs as discussed in the Introduction. For the wavelet spectra, the variations are continuously dependent on the smaller variation of the external forcing, which is not consistent with the power spectrum in Fig. 4.2.7. However, as mentioned above, the power spectrum analysis is not ideal for a non-stationary process such as an MJO event. Thus, we believe the results of the wavelet analysis are quantitatively more reliable.

4.2.4 Conclusions and discussion

With theoretical and numerical models, the oceanic and atmospheric responses to small external forcing are studied. The external forcing has two effects on the oscillations in the climate-system. One is the continuous frequency shift, which is mainly determined by the temporal gradient of $F(\omega; k)$, a function of frequency and wavenumber. Note that the wavelength is also relevant, because k is a parameter and

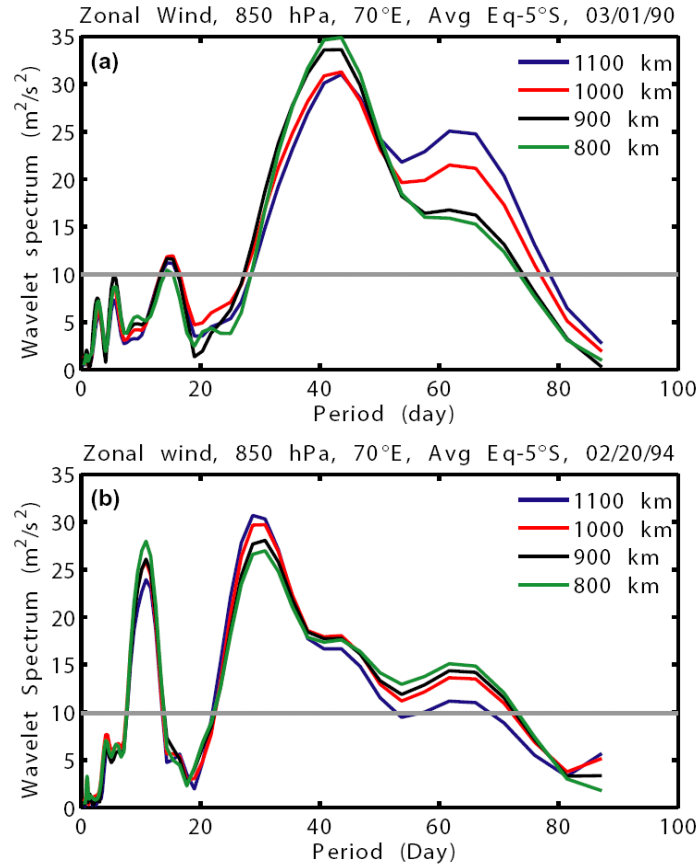


Figure 4.2.12 Wavelet spectra of the zonal winds at 70°E and on Mar 1, 1990 (a) and on Feb 20, 1994 (b) in the four atmospheric model runs. The gray lines are the 95% confidence limits, calculated following Torrence and Compo (1998).

is variable. The second avenue for the external forcing is via the appearance or disappearance of oscillations, i.e., the discontinuous response to an external forcing, which is mainly determined by the position of the turning point of $F(\omega; k)$. These conclusions are applicable to both the oceanic response to the atmospheric forcing and the atmospheric response to the oceanic forcing.

The function $F(\omega; k)$ is critical to the responses to external forcing. The amplitude of frequency shift is significantly influenced by its gradient with respect to frequency. The period of the discontinuous response is determined by the position of its turning point ω_{tp} and the possibility that the discontinuous response can occur is

determined by the distance between $F(\omega_p; k)$ and zero. When studying free oscillations, dispersion relation of $F(\omega; k)=0$ is regarded as an “ID card” of a specific wave; for instance, the dispersion relation in Eq. (4.2.4) represents the Mixed-Rossby-Gravity waves (Gill 1982). Contrarily, when studying the forced oscillations, dispersion relation is not the sole determinant of the response. Instead, the range of properties of $F(\omega; k)$ is required to capture the range of responses. Moreover, the function $F(\omega; k)$ actually contains all information about the system that we are concerned with (referring to the processes that Eq. (4.2.3) is obtained in Gill 1982). Thus, we can call $F(\omega; k)$ the intrinsic function of the system.

The frequency shifts can be clearly seen from the model results in Section 4.2.3. Although the external forcing is deterministic and only has a single period, both the oceanic and the atmospheric responses have wide range of periods. This feature is qualitatively similar to the well-recorded broad frequency band of ENSO and MJO. Therefore, the frequency shift mechanism we propose in this study provides a different way, in which nonlinearity and stochasticity are not the important players, to address the irregularity in the natural oscillations. Nevertheless, the model configurations are not realistic enough. For example, there are differences in the spatial scale of SST anomalies between what we use to drive the atmospheric RSM and the observations. In addition, the perturbations to the models are all generated with analytical forms, rather than from observations. Thus, more quantitative tests on this hypothesis with more realistic situations are still needed. Meanwhile, the crucial next step is to extract such frequency shifts in the coupled climate system to understand the details of the processes to fully understand how models can translate

the knowledge to predictive understanding. A better understanding and resolution of this mechanism is hopeful to help improve the model simulations of the natural irregularity.

Chapter 5: Conclusions and future plans

5.1 Summary

In this dissertation research, the interactions between MJOs and sea surface temperature (SST) anomalies in the Indian Ocean are studied in a multi-scale framework. The main conclusions in each chapter are summarized in this section.

In Chapter 2, with forced ocean model simulations, the dynamic and thermodynamic influences of the Indonesian Throughflow (ITF) on the southwestern Indian Ocean (SWIO) were examined. It is found that the baroclinic instabilities and oceanic intraseasonal variabilities (OISVs) are enhanced and the subtle balance between the stratification and the mixing in the SWIO is modified due to the ITF influence. As a result, from October to early December the cold entrainment is dramatically reduced, and the SSTs warm faster than just due to the net surface heat fluxes. Since the SWIO is the genesis region of Madden-Julian Oscillations (MJOs), the warm SST anomalies are likely to generate a favorable condition for the onset of MJOs, by inducing the low-level moisture convergence.

In Chapter 3, kinetic energy sources for the MJOs are calculated with NCEP reanalysis. As the dominant intraseasonal oscillations in the atmosphere, MJOs are associated with enhanced perturbed kinetic energy. The energy sources for MJOs are explored by examining the energy sources of the perturbed kinetic energy in the Lorenz energy cycle. Averaging over all MJO events from 1979 to 2006, it is found that the energy conversion from perturbed potential energy to perturbed kinetic energy is the dominant energy source for MJOs but surface heat flux can also be an

important energy source while the energy conversion from mean kinetic energy to the perturbed kinetic energy is a very weak energy sink for MJOs. The relative contributions of the three energy sources are consistent with the observed energy cycle by Oort and Peixoto (1974). However, for any specific MJO event, the importance of the three energy sources can vary significantly. For most MJO events, the energy is obtained from the perturbed potential energy. During the calm phase of the MJO event, the ocean surface is warmed due to the reduction of the latent heat loss. As a result, warm SST anomalies occur after the onset of MJOs and they can feedback to the atmosphere, prolonging the life-span of the MJO event. For a few MJO events, the energy supply by surface heat flux dominates, which is closely related to the warm SST anomalies. In these MJO events, the warm SST anomalies drive the atmosphere actively, leading to low-level moisture convergence. In boreal summer, a few MJO events gain energy from the mean kinetic energy, which is attributable to changes in the background circulation during the inter-monsoon season. This class of MJO events usually occurs during the transition periods between monsoon seasons, since the meridional gradient of zonal winds is large enough to overcome the gradient of the Coriolis effect β , and thus the barotropic instability can be triggered. As a conclusion, although all MJO events have a similar period ranging between 30-60 days, their energy sources can be different. In order to explain and simulate a specific MJO event, one probably needs to capture the appropriate mechanism and to resolve the relevant processes in a model.

The energy conversion between the perturbed potential energy and the perturbed kinetic energy $P' \cdot K'$ is proportional to $w' \frac{\partial \Phi'}{\partial z}$ (Eq. 3.7). Since $\partial \Phi' / \partial z = R_d T' / H$,

after averaging over time (e.g., the life time of the MJO events as in Chapter 3), $P' \cdot K'$ is determined by the covariance between the vertical velocity and the perturbed air temperature. Thus, the energy source from the perturbed potential energy during MJOs can be diagnosed from the updraft winds and the temperature perturbations. As for the energy source due to the surface heat flux, a direct monitor on SSTAs is simple and straightforward, but warm SSTAs do not definitely indicate an enhanced surface heat flux. As discussed in Section 3.3.1.1, other than SSTAs, the surface heat flux is also subject to the surface winds (the WISHE mechanism). However, direct observations on the air-sea heat exchange are really a challenge. Most recently, Grodsky et al. (2009) produced the intraseasonal latent heat flux (which is the major component of the air-sea heat exchange) with various satellite observations (such as QuikSCAT and SSM/I). Their products could be very useful for estimating the energy source for MJOs due to the surface heat flux more accurately and promptly. For energy source from the mean kinetic energy (Eq. 3.8), it is determined by the horizontal wind fields, which can be well observed and assimilated into forecast models and reanalyses.

As the intraseasonal and meso-scale variabilities in the atmosphere, MJOs are intimately related to processes with broad scales, for example, the deep convection with smaller scales and the background circulation with larger scales. Therefore, MJOs are an important component for the energy cascade among various scales, which has been introduced in Section 1.3 and will be discussed in more details in Section 5.3. It is important to emphasize that what I calculated are the energy sources for the perturbed kinetic energy on the MJO scale. The energy equations I used in

Chapter 3 are not able to resolve the energy transfers between the MJO scale and smaller scales, because the approximations made during the derivation of the energy equations (see Section 3.3) may not be valid for the small-scale processes. Since main energy for MJOs is obtained from the perturbed potential energy, one may wonder how the perturbed potential energy is built up. The perturbed potential energy is proportional to $(\partial\Phi'/\partial z)^2$. Since $\partial\Phi'/\partial z = R_d T'/H$, P' is proportional to T'^2 , which is usually determined by strong but small-scale deep convection (refer to the weak temperature gradient approximation; Sobel et al. 2001; Bretherton and Sobel 2002). Therefore, the current results alone cannot answer the above question. However, an international project called Year of Tropical Convection (YOTC) is now underway (<http://www.ucar.edu/yotc/index.html>). I expect that the energy transfer from small scales to the MJO scale could be resolved better with the help of intensified observations (*in situ* and satellite network) and improved model parameterizations during this project.

In the first part of Chapter 4, the possibility of ocean-atmosphere interactions with different spatial and temporal scales in each medium is demonstrated with analytical solutions to idealized linear governing equations. The major finding is that in the ocean-atmosphere system, the coupling requires a match of the dispersion relations (i.e., the combination of frequency and wavenumber) of the oceanic and the atmospheric oscillations, rather than proximity of the frequency or the wavenumber alone. Especially, the results imply that the meso-scale oceanic variabilities can interact with large-scale atmospheric variabilities, leading to unstable waves in the intraseasonal band. Although the theoretical model is simple and idealized, the

findings provide a framework for the study of the oceanic feedbacks to MJOs. As a follow-up step, in the second part of Chapter 4, the oceanic and the atmospheric responses to the external forcing with distinct scales are tested with GCMs for the ocean and the atmosphere. Specifically, two MJO events in which the surface heat flux is the dominant energy source (Chapter 3) are found to be sensitive to moderate changes in meso-scale warm SST anomalies in the SWIO, with scales comparable to observations. Therefore, in order to further our understanding and to improve model simulations of MJOs, we need to treat MJOs as a phenomenon in an ocean-atmosphere coupled, multi-scale system.

It is necessary to emphasize that although the studies in Chapter 4 aim at MJOs, since the theoretical models (Section 4.1 and Section 4.2.2) are very simple and idealized, they cannot be compared quantitatively to any observations. Especially, the observed MJOs have a first baroclinic mode structure, so that the zonal winds at an upper layer (250 hPa) and a lower layer (850 hPa) are usually used to capture MJO signatures. However, for simplicity of the analytical solutions, I only use a barotropic theoretical model (see more discussion on Section 4.1.4). In the simple and idealized ROMS experiment in Section 4.2.2.2, the ocean is only 150 m deep (the depth of the main thermocline) and the temperature is set to be uniform everywhere to remove the barolinicity. This configuration is quite far from reality, but it enables a comparison between this numerical experiment and the theoretical results in Section 4.2.2.1. However, in the ROMS experiments in Section 4.2.3.1, the topography obtained from the ETOPO2v2 database (NOAA, National Geophysical Data Center, 2006) is realistic. And with more realistic configurations in the ROMS and RSM experiments

(baroclinic structures are allowed), the results can be qualitatively compared to observations.

5.2 Significance of current results

In summary, the results presented in this thesis support the idea that the ocean can have discernible influence on MJOs. There are two ways for the ocean to have impacts on MJOs. One is a passive way, in which the oceanic variabilities are caused initially by the atmospheric forcing and the ensuing ocean response feeds back to the atmosphere. Specifically, the ocean surface is heated due to the reduced latent heat flux during the suppressed phase of the MJOs (Fig. 3.4). The consequent warm SST anomalies provide energy to the perturbations in the atmosphere, prolonging the life time of MJOs. The second way for the oceanic influence on MJOs is more of an active path, in which the warm SST anomalies are independently generated and are attributable to the internal variability in the ocean. As shown in Chapter 2, the influence of the warm ITF water is one important oceanic process which leads to the warm SST anomalies in the western Indian Ocean. The enhanced surface heat flux due to these warm SST anomalies provides energy to the atmospheric perturbations and triggers an MJO event. But the cases in which the ocean actively drives the atmosphere are relatively few. Actually, the role that the ocean-atmosphere coupling can play in MJOs has been debated for long. The calculation of energy sources for MJOs helps to understand the contradiction some model experiments exposed in that the ocean has no detectable influence on MJOs according to some studies (e.g. Hendon 2000; Shinoda et al. 1998) while some other experiments argued that the ocean can improve the MJO simulations (e.g. Jones et al. 1998; Waliser et al. 1999;

Bellon et al. 2008). For simulations of a composite MJO event (an average over many randomly-chosen MJO events, a common technique used in MJO simulation), the perturbed potential energy is likely to provide most energy to the MJO events. Therefore, without the oceanic feedbacks, it is still prone to have reinforced ISVs in the model renditions due to some other sources. Nevertheless, the shorter period of the simulated MJOs, which is a common deficiency in MJO simulations, is evidence for the impact of neglecting the oceanic feedbacks. Therefore, I conclude that the ocean can have influence on the MJOs and is possibly helpful to the improvement of MJO simulations, but overall, the oceanic influence is not the dominant one and its influence varies from event to event.

The theoretical analysis in Chapter 4 raises a fundamental problem about how to represent the oceanic influence on MJOs. General practice is to parameterize the influence of SST anomalies on the latent heat flux (the major communication medium between the ocean and the atmosphere) simply with a bulk formula (e.g., Grodsky et al. 2009), which implies that SST anomalies induce atmospheric variability immediately and with the same scale and *vice versa*. However, according to the theoretical results in this thesis, this *a priori* assumption is not necessarily true. Therefore, connections between the ocean and the atmosphere in current models are questionable. This is not simply a problem of underestimation or overestimation of the oceanic influence on MJOs, but is a problem of misrepresentation of the oceanic influence. Nevertheless, I am aware that the conclusions in Chapter 4 are only based on theoretical models and simplified numerical models, therefore they cannot be quantitatively compared with observations. Thus, the results in the thesis simply raise

the relevant issues rather than offer complete solutions. More studies are certainly needed on how to represent the multi-scale coupling in a simplified framework to facilitate process understanding.

5.3 Implications and future plans

I admit that MJOs must be simulated in coupled ocean-atmosphere models for any potential enhancements in the realism of MJO depictions in models. The results reported in this thesis have important and interesting implications for future work in the following fields:

(1) *Model simulations of MJOs.* I certainly concur that MJOs must be studied in a coupled ocean-atmosphere model. Other than increasing model resolution and applying appropriate parameterizations for deep convection, resolving the oceanic influence is also expected to improve the simulations for many MJO events. One can see from Chapter 2 and Chapter 3 that the key ingredient for the oceanic influence on MJOs is the warm SST anomalies. If the warm SST anomalies are generated by the internal oceanic processes (Chapter 2), the ocean component in the coupled model is required to resolve the mesoscale variabilities both at and below the surface. Thus, a slab ocean model is not likely to be an optimal choice. The atmospheric model should be coupled to an ocean GCM, which has a high enough horizontal resolution (such as $1/3^\circ$ in latitude and $1/2^\circ$ in longitude used in Chapter 2) to resolve the meso-scale processes and enough vertical layers to resolve the variations of the thermocline. If the warm SST anomalies are generated by variations in air-sea heat exchanges, the parameterization of surface heat flux becomes the focus. As implied by the theoretical

results in Chapter 4, the coupling between SST anomalies and surface heat flux may not be on the same scale. Thus, it is reasonable to wonder whether the oceanic footprint in the atmosphere is represented accurately in the present-day CGCMs. This misrepresentation may explain some common deficits in present simulations, such as more regular simulated MJOs than observations (Chapter 4.2). However, it is not easy to foresee a significant improvement in the parameterization of the surface heat flux merely from reanalysis products (NCEP or ERA-40). As discussed above in Section 5.1, more observations (e.g., the ongoing YOTC program) are required to have a better understanding of the ocean-atmosphere heat exchanges in theory and to develop better numerical parameterizations.

(2) *Forecast of MJOs.* A relatively long-lead and accurate prediction of MJOs should definitely be the final goal of such process studies. Currently, MJOs are forecasted with both statistical models and dynamical models (Waliser et al. 2003b, 2006).

The statistical prediction (e.g., Wheeler and Hendon 2004) usually depends on EOF and regression analysis. The EOF analysis is conducted on various variables, such as OLR, the zonal winds (at 200 hPa and 850 hPa), precipitation, and also on a combination of some of these variables (so called multi-variate analysis; e.g., Wheeler and Hendon 2004). Due to the heavy computational burden of EOF analysis, canonical leading EOF modes are established and thereafter they are assumed to be stationary (e.g., the products by NOAA Climate Prediction Center). The regression analysis is conducted on lots of variables with respect to different index for MJOs.

Usually, the regressed variables include OLR, zonal winds at several levels (200, 250, 850 hPa), stream function, velocity potential, and rainfall. But almost no statistical model predicts all variables listed above. The indexes for regression are also defined with various methods, such as EOF, filtering (on frequency bands with slight differences), and the singular variable decomposition (SVD). So far, there has been no agreement on the optimal choice of an index for capturing all of the MJO statistics. The challenge of statistical prediction is obvious, since its accuracy heavily depends on how stationary the process is. The MJOs have pronounced seasonality, irregularity, and a dependence on the background state, none of which are stationary processes. The predictive ability of the statistical method is determined by the time at which the observed state deviates significantly away from the *a priori* assumed stationary state. Therefore, as I understand, the fundamental purpose for research on the statistical predictions is to find a variable or a combination of variables, which can be stationary for as long time as possible. Generally, the statistical prediction procedure derive expressions like

$$X(t + \tau) = X_0(t) + \sum_j \alpha_j \times PC_j(t),$$

where X is the predictand, τ is the time interval for prediction, α is the regression coefficient for the j th principal components (PCs). The PCs are usually created from multi-variables with various methods (as listed above). What I did in this thesis was to try and use a dynamic framework. Broadly speaking, the dynamic analysis can guide the search for an appropriate statistical predictand, so that the search process could be more efficient and more physically meaningful. Specifically for the current results in the thesis, I conclude that different MJO events have different energy

sources, which implies that different physical mechanisms dominate. Therefore, when creating the PCs for MJOs with multiple variables, it seems reasonable to assign appropriate weights to different variables according to the relative importance of different physical mechanisms. For example, as shown in Fig. 3.7, the stability of the air column can be represented by the moist static energy. However, at the beginning of MJO events in which $P'K'$ dominates (Fig. 3.7a & b), the increase of the moist static energy is only due to the variation in Lq at the upper level. While for the MJO events in which R' dominates (Fig. 3.7c), the variation in Lq in the lower atmosphere becomes more important. Hence, we should put different weights on the low-level and high-level variations for different MJO events, when combining them together. Nevertheless, how to assign the weights is a very specific and technical question, which requires careful explorations and tests. Since I mainly focus on the dynamical mechanisms of MJOs, the connections of current results to the statistical prediction are not straightforward, but they can definitely contribute to the improvement of the dynamical prediction of MJOs, as discussed below.

The dynamical prediction (e.g., Vitart et al. 2007), uses GCMs. At present, the skill of the statistical prediction is superior to dynamical forecasts. Hence, it is likely that the predictive ability of the dynamical models is limited by our understanding of the mechanism of MJOs. As introduced in Chapter 1, the mechanisms that drive MJOs are still highly debated. With the analyses in this thesis, it is clearer that the complex behavior of MJOs is hard to be interpreted with any single mechanism or just in the intraseasonal band or with atmospheric processes alone. The results in Chapter 3 and Chapter 4 are expected to contribute to a better understanding of

MJOs. A proper representation of appropriate physical processes is a solid basis for the success of a dynamical model. Thus, one challenge that I will face in the next step will be how to represent the multi-scale interactions (Chapter 4) in a model when all the relevant scales are not explicitly resolved. As emphasized in Section 5.1, the energy sources I calculated in Chapter 3 are only on the MJO scale, without resolving the energy exchange between the MJO scale and the smaller scales. Although NCEP reanalysis cannot resolve small-scale processes either, because of assimilating observation data, NCEP is still reliable on the MJO scale and larger scales (Milliff et al. 2004). However, for a coupled prediction model without data assimilations, the influence of not resolving the small-scale energy exchanges may be a concern, based on the theory in Chapter 4. Therefore, how to parameterize the energy cascade among broad scales in a coupled model is a broad and interesting topic for further study.

Thus far, some dynamical predictions have been conducted with a coupled model. However, the horizontal resolutions in the ocean models involved are usually too coarse to resolve the meso-scale processes in the ocean. Thus, it would not be surprising if the oceanic ISVs (Chapter 2) are small and the oceanic contribution to prolonging the MJOs is not fully captured. Therefore, an eddy-resolving ocean model is desired for the MJO prediction with a coupled model. However, increasing the model resolution (both in the ocean and in the atmosphere) alone does not guarantee a better prediction of MJOs because as discussed above, the parameterization for ocean-atmosphere heat exchange is still a big challenge. Thus, more studies based on observations (like in YOTC) and theoretical analyses are needed to propose a better

parameterization for the surface heat flux and a serious scrutiny of the coupling strength and the coupling mechanisms in the coupled models is timely.

The initial conditions for the MJO forecast are also important (Vitart et al. 2007). Although this issue is not explicitly addressed in the thesis, one can glean some hints from the analysis in Chapter 4.2, which shows that small variations in the external forcing can lead to frequency shifts in the response. Therefore, a large error in the initial value will lead to deficiencies (uncertainty) in the ensuing development of MJOs in a prediction model. Data assimilation, which can incorporate observations and reduce errors in the initial state, is likely to be an excellent approach to reduce initialization errors. Actually, the reanalysis products (NCEP and ERA-40) have been widely used as initial state for the MJO predictions (e.g., Jones et al. 2000; Seo et al. 2005).

In short, in order to achieve a better dynamical prediction of MJOs, I would use an ocean-atmosphere coupled model, which can resolve the meso-scale processes in both the ocean and the atmosphere. A state-of-art parameterization on convection is important, according to many previous studies (Hendon 2000; Woolnough et al. 2001; Waliser 2006). Based on my analysis in the thesis, I also need to pursue improvements in the parameterizations of surface heat flux and the energy cascade among various scales. The initial conditions from the reanalysis products (NCEP and ERA-40) may be good enough for the prediction problem so that attention can be focused on these other issues.

(3) *Other application of the multi-scale coupling hypothesis.* Although the hypothesis of multi-scale interactions is evidently important in my study on MJOs, I expect that it can be applied to studies of other phenomenon. For example, MJOs were found to be related to the low-frequency ENSO by modifying its amplitude and life cycle (Kessler and Kleeman 2000; Zavala-Garay et al. 2005; Neale et al. 2008). A better simulation of MJOs based on current results can hopefully contribute to a better simulation of ENSO. Especially, MJOs are considered to be the leading candidate for the differences in the ENSO strength from event to event (Roulston and Neelin 2000). The concept of multi-scale coupling is expected to help simulate the MJO irregularity (Chapter 4.2). If it turns out to be true in reality, this will also contribute to the simulation of the ENSO irregularity. In addition, as described in Chapter 1, now it is recognized that weather and climate are inseparable parts of an integrated continuum. The intraseasonal oscillations, such as MJOs, serve as a bridge from synoptic scale to planetary-scale features. A better understanding and simulation of MJOs in the multi-scale framework will hopefully lead to further improvement of weather and climate predictions. My preliminary approach to this multi-scale approach has been to investigate the energetics of the MJOs in the new CCSM which appears to have a better representation of ISVs compared to the older version (Neale et al. 2008) and, more interestingly, the better rendition of the background large-scale zonal winds in the new CCSM seems to help the organization of MJOs.

In summary, as discussed in this section, I will continue the dynamical study on MJOs, focusing on translating the process understanding from my analysis to

predictive understanding in high-resolution regional and global coupled climate models and further explore the theoretical aspects of energy cascades related to MJOs between the scales that emerge from these analyses.

Bibliography

- Anderson, D. L. T. and J. P. McCreary, 1985: Slowly Propagating Disturbances in a Coupled Ocean Atmosphere Model. *J. Atmos. Sci.*, **42**, 615-629.
- Annamalai, H., P. Liu, and S. P. Xie, 2005: Southwest Indian Ocean SST variability: Its local effect and remote influence on Asian monsoons. *J. Clim.*, **18**, 4150-4167.
- Annamalai, H., R. Murtugudde, J. Potemra, S. P. Xie, P. Liu, and B. Wang, 2003: Coupled dynamics over the Indian Ocean: spring initiation of the Zonal Mode. *Deep-sea Res. II*, **50**, 2305-2330.
- Bellon, G., A. H. Sobel, and J. Vialard, 2008: Ocean-Atmosphere Coupling in the Monsoon Intraseasonal Oscillation: A Simple Model Study. *J. Clim.*, **21**, 5254-5270.
- Benedict, J. J. and D. A. Randall, 2007: Observed characteristics of the MJO relative to maximum rainfall. *J. Atmos. Sci.*, **64**, 2332-2354.
- Biello, J. A. and A. J. Majda, 2005: A new multiscale model for the Madden-Julian oscillation. *J. Atmos. Sci.*, **62**, 1694-1721.
- Bjerknes, J., 1969: Atmospheric Teleconnections from Equatorial Pacific. *Mon. Wea. Rev.*, **97**, 163-172.
- Blade, I. and D. L. Hartmann, 1993: Tropical Intraseasonal Oscillations in a Simple Nonlinear Model. *J. Atmos. Sci.*, **50**, 2922-2939.
- Boyer, T., S. Levitus, H. Garcia, R. A. Locarnini, C. Stephens, and J. Antonov, 2005: Objective analyses of annual, seasonal, and monthly temperature and salinity for the world ocean on a 0.25 degrees grid. *Int. J. Clim.*, **25**, 931-945.
- Carton, J. A. and B. S. Giese, 2008: A reanalysis of ocean climate using Simple Ocean Data Assimilation (SODA). *Mon. Wea. Rev.*, **136**, 2999-3017.
- Carton, J. A., G. Chepurin, and X. H. Cao, 2000a: A Simple Ocean Data Assimilation analysis of the global upper ocean 1950-95. Part II: Results. *J. Phys. Oceanogr.*, **30**, 311-326.
- Carton, J. A., G. Chepurin, X. H. Cao, and B. Giese, 2000b: A Simple Ocean Data Assimilation analysis of the global upper ocean 1950-95. Part I: Methodology. *J. Phys. Oceanogr.*, **30**, 294-309.
- Cassou, C., 2008: Intraseasonal interaction between the Madden-Julian Oscillation and the North Atlantic Oscillation. *Nature*, **455**, 523-527.
- Chambers, D. P., B. D. Tapley, and R. H. Stewart, 1999: Anomalous warming in the Indian Ocean coincident with El Nino. *J. Geophys. Res.*, **104**, 3035-3047.
- Chelton, D. B. and M. G. Schlax, 1996: Global observations of oceanic Rossby waves. *Science*, **272**, 234-238.

- Chen, D., L. M. Rothstein, and A. J. Busalacchi, 1994: A Hybrid Vertical Mixing Scheme and Its Application to Tropical Ocean Models. *J. Phys. Oceanogr.*, **24**, 2156-2179.
- Chen, D., M. A. Cane, A. Kaplan, S. E. Zebiak, and D. J. Huang, 2004: Predictability of El Nino over the past 148 years. *Nature*, **428**, 733-736.
- Chou, S. H., E. Nelkin, J. Ardizzone, and R. M. Atlas, 2004: A comparison of latent heat fluxes over global oceans for four flux products. *J. Clim.*, **17**, 3973-3989.
- Chou, S. H., E. Nelkin, J. Ardizzone, R. M. Atlas, and C. L. Shie, 2003: Surface turbulent heat and momentum fluxes over global oceans based on the Goddard Satellite retrievals, version 2 (GSSTF2). *J. Clim.*, **16**, 3256-3273.
- Conkright, M. E., J. I. Antonov, O. K. Baranova, T. P. Boyer, H. E. Garcia, R. Gelfeld, D. Johnson, R. A. Locarnini, P. P. Murphy, T. D. O'Brien, I. Smolyar, and C. Stephens, 2002: World Ocean Database 2001 Volume 1: Introduction, U. S. Government Printing Office: Washington, D. C.
- Crum, F. X. and D. E. Stevens, 1983: A Comparison of 2 Cumulus Parameterization Schemes in a Linear-Model of Wave-Cisk. *J. Atmos. Sci.*, **40**, 2671-2688.
- Dewitte, B., S. Purca, S. Illig, L. Renault, and B. S. Giese, 2008: Low-Frequency Modulation of Intraseasonal Equatorial Kelvin Wave Activity in the Pacific from SODA: 1958-2001. *J. Clim.*, **21**, 6060-6069.
- Du, Y., T. D. Qu, G. Meyers, Y. Masumoto, and H. Sasaki, 2005: Seasonal heat budget in the mixed layer of the southeastern tropical Indian Ocean in a high-resolution ocean general circulation model. *J. Geophys. Res.*, **110**.
- Edwards, L. A., R. E. Housego-Stokes, and P. Cipollini, 2006: Altimeter observations of the MJO/ENSO connection through Kelvin waves. *International Journal of Remote Sensing*, **27**, 1193-1203.
- Emanuel, K. A., 1987: An Air-Sea Interaction-Model of Intraseasonal Oscillations in the Tropics. *J. Atmos. Sci.*, **44**, 2324-2340.
- Farrar, J. T. and R. A. Weller, 2006: Intraseasonal variability near 10 degrees N in the eastern tropical Pacific Ocean. *J. Geophys. Res.*, **111**.
- Feng, L. C. and J. P. Li, 2006: A comparison of latent heat fluxes over global oceans for ERA and NCEP with GSSTF2. *Geophys. Res. Lett.*, **33**.
- Feng, M. and S. Wijffels, 2002: Intraseasonal variability in the south equatorial current of the east Indian Ocean. *J. Phys. Oceanogr.*, **32**, 265-277.
- Flügel, M., P. Chang, and C. Penland, 2004: The role of stochastic forcing in modulating ENSO predictability. *J. Clim.*, **17**, 3125-3140.
- Fu, X. H., B. Wang, T. Li, and J. P. McCreary, 2003: Coupling between northward-propagating, intraseasonal oscillations and sea surface temperature in the Indian Ocean. *J. Atmos. Sci.*, **60**, 1733-1753.
- Garrett, C., 2001: What is the "near-inertial" band and why is it different from the rest of the internal wave spectrum? *J. Phys. Oceanogr.*, **31**, 962-971.

- Gill, A. E., 1982: Atmosphere-Ocean Dynamics, Academic Press, New York, NY.
- Godfrey, J. S., 1996: The effect of the Indonesian throughflow on ocean circulation and heat exchange with the atmosphere: A review. *J. Geophys. Res.*, **101**, 12217-12237.
- Gordon, A. L., R. D. Susanto, and K. Vranes, 2003: Cool Indonesian throughflow as a consequence of restricted surface layer flow. *Nature*, **425**, 824-828.
- Gordon, A. L., 2001: Interocean exchange. Ocean Circulation and Climate, G. Siedler et al., Eds., Academic Press, 303-314.
- Grodsky, S. A., A. Bentamy, J. A. Carton, and R. T. Pinker, 2009: Intraseasonal Latent Heat Flux Based on Satellite Observations. *J. Clim.*, **22**, 4539-4556.
- Han, W. Q., 2005: Origins and dynamics of the 90-day and 30-60-day variations in the equatorial Indian Ocean. *J. Phys. Oceanogr.*, **35**, 708-728.
- Han, W. Q., P. J. Webster, J. L. Lin, W. T. Liu, R. Fu, D. L. Yuan, and A. X. Hu, 2008: Dynamics of intraseasonal sea level and thermocline variability in the equatorial Atlantic during 2002-03. *J. Phys. Oceanogr.*, **38**, 945-967.
- Hansen, D. V. and C. A. Paul, 1984: Genesis and Effects of Long Waves in the Equatorial Pacific. *J. Geophys. Res.*, **89**, 431-440.
- Hendon, H. H., 2000: Impact of air-sea coupling on the Madden-Julian oscillation in a general circulation model. *J. Atmos. Sci.*, **57**, 3939-3952.
- Hendon, H. H. and J. Glick, 1997: Intraseasonal air-sea interaction in the tropical Indian and Pacific Oceans. *J. Clim.*, **10**, 647-661.
- Hendon, H. H., B. Liebmann, and J. D. Glick, 1998: Oceanic Kelvin waves and the Madden-Julian oscillation. *J. Atmos. Sci.*, **55**, 88-101.
- Hermes, J. C. and C. J. C. Reason, 2008: Annual cycle of the South Indian Ocean (Seychelles-Chagos) thermocline ridge in a regional ocean model. *J. Geophys. Res.*, **113**.
- Hirst, A. C., 1986: Unstable and Damped Equatorial Modes in Simple Coupled Ocean Atmosphere Models. *J. Atmos. Sci.*, **43**, 606-630.
- Hirst, A. C. and J. S. Godfrey, 1993: The Role of Indonesian Throughflow in a Global Ocean Gcm. *J. Phys. Oceanogr.*, **23**, 1057-1086.
- , 1994: The Response to a Sudden Change in Indonesian Throughflow in a Global Ocean Gcm. *J. Phys. Oceanogr.*, **24**, 1895-1910.
- Holton, J. R., 2004: An Introduction to Dynamic Meteorology (4th edition). Academic Press, New York, 535 pp.
- Hu, Q. and D. A. Randall, 1995: Low-Frequency Oscillations in Radiative Convective Systems .2. An Idealized Model. *J. Atmos. Sci.*, **52**, 478-490.
- Iskandar, I., W. Mardiansyah, Y. Masumoto, and T. Yamagata, 2005: Intraseasonal Kelvin waves along the southern coast of Sumatra and Java. *J. Geophys. Res.*, **110**.

- Iskandar, I., T. Tozuka, H. Sasaki, Y. Masumoto, and T. Yamagata, 2006: Intraseasonal variations of surface and subsurface currents off Java as simulated in a high-resolution ocean general circulation model. *J. Geophys. Res.*, **111**.
- Jiang, N., J. D. Neelin, and M. Ghil, 1995: Quasi-quadrennial and quasi-biennial variability in the equatorial Pacific. *Clim. Dyn.*, **12**, 101-112.
- Jin, F. F., J. D. Neelin, and M. Ghil, 1994: El-Nino on the Devils Staircase - Annual Subharmonic Steps to Chaos. *Science*, **264**, 70-72.
- Jochum, M. and P. Malanotte-Rizzoli, 2003: On the generation of North Brazil current rings. *J. Mar. Res.*, **61**, 147-173.
- Jochum, M. and R. Murtugudde, 2005: Internal variability of Indian Ocean SST. *J. Clim.*, **18**, 3726-3738.
- Jochum, M., R. Murtugudde, R. Ferrari, and P. Malanotte-Rizzoli, 2005: The impact of horizontal resolution on the tropical heat budget in an Atlantic ocean model. *J. Clim.*, **18**, 841-851.
- Jones, C., 2009: A Homogeneous Stochastic Model of the Madden-Julian Oscillation. *J. Clim.*, **22**, 3270-3288.
- Jones, C., D. E. Waliser, J. K. E. Schemm, and W. K. M. Lau, 2000: Prediction skill of the Madden and Julian Oscillation in dynamical extended range forecasts. *Clim. Dyn.*, **16**, 273-289.
- Jones, C., D. E. Waliser, and C. Gautier, 1998: The influence of the Madden-Julian oscillation on ocean surface heat fluxes and sea surface temperature. *J. Clim.*, **11**, 1057-1072.
- Kalnay, E., and Coauthors, 1996: The NCEP/NCAR 40-Year Reanalysis Project. *Bull. Amer. Meteor. Soc.*, **77**, 437-471.
- Kanamaru, H. and M. Kanamitsu, 2007: Scale-selective bias correction in a downscaling of global analysis using a regional model. *Mon. Wea. Rev.*, **135**, 334-350.
- Kanamitsu, M., W. Ebisuzaki, J. Woollen, S. K. Yang, J. J. Hnilo, M. Fiorino, and G. L. Potter, 2002: NCEP-DOE AMIP-II reanalysis (R-2). *Bull. Amer. Meteor. Soc.*, **83**, 1631-1643.
- Kemball-Cook, S. R. and B. C. Weare, 2001: The onset of convection in the Madden-Julian oscillation. *J. Clim.*, **14**, 780-793.
- Kessler, W. S. and R. Kleeman, 2000: Rectification of the Madden-Julian oscillation into the ENSO cycle. *J. Clim.*, **13**, 3560-3575.
- Kessler, W. S., M. J. McPhaden, and K. M. Weickmann, 1995: Forcing of Intraseasonal Kelvin Waves in the Equatorial Pacific. *J. Geophys. Res.*, **100**, 10613-10631.
- Kim, H. M., C. D. Hoyos, P. J. Webster, and I. S. Kang, 2008: Sensitivity of MJO Simulation and Predictability to Sea Surface Temperature Variability. *J. Clim.*, **21**, 5304-5317.

- Kleeman, R., 2008: Stochastic theories for the irregularity of ENSO. *Phil. Trans. R. Soc. A*, **366**, 2511-2526.
- Kleeman, R. and A. M. Moore, 1997: A theory for the limitation of ENSO predictability due to stochastic atmospheric transients. *J. Atmos. Sci.*, **54**, 753-767.
- Klein, S. A., B. J. Soden, and N. C. Lau, 1999: Remote sea surface temperature variations during ENSO: Evidence for a tropical atmospheric bridge. *J. Clim.*, **12**, 917-932.
- Krishnamurti, T. N., D. K. Oosterhof, and A. V. Mehta, 1988: Air Sea Interaction on the Time Scale of 30 to 50 Days. *J. Atmos. Sci.*, **45**, 1304-1322.
- Lau, K. M. and L. Peng, 1987: Origin of Low-Frequency (Intraseasonal) Oscillations in the Tropical Atmosphere .1. Basic Theory. *J. Atmos. Sci.*, **44**, 950-972.
- Lau, K. M. and C. H. Sui, 1997: Mechanisms of short-term sea surface temperature regulation: Observations during TOGA COARE. *J. Clim.*, **10**, 465-472.
- Liebmann, B. and C. A. Smith, 1996: Description of a complete (interpolated) outgoing longwave radiation dataset. *Bull. Amer. Meteor. Soc.*, **77**, 1275-1277.
- Lin, H., G. Brunet, and J. Derome, 2009: An Observed Connection between the North Atlantic Oscillation and the Madden-Julian Oscillation. *J. Clim.*, **22**, 364-380.
- Lin, X. and R. H. Johnson, 1996: Kinematic and thermodynamic characteristics of the flow over the western Pacific warm pool during TOGA COARE. *J. Atmos. Sci.*, **53**, 695-715.
- Lindzen, R. S., 1974: Wave-Cisk in Tropics. *J. Atmos. Sci.*, **31**, 156-179.
- Lorenz, E. N., 1955: Available potential energy and the maintenance of the general circulation. *Tellus*, **7**, 157-167.
- Lukas, R. and E. Lindstrom, 1991: The Mixed Layer of the Western Equatorial Pacific-Ocean. *J. Geophys. Res.*, **96**, 3343-3357.
- Madden, R. A. and P. R. Julian, 1971: Detection of a 40-50 Day Oscillation in Zonal Wind in Tropical Pacific. *J. Atmos. Sci.*, **28**, 702-708.
- , 1972: Description of Global-Scale Circulation Cells in Tropics with a 40-50 Day Period. *J. Atmos. Sci.*, **29**, 1109-1123.
- , 1994: Observations of the 40-50-Day Tropical Oscillation - a Review. *Mon. Wea. Rev.*, **122**, 814-837.
- , 2005: Historical perspective. *Intraseasonal Variability in the Atmosphere-Ocean Climate System*, W. K.-M. Lau and D. Waliser, Eds., Springer-Praxis, 1 - 16.
- Maloney, E. D. and A. H. Sobel, 2004: Surface fluxes and ocean coupling in the tropical intraseasonal oscillation. *J. Clim.*, **17**, 4368-4386.
- Masumoto, Y. and G. Meyers, 1998: Forced Rossby waves in the southern tropical Indian Ocean. *J. Geophys. Res.*, **103**, 27589-27602.

- McClain, E. P., W. G. Pichel, and C. C. Walton, 1985: Comparative Performance of Avhrr-Based Multichannel Sea-Surface Temperatures. *J. Geophys. Res.*, **90**, 1587-1601.
- Meyers, G., 1996: Variation of Indonesian throughflow and the El Nino Southern Oscillation. *J. Geophys. Res.*, **101**, 12255-12263.
- Meyers, S. D., B. G. Kelly, and J. J. O'Brien, 1993: An Introduction to Wavelet Analysis in Oceanography and Meteorology - with Application to the Dispersion of Yanai Waves. *Mon. Wea. Rev.*, **121**, 2858-2866.
- Milliff, R. F., J. Morzel, D. B. Chelton, and M. H. Freilich, 2004: Wind stress curl and wind stress divergence biases from rain effects on QSCAT surface wind retrievals. *J. Atmos. Oceanic Technol.*, **21**, 1216-1231.
- Moore, A. M. and R. Kleeman, 1998: Skill assessment for ENSO using ensemble prediction. *Q. J. R. Meteorol. Soc.*, **124**, 557-584.
- Morrow, R. and F. Birol, 1998: Variability in the southeast Indian Ocean from altimetry: Forcing mechanisms for the Leeuwin Current. *J. Geophys. Res.*, **103**, 18529-18544.
- Murtugudde, R. and A. J. Busalacchi, 1999: Interannual variability of the dynamics and thermodynamics of the tropical Indian Ocean. *J. Clim.*, **12**, 2300-2326.
- Murtugudde, R., R. Seager, and A. Busalacchi, 1996: Simulation of the tropical oceans with an ocean GCM coupled to an atmospheric mixed-layer model. *J. Clim.*, **9**, 1795-1815.
- Murtugudde, R., A. J. Busalacchi, and J. Beauchamp, 1998: Seasonal-to-interannual effects of the Indonesian throughflow on the tropical Indo-Pacific Basin. *J. Geophys. Res.*, **103**, 21425-21441.
- Murtugudde, R., J. P. McCreary, and A. J. Busalacchi, 2000: Oceanic processes associated with anomalous events in the Indian Ocean with relevance to 1997-1998. *J. Geophys. Res.*, **105**, 3295-3306.
- Neale, R. B., J. H. Richter, and M. Jochum, 2008: The Impact of Convection on ENSO: From a Delayed Oscillator to a Series of Events. *J. Clim.*, **21**, 5904-5924.
- Neelin, J. D., I. M. Held, and K. H. Cook, 1987: Evaporation-Wind Feedback and Low-Frequency Variability in the Tropical Atmosphere. *J. Atmos. Sci.*, **44**, 2341-2348.
- Neelin, J. D., D. S. Battisti, A. C. Hirst, F. F. Jin, Y. Wakata, T. Yamagata, and S. E. Zebiak, 1998: ENSO theory. *J. Geophys. Res.*, **103**, 14261-14290.
- Oort, A. H. and J. P. Peixoto, 1974: Annual Cycle of Energetics of Atmosphere on a Planetary Scale. *J. Geophys. Res.*, **79**, 2705-2719.
- Pedlosky, J., 1987: *Geophysical Fluid Dynamics*, Springer-Verlag, New York, 2nd edition.
- , 2003: *Waves in the Ocean and Atmosphere: Introduction to Wave Dynamics*, Lecture 9. Springer-Verlag, New York, 260 pp.

- Pegion, K. and B. P. Kirtman, 2008a: The Impact of Air-Sea Interactions on the Predictability of the Tropical Intraseasonal Oscillation. *J. Clim.*, **21**, 5870-5886.
- , 2008b: The Impact of Air-Sea Interactions on the Simulation of Tropical Intraseasonal Variability. *J. Clim.*, **21**, 6616-6635.
- Peña, M., E. Kalnay, and M. Cai, 2003: Statistics of locally coupled ocean and atmosphere intraseasonal anomalies in Reanalysis and AMIP data. *Nonlinear Processes in Geophysics*, **10**, 245-251.
- Plumb, R. A., 1983: A New Look at the Energy Cycle. *J. Atmos. Sci.*, **40**, 1669-1688.
- Potemra, J. T., S. L. Hautala, J. Sprintall, and W. Pandoe, 2002: Interaction between the Indonesian Seas and the Indian Ocean in observations and numerical models. *J. Phys. Oceanogr.*, **32**, 1838-1854.
- Reichler, T. and J. O. Roads, 2005: Long-range predictability in the tropics. Part II: 30-60-day variability. *J. Clim.*, **18**, 634-650.
- Reppin, J., F. A. Schott, J. Fischer, and D. Quadfasel, 1999: Equatorial currents and transports in the upper central Indian Ocean: Annual cycle and interannual variability. *J. Geophys. Res.*, **104**, 15495-15514.
- Reverdin, G., 1987: The Upper Equatorial Indian-Ocean - the Climatological Seasonal Cycle. *J. Phys. Oceanogr.*, **17**, 903-927.
- Rogers, R. R. and M. K. Yau, 1989: A Short Course in Cloud Physics, Chapter 2. Pergamon Press, Elmsford, NY, 293 pp.
- Roulston, M. S. and J. D. Neelin, 2000: The response of an ENSO model to climate noise, weather noise and intraseasonal forcing. *Geophys. Res. Lett.*, **27**, 3723-3726.
- Roundy, P. E. and G. N. Kiladis, 2006: Observed relationships between oceanic kelvin waves and atmospheric forcing. *J. Clim.*, **19**, 5253-5272.
- Roundy, P. E. and J. R. Kravitz, 2009: The Association of the Evolution of Intraseasonal Oscillations to ENSO Phase. *J. Clim.*, **22**, 381-395.
- Roulston M. S. and J. D. Neelin, 2000: The response of an ENSO model to climate noise, weather noise and intraseasonal forcing, *Geophys. Res. Lett.*, **27**, 3723-3726.
- Sardeshmukh, P. D. and P. Sura, 2007: Multiscale impacts of variable heating in climate. *J. Clim.*, **20**, 5677-5695.
- Schiller, A. and J. S. Godfrey, 2003: Indian Ocean intraseasonal variability in an ocean general circulation model. *J. Clim.*, **16**, 21-39.
- Schott, F. A., M. Dengler, and R. Schoenefeldt, 2002: The shallow overturning circulation of the Indian Ocean. *Prog. Oceanogr.*, **53**, 57-103.
- Seager, R., M. B. Blumenthal, and Y. Kushnir, 1995: An Advective Atmospheric Mixed-Layer Model for Ocean Modeling Purposes - Global Simulation of Surface Heat Fluxes. *J. Clim.*, **8**, 1951-1964.

- Sengupta, D., R. Senan, and B. N. Goswami, 2001: Origin of intraseasonal variability of circulation in the tropical central Indian Ocean. *Geophys. Res. Lett.*, **28**, 1267-1270.
- Seo, K. H., J. K. E. Schemm, C. Jones, and S. Moorthi, 2005: Forecast skill of the tropical intraseasonal oscillation in the NCEP GFS dynamical extended range forecasts. *Clim. Dyn.*, **25**, 265-284.
- Shchepetkin, A. F. and J. C. McWilliams, 2003: A method for computing horizontal pressure-gradient force in an oceanic model with a nonaligned vertical coordinate. *J. Geophys. Res.*, **108**.
- , 2005: The regional oceanic modeling system (ROMS): a split-explicit, free-surface, topography-following-coordinate oceanic model. *Ocean Modelling*, **9**, 347-404.
- Shinoda, T., H. H. Hendon, and J. Glick, 1998: Intraseasonal variability of surface fluxes and sea surface temperature in the tropical western Pacific and Indian Oceans. *J. Clim.*, **11**, 1685-1702.
- Simmons, A. J., and J. K. Gibson, Eds., 2000: The ERA-40 project plan. ERA-40 Project Report Series 1, 62 pp.
- Slingo, J. M., K. R. Sperber, J. S. Boyle, J. P. Ceron, M. Dix, B. Dugas, W. Ebisuzaki, J. Fyfe, D. Gregory, J. F. Gueremy, J. Hack, A. Harzallah, P. Inness, A. Kitoh, W. K. M. Lau, B. McAvaney, R. Madden, A. Matthews, T. N. Palmer, C. K. Park, D. Randall, and N. Renno, 1996: Intraseasonal oscillations in 15 atmospheric general circulation models: Results from an AMIP diagnostic subproject. *Clim. Dyn.*, **12**, 325-357.
- Sobel, A. H., E. D. Maloney, G. Bellon, and D. M. Frierson, 2008: The role of surface heat fluxes in tropical intraseasonal oscillations. *Nature Geoscience*, **1**, 653-657.
- Song, Q. and A. L. Gordon, 2004: Significance of the vertical profile of the Indonesian Throughflow transport to the Indian Ocean. *Geophys. Res. Lett.*, **31**.
- Song, Q., A. L. Gordon, and M. Visbeck, 2004: Spreading of the Indonesian throughflow in the Indian Ocean. *J. Phys. Oceanogr.*, **34**, 772-792.
- Sperber, K. R., 2003: Propagation and the vertical structure of the Madden-Julian oscillation. *Mon. Wea. Rev.*, **131**, 3018-3037.
- Sperber, K. R., J. M. Slingo, P. M. Inness, and W. K. M. Lau, 1997: On the maintenance and initiation of the intraseasonal oscillation in the NCEP/NCAR reanalysis and in the GLA and UKMO AMIP simulations. *Clim. Dyn.*, **13**, 769-795.
- Sprintall, J. and M. Tomczak, 1992: Evidence of the Barrier Layer in the Surface-Layer of the Tropics. *J. Geophys. Res.*, **97**, 7305-7316.
- Sprintall, J., A. L. Gordon, R. Murtugudde, and R. D. Susanto, 2000: A semiannual Indian Ocean forced Kelvin wave observed in the Indonesian seas in May 1997. *J. Geophys. Res.*, **105**, 17217-17230.

- Starr, V. P., 1968: Physics of Negative Viscosity Phenomena. McGraw-Hill, New York, 256 pp.
- Tignol, J.-P., 2001: Galois' Theory of Algebraic Equations. World Scientific, New Jersey, 333pp.
- Torrence, C. and G. P. Compo, 1998: A practical guide to wavelet analysis. *Bull. Amer. Meteor. Soc.*, **79**, 61-78.
- Tozuka, T., T. D. Qu, and T. Yamagata, 2007: Dramatic impact of the South China Sea on the Indonesian Throughflow. *Geophys. Res. Lett.*, **34**.
- Tziperman, E., M. A. Cane, and S. E. Zebiak, 1995: Irregularity and Locking to the Seasonal Cycle in an Enso Prediction Model as Explained by the Quasi-Periodicity Route to Chaos. *J. Atmos. Sci.*, **52**, 293-306.
- Tziperman, E., L. Stone, M. A. Cane, and H. Jarosh, 1994: El-Nino Chaos - Overlapping of Resonances between the Seasonal Cycle and the Pacific Ocean-Atmosphere Oscillator. *Science*, **264**, 72-74.
- Vallis, G. K., 2006. Atmospheric and Oceanic Fluid Dynamics: Fundamentals and Large-Scale Circulation. Cambridge University Press, 745 pp.
- Vitart, F., S. Woolnough, M. A. Balmaseda, and A. M. Tompkins, 2007: Monthly forecast of the Madden-Julian oscillation using a coupled GCM. *Mon. Wea. Rev.*, **135**, 2700-2715.
- Vranes, K., A. L. Gordon, and A. Field, 2002: The heat transport of the Indonesian Throughflow and implications for the Indian Ocean heat budget. *Deep-Sea Res.*, **49**, 1391-1410.
- Waliser, D. E., K. M. Lau, and J. H. Kim, 1999: The influence of coupled sea surface temperatures on the Madden-Julian oscillation: A model perturbation experiment. *J. Atmos. Sci.*, **56**, 333-358.
- Waliser, D. E., R. Murtugudde, and L. E. Lucas, 2003a: Indo-Pacific Ocean response to atmospheric intraseasonal variability: 1. Austral summer and the Madden-Julian Oscillation. *J. Geophys. Res.*, **108**.
- , 2004: Indo-Pacific Ocean response to atmospheric intraseasonal variability: 2. Boreal summer and the Intraseasonal Oscillation. *J. Geophys. Res.*, **109**.
- Waliser, D. E., K. M. Lau, W. Stern, and C. Jones, 2003b: Potential predictability of the Madden-Julian oscillation. *Bull. Amer. Meteor. Soc.*, **84**, 33-50.
- Waliser, D. E., 2005: Predictability and forecasting. Intraseasonal Variability in the Atmosphere-Ocean Climate System. W. K.-M. Lau and D. Waliser, Eds., Springer-Praxis, 389-424.
- Waliser, D., K. Weickmann, R. Dole, S. Schubert, O. Alves, C. Jones, M. Newman, H. L. Pan, A. Roubicek, S. Saha, C. Smith, H. van den Dool, F. Vitart, M. Wheeler, and J. Whitaker, 2006: The experimental MJO prediction project. *Bull. Amer. Meteor. Soc.*, **87**, 425-431.

- Wang, B. and H. Rui, 1990: Synoptic Climatology of Transient Tropical Intraseasonal Convection Anomalies - 1975-1985. *Meteorology and Atmospheric Physics*, **44**, 43-61.
- Wang, L. P., C. J. Koblinsky, and S. Howden, 2001: Annual Rossby wave in the southern Indian Ocean: Why does it "appear" to break down in the middle ocean? *J. Phys. Oceanogr.*, **31**, 54-74.
- Wang, B., 2005: Theory. Intraseasonal Variability in the Atmosphere-Ocean Climate System, W. K.-M. Lau and D. Waliser, Eds., Springer-Praxis, 307 - 360.
- Webster, P. J., V. O. Magana, T. N. Palmer, J. Shukla, R. A. Tomas, M. Yanai, and T. Yasunari, 1998: Monsoons: Processes, predictability, and the prospects for prediction. *J. Geophys. Res.*, **103**, 14451-14510.
- Weisberg, R. H. and T. J. Weingartner, 1988: Instability Waves in the Equatorial Atlantic-Ocean. *J. Phys. Oceanogr.*, **18**, 1641-1657.
- Wheeler, M. and G. N. Kiladis, 1999: Convectively coupled equatorial waves: Analysis of clouds and temperature in the wavenumber-frequency domain. *J. Atmos. Sci.*, **56**, 374-399.
- Wheeler, M. C. and H. H. Hendon, 2004: An all-season real-time multivariate MJO index: Development of an index for monitoring and prediction. *Mon. Wea. Rev.*, **132**, 1917-1932.
- Woolnough, S. J., J. M. Slingo, and B. J. Hoskins, 2001: The organization of tropical convection by intraseasonal sea surface temperature anomalies. *Q. J. R. Meteorol. Soc.*, **127**, 887-907.
- Woolnough, S. J., F. Vitart, and M. A. Balmaseda, 2007: The role of the ocean in the Madden-Julian Oscillation: Implications for MJO prediction. *Q. J. R. Meteorol. Soc.*, **133**, 117-128.
- Xie, S. P., A. Kubokawa, and K. Hanawa, 1993: Evaporation Wind Feedback and the Organizing of Tropical Convection on the Planetary Scale .2. Nonlinear Evolution. *J. Atmos. Sci.*, **50**, 3884-3893.
- Xie, S. P., H. Annamalai, F. A. Schott, and J. P. McCreary, 2002: Structure and mechanisms of South Indian Ocean climate variability. *J. Clim.*, **15**, 864-878.
- Yang, S., K. M. Lau, and K. M. Kim, 2002: Variations of the East Asian jet stream and Asian-Pacific-American winter climate anomalies. *J. Clim.*, **15**, 306-325.
- Yu, Z. and J. Potemra, 2006: Generation mechanism for the intraseasonal variability in the Indo-Australian basin. *J. Geophys. Res.*, **111**.
- Zavala-Garay, J., C. Zhang, A. M. Moore, and R. Kleeman, 2005: The linear response of ENSO to the Madden-Julian oscillation. *J. Clim.*, **18**, 2441-2459.
- Zebiak, S. E., 1993: Air-Sea Interaction in the Equatorial Atlantic Region. *J. Clim.*, **6**, 1567-1568.
- Zebiak, S. E. and M. A. Cane, 1987: A Model El-Nino Southern Oscillation. *Mon. Wea. Rev.*, **115**, 2262-2278.

- Zhang, C. D., 1996: Atmospheric intraseasonal variability at the surface in the tropical western Pacific Ocean. *J. Atmos. Sci.*, **53**, 739-758.
- , 2005: Madden-Julian oscillation. *Reviews of Geophysics*, **43**.
- Zhang, C. D., M. Dong, S. Gualdi, H. H. Hendon, E. D. Maloney, A. Marshall, K. R. Sperber, and W. Q. Wang, 2006: Simulations of the Madden-Julian oscillation in four pairs of coupled and uncoupled global models. *Clim. Dyn.*, **27**, 573-592.
- Zhou, L. and R. Murtugudde, 2009: Ocean-Atmosphere Coupling on Different Spatiotemporal Scales: A Mechanism for Intraseasonal Instabilities. *J. Atmos. Sci.*, **66**, 1834-1844.
- Zhou, L., R. Murtugudde, and M. Jochum, 2008a: Dynamics of the intraseasonal oscillations in the Indian Ocean South Equatorial Current. *J. Phys. Oceanogr.*, **38**, 121-132.
- , 2008b: Seasonal influence of Indonesian Throughflow in the southwestern Indian Ocean. *J. Phys. Oceanogr.*, **38**, 1529-1541.